PHD

Measurement and prediction of the fluid borne noise characteristics of hydraulic components and systems

Johnston, David Nigel

Award date:
1987

Awarding institution:
University of Bath

MEASUREMENT AND PREDICTION OF THE FLUID BORNE NOISE CHARACTERISTICS OF HYDRAULIC COMPONENTS AND SYSTEMS

submitted by

DAVID NIGEL JOHNSTON

for the degree of

Ph.D

of the University of Bath

1987

ProQuest LLC
789 East Eisenhower Parkway
P.O. Box 1346
Ann Arbor, MI 48106-1346

SUMMARY

The flow ripple from positive displacement pumps is one of the main sources of fluid-borne noise in hydraulic systems. A new experimental method for the measurement of the source flow ripple and source impedance characteristics of positive displacement pumps, called the 'Secondary Source' method, has been developed. Extensive testing on a variety of pumps proved that the method is effective and that it has several advantages over previous methods, being quick, accurate and versatile. Experimental flow ripple and source impedance results are compared with theoretical models. Correlation with and deviations from the models are investigated.

The Secondary Source method was also applied to the measurement of the impedance characteristics of valves and an accumulator. The accumulator impedance results show very good correlation with a simple theoretical model. Discrepancies are observed between valve impedance measurements and a simple resistance model. Several causes of these discrepancies are isolated, including fluid compressibility and inertia, and valve vibration.

A method for the accurate measurement of the speed of sound in the fluid in a pipe is described. This was applied as an integral part of the Secondary Source method, and is shown to give good results.

Using information obtained from the Secondary Source method, a computer-based simulation package was developed for the prediction of the pressure ripple characteristics of complete hydraulic circuits. This package is useful for the study of the resonant characteristics of circuits, in order that low pressure ripple circuits can be designed. The effectiveness of several different methods for the reduction of fluid-borne noise is discussed.

ACKNOWLEDGEMENTS

I would like to express my gratitude to all the staff of the Fluid Power Centre at the University of Bath who assisted in making this thesis a reality.

Particular thanks are due to the following:

My supervisor, Dr. K.A. Edge, for his unfailing encouragement and guidance.

The laboratory staff for constructing the test apparatus.

Dr. D.G. Tilley for day-to-day advice and discussion.

Thanks are also due to the staff of the University of Bath computer centre for their assistance in the word-processing for this thesis, and to my father, Mr. T.D. Johnston, for his painstaking proof-reading of it.

CONTENTS

Title	Page no.
COPYRIGHT	i
SUMMARY	ii
ACKNOWLEDGEMENTS	iii
NOTATION	ix
1. INTRODUCTION	1
1.1. Background	1
1.2. Objective of Work	3
1.3. Scope of Thesis	3
2. THE ANALYSIS OF WAVE PROPAGATION IN HYDRAULIC SYSTEMS	5
2.1. Positive Displacement Pumps and Flow Ripple	6
2.1.1. Source Flow Ripple from an Axial Piston Pump	7
2.1.2. Source Flow Ripple from External Gear Pumps	8
2.2. Wave Analysis of Fluid-Borne Noise in a Simple Pipe	9
2.3. Application of the Wave Equations to a Simple System	14
2.4. Standing Waves	17
2.5. Resonance	17
2.6. Derivation of the Reflection Coefficient as a Function of Z_0 and Z_T	18
2.7. Limitations on the Range of the Reflection Coefficient	19
2.8. Values of Reflection Coefficient for Special Cases of Termination Impedance	20
2.9. Entry Impedance	21
2.10. Modelling of Systems with More than One Source of Fluid-Borne Noise	22
2.11. Lumped Parameter and Distributed Parameter Modelling of Components	23
2.12. Two-port Models and Transfer Matrices	23
2.12.1. Derivation of the Transfer Matrices for a Rigid Pipe	24

3. EXPERIMENTAL METHODS FOR PRODUCING A PUMP FLUID-BORNE NOISE RATING 26

3.1. Unruh's Method 28
3.2. Szerlag's Method 29
3.3. Davidson and Taylor's Method 29
3.4. 'High Impedance Pipe' Method 30
3.5. 'Additional Capacity' Method 32
3.6. 'Insert' Method 33
3.7. 'Extending Pipe Length' and 'Hydraulic Trombone' Methods 33
3.8. 'Reflectionless Termination' Method 34

4. THE MEASUREMENT OF PUMP FLOW RIPPLE AND SOURCE IMPEDANCE 37

4.1. The 'Intensity' Method 38
4.2. The Standing Wave Method 39
4.3. The Secondary Source Method 41
4.3.1. Source Impedance Measurement 42
4.3.2. The Secondary Fluid-Borne Noise Source 43
4.3.3. Optimisation of Test Rig Configuration 45
4.3.3.1. Pipe Length and Transducer Spacing Optimisation 45
4.3.3.2. Pipe Diameter Optimisation 47
4.3.4. Description of Hydraulic Circuit 48
4.3.4.1. Measurement Section 49
4.3.5. Instrumentation 50
4.3.5.1. Pressure Transducers 50
4.3.5.2. Frequency Response Analyser 50
4.3.6. Computer Control of Data Acquisition 53
4.3.7. Data Acquisition for Source Impedance Calculation 53
4.3.8. Data Acquisition for Flow Ripple Calculation 54
4.3.9. Modelling the Source Impedance Characteristics of a Positive Displacement Pump or Motor 54
4.3.9.1. Modified Model Taking Distributed Friction Into Account 57
4.3.10. Referral of the Source Flow Ripple within the Pump 58

5. RESULTS OF PUMP TESTS USING THE 'SECONDARY SOURCE' TECHNIQUE 60

5.1. Results of Source Impedance Tests 60
5.1.1. Pump 'B' - Fixed Capacity Axial Piston Pump 60
5.1.2. Pump 'A' - Variable Displacement Axial Piston Pump 61
5.1.3. Pumps 'C' - External Gear Pumps 62
5.1.4. Pumps 'D' - External Gear Pumps 62
5.1.5. Pump 'E' - Balanced Vane Pump 63
5.2. Source Flow Ripple Experimental Results 63
5.2.1. Pump 'A' - Variable Displacement Axial Piston Pump 63
5.2.2. Pump 'B' - Fixed Capacity Axial Piston Pump 65
5.2.3. Pumps 'C' - External Gear Pumps 66
5.2.4. Pump 'D1' - External Gear Pump 66
5.2.5. Pump 'D2' - External Gear Pump 67
5.2.6. Pump 'E' - Balanced Vane Pump 67

6. RESULTS OF IMPEDANCE TESTS ON PASSIVE COMPONENTS 68

6.1. Accumulator Impedance Tests 68
6.1.1. Theoretical Impedance 68
6.1.2. Experimental Technique 70
6.1.3. Results 71
6.2. Restrictor Valve Impedance Tests 73
6.2.1. Experimental Technique 74
6.2.2. Variation of Resistance with Mean Pressure Drop and Flow Rate 77
6.2.3. Correlation between Steady State Characteristics and Dynamic Resistance 79
6.2.4. Variation of the Flow Coefficient with Reynold's Number 80
6.3. Results of Tests on Pressure Compensated Flow Control Valve 'V2' 81
6.4. Results of Impedance Tests on Relief Valves 84
6.4.1. Valve 'V3' - Single Stage Cartridge Relief Valve 85
6.4.2. Valve 'V4' - Two Stage Cartridge Relief Valve 86
6.4.3. Valve 'V5' - Two Stage Relief Valve 87
6.5. Simulation of the Impedance Characteristics of Two-Stage Relief Valves 88
6.5.1. Derivation of Mathematical Model of Valve 'V5' 89
6.5.2. Simulation Results for Valve 'V5' 94
6.5.3. Simulation Results for Valve 'V4' 94

6.5.4. Relief Valve Mathematical Modelling - Conclusions 95

7. EXPERIMENTAL DETERMINATION OF THE WAVE PROPAGATION CHARACTERISTICS OF A HYDRAULIC LINE 98

7.1. Evaluation of the Speed of Sound 98
7.1.1. Evaluation of the Experimental Speed of Sound using Three Unequally Spaced Pressure Transducers 102
7.1.2. Experimental Speed of Sound Results 104
7.2. Wave Propagation Measurements using a Small Diameter Pipe 105
7.2.1. Measurement of the Pipe Resistance 105
7.2.2. Experimental Results 108

8. SIMULATION OF THE FLUID-BORNE NOISE CHARACTERISTICS OF HYDRAULIC CIRCUITS 110

8.1. Mode of Operation of the Pressure Ripple Automatic Simulation Package 110
8.1.1. Generation of Circuit Configuration 111
8.1.2. Definition of Component Parameters 112
8.1.3. Sweep Definition 112
8.1.4. Generation and Solution of Simultaneous Equations Defining System Response 113
8.1.5. Output of Results in the Required Format 115
8.2. Formulation of a Comprehensive Model for a Flexible Hose 115
8.2.1. Evaluation of Accuracy of Hose Model 119
8.3. Modelling of Pump Flow Ripple Characteristics 120
8.3.1. External Gear Pump Flow Ripple Model 120
8.3.2. Axial Piston Pump Flow Ripple Model 121
8.4. Validation of Simulation Results 124
8.5. Simulation of Pump Source Impedance Characteristics 125
8.5.1. Source Impedance Simulation - Pump 'A' 126
8.5.2. Source Impedance Simulation - Pump 'C' 126
8.5.3. Source Impedance Simulation - Pump 'D' 126

9. PRACTICAL METHODS OF REDUCTION OF FLUID-BORNE NOISE 129

9.1. Reduction of the Source Flow Ripple of Positive Displacement Pumps 129
9.1.1. Case study: Axial Piston Pump Flow Ripple Simulation 130
9.1.1.1. Effect of Port Plate Modification 131
9.1.1.2. Effect of Port Plate Timing 132
9.1.1.3. Effect of Solid Pistons 132
9.1.2. Reduction of External Gear Pump Flow Ripple 133
9.2. Source Impedance Modification 134
9.3. Tuning of the Overall Hydraulic System 135
9.4. Fluid-Borne Noise Attenuators 136
9.4.1. Accumulators as Fluid-Borne Noise Attenuators 136
9.4.2. The Herschel-Quincke Tube 138
9.4.2.1. Analysis of the Herschel-Quincke Tube 138
9.4.2.2. Simulation Results 141

10. CONCLUSIONS 143

10.1. Recommendations for Further Work 145

REFERENCES 147

APPENDICES:

A1. DETAILS OF COMPONENTS 155

A1.1. Details of Instrumentation 156

A2. DESCRIPTION OF FLOW RIPPLE GENERATOR 158

A3. ALGORITHM USED FOR THE ANALYSIS OF THE PRESSURE STANDING WAVE 160

A3.1. Calculation of the Source Flow Ripple 162

A4. ALGORITHM USED FOR THE MATHEMATICAL MODELLING OF THE SOURCE IMPEDANCE 165

A4.1. Stability of Iteration 168

NOTATION

Except where otherwise stated in the text, the following definitions apply.

SYMBOL	DESCRIPTION
A	Internal cross-sectional area of pipe
A_v	Area of orifice
b	Gear width
B	Bulk modulus
B_{eff}	Effective bulk modulus
B_T	Isentropic tangent bulk modulus of fluid
c	ha dependent phase velocity in fluid
c_0	Speed of sound in fluid
c_D	Discharge coefficient
c_Q	Flow coefficient
$c_1 - c_4$	Model coefficients
C	Capacitance
d	Pipe internal diameter
$\tilde{d}$	Mean of pipe internal and external diameters
d_H	Hydraulic mean diameter
E	Young's modulus of pipe
E	Sum of squares error
F	Forward travelling pressure wave
G	Reverse travelling pressure wave
h	Perimeter
H_{ij}	Pressure transfer function P_i / P_j
ha	Wave shear number
j	$\sqrt{-1}$
k	Spring stiffness
l	Pipe length
L	Inductance
m	Mass
N	Modal ratio for hose
N_R	Reynold's number
p	Pressure ripple (time domain)
P	Pressure ripple (frequency domain)
$\tilde{P}$	Mean pressure

P_B	Blocked acoustic pressure
P_l	Pressure ripple at position $x = l$
P_x	Pressure ripple at position x
P_0	Pressure ripple at position $x = 0$
q	Flow ripple (time domain)
Q	Flow ripple (frequency domain)
$\tilde{Q}$	Mean flow rate
Q_k	Kinematic flow ripple
Q_l	Flow ripple at position $x = l$
$\tilde{Q}_{leakage}$	mean leakage flow rate
q_{max}	Maximum instantaneous flow rate
Q_S	Source flow ripple
Q_S^*	Source flow ripple referred inside pump
Q_x	Flow ripple at position x
Q_0	Flow ripple at position $x = 0$
r	gear pitch circle radius
R	Resistance
R	Steady state resistance of pipe (pressure drop/unit length/unit flow)
R_{eff}	ha dependent effective resistance of pipe
t	Pipe wall thickness
t	Time
U	Velocity
$\tilde{v}$	Mean fluid velocity
V	Lumped volume
x	Distance from source
X	Reactance
z	Number of pumping elements
Z	Impedance
Z_E	Entry impedance
Z_P	Characteristic displacement impedance of hose
Z_S	Source impedance
Z_{sys}	Circuit impedance
Z_T	Termination impedance
Z_0	Pipe characteristic impedance
α	Wave attenuation coefficient (real part of γ)
γ	Wave propagation coefficient
γ	Ratio of specific heats
$\Delta\tilde{P}$	Mean pressure difference across component
Δx	Distance between pressure transducers

ϵ	Error between experimental point and model
θ	Poppet angle relative to axis of symmetry
θ_p	Gear pressure angle
μ	Dynamic viscosity
ν	Poisson's ratio of pipe wall
ν	Kinematic viscosity
ξ	Complex wave profile factor
ρ_E	Entry reflection coefficient
ρ_S	Source reflection coefficient
ρ_T	Termination reflection coefficient
ρ	Density of fluid
ρ_{eff}	*ha* dependent effective density
τ	time delay/advance
ϕ	phase angle
ψ	rotation of gears
ω	Angular frequency
Ω	Shaft angular velocity

SUBSCRIPTS (except where included above)

a	Accumulator
c	Capacitive
e	Experimental value
eff	Effective value
i	Incident wave
IN	Inlet
OUT	Outlet
p	Pump
PC	Precharge condition
r	Reflected wave
t	Theoretical or modelled value
U	Upstream
V	Downstream
v	Valve

note: $\bar{x}$ represents the complex conjugate of x.

$\tilde{x}$ represents the mean value of x.

CHAPTER 1

INTRODUCTION

1.1. Background

In recent years, there has been a growing awareness of the hazards of industrial noise. Apart from the general nuisance factor of noise, it can be damaging to health and safety. Prolonged exposure to excessive noise levels can lead to premature deafness, and the associated structural vibration can be a cause of machine failure due to fatigue or components being shaken loose.

Hydraulic circuits often tend to cause severe noise. Much research has been carried out in the past in this field. Broadly speaking, in the study of hydraulic system noise, three distinct areas can be defined, commonly known as 'Air-borne noise' ('ABN'), 'Structure-borne noise' ('SBN') and 'Fluid-borne noise' ('FBN'). As its name implies, ABN is that noise which is propagated through the air and detected by the ear. SBN takes the form of mechanical vibration of the circuit components, such as pipes, and also of associated components such as panels to which the vibrations can be transmitted. SBN tends to be the direct cause of ABN. FBN is perhaps the least tangible type of noise and takes the form of pressure fluctuations or 'pressure ripple' in the fluid. Although it is not directly damaging, it is a major cause of SBN, and hence ABN. Furthermore, FBN can be propagated great distances along hydraulic pipes. Thus, in a typical factory ring main system, noise from the pump can be transmitted via FBN to remote parts of the factory.

Hydraulic system noise can also be important in a number of other areas, notably in transport and mobile machinery. For example, automotive power steering systems employ simple hydraulic circuits which can cause substantial noise unless great care is taken in their design. At the other extreme, hydraulic circuits in submarines can generate low frequency noise which can be transmitted great distances through the ocean and be detected by hostile surveillance systems.

The relationships between FBN, SBN and ABN are extremely complex. Transmission from fluid-borne to structure-borne noise is dependent upon a large number of factors, including the type and spacing of pipe mounts, the number of bends and the lengths of pipe and flexible hose. Similarly, the transmission from SBN to ABN depends on a number of factors, including the overall acoustic characteristics of the environment in which the system is situated. Steps can be taken to reduce the amount of ABN, for example by the lagging of pipes and components.

The work presented in this thesis is concentrated on fluid-borne noise. Although FBN is by no means the whole story as far as hydraulic system noise is concerned, it is one of the fundamental causes of SBN and ABN. Thus any improvements which can be made to the FBN characteristics of a system should produce a consequent improvement in the SBN and ABN.

The main sources of FBN in a hydraulic system tend to be pumps, motors and valves. This thesis is concerned with the FBN produced by positive displacement pumps and, to a lesser extent, by motors. Valves can cause FBN through oscillation of spools or poppets, or from cavitation. The cavitation characteristics of valves are not considered here but this is a broad field which has been covered by other researchers.

Positive displacement pumps tend not to produce an absolutely steady flow rate. Instead, the flow consists of a mean flow rate, on which is superimposed a flow ripple. The magnitude of the flow ripple is dependent upon the pump type and operating conditions, but in general has a peak-to-peak amplitude of between 1% and 50% of the mean flow rate. Pump flow ripple tends to have a periodic waveform due to the cyclic nature of a pump's operation, and different classes of pump have different characteristic flow ripple waveforms [1-7]. This flow ripple interacts with the characteristics of the connected circuit to produce a pressure ripple. A great deal of work has been performed in the past concerning the behaviour of the flow ripple and pressure ripple in circuits [8-18], and this is closely related to the behaviour of water hammer, and indeed to that of high frequency electrical transmission lines [19].

There is a need to produce a simple measure by which the fluid-borne noise characteristics of pumps can be compared. A direct measure of the pressure ripple in a circuit is, in general, not of much use because it is strongly dependent upon the characteristics of the circuit. A large amount of work has been undertaken in the past [20-29] in order to devise a means for evaluating a pump FBN rating which is a function of the pump alone, and not of the circuit in which the measurements are made. Because of the complex pump-circuit interactions it is extremely difficult to measure the source

flow ripple of a pump.

1.2. Objective of Work

The research reported in this thesis was undertaken as part of a broader investigation into various aspects of FBN in hydraulic systems at the University of Bath [7-11,25-27,30-32].

The principal aim of this project was to advance the understanding of the behaviour of fluid-borne noise in hydraulic circuits, and to continue work by Wing [26] on the development and refinement of a viable technique for the assessment of the FBN characteristics of positive displacement pumps and motors. A further aim was to develop means for the mathematical modelling of the FBN characteristics of hydraulic circuits of arbitrary complexity. This was to entail the development of mathematical models of components such as pumps, valves and hoses, and the validation of these models by experimental testing.

1.3. Scope of Thesis

The general theory of wave propagation in fluid lines is outlined in chapter 2. The case of a simple hydraulic circuit consisting of a pump, a pipe and a load is examined, and standing waves and resonance characteristics are discussed.

Chapter 3 contains a discussion of the problems involved in the rating of the fluid-borne noise potential of positive displacement pumps. Several methods proposed by previous researchers for the experimental evaluation of such a rating are examined.

Chapter 4 is a description of a new method for the experimental evaluation of the fluid-borne noise characteristics of positive displacement pumps. The theoretical basis of the method is examined in detail, and a description of the experimental hardware and techniques is given.

Results obtained using the test method proposed in chapter 4 are presented in chapter 5. These are compared with theoretical simulations.

An adaptation of the method was applied to the testing of the characteristics of passive components such as valves and accumulators, and the experimental results are presented in chapter 6. Again the results are compared with simulations, and the validity of the assumptions used in the simulations assessed.

Chapter 7 contains a description of a method for the experimental evaluation of the speed of sound in the fluid, from which the effective bulk modulus can be calculated. Experimental results are compared with theoretical values.

In chapter 8, a program for the simulation of the fluid-borne noise characteristics of hydraulic circuits of arbitrary complexity is described. Simulated results are compared with experimental pressure measurements in order to check the validity of the simulations. The derivation of a comprehensive flexible hose model is described.

Chapter 9 contains a discussion of different methods which are available for the practical reduction of fluid-borne noise in order that low-noise circuits can be produced. The effectiveness of some of the methods is assessed by simulation using the program described in chapter 8.

Conclusions and suggestions as to how this research could be continued are presented in chapter 10.

Appendices 1-4 contain theoretical and experimental aspects of the test method described in chapter 4, including curve fitting algorithms and component descriptions.

Computer program documentation is included in a separate report [33]. This includes a users guide and detailed program documentation for the data reduction software used with the Secondary Source Method, and detailed program documentation for the 'PRASP' package.

CHAPTER 2

ANALYSIS OF WAVE PROPAGATION IN HYDRAULIC SYSTEMS

In this analysis, an analogy is drawn between hydraulic and electrical transmission lines as in many ways their behaviour is similar. In certain electrical transmission systems, such as long distance power lines, telephone lines or microwave lines, the signal wavelength may be similar to or less than the transmission line length, and in such a case simple low frequency lumped parameter theory breaks down. A similar situation applies in fluid-borne noise analysis: the frequencies involved are higher than those normally considered in the dynamic analysis of hydraulic systems. It is necessary to consider the propagation of waves in the line, with the resultant standing wave and resonance effects.

Fluid flow rate can be considered to be equivalent to electric current, and pressure equivalent to voltage. The electrical impedance concept can be extended to the hydraulic impedance, i.e.

Electrical: $$impedance = \frac{voltage}{current}$$

Hydraulic: $$impedance = \frac{pressure}{flow\ rate}$$

Similarly, the concepts of electrical inductance, capacitance, resistance and reactance can also be extended to their hydraulic equivalents.

The theory of wave propagation in electrical transmission lines is covered in depth by Chipman [19].

2.1. Positive Displacement Pumps and Flow Ripple

It is well known that the flow from a positive displacement pump is not uniform but consists of a mean flow with a superimposed periodic fluctuation. This fluctuation is a major cause of fluid-borne noise and is known as the 'source flow ripple' of the pump. The waveform of this flow ripple may be complex, and normally has a fundamental frequency equal to the 'pumping frequency', where the pumping frequency is related to the rotational speed and the number of pumping elements, i.e.

fundamental frequency = shaft frequency × no. of elements ... (2.1)

There may also be flow ripple components with a fundamental frequency equal to the shaft frequency. Such components, caused by slight variations in the pumping characteristics over one revolution, are normally small and unpredictable so are generally ignored. Flow ripple also occurs in the inlet flow of positive displacement pumps. A study of this flow ripple was undertaken by Freitas [30]. The work presented in this thesis is mainly concerned with the outlet flow ripple, although much of it is applicable to the inlet flow ripple.

Different classes of pump tend to have characteristic flow ripple waveforms associated with them. For example, different models of axial piston pump are likely to produce flow ripples which, though not identical, will be qualitatively similar, due to the similar pumping mechanisms involved. Certain classes of pump, for example internal gear pumps, by their nature produce flow ripples significantly smaller than those of axial piston pumps or external gear pumps. Such pumps will, in general, be quieter.

The source flow ripple from a pump can be considered to consist of two superimposed components. The 'kinematic' ripple is a function of the pump geometry and is independent of pressure. The 'dynamic' ripple is pressure dependent and may be due to fluid compressibility, leakage and inertia. In general, the kinematic ripple may be predicted quite accurately from knowledge of the pump geometry. However, the dynamic ripple tends to be rather more difficult to predict.

2.1.1. Source Flow Ripple from an Axial Piston Pump

A typical axial piston pump will have between five and ten identical cylinder/piston assemblies. The overall flow from the pump can be considered to be the sum of the individual flow from each cylinder. Consider the idealised action of just one cylinder during one revolution. During this period the piston will be forced to move sinusoidally through one cycle by the swash plate. The idealised porting arrangement to the cylinder as shown in Fig. 2.1(a) is assumed, so that at all times when the piston is retracting towards bottom dead centre (BDC) the cylinder is connected to the suction port. Conversely, when the piston is moving towards top dead centre (TDC) the cylinder is connected to the discharge (high pressure) port. The idealised flow from the discharge port will then be similar to a 'half-rectified sine wave' as shown in Fig. 2.1(b). By summing the flow from all the cylinders, the overall flow is found to exhibit a small kinematic ripple, this having a fundamental frequency equal to twice the pumping frequency for a pump with an odd number of cylinders (Fig. 2.2(a)), and equal to the pumping frequency with an even number of cylinders (Fig. 2.2(b)) (most pumps tend to have an odd number, in which case the kinematic flow ripple is smaller). This ripple, however, is normally of small amplitude and only consists of two or three significant harmonics.

The compressibility of the fluid also plays an important part in the source flow ripple. When the piston is on the suction stroke, the oil in the cylinder will be approximately at the inlet line pressure, which will be low. As the cylinder rotates past BDC, the suction port closes and the discharge port opens. The resultant pressure imbalance causes a reverse flow into the cylinder of short duration but sufficient to compress the fluid and equalise the pressure. The inertia of the fluid in the vicinity of the port-plate and the compressibility of the fluid in the cylinder may cause a mass-spring-damper effect and oscillations in the flow ripple waveform [7], as shown in Fig. 2.3. The magnitude of the backflow is strongly dependent upon the working pressure; the degree of compression is proportional to the mean pressure difference between the outlet and inlet. A similar effect will occur in reverse as the cylinder passes TDC and opens to the inlet port, causing fluid-borne noise in the inlet line.

The backflow produced by some axial piston pumps can be quite large and can lead to severe system noise. Furthermore, such a flow ripple will have a broad harmonic spectrum with perhaps 10 or 15 significant harmonics. Some methods of reducing the flow ripple from axial piston pumps are discussed in section 9.1.1.

2.1.2. Source Flow Ripple from External Gear Pumps

The idealised form of the source flow ripple from an external gear pump is well known [1-4]. It is generally assumed to be independent of pressure and to be purely a function of kinematic effects due to the changing geometry of the meshing of the gears as they rotate. Fluid compression, although it does take place between the inlet and outlet ports, normally tends to be less sudden as it is spread over a large angle of gear rotation and is therefore not as significant as for axial piston pumps.

Assuming the ideal configuration of relief grooves as shown in Fig. 2.4(a), the flow ripple takes the form of a train of inverted parabolic waves as shown in Fig. 2.4(b), and can be described by the equation

$$q(\psi) = q_{max} - K\psi^2 \quad \text{for } -\pi/z < \psi < \pi/z \qquad \ldots (2.2)$$

where, for involute gear teeth, $K = b\,\Omega r^2 \cos^2\theta_p$ $\ldots (2.3)$

and, for cycloidal gear teeth, $K \approx b\,\Omega r^2$ $\ldots (2.4)$

ψ represents the rotation of the gears relative to the position at which the contact point between the gears lies on the straight line between the gear centres.

or $\psi = \Omega(t - t_0)$ $\ldots (2.5)$

b is the gear width, Ω is the angular velocity of the gears, θ_p is the pressure angle of the gears, z is the number of teeth on each gear, and r is the pitch circle radius of the gears.

Harmonically, this flow ripple consists of a very strong fundamental at the pumping frequency, and few significant higher harmonics. In practice the flow ripple may be significantly worse due to poor design, and may be pressure dependent. Again, numerous methods are available for the reduction of the flow ripple; these are discussed in section 9.1.2.

2.2. Wave Analysis of Fluid-Borne Noise in a Simple Pipe

In order to facilitate a reasonably simple analysis, a number of assumptions must be made [17,34].

1) The fluid is homogeneous and Newtonian.

2) Heat transfer effects are negligible, and conditions are isentropic.

3) Flow is laminar and axisymmetric.

4) The pressure distribution across the pipe is uniform

5) Perturbations are small such that any variations in the fluid properties are negligible.

6) The velocity profile across the cross section is uniform; i.e. plane waves are assumed.

7) Waves propagating in the pipe wall are neglected.

8) The mean fluid velocity is negligible compared with the speed of sound in the fluid.

Consider an infinitesimal element of fluid in a rigid pipeline, subject to a plane wave, Fig. 2.5 [18,35].

By considering continuity of the fluid,

$$-\frac{\partial q}{\partial x} = \frac{A}{B_{eff}} \frac{\partial p}{\partial t} \qquad \ldots (2.6)$$

and by considering forces acting on the fluid,

$$-\frac{\partial p}{\partial x}=Rq+\frac{\rho}{A}\frac{\partial q}{\partial t}. \qquad \ldots (2.7)$$

As the analysis is to be performed in the frequency domain, applying the Fourier transformation

$$F(\partial/\partial t) = j\omega, \qquad \ldots (2.8)$$

$$\text{then } -\frac{\partial Q}{\partial x}=\frac{A}{B_{eff}} j\omega P \qquad \ldots (2.9)$$

$$\text{and } -\frac{\partial P}{\partial x}=\left(R+\frac{j\omega\rho}{A}\right)Q. \qquad \ldots (2.10)$$

By combining these equations, the wave equations are obtained

$$-\frac{\partial^2 Q}{\partial x^2} = \gamma^2 Q \qquad \ldots (2.11)$$

$$-\frac{\partial^2 P}{\partial x^2} = \gamma^2 P \qquad \ldots (2.12)$$

where γ, the wave propagation coefficient, is given by

$$\gamma = j\omega\sqrt{\rho/B_{eff}}\ \xi \qquad \ldots (2.13)$$

$$\xi = \left(1+\frac{AR}{j\omega\rho}\right)^{1/2}. \qquad \ldots (2.14)$$

B_{eff} is the effective bulk modulus. This can be difficult to predict and can be affected by the compliance of the pipe wall and the presence of entrained air in the fluid.

The effect of pipe wall compliance can be taken into account by the equation [16]

$$B_{eff} = \frac{B_T}{1+\frac{B_T}{E}\frac{\tilde{d}}{t}c_1} \qquad \ldots (2.15)$$

where $\tilde{d}$ is the mean of pipe internal and external diameters, and t is the pipe wall thickness. B_T is the isentropic tangent bulk modulus of the fluid (since small, rapid changes in pressure are considered [26,30]). B_T is a function of the mean pressure and temperature, and may normally be found from the fluid manufacturer's published fluid properties data.

c_1 is a factor which is a function of the longitudinal stresses and strains in the pipe, which are dependent upon the way in which the pipe is anchored [36]. The effect of these is difficult to predict, particularly in the case of pressure ripple where the instantaneous pressure varies along the length of the pipe. However, this effect is small and it is assumed here that longitudinal stresses can be ignored, in which case

$$c_1 = \frac{2t(1+\nu)}{\tilde{d}} + \frac{\tilde{d}}{\tilde{d}+t}. \qquad \ldots (2.16)$$

Wave propagation effects within the material of the pipe wall are ignored in this analysis. It is normally considered that in the case of a rigid pipe such effects have minimal influence on the wave propagation properties of the fluid. For a flexible hose, however, such effects tend to be important; there is a strong and complex interaction between waves propagating in the fluid and in the hose walls [37-39].

R is the resistance coefficient, defined as the pressure drop per unit length, per unit flow rate. In theory, for a plane wave there would be an infinite velocity gradient at the pipe wall, and hence infinite shear stress, in which case the resistance coefficient would also be infinite. This is clearly nonsensical and shows that this simplified model has serious shortcomings. Indeed, for steady, fully developed laminar flow the velocity profile is parabolic.

The model can be improved by allowing for a non-uniform velocity profile across the pipe. Foster and Parker [10] presented a solution of the wave equations for this case. This analysis is considerably more complicated, involving the use of Bessel functions. The solution is as eqns (2.11)-(2.13), where [12,17]

$$\xi = \left[1 - \frac{2}{haj^{3/2}} \frac{J_1(haj^{3/2})}{J_0(haj^{3/2})} \right]^{-\frac{1}{2}} \qquad \ldots (2.17)$$

where J_0 and J_1 are Bessel functions of the first kind of order 0 and 1 respectively, and ha is the non-dimensional 'wave shear number', which may be considered as a function of the ratio of inertial forces to viscous forces.

$$ha = \frac{d}{2}\sqrt{\omega/\nu}. \qquad \ldots (2.18)$$

ξ is plotted against ha in Fig. 2.6.

The Bessel functions in equation (2.17) tend to be difficult to evaluate. However, it was shown by Foster and Parker [12] that the effect of the non-uniform velocity profile can be allowed for in the original model (equation (2.14)) by considering the density ρ and resistance R as functions which vary with the wave shear number. The variation in effective density is plotted in Fig. 2.7(a), relative to the actual density. The variation in effective resistance is plotted in Fig. 2.7(b), relative to the steady state value for laminar flow, which is obtained from the Hagen-Pouseuille formula, as

$$R = \frac{128\mu}{\pi d^4}. \qquad \ldots (2.19)$$

As can be seen from Fig. 2.7(b), the resistance approaches its steady state value at low wave shear number, i.e. low frequency. This is to be expected and implies that the velocity profile approaches a parabolic form. At high values of the wave shear number, inertial forces predominate over viscous forces. This has the effect of 'flattening' the velocity profile, increasing the shear near the pipe walls and hence increasing the resistance.

The kinetic energy associated with a particular mean flow rate in the steady state, where the velocity profile is parabolic, can be shown to be 4/3 of that which would be associated with the same mean flow rate if the velocity profile was uniform. This increase in kinetic energy can be represented by an increase in the effective density. Thus, as ha tends to zero, the effective density approaches 4/3 of the actual density. At high values of ha the velocity profile flattens out, so that the effective density approaches the actual density. The variation in the effective density is shown in Fig. 2.7(a).

In most hydraulic fluid-borne noise situations, the frequency and viscosity are such that the wave shear number exceeds 10. In this region, the effective density and resistance can be defined accurately by the asymptotic approximations [11,12]

$$\frac{\rho_{eff}}{\rho} = 1+\frac{\sqrt{2}}{ha}, \qquad \ldots (2.20)$$

$$\frac{R_{eff}}{R} = 0.425+0.175ha. \qquad \ldots (2.21)$$

For $ha < 10$, these curves can be approximated using a cubic spline. At high values of ha, the value of ξ approaches unity, as can be seen from Fig. 2.6, in which case it may be reasonable to assume frictionless conditions. However, with modern digital computation techniques the added complexity involved in the inclusion of viscous effects can easily be incorporated.

The wave equations (2.11) and (2.12) have as general solutions

$$P(\omega,x) = Fe^{-\gamma x} + Ge^{\gamma x} \qquad \ldots (2.22)$$

$$Q(\omega,x) = \frac{Fe^{-\gamma x} - Ge^{\gamma x}}{Z_0} \qquad \ldots (2.23)$$

$$\text{where } Z_0 = \frac{\sqrt{\rho B_{eff}}}{A}\xi \qquad \ldots (2.24)$$

and F and G depend upon the boundary conditions. γ represents the way in which the wave is propagated along the line.

The $Fe^{-\gamma x}$ term represents a wave travelling in the positive direction along the pipe. Z_0 is known as the 'characteristic impedance' and is the complex ratio of the pressure wave to the flow wave. Similarly the $Ge^{\gamma x}$ term represents a wave travelling in the opposite direction (note that P is a scalar quantity and Q is a vector quantity, so a minus sign is necessary in equation (2.23) to indicate the reverse direction).

If frictionless conditions are assumed, then

$$\gamma = j\omega\sqrt{\rho/B_{eff}} = \frac{j\omega}{c_0} \qquad \ldots (2.25)$$

where the speed of sound, $c_0 = \sqrt{B_{eff}/\rho}$.

Consider a wave travelling in the positive direction only.

$$P = Fe^{-j\omega x/c_0}. \qquad \ldots (2.26)$$

The exponential term represents a phase lag with increasing x. This can be thought of as a delay, and indicates that the wave travels at the speed of sound in the direction of increasing x.

Including viscous effects, it is possible to represent γ by

$$\gamma = j\omega/c + \alpha \qquad \ldots (2.27)$$

where c and α are real functions of ha.

c is the phase velocity of the wave (note: if viscous effects are neglected, it becomes equal to c_0). The value of c/c_0 is plotted against ha in Fig. 2.8. It can be seen that c approaches c_0 as ha increases. In the range of interest, c is roughly equal to c_0. At low values of ha, c/c_0 tends to zero.

Including viscous effects, a wave travelling in the positive direction can be represented by

$$P = Fe^{-j\omega x/c}e^{-\alpha x}. \qquad \ldots (2.28)$$

The $e^{-\alpha x}$ term represents an exponential decay. Thus if viscous effects are significant a wave will decay exponentially as it travels along the pipe.

2.3. Application of the Wave Equations to a Simple System

Consider the simple system shown in Fig. 2.9(a), which consists of a pump, a rigid pipe and a load valve. This can be represented using impedance notation as in Fig. 2.9(b).

The pump acts as a source of fluid-borne noise, and produces a flow ripple, Q_S. It is assumed that the flow ripple is generated at the exit of the pump. (This is not the case in practice; the flow ripple will be generated at a point within the pump. A more precise model is described in section 4.3.10.).

The pump can also be considered to have an impedance in parallel with the flow ripple. This is known as the 'source impedance' Z_S. The form of this impedance may be complex, but basically it encompasses any capacitive, inductive or resistive effects in the fluid which is contained within the pump. The form of this impedance is investigated in section 4.3.9. This pump model with a flow ripple in parallel with an impedance is equivalent to Norton's model as used in electrical engineering as a model of current sources.

The load valve may be a source of FBN, due to cavitation and/or oscillation. Such effects are ignored in this analysis, and the valve is assumed to be a purely passive device, represented by an impedance Z_T.

Applying these boundary conditions to equations (2.22) and (2.23), expressions can be derived to define the pressure ripple and flow ripple at any point x along the pipe [11]:

$$P_x = \frac{Q_S Z_S Z_0}{Z_S + Z_0} \cdot \frac{e^{-\gamma x} + \rho_T e^{-\gamma(2l-x)}}{1 - \rho_S \rho_T e^{-2\gamma l}} \qquad \ldots (2.29)$$

$$Q_x = \frac{Q_S Z_S}{Z_S + Z_0} \cdot \frac{e^{-\gamma x} - \rho_T e^{-\gamma(2l-x)}}{1 - \rho_S \rho_T e^{-2\gamma l}} \qquad \ldots (2.30)$$

where ρ_T is the termination reflection coefficient, and is defined as the complex ratio of the incident pressure wave to the reflected pressure wave at that point. Similarly, ρ_S is the source reflection coefficient, and represents the way in which the wave travelling from the termination is reflected at the source.

Equations (2.29) and (2.30) are fundamental to understanding the behaviour of fluid-borne noise in hydraulic systems. They can be extended to describe some more complicated circuits, such as those incorporating changes in pipe section, or multiple pipe branches. [8,9,40,41]. They are, however, rather complicated expressions and it may be helpful to explain the physical relevance of the terms.

Consider equation (2.29). The right hand side may be split into two distinct parts:

$$P_x = \left[\frac{Q_S Z_S Z_0}{Z_S + Z_0}\right] . \left[\frac{e^{-\gamma x} + \rho_T e^{-\gamma(2l-x)}}{1 - \rho_S \rho_T e^{-2\gamma l}}\right]$$

$$= [\quad A \quad] . [\quad\quad B \quad\quad].$$

Part A has the units of pressure, and represents the pressure which would be generated at the pump exit in the absence of any reflections from the termination. The flow ripple, Q_S, is discharged into a load which consists of the source impedance and the pipe characteristic impedance in parallel.

Part B is non-dimensional and represents the behaviour of the waves which are generated by part A. The $e^{-\gamma x}$ term in the numerator represents the wave which is propagating in the positive direction. The $\rho_T e^{-\gamma(2l-x)}$ term represents the wave after reflection at the termination, ρ_T being the amplitude and phase change which occurs at the reflection, and $(2l-x)$ the total distance which the wave has travelled from the source. The denominator represents the cumulative effect of subsequent reflections of the wave. This is made clearer if this term is expanded into an infinite series by a binomial expansion, as follows:

$$B = e^{-\gamma x} + \rho_T e^{-\gamma(2l-x)} + \rho_S \rho_T e^{-\gamma(2l+x)} + \rho_S \rho_T^2 e^{-\gamma(4l-x)} + \rho_S^2 \rho_T^2 e^{-\gamma(4l+x)} + \cdots \qquad \ldots (2.31)$$

The odd numbered terms in this expression represent waves travelling in the positive direction, and the even numbered terms represent waves travelling in the other direction. Each subsequent term represents a subsequent reflection. Eventually, due to pipe friction and incomplete reflections ($|\rho_T|$ or $|\rho_S|$ less than unity), these terms will decay to zero.

Although the analysis is performed in the frequency domain, it is helpful to visualise the implications of the above in the time domain. Fig. 2.10 shows some experimental traces of pressure ripple plotted against time at different positions along the pipe for such a system. Rather than the source of the flow ripple being a pump, however, it is in this case generated artificially using a pulse generator (section 4.3.2.), which periodically produces a short duration flow pulse, as shown. The pressure traces clearly show the propagation of this pulse along the line. There is an initial large amplitude pulse which is increasingly retarded as the distance from the source becomes greater. This is followed by another pulse of slightly smaller amplitude which travels in the opposite direction (this indicates that $|\rho_T| < 1$), followed by another pulse travelling in the same direction as the first

pulse, etcetera. The pulses decay away exponentially, due mainly to incomplete reflections, with viscous losses in the pipe also having a minor effect.

2.4. Standing Waves

Consider the behaviour of one single harmonic pressure ripple component in this simple system. Fig. 2.11(a) shows the effect of different values of $|\rho_T|$ on the amplitude of the pressure ripple along the pipe (assuming friction in the pipe is negligible).

For the case where $|\rho_T| = 0$, the pressure amplitude is constant along the pipe length. This represents a pure travelling wave, as would be expected since there is no reflected wave.

Where $|\rho_T| = 1$, the reflected wave interferes with the incident wave to form a pure standing wave. For smaller values of $|\rho_T|$, a partial standing wave is formed. At those points where the incident and reflected waves are in phase, the sum of the two waves is at its maximum. This maximum is termed an 'anti-node'. Where the two waves are 180° out of phase, they cancel each other out wholly or partially to produce a minimum, or a 'node'. The distance between consecutive nodes or consecutive anti-nodes is half of the wavelength. There is a high rate of change of pressure amplitude with length near a node, and a gradual change near an anti-node.

The effect of variations in the phase of ρ_T, where $|\rho_T| = 1$, is shown in Fig. 2.11(b). As can be seen, the effect is simply to move the position of the nodes and anti-nodes relative to the termination.

2.5. Resonance

Consider the denominator of part B of equation (2.29), i.e. $(1-\rho_S \rho_T e^{-2\gamma l})$. If the value of $\rho_S \rho_T e^{-2\gamma l}$ approaches +1, this term can become small and consequently the pressure ripple amplitude may become very large. This phenomenon is known as resonance and, in severe cases, can cause FBN levels to become very high, a condition to be avoided if possible. The effect is most marked where $|\rho_S|$ and $|\rho_T|$ are large, which is often the case in certain hydraulic circuits such as hydrostatic transmissions. The $e^{-2\gamma l}$ term indicates that resonance is strongly dependent upon harmonic frequency and pipe length.

Fig. 2.12 shows a plot of pressure amplitude at the source as a function of the pipe length, where it is assumed that $\rho_S = +1$. It can be seen that for large values of $|\rho_T|$ the resonances are sharply defined and the pressure levels at resonance very high. The effect is less marked for smaller values of $|\rho_T|$.

2.6. Derivation of the Termination Reflection Coefficient as a Function of Z_0 and Z_T

Consider the reflection which occurs at the termination. The pressure ripple at the termination is given by the sum of the incident and reflected pressure waves, i.e.

$$P_l = P_i + P_r . \qquad \ldots (2.32)$$

The flow ripple at this point is similarly given by the algebraic sum of the incident and reflected flow waves.

$$Q_l = Q_i - Q_r \qquad \ldots (2.33)$$

$$\text{but } \frac{P_i}{Q_i} = \frac{P_r}{Q_r} = Z_0 . \qquad \ldots (2.34)$$

Substituting (2.34) into (2.33)

$$Q_l = \frac{P_i - P_r}{Z_0} . \qquad \ldots (2.35)$$

$$\text{By definition, } Z_T = \frac{P_l}{Q_l}. \qquad \ldots (2.36)$$

Substituting (2.35) and (2.33) into (2.36),

$$Z_T = Z_0 \frac{P_i + P_r}{P_i - P_r}. \qquad \ldots (2.37)$$

By definition, $\rho_T = \frac{P_r}{P_i}$. ... (2.38)

Hence $Z_T = Z_0 \frac{1+\rho_T}{1-\rho_T}$ ... (2.39)

or, rearranging, $\rho_T = \frac{Z_T - Z_0}{Z_T + Z_0}$. ... (2.40)

A similar argument applies to the source reflection coefficient.

2.7. Limitations on the Range of the Reflection Coefficient

The characteristic impedance is shown in equation (2.24) to be a complex number which is dependent upon the wave shear number. Normally viscous effects are small, and if they are ignored,

$$Z_0 = \frac{\rho c_0}{A} \quad \ldots (2.41)$$

i.e. Z_0 is a positive real number and is independent of frequency.

The value of termination impedance may have real and imaginary parts, which by using the electrical impedance analogy can be called 'resistance' and 'reactance' respectively. A true passive termination cannot have a negative resistance, so the real part of Z_T must be positive.

Putting $Z_T = R_T + jX_T$ ... (2.42)

where R_T = termination resistance
X_T = termination reactance

then $\rho_T = \frac{(R_T - Z_0) + jX_T}{(R_T + Z_0) + jX_T}$. ... (2.43)

For positive or zero R_T, this expression cannot have a magnitude greater than 1. Therefore, in the case of a passive termination and a frictionless line the magnitude of the reflected wave cannot exceed the magnitude of the incident wave. This implies that the energy of the wave cannot be increased upon reflection, as would be expected. There are, however two possible exceptions to this rule:

a) the termination is not truly passive (see section 6.4.2.)

b) viscous effects in the line are not negligible. Under certain conditions the phase of Z_0 and Z_T may be such that the magnitude of the reflection coefficient exceeds unity. This condition was explained in some detail by Chipman [19], who showed that the maximum possible value of $|\rho_T| = 1+\sqrt{2}$. Although it appears to violate the principle of conservation of energy, it was shown by Chipman that, because of the highly reactive nature of the characteristic impedance, this is in fact not the case. This condition is unlikely to occur in hydraulic systems as it can only occur at very low values of ha.

2.8. Values of Reflection Coefficient for Special Cases of Termination Impedance

i) Closed end

In this situation $Z_T = \infty$ and $\rho_T = 1$, i.e. the reflected pressure wave has the same amplitude and phase as the incident wave. The incident and reflected pressure waves will sum together to produce a maximum or an 'antinode' at the termination.

ii) Open end

In this case $Z_T = 0$ and $\rho_T = -1$. The reflected pressure wave is of the same amplitude as the incident wave but is inverted, so the pressure ripple at the termination is zero (a 'node').

iii) Purely reactive termination

In this case $R_T = 0$. Assuming a frictionless line, the reflection coefficient will have a magnitude of unity and a phase of anything between $-180°$ and $+180°$, depending upon the reactance.

iv) Termination impedance equal to characteristic impedance

This condition produces a reflection coefficient of zero, i.e. there is no reflection. This very important case is known as a 'non-reflective termination' and all the energy of the wave is absorbed by, or transmitted through, the termination. No standing wave is set up in the pipe and the wave amplitude is constant along the line.

In cases (*i* –*iii*), no energy can be absorbed by the termination and so the wave is reflected with no loss of energy.

2.9. Entry Impedance

The entry impedance, Z_E, of a hydraulic circuit is defined as the ratio of the pressure ripple to the flow ripple at the entry to that circuit. For example, in the simple system of Fig. 2.9, one can define the entry impedance at the position $x = 0$ as representing the overall impedance of the pipe and termination.

Substituting $x = 0$ into equations (2.29) and (2.30), and dividing (2.29) by (2.30), the following expression is obtained:

$$Z_E = \frac{P_0}{Q_0} = Z_0 \frac{1+\rho_T e^{-2\gamma l}}{1-\rho_T e^{-2\gamma l}}. \qquad \ldots (2.44)$$

It is also possible to define an 'entry reflection coefficient' ρ_E, where

$$\rho_E = \frac{Z_E - Z_0}{Z_E + Z_0} = \rho_T e^{-2\gamma l}. \qquad \ldots (2.45)$$

Substituting equations (2.44) and (2.45) into (2.29), an alternative expression for the pressure ripple is obtained:

$$P_x = \frac{Q_S Z_S Z_E}{Z_S + Z_E} \cdot \frac{e^{-\gamma x} + \rho_E e^{\gamma x}}{1+\rho_E} \qquad \ldots (2.46)$$

and the pressure at the pump outlet is then given by

$$P_0 = \frac{Q_S Z_S Z_E}{Z_S + Z_E} \qquad \ldots (2.47)$$

where $\frac{Z_S Z_E}{Z_S + Z_E}$ is the impedance obtained by combining the source impedance and the circuit entry impedance in parallel.

2.10. Modelling of Systems with More than One Source of Fluid-Borne Noise

It is common for a hydraulic circuit to have more than one component acting as sources of fluid-borne noise. For example, consider the much simplified hydrostatic transmission shown in Fig. 2.13. The motor has a flow ripple and a source impedance associated with it in much the same way as the pump [30].

It is an implicit assumption in the impedance method that there is a linear relationship between the source flow ripple Q_S and the pressure ripple in the circuit (equation (2.29)). In practice this is normally a valid assumption since the pressure fluctuations considered are generally small compared to the mean pressure, and therefore non-linear characteristics of any component should be insignificant. Based upon this assumption, it is possible to determine the overall pressure ripple or flow ripple in this hydrostatic transmission circuit by considering the effect of each source in turn, and summing the results using the principle of superposition. The procedure is described in more detail by Freitas [30].

In general, the two sources of fluid-borne noise will not have the same fundamental frequency, and so the frequencies of the harmonics of the pressure ripple from each source will be different. This may well result in the phenomenon of 'beating', where there is a marked periodic rise and fall in the pressure ripple amplitude which is commonly audible as a variation in noise level. An experimental pressure waveform showing this effect is shown in Fig. 2.14(a). The harmonic spectrum of such a signal is shown in Fig. 2.14(b). As can be seen, since the harmonic frequencies from each source are different, the components generated by either source can be readily distinguished from one another, except at those frequencies where the harmonics happen to coincide. If, however, the fundamental frequencies of the two sources are equal, it will be impossible to discriminate between the components of either source.

2.11. Lumped Parameter and Distributed Parameter Modelling of Components

If the dimensions of a component are insignificant compared to the wavelengths of the fluid borne noise components under consideration, then that component can be modelled using a simple 'lumped parameter' approach. Components such as pipes or hoses, however, are likely to have lengths which are significant compared to the wavelengths of the fluid-borne noise. In such cases it is necessary to take wave propagation effects into account in their modelling. This is known as 'distributed parameter' modelling.

2.12. Two-port Models and Transfer Matrices

Most hydraulic components, for example a pipe or a restrictor valve, can be thought of as having two ports, namely the inlet port and the outlet port. Such a component can be modelled as a 'black box' so that the only variables are the pressure and flow ripple at each port. It can be represented as shown below:

This representation is analogous to that commonly used in electrical engineering [19], and can be applied to both lumped and distributed parameter models. The four variables (P_{IN} , Q_{IN} , P_{OUT} , Q_{OUT}) are functions of the characteristics of the model itself and also of the system to which the model is connected. It is, however, possible to derive a relationship expressing a pair of the variables in terms of the other pair, which is a function of the model characteristics alone. This takes the form of two simultaneous equations which can be represented by a matrix equation. The matrix describing the model can take many forms, depending upon which pair of variables is expressed as a function of the other pair, and is described generically as a 'transfer matrix'.

2.12.1. Derivation of the Transfer Matrices for a Rigid Pipe

Consider equations (2.22) and (2.23). At the pipe inlet, $x = 0$

$$P_{IN} = F + G \qquad \ldots (2.48)$$

$$Q_{IN} = \frac{F - G}{Z_0} \qquad \ldots (2.49)$$

or, expressing in matrix form

$$\begin{bmatrix} P_{IN} \\ Q_{IN} \end{bmatrix} = \begin{bmatrix} 1 & 1 \\ 1/Z_0 & -1/Z_0 \end{bmatrix} \begin{bmatrix} F \\ G \end{bmatrix} \qquad \ldots (2.50)$$

and at the pipe outlet, $x = l$

$$P_{OUT} = Fe^{-\gamma l} + Ge^{\gamma l} \qquad \ldots (2.51)$$

$$Q_{OUT} = \frac{Fe^{-\gamma l} - Ge^{\gamma l}}{Z_0} . \qquad \ldots (2.52)$$

Rearranging (2.51) and (2.52) and expressing in matrix form

$$\begin{bmatrix} F \\ G \end{bmatrix} = \begin{bmatrix} \tfrac{1}{2}e^{\gamma l} & \tfrac{1}{2}Z_0 e^{\gamma l} \\ \tfrac{1}{2}e^{-\gamma l} & \tfrac{1}{2}Z_0 e^{-\gamma l} \end{bmatrix} \begin{bmatrix} P_{OUT} \\ Q_{OUT} \end{bmatrix} . \qquad \ldots (2.53)$$

Substituting (2.53) into (2.50)

$$\begin{bmatrix} P_{IN} \\ Q_{IN} \end{bmatrix} = \mathbf{T} \begin{bmatrix} P_{OUT} \\ Q_{OUT} \end{bmatrix} \qquad \ldots (2.54)$$

where $\mathbf{T} = \begin{bmatrix} \cosh \gamma l & Z_0 \sinh \gamma l \\ \dfrac{\sinh \gamma l}{Z_0} & \cosh \gamma l \end{bmatrix} .$ $\qquad \ldots (2.55)$

The matrix **T** is known as the transmission matrix, because it relates the transmission characteristics between the inlet and outlet. By simple algebra, different forms of the transfer matrices may be derived, the most important being listed below:

Inverse Transmission Matrix

$$\begin{bmatrix} P_{OUT} \\ Q_{OUT} \end{bmatrix} = \mathbf{T}^{-1} \begin{bmatrix} P_{IN} \\ Q_{IN} \end{bmatrix} \quad \ldots (2.56)$$

$$\text{where } \mathbf{T}^{-1} = \begin{bmatrix} \cosh \gamma l & -Z_0 \sinh \gamma l \\ -\dfrac{\sinh \gamma l}{Z_0} & \cosh \gamma l \end{bmatrix}. \quad \ldots (2.57)$$

Impedance Matrix

$$\begin{bmatrix} P_{IN} \\ P_{OUT} \end{bmatrix} = \mathbf{Z} \begin{bmatrix} Q_{IN} \\ Q_{OUT} \end{bmatrix} \quad \ldots (2.58)$$

$$\text{where } \mathbf{Z} = \begin{bmatrix} Z_0 \coth \gamma l & Z_0 \operatorname{cosech} \gamma l \\ Z_0 \operatorname{cosech} \gamma l & Z_0 \coth \gamma l \end{bmatrix}. \quad \ldots (2.59)$$

In this case, all the elements of **Z** have the units of impedance.

Admittance Matrix

$$\begin{bmatrix} P_{IN} \\ Q_{IN} \end{bmatrix} = \mathbf{Y} \begin{bmatrix} P_{OUT} \\ Q_{OUT} \end{bmatrix} \quad \ldots (2.60)$$

$$\text{where } \mathbf{Y} = \begin{bmatrix} \dfrac{1}{Z_0} \coth \gamma l & \dfrac{1}{Z_0} \operatorname{cosech} \gamma l \\ \dfrac{1}{Z_0} \operatorname{cosech} \gamma l & \dfrac{1}{Z_0} \coth \gamma l \end{bmatrix}. \quad \ldots (2.61)$$

Here the elements of Y have the units of admittance.

The transfer matrix approach offers a powerful method for the analysis of the fluid-borne noise characteristics of hydraulic systems whilst, particularly for complex systems, it involves a significant reduction in algebra over other methods. For this reason this technique is extensively employed in later sections of this work.

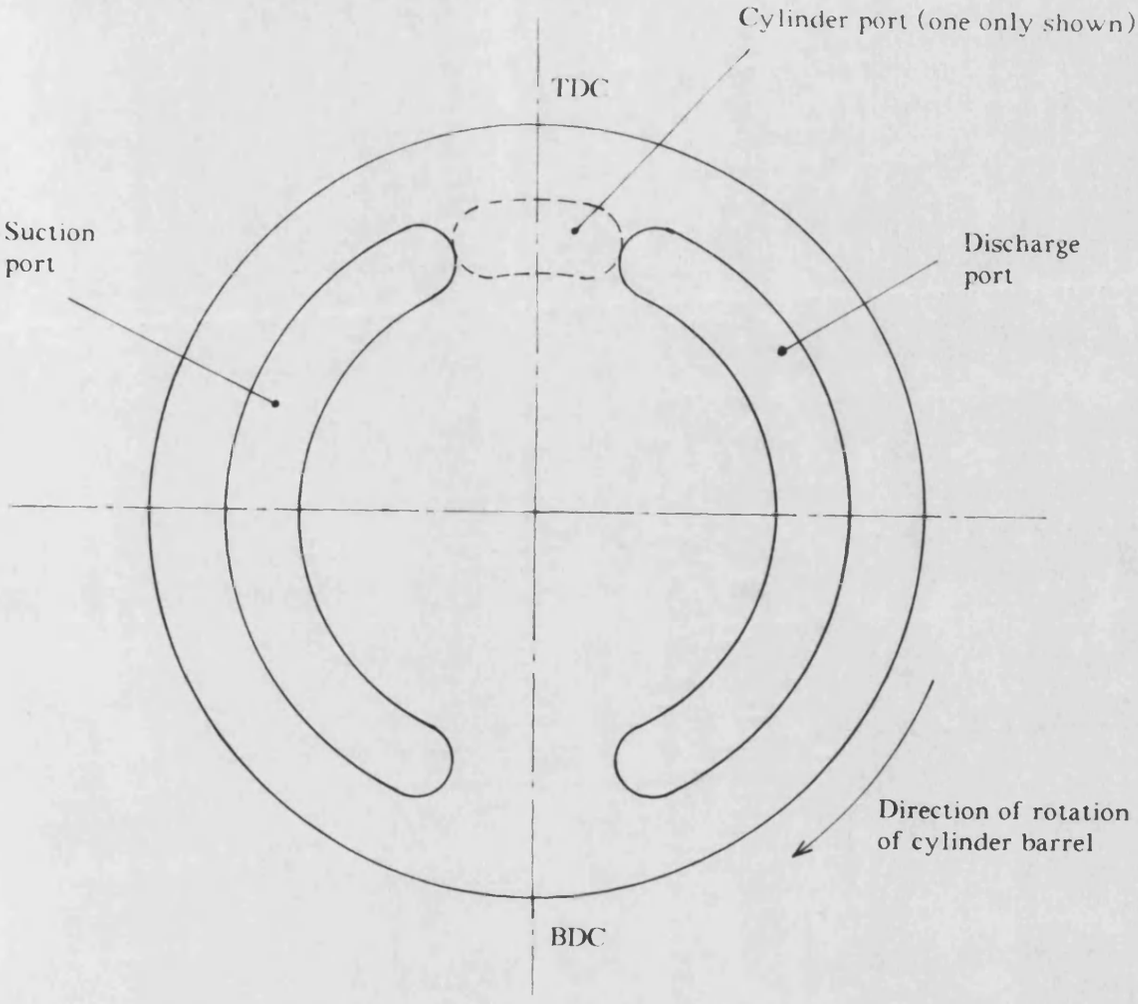

Fig. 2.1(a) Idealised Port Plate Geometry

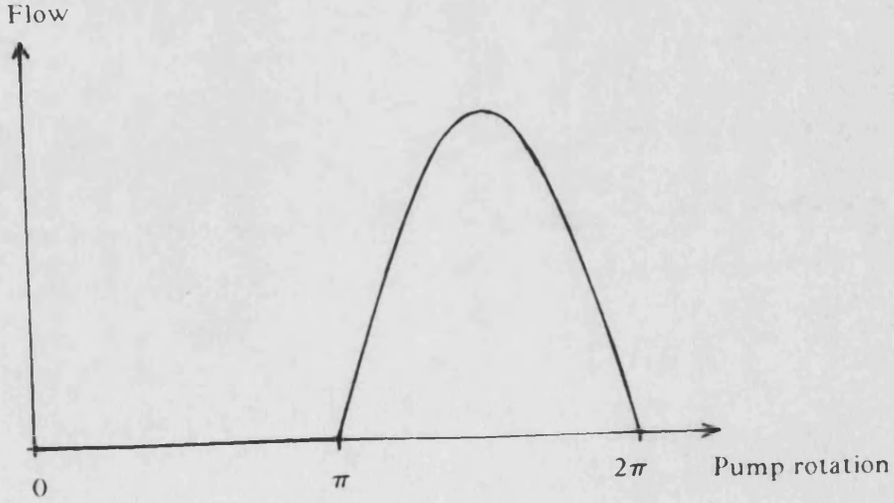

Fig. 2.1(b) Idealised Flow from One Cylinder over One Revolution

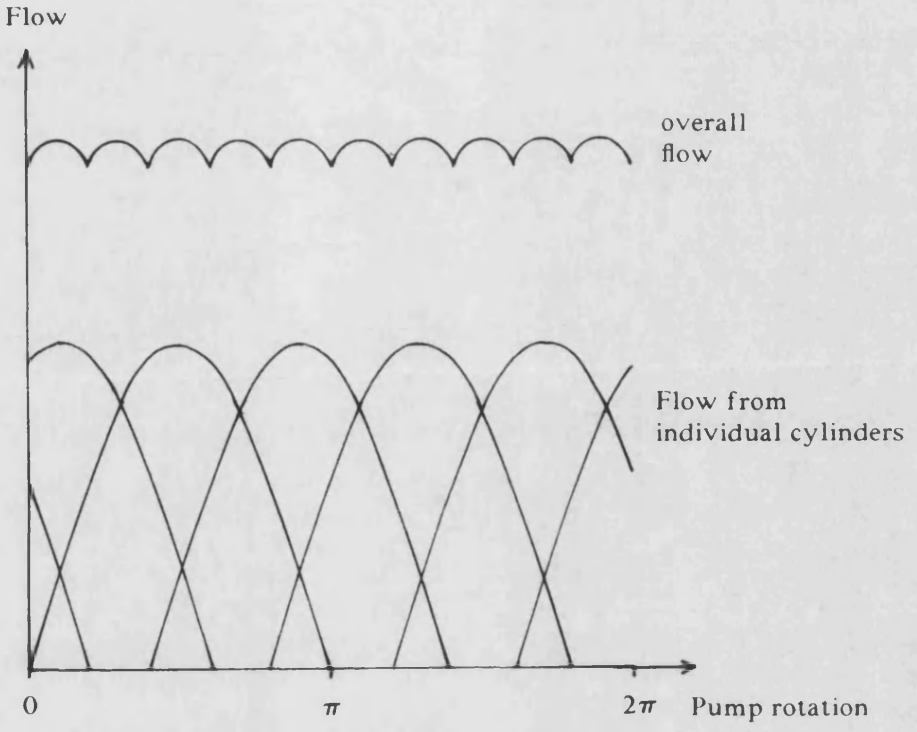

(a) Odd number of cylinders

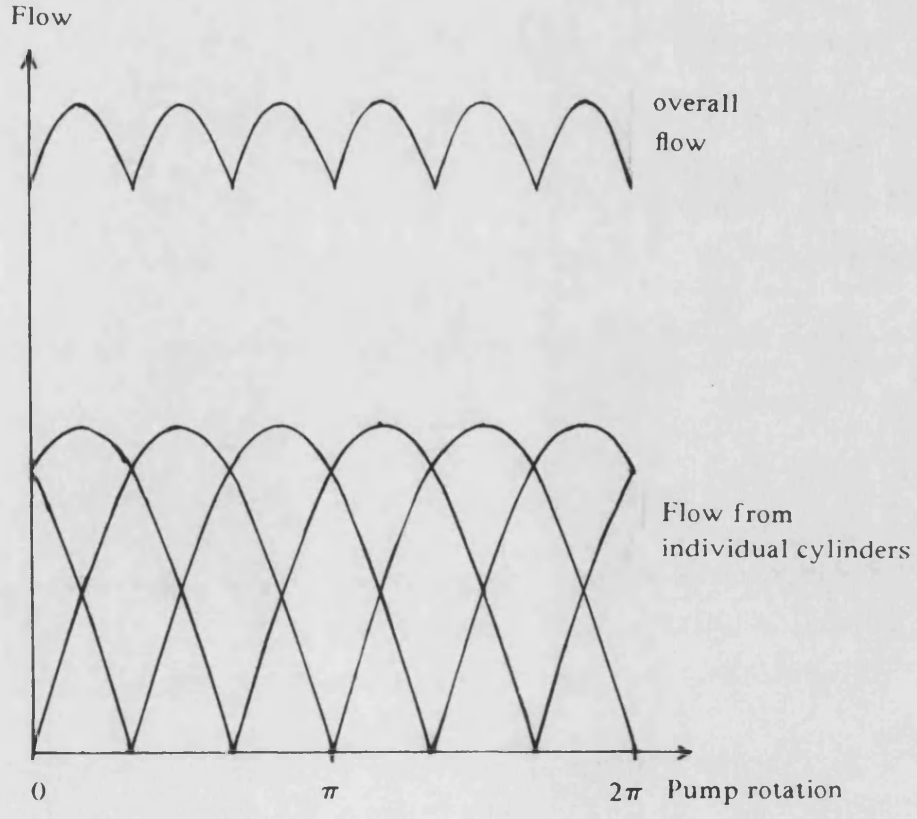

(b) Even number of cylinders

Fig. 2.2 Kinematic Flow Ripple from Axial Piston Pump

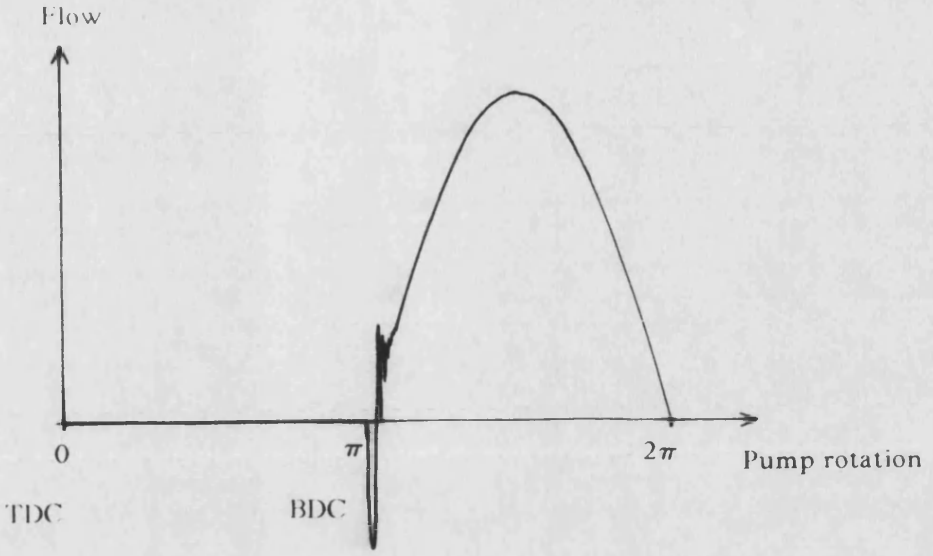

(a) Flow from individual cylinder

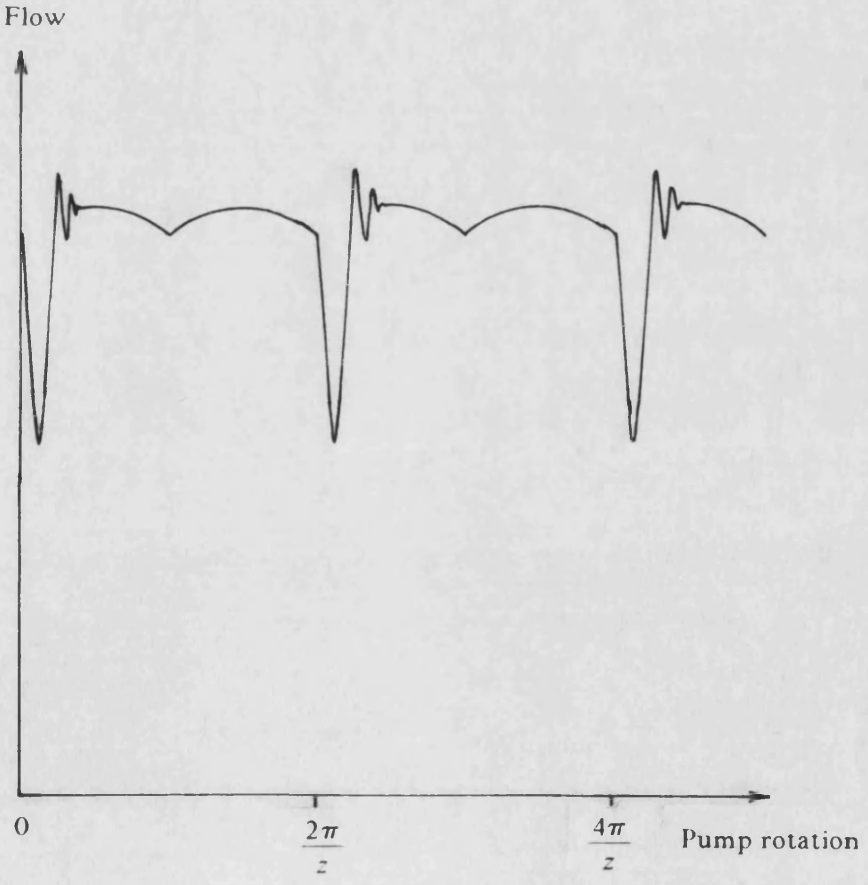

(b) Overall flow

Fig. 2.3 Typical Axial Piston Pump Flow Ripple

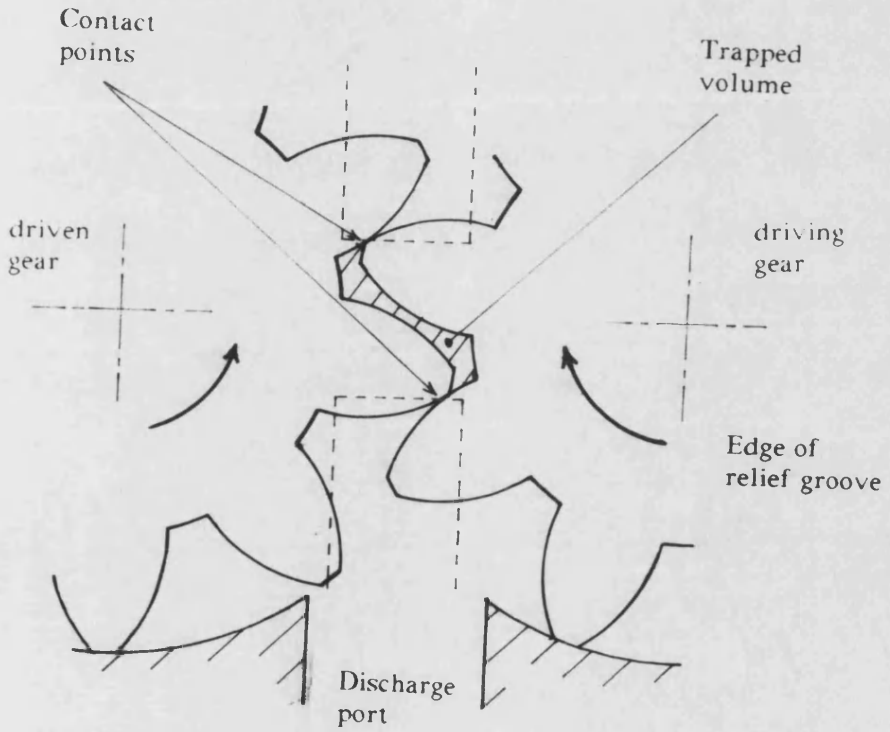

(a) Relief groove configuration

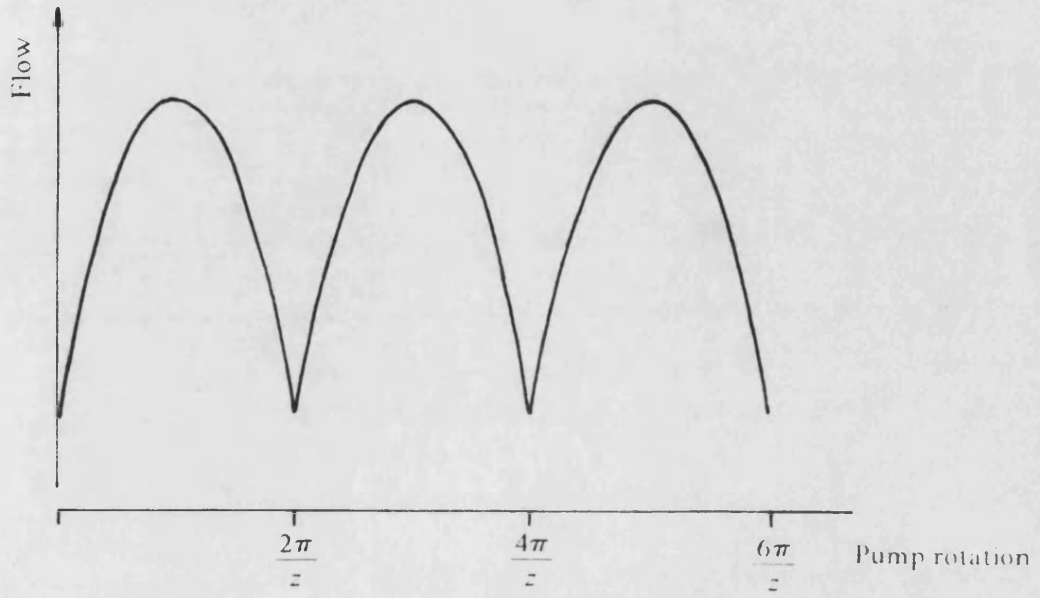

(b) Flow ripple

Fig. 2.4 Ideal External Gear Pump Flow Ripple

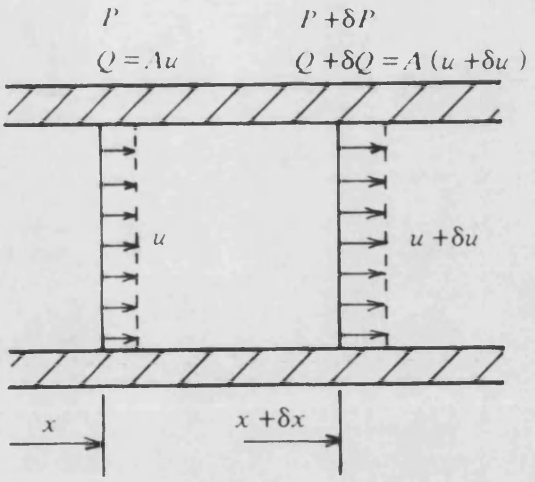

Fig. 2.5 Fluid Element in Pipeline

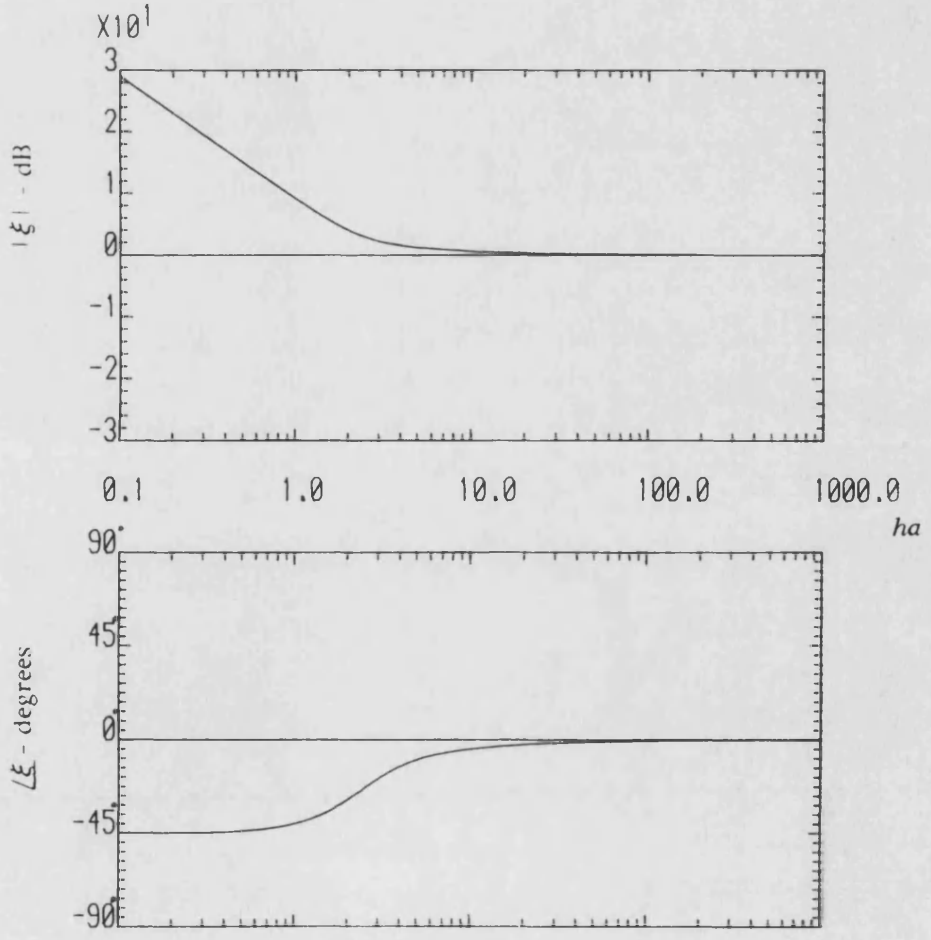

Fig. 2.6 Bode Plot of ξ against Wave Shear Number ha

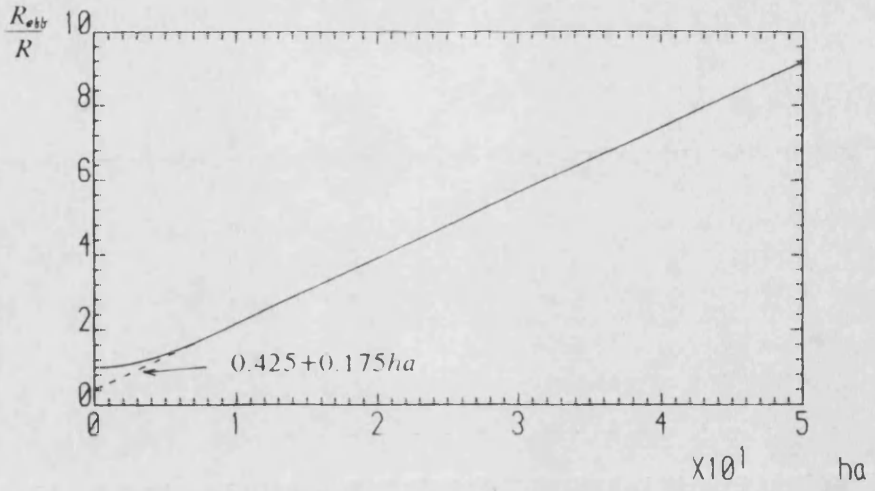

Fig. 2.7(a) Variation of Effective Resistance with *ha*

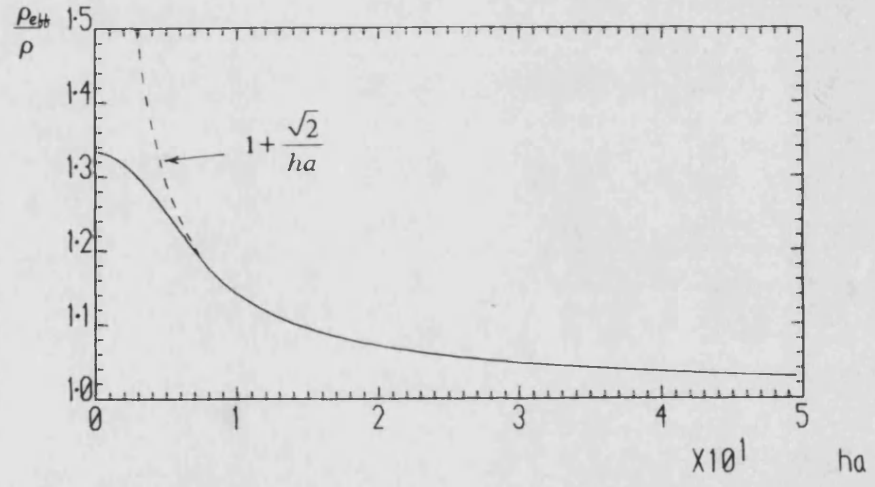

Fig. 2.7(b) Variation of Effective Density with *ha*

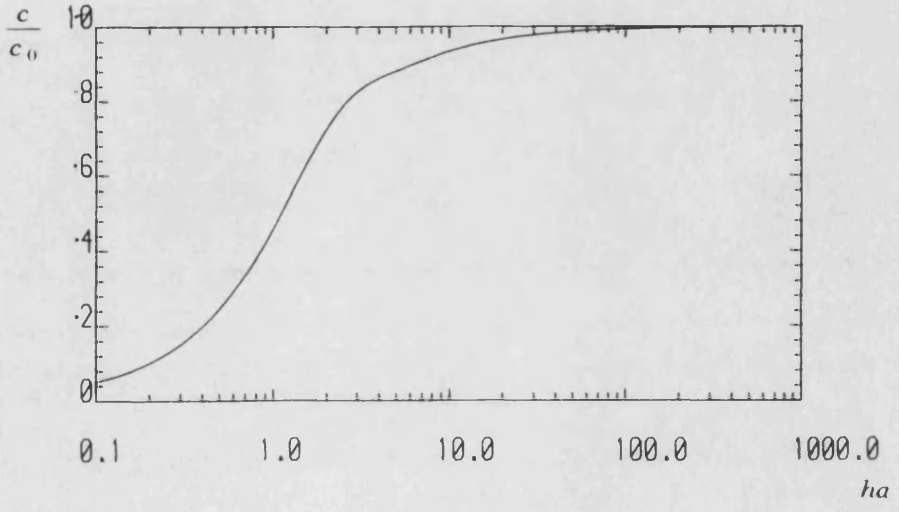

Fig. 2.8 Variation of Phase Velocity with *ha*

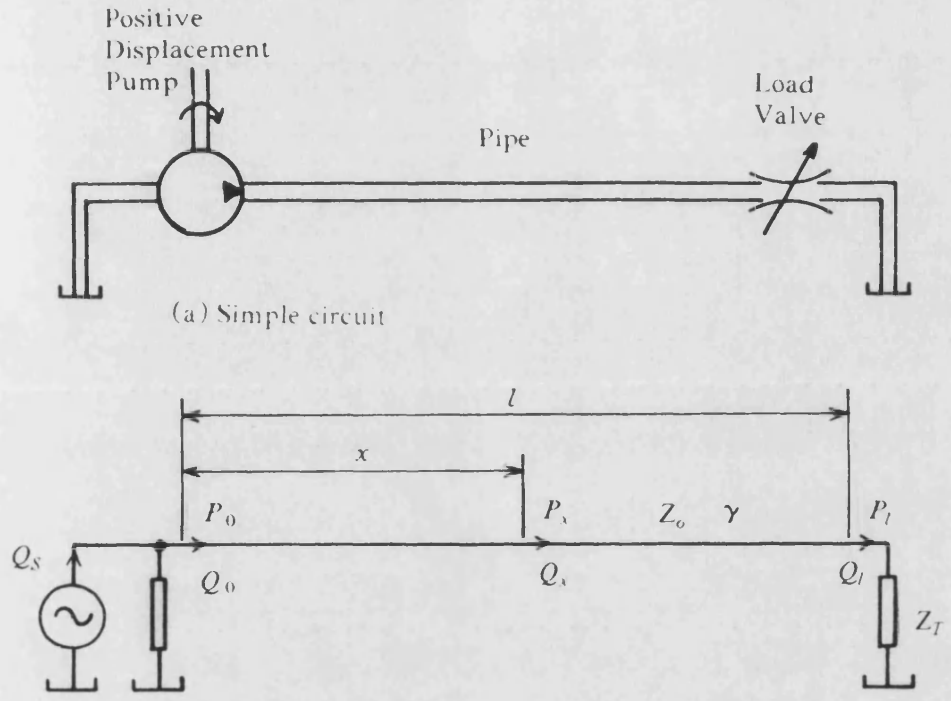

Fig. 2.9 **Application of Impedance Notation to a Simple Hydraulic Circuit**

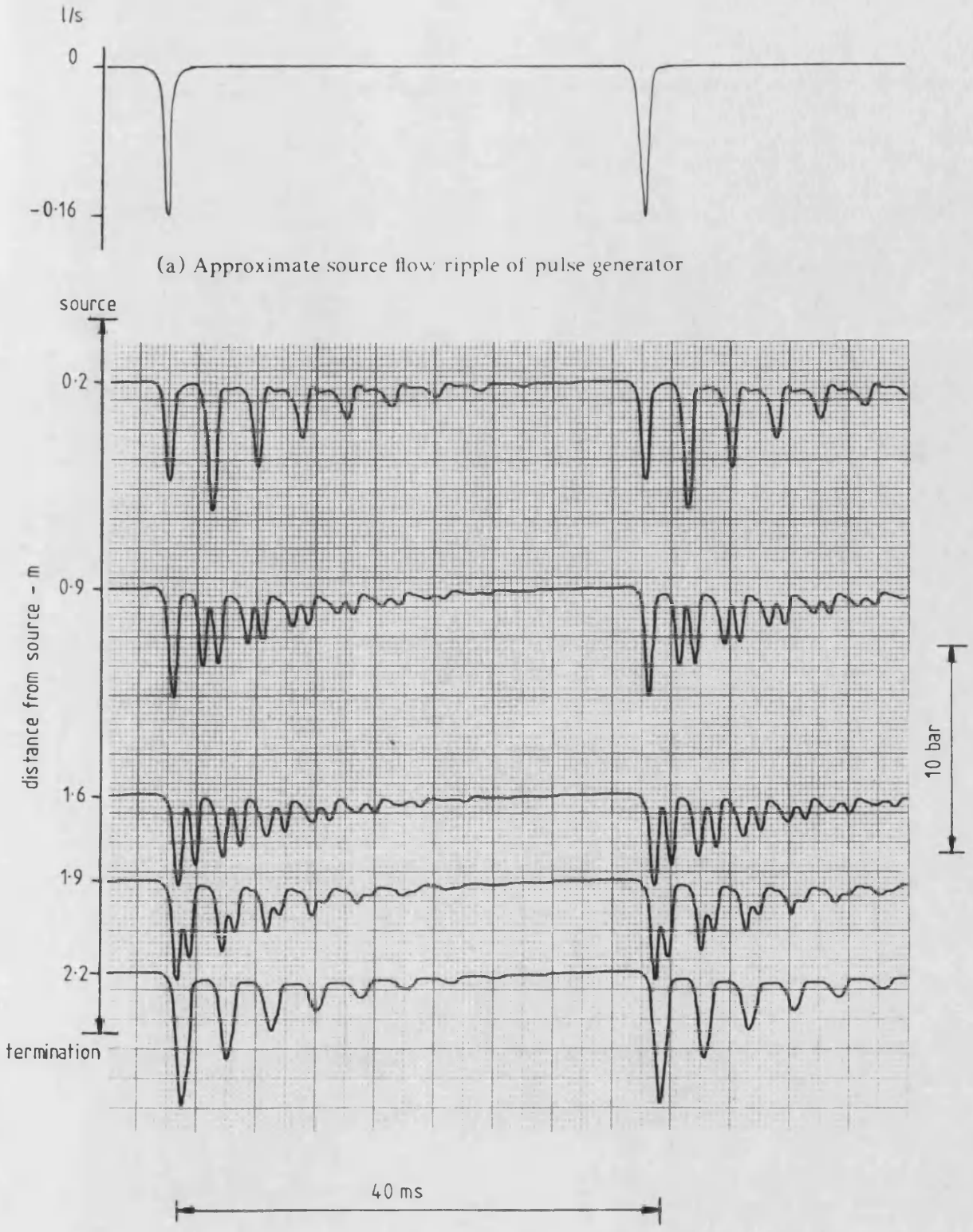

(a) Approximate source flow ripple of pulse generator

(b) Measured Pressure waveforms

Fig. 2.10 Pressure Ripple Measurements at Various Points along a Length of Pipe

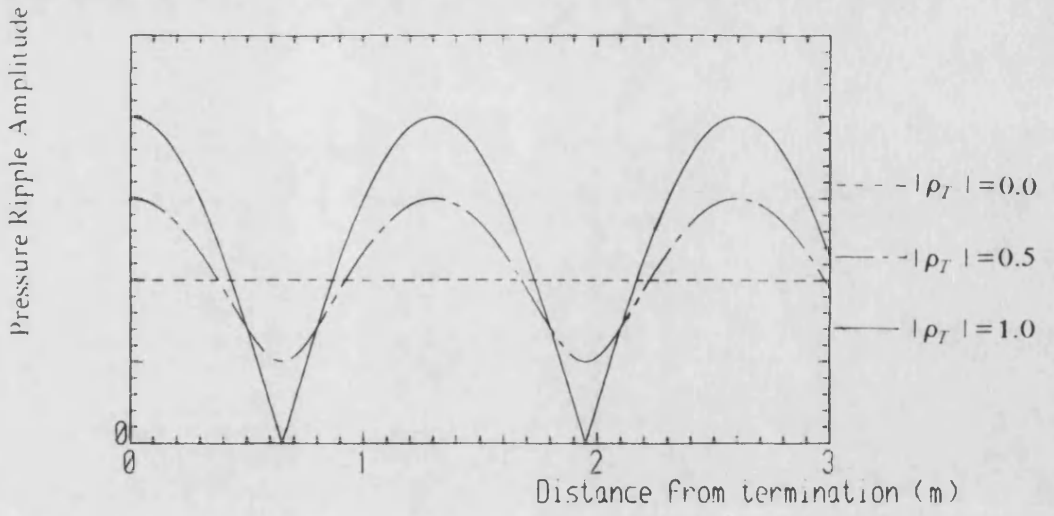

(a) Effect of $|\rho_T|$ where $\angle\rho_T = 0$

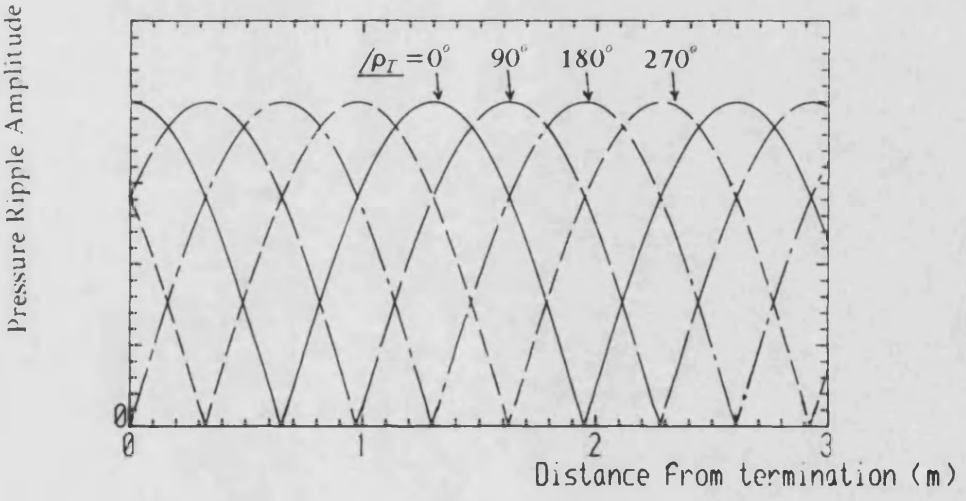

(b) Effect of $\angle\rho_T$ where $|\rho_T| = 1.0$

Fig. 2.11 Effect of ρ_T on Pressure Standing Wave in a Pipe

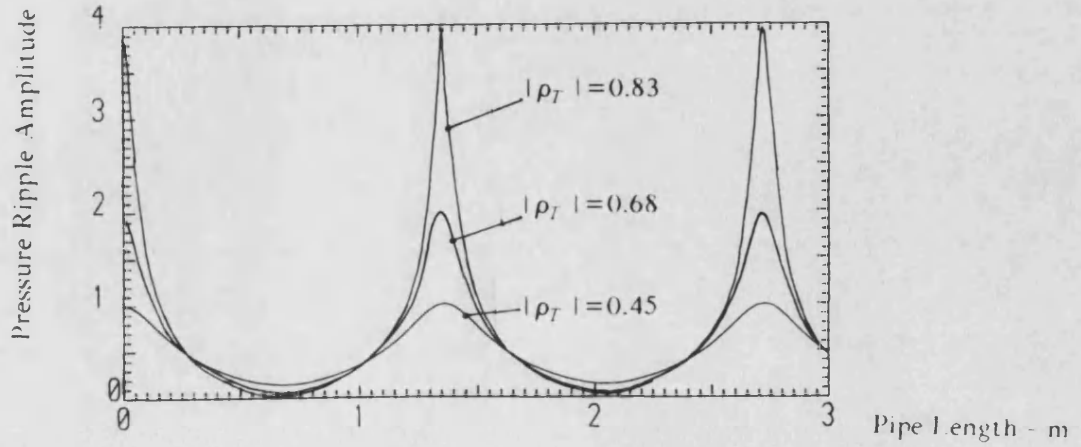

Fig. 2.12 Effect of Pipe Length on Pressure Ripple Amplitude for Various Values of $|\rho_T|$, where $\angle\rho_T = 0$

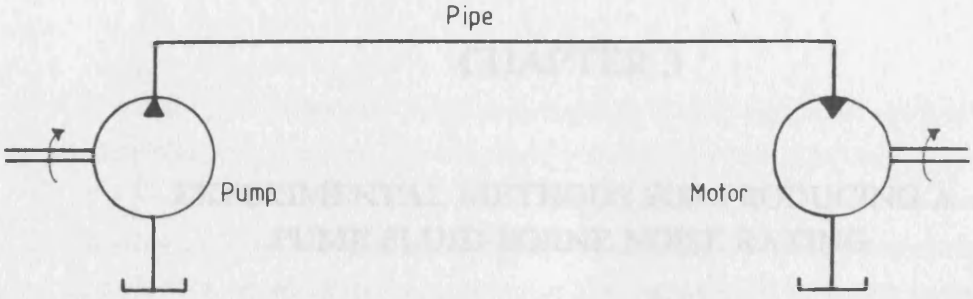

Fig. 2.13 Simplified Hydrostatic Transmission

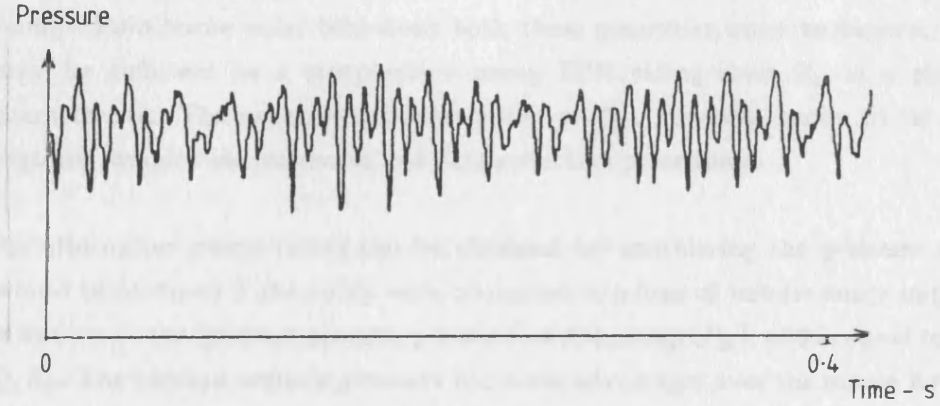

(a) Time domain waveform, showing 'beating'

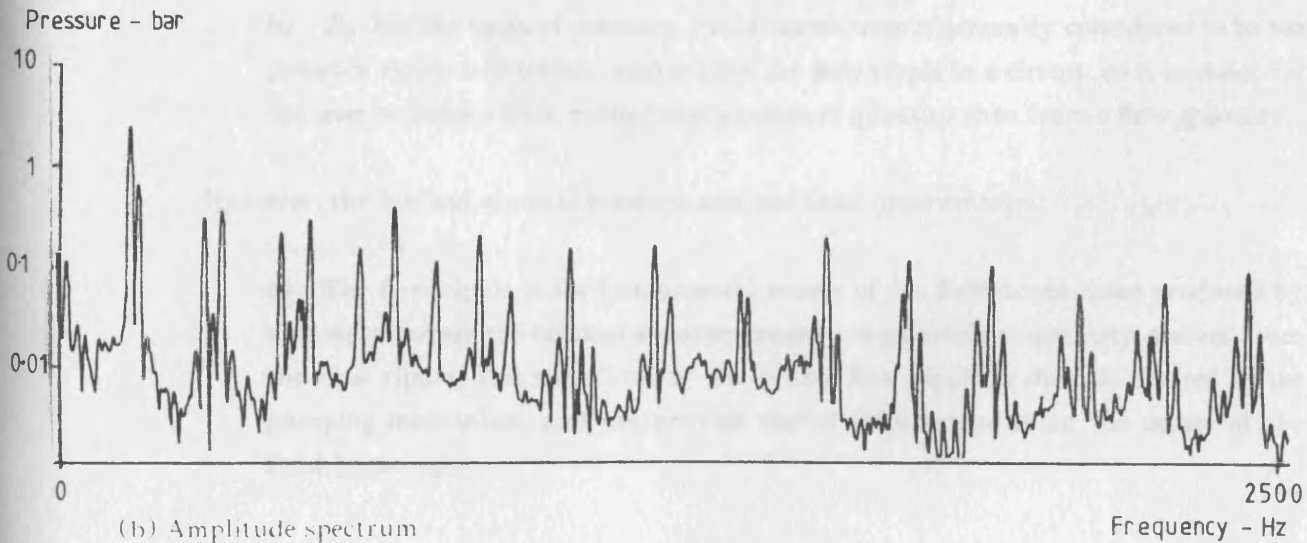

(b) Amplitude spectrum

Fig. 2.14 Pressure Ripple in a Hydrostatic Transmission

CHAPTER 3

EXPERIMENTAL METHODS FOR PRODUCING A PUMP FLUID-BORNE NOISE RATING

Numerous experimental techniques for the determination of the fluid-borne noise characteristics of positive displacement pumps have been proposed by various researchers [24,26,42]. These techniques vary widely in their complexity; some are more comprehensive than others and are suited to different applications.

As described in chapter 2, using impedance notation a pump is generally described by the 'source flow ripple', Q_S, and the 'source impedance', Z_S. In order to fully describe the pump's fluid-borne noise behaviour both these quantities must be known, although Q_S may be sufficient as a comparative pump FBN rating since Z_S is a purely passive characteristic. The experimental evaluation of Q_S, however, tends to be difficult and requires complex measurement and data reduction procedures.

An alternative pump rating can be obtained by considering the pressure ripple which would be obtained if the pump were connected to a load of infinite entry impedance. This is known as the 'blocked acoustic pressure' of the pump (P_B), and is equal to the product $Q_S Z_S$. The blocked acoustic pressure has some advantages over the source flow ripple as a FBN rating, these being:

a) The blocked acoustic pressure tends to be rather simpler to evaluate experimentally than the source flow ripple.

b) P_B has the units of pressure. Fluid-borne noise is generally considered to be the pressure ripple in a circuit, rather than the flow ripple in a circuit, so it is easier for the user to judge a FBN rating from a pressure quantity than from a flow quantity.

However, the blocked acoustic pressure also has some disadvantages:

a) The flow ripple is the fundamental source of the fluid-borne noise produced by a pump, whereas the blocked acoustic pressure is an artificial quantity derived from the flow ripple. The waveform of the source flow ripple is directly related to the pumping mechanism, and can provide useful information about the causes of the fluid-borne noise.

b) Over the frequency range considered in fluid-borne noise analysis, the source impedance is, in general, predominantly capacitive. This will tend to over-emphasise the lower frequency harmonics of the blocked acoustic pressure, so that the higher harmonics will be negligible. However, the higher frequency harmonics of pressure ripple in a circuit often tend to be the greater nuisance in practice, since they may be more readily propagated as air-borne noise [43]. Thus, for example, an axial piston pump which produces a broad spectrum of fluid-borne noise may have a lower blocked acoustic pressure rating than a gear pump which produces a narrower spectrum, although in practice it may be much more noisy in most situations.

c) At any given frequency, the blocked acoustic pressure is proportional to the source impedance. Thus, a reduction in the source impedance will cause a reduction in the blocked acoustic pressure. However, it will also alter the resonant characteristics of the circuit, and could cause an increase in the generated pressure ripple level. There is a linear relationship between the source flow ripple and the consequent pressure ripple, however, so that at a given frequency a reduction in Q_S will cause a proportionate reduction in the pressure ripple.

For the above reasons, the author is of the opinion that the source flow ripple forms a better basis for a pump FBN rating than the blocked acoustic pressure, although the latter may be useful in some situations, particularly in view of the fact that it tends to be rather simpler to evaluate.

Perhaps the simplest form of FBN rating available is that based on a single measurement of the pressure ripple at the pump outlet. However, such a measurement would not be a function of the pump alone, but would be affected by the impedance characteristics of the system into which the pump discharges. Thus a direct pressure ripple measurement is only meaningful if:

a) a standard delivery circuit is used, or

b) the effect of the loading circuit characteristics can be predicted and compensated for, or

c) the effect of the loading circuit characteristics is negligible.

3.1. Unruh's Method

In 1975, Unruh [20] proposed a simple technique for the experimental determination of the source flow ripple of a pump. The test procedure involves the measurement of the pressure ripple at the discharge port of the pump. By making assumptions about the nature of the impedance characteristics of the components, Unruh proposed that it should then be possible to determine the harmonic amplitudes of the source flow ripple, using the equation

$$|Q_S| = \frac{|P_0|}{|Z_{sys}|} \qquad \ldots (3.1)$$

where P_0 is the measured pressure ripple, and Z_{sys} is the combined predicted impedance of the pump and loading system.

The technique requires that the pump should be loaded using a simple restrictor valve, connected as close as possible to the pump in order that wave propagation effects in the discharge line should be insignificant, permitting the use of simple lumped parameter theory. The impedance of the restrictor valve is assumed to be independent of frequency and dependent only upon the steady state characteristic of the valve, i.e.

$$Z_T = \frac{\partial \tilde{P}}{\partial \tilde{Q}} \qquad \ldots (3.2)$$

where it is assumed that

$$\tilde{P} = k\tilde{Q}^2 \qquad \ldots (3.3)$$

$$\text{thus } Z_T = \frac{2\tilde{P}}{\tilde{Q}}. \qquad \ldots (3.4)$$

The pump impedance is assumed to be a function of its internal volume and leakage.

Although this technique has the attraction of being very simple, it is unlikely that the results would be accurate. Considerable errors could be incurred in the prediction of the impedance Z_{sys}. It has been found [26] that the dynamic impedance of a restrictor valve shows significant reactive effects, such that errors will be incurred by the assumption of a pure resistance based upon the steady state characteristics. Furthermore, Edge [32] has shown that the pump impedance cannot be predicted accurately in terms of its measured internal volume and leakage alone, especially at high frequency where fluid inertia and

wave propagation effects will become significant.

3.2. Szerlag's Method

Also in 1975, Szerlag [21] proposed a method for determining a fluid-borne noise rating for a pump. The experimental procedure is very similar to that used by Unruh, in that the pump is loaded by a restrictor valve through a short length of line. Szerlag, however, considered the blocked acoustic pressure of the pump to be the relevant parameter. A correction factor is applied to the pressure ripple measurements in order to allow for the impedance of the load and discharge line. The resultant spectrum is then 'A' weighted to compensate for the response of the human ear, and the pump rating is assumed to be equal to the amplitude of the most significant harmonic.

Szerlag's method suffers from similar limitations to Unruh's, because of the difficulty in the accurate prediction of the impedance of components. Hence this method is rather limited in application, and the pump rating is only useful as a guide to the relative FBN levels of different pumps.

It is questionable as to whether the pump rating should be dependent on one harmonic only. Although this may give a reasonable comparison between pumps of a similar type, it may be meaningless when comparing dissimilar pumps. For example, an external gear pump, which only produces a few significant flow ripple harmonics, may have a higher rating by this method than an axial piston pump which generates a much broader spectrum, although in practice the latter may tend to be far noisier.

3.3. Davidson and Taylor's Method

A technique was described in 1976 by Davidson and Taylor [28] for the experimental evaluation of the characteristics of a pump. A critical appraisal of the technique is given by Wing [26].

The technique involves the measurement of the pressure ripple at the pump exit using two different types of load with different entry impedances, these being:

a) a restrictor valve connected to the pump by a length of pipe. Davidson and Taylor assumed that the impedance of the valve was significantly higher than the pipe characteristic impedance, so that the entry impedance of the pipe could be approximated to that of a closed line.

b) a load as in (a), but with an accumulator connected in parallel with the restrictor valve. Assuming that the accumulator presents a very low impedance, the entry impedance of the pipe approximates to that of an open-ended line.

By analysis of the resonant characteristics of the system with these two loads, it was proposed that the source impedance could be predicted, assuming it to be purely capacitive. Using this information, the source flow ripple could also be evaluated.

This method suffers from some similar problems to Unruh's and Szerlag's methods. It may be difficult to produce a good approximation to an open-ended and closed-ended line experimentally; results reported later in this thesis show that the assumption of an accumulator having a very low entry impedance is erroneous at high frequencies, where it has a strong inductive characteristic. Furthermore, the frequency range is limited by the assumption that the pump source impedance is purely capacitive.

3.4. 'High Impedance Pipe' Method

If the entry impedance of the discharge line is much greater than the pump source impedance, the pressure ripple at the pump outlet is independent of the system and equal to the 'blocked acoustic pressure', P_B.

i.e. $$P_0 = \frac{Q_S Z_S}{1 + Z_S / Z_E}. \qquad \ldots (3.5)$$

If $|Z_E| >> |Z_S|$, then $P_0 \approx Q_S Z_S = P_B$.

A method has been developed at Bath [23,24,26] based upon this principle. This is known as the 'High Impedance Pipe' method, and, as its name implies, employs a small diameter pipe of high characteristic impedance in an attempt to produce a high entry impedance. The pipe is terminated by a restrictor valve.

Thus $$Z_E = Z_0 \left\{ \frac{1+\rho_T e^{-2\gamma l}}{1-\rho_T e^{-2\gamma l}} \right\} \quad \ldots (3.6)$$

where $$\rho_T = \frac{Z_T - Z_0}{Z_T + Z_0} \quad \ldots (3.7)$$

or, ignoring pipe friction,

$$Z_E = Z_0 \left\{ \frac{Z_T \cos(\omega l / c_0) + jZ_0 \sin(\omega l / c_0)}{jZ_T \sin(\omega l / c_0) + Z_0 \cos(\omega l / c_0)} \right\}. \quad \ldots (3.8)$$

If $(\omega l / c_0) = n\pi$, where n is an integer, then $\sin(\omega l / c_0) = 0$, and $Z_E = Z_T$. If $(\omega l / c_0) = (n + \frac{1}{2})\pi$, then $\cos(\omega l / c_0) = 0$, and $Z_E = Z_0^2 / Z_T$. By use of a small diameter pipe, $|Z_0|$ can be made greater than $|Z_T|$, in which case the highest entry impedance is obtained where $(\omega l / c_0) = (n + \frac{1}{2})\pi$. Unfortunately this condition cannot be achieved for a whole harmonic series with just one pipe length. Thus a number of different pipe lengths must be used. It was proposed that the analysis should be performed over 10 harmonics, in which case 4 different pipe lengths would be required, one for harmonic no's 1,3,5,7 and 9, one for harmonic no's 2,6 and 10, one for harmonic no. 4 and one for harmonic no. 8.

The pipe diameter is selected such that up to 75% of the mean pressure is dropped along its length, and the remaining 25% across the valve.

Considerable success has been achieved using this technique, and it has been adopted as a British Standard [25]. Results can be obtained with a high degree of accuracy, provided that it is possible to achieve the situation where $|Z_E| >> |Z_S|$. Problems may be encountered under one or more of the following conditions:

a) when the pump under test has a small discharge volume.

b) at low harmonic frequencies.

c) at frequencies at which the source impedance has a resonant peak (normally this will tend to be above the range of frequencies under consideration).

d) at high mean flowrate.

e) at low mean pressure.

Conditions (a), (b) and (c) lead to relatively high values of $|Z_S|$. Conditions (d) and (e) lead to relatively large diameter pipes being necessary, reducing the value of $|Z_E|$. Problems are most likely at the fundamental frequency, at which the source impedance is of high magnitude. Unfortunately, in practice this tends to be the most significant harmonic.

A number of different pipe lengths and diameters are needed to perform a test. These will not necessarily be suitable for testing at a different mean pressure, mean flowrate or pump speed, so that a complete series of tests on a pump over a range of conditions would require a large number of different pipes.

3.5. 'Additional Capacity' Method

This technique [23] is an extension of the High Impedance Pipe method and is intended to enable the source flow ripple and source impedance to be evaluated, rather than the blocked acoustic pressure alone.

If an expansion chamber is fitted between the pump and the high impedance pipe, such that the entry impedance of the pipe greatly exceeds the expansion chamber impedance, then the pressure fluctuation at the pipe entry is given by

$$P_0 = \frac{Q_S Z_S}{1 + Z_S / Z_C} \qquad \ldots (3.9)$$

where Z_C is the impedance of the additional capacity, given by

$$Z_C = \frac{B}{j\omega V} \qquad \ldots (3.10)$$

provided that the expansion chamber dimensions are small so that wave propagation effects are negligible.

If the blocked acoustic pressure, $Q_S Z_S$, is known from a previous High Impedance Pipe test, then Q_S and Z_S can be determined by algebraic manipulation. To obtain more reliable results, a number of different expansion chamber volumes could be employed.

Unfortunately, in practice some erroneous results were obtained, probably due to difficulty in estimating the impedance of the expansion chamber, possibly caused the lumped parameter model of the expansion chamber being in error. Tests by Wing [26] showed that the correlation between the simple capacitive model and experimental results for the impedance of the expansion chamber tended to be poor.

3.6. 'Insert' Method

The Insert method [26] was a development of the Additional Capacity method, and entailed the use of a pipe insert as opposed to an expansion chamber, since its impedance characteristics could be modelled more reliably taking wave propagation effects into account.

Although some good results were obtained in practice, problems were encountered under certain conditions, in particular where the length of insert corresponded to an integral multiple of half a wavelength, in which case the solution was ill-conditioned and reliable results could not be obtained.

3.7. 'Extending Pipe Length' and 'Hydraulic Trombone' Methods

The Insert method could be very susceptible to small errors in pressure measurement. The Extending Pipe Length method was an attempt to reduce this problem by the use of a large number of different lengths of pipe at the pump outlet and measuring the pressure ripple at either end of the pipe in each case. From this information the pump parameters could then be calculated, using a curve fitting technique.

Although good results were obtained by this method, it was very time-consuming when a large number of different lengths of pipe had to be connected into the system. For this reason, a more practical system was developed [26]. Termed the 'Hydraulic Trombone', it involved a section of large diameter pipe which could effectively be varied in length by means of a piston arrangement, as shown in Fig. 3.1. Pressure ripple was measured at a number of points along the larger diameter pipe, and up to 9 different pipe lengths could be selected. By means of a curve fitting technique, the pump parameters could be determined with a good degree of accuracy.

Although rather more practical than the Extending Pipe Length method, the Hydraulic Trombone method was still time-consuming. The method suffered from inaccuracy under certain conditions, particularly in the prediction of the source impedance, which was ill-defined under the following conditions:

a) When the harmonic amplitudes of Q_S were low or unstable.

b) When near-reflectionless termination conditions occurred. The calculation of Z_S was based upon analysis of the behaviour of the reflection occurring at the source. If no reflection took place at the termination, there would be no subsequent reflection at the source, so the source impedance would be indeterminate.

c) When the range of pipe lengths was such that the system was predominantly at or near an anti-resonant condition. In such cases the measured pressure ripple levels showed little variation with pipe length, and were relatively independent of the source impedance. This condition could be avoided by altering the termination impedance characteristics by inserting additional lengths of pipe between the Hydraulic Trombone and the loading valve. The selection of this additional length, however, required considerable expertise.

3.8. 'Reflectionless Termination' Method

If the pump could be connected to a pipe in which no reflections were to occur, the analysis of the fluid-borne noise in such a system would be greatly simplified, and the pressure ripple at the pump outlet would simplify to:

$$P_0 = \frac{Q_S Z_S Z_0}{Z_S + Z_0}. \qquad \ldots (3.11)$$

This is not a function of the pump alone, but is also dependent on the pipe diameter. It could, however, be used as a rating, if a standard pipe diameter was used (perhaps equal to the diameter of the pump discharge port). Alternatively, this test could be used as a supplement to the High Impedance Pipe method. If the blocked acoustic pressure is already known, it is possible, by algebraic manipulation of the above equation, to separate the terms Q_S and Z_S.

An alternative approach was used by Larsson *et al* [22]. If it is assumed that the discharge passageway can be modelled as a length of uniform pipe, and the diameter of the connected pipe is chosen such that its characteristic impedance is equal to that of the pump discharge passageway, then, for a reflectionless line,

$$P_0 = Q_S^* Z_0 e^{-j\omega l_p/c} \qquad \ldots (3.12)$$

where Q_S^* is an alternative representation of the source flow ripple in which it is referred inside the pump to the end of the discharge passageway (section 4.3.10.). The $e^{-j\omega l_p/c}$ term represents a pure time delay and may be ignored, and Z_0 is a real constant. Thus the source flow ripple is directly proportional to the measured pressure.

Some good results were obtained by Larsson *et al* using this method. However, there were some practical difficulties:

a) A truly reflectionless line was difficult to achieve.

b) It was difficult to obtain good matching between the characteristic impedances of the pump discharge passageway and the pipe. Any mismatch would adversely affect the results, particularly at high frequency. The characteristic impedance of the pump discharge passageway is extremely difficult to estimate accurately without evaluating the pump source impedance experimentally.

There are two generally accepted ways of producing a non-reflective termination:

a) By the use of a very long pipe or hose. This method relies on the attenuation properties of the line, such that the wave is almost completely attenuated by the time it returns to the source. An extremely long rigid pipe (100-200 m) would be required to provide sufficient attenuation. Flexible hose tends to be more 'lossy', so that a shorter length ($\approx$ 50 m) would be sufficient. However, the behaviour of flexible hose is quite complex [37-39], and its characteristic impedance can be difficult to evaluate.

b) By the use of a 'tuned' termination. Such a termination was developed by Theissen [44], and is shown in Fig. 3.2. The upstream restrictor is set so that its resistance is matched to the pipe characteristic impedance. The expansion chamber downstream of this is intended to present a low impedance, in order that the entry impedance of the valve should be virtually equal to the resistance of the upstream restrictor. A second restrictor is situated downstream of the expansion chamber in

order to control the mean system pressure. The effectiveness of the tuned termination depends on the presumption that the impedance of the upstream restrictor can be modelled as a simple resistance, and that the expansion chamber is large enough to present a sufficiently low impedance over the whole range of frequencies under consideration. It is considered that it may be difficult or impossible to tune the valve to provide a sufficiently low reflection over the whole frequency range in practice, particularly in view of the restrictor valve impedance results in section 6.2., which show significant deviation from the simple model.

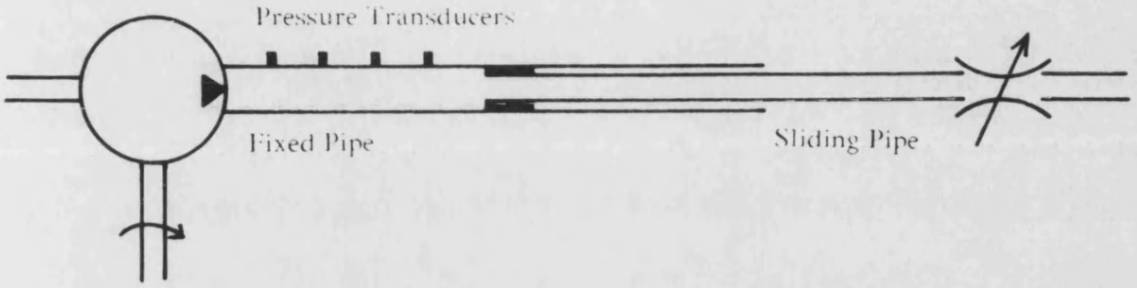

Fig. 3.1 'Hydraulic Trombone' Test Rig

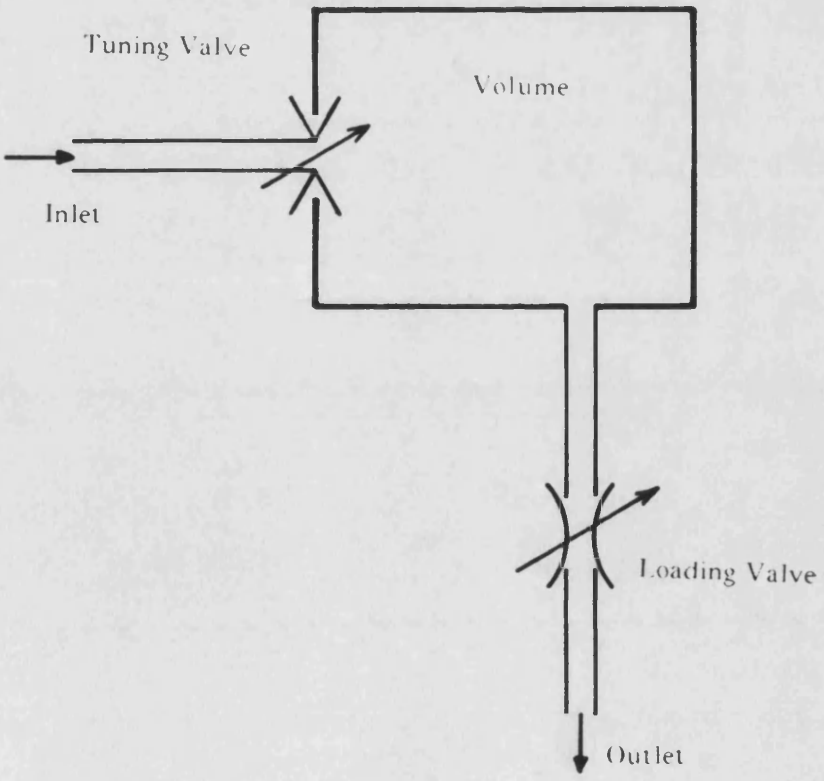

Fig. 3.2 Reflectionless Termination

CHAPTER 4

MEASUREMENT OF PUMP FLOW RIPPLE AND SOURCE IMPEDANCE

In this chapter a new method is described for the measurement of the fluid-borne noise characteristics of positive displacement pumps. The method is based around the analysis of the standing wave characteristics in a rigid pipe.

Because of the complex nature of the standing wave within a pipe, it is not sufficient simply to measure the pressure or flow ripple at one point; in order to obtain a complete definition of the wave characteristics, more information is required. At any frequency, the pressure and flow ripple at any point along a pipe can be defined by the following equations:

$$P_x = Fe^{-\gamma x} + Ge^{\gamma x} \qquad \ldots (4.1)$$

$$Q_x = \frac{F}{Z_0}e^{-\gamma x} - \frac{G}{Z_0}e^{\gamma x}. \qquad \ldots (4.2)$$

It is necessary to know both of the complex coefficients F and G, which represent the pressure waves travelling in either direction, in order to define the standing wave characteristics in the pipe (it is assumed that Z_0 and γ can be evaluated). These coefficients are not directly measurable; at any point in the pipe the measured pressure or flow ripple is the sum of the two pressure or flow waves. The two waves can be inferred, however, provided that at least two separate measurements (amplitude and phase) have been taken, which may be:

a) pressure ripple and flow ripple measurement at any point along the pipe

b) two pressure ripple measurements at different positions

c) two flow ripple measurements at different positions

The measurement of flow ripple is difficult; expensive techniques, such as hot wire probes

or Laser-Doppler anemometry must be used [9] in order to respond to the high frequencies. Furthermore, these techniques may be intrusive to the flow and may affect the system characteristics. Pressure ripple can be measured more easily; high frequency pressure transducers are readily available and less expensive, and the techniques involved are much simpler and need not be intrusive. For these reasons, it is usual to use pressure ripple measurements exclusively [26,30].

Two different approaches may be used in the analysis of the standing wave from the pressure ripple data, and these will now be discussed.

4.1. The 'Intensity' Method

This method is based upon a technique used in acoustic engineering for the measurement of acoustic intensity [45,46]. It involves the measurement of pressure ripple at two closely separated points, as shown in Fig. 4.1. This information is used to estimate the pressure and flow ripple at the intermediate point between the transducers. The pressure is assumed to be the mean of the measured pressures:

$$P' = \frac{P_U + P_D}{2}. \qquad \ldots (4.3)$$

The flow is assumed to be proportional to the gradient of the measured pressures:

$$Q' = \frac{A}{j\omega\rho}\frac{(P_U - P_D)}{\Delta x}. \qquad \ldots (4.4)$$

In fact the exact pressure and flow ripple values at the intermediate point are given by the following equations [45] (assuming frictionless pipes):

$$P = \frac{P_U + P_D}{2}\cos\frac{\omega\Delta x}{2c_0} \qquad \ldots (4.5)$$

$$Q = \frac{A}{\rho c_0}\frac{P_U - P_D}{2j\sin\frac{\omega\Delta x}{2c_0}}. \qquad \ldots (4.6)$$

Provided that $\omega\Delta x/2c_0$ is small, the approximations of equations (4.3) and (4.4) are valid. This condition can be achieved by making the distance between the transducers small. At low frequencies, however, the values measured at each transducer may be very similar, making it difficult to obtain accurate measurements of the pressure gradient in order to determine the flow ripple. Results at low frequencies will tend to be inaccurate and be affected strongly by random measurement error and transducer calibration error. Thus the bandwidth for accurate results is severely limited. It can, however, be greatly increased by using the exact equations (4.5) and (4.6). These equations are valid for any value of $\omega\Delta x/2c_0$, and so larger transducer spacings can be used thus improving the low frequency results.

The advantage of equations (4.3) and (4.4) is their simplicity. They can be implemented quite simply using analogue techniques in order to give a real time measurement of the pressure and flow ripple. However, in this work analysis is performed using a digital computer in which case the exact equations could easily be used.

4.2. The Standing Wave Method

As described in section 4.1., the approach used in the intensity method is to predict the pressure and flow ripple at the midpoint between two pressure transducers. An alternative is to define the standing wave in terms of the pressure wave in either direction, i.e. to calculate F and G as defined in equations (4.1) and (4.2). This method is referred to as the 'standing wave method' and is, in effect, equivalent to the exact intensity method.

Having measured the complex pressure at two points x_1 and x_2, then F and G can be found by manipulation of equation. (4.1), i.e.

$$F = \frac{P_1 e^{\gamma x_2} - P_2 e^{\gamma x_1}}{e^{-\gamma(x_1 - x_2)} - e^{\gamma(x_1 - x_2)}} \qquad \ldots (4.7)$$

$$G = \frac{P_1 e^{-\gamma x_2} - P_2 e^{-\gamma x_1}}{e^{-\gamma(x_1 - x_2)} - e^{\gamma(x_1 - x_2)}} \qquad \ldots (4.8)$$

Consider the simple system in Fig. 4.2. From equation (2.29), the pressure ripple at a position x is given by

$$P_x = \frac{Q_S Z_S Z_0}{Z_S + Z_0} \cdot \frac{e^{-\gamma x} + \rho_T e^{-\gamma(2l-x)}}{1 - \rho_S \rho_T e^{-2\gamma l}}.$$

By comparison of equation (2.29) with equation (4.1),

$$F = \frac{Q_S Z_S Z_0}{Z_S + Z_0} \cdot \frac{1}{1 - \rho_S \rho_T e^{-2\gamma l}} \qquad \ldots (4.9)$$

$$G = \frac{Q_S Z_S Z_0}{Z_S + Z_0} \cdot \frac{\rho_T e^{-2\gamma l}}{1 - \rho_S \rho_T e^{-2\gamma l}}. \qquad \ldots (4.10)$$

$$\text{Hence } \rho_T = \frac{G}{F} e^{2\gamma l} = \frac{e^{-\gamma(x_2 - x_1)} - \frac{P_2}{P_1}}{e^{\gamma(x_2 - x_1)} - \frac{P_2}{P_1}} \cdot e^{2\gamma(l - x_1)}. \qquad \ldots (4.11)$$

Therefore it is possible to calculate the termination reflection coefficient, and hence the termination impedance, by measuring pressure ripple at two or more points along a pipe. If ρ_S and Z_S were also known, it would be possible to calculate the source flow ripple. However, ρ_S or Z_S cannot be calculated by this method, no matter how many pressure transducers are used. The physical reason for this is that the effect of reflections at the source is to produce waves which travel in the same direction as the original wave from the source. These waves are indistinguishable from each other as they travel at the same velocity, so ρ_S cannot be calculated, no matter how well the standing wave form is defined.

More information is necessary to measure the source impedance and reflection coefficient. The technique used in the 'Hydraulic Trombone' [26] and related methods is to alter the circuit dimensions or configuration physically during the course of a test. In theory, by changing the entry impedance of the system in this way, it is possible to calculate ρ_S and Z_S. However, this can be very prone to error in practice. This was countered in the Hydraulic Trombone technique by recording data for a large number of line lengths; this was tedious and could still be highly error-prone under certain conditions, as described in section 3.7.

In order to overcome the problems of methods such as the Extending Pipe Length technique, an alternative method is proposed, termed the 'Secondary Source' method.

4.3. The Secondary Source Method

The basis of this technique is to employ a secondary source of fluid-borne noise, situated at the termination of the simple system in Fig. 4.2. For the purpose of the analysis of fluid-borne noise, this becomes equivalent to the hydrostatic transmission system as described in section 2.10., Fig. 4.3(a). The system can then be analysed as the two sub-systems in Fig. 4.3(b) and (c). Sub-system (ii) has as its termination the pump under test. The pressure ripple at any point due to the secondary source only is given by the equation

$$P_x = \frac{Q_{S2} Z_T Z_0}{Z_T + Z_0} \cdot \frac{e^{-\gamma(l-x)} + \rho_S e^{-\gamma(l+x)}}{1 - \rho_T \rho_S e^{-2\gamma l}} . \qquad \ldots (4.12)$$

It is assumed that the fluid-borne noise from one source is separable from that from the other source. By analysing the standing wave characteristics of the pressure ripple from the secondary source alone, it is possible to calculate the source impedance ρ_S. By analysing the pressure ripple from the pump under test, as in sub system (i), the termination reflection coefficient can be evaluated, and sufficient information becomes available to calculate the source flow ripple Q_S, using the equation

$$Q_S = \frac{F(Z_S + Z_0)(1 - \rho_S \rho_T e^{-2\gamma l})}{Z_S Z_0} \qquad \ldots (4.13)$$

This forms the basis of a technique for the measurement of the fluid-borne noise characteristics of positive displacement pumps. The technique can be split into two distinct sections:

a) measurement of the source impedance

b) measurement of the source flow ripple. This section also involves the measurement of the termination impedance, in order that the impedance characteristics of the system are fully defined.

4.3.1. Source Impedance Measurement

In order to measure Z_S and ρ_S, it is necessary to examine the pressure ripple generated by the secondary source. It is essential that this can be isolated from any pressure ripple from the pump under test. This condition can be achieved in two ways:

a) the pump under test is shut down. This is undesirable as it would be a change in the working condition of the pump which may possibly affect the source impedance characteristics.

b) the harmonic frequencies of the two sources are different (assuming that the pressure ripple from the secondary source is periodic).

Therefore, rather than shutting down the pump under test, it is necessary to ensure that the harmonic frequencies of the secondary source do not coincide with those of the pump. The data acquisition system must have sufficient frequency selectivity to be capable of rejecting the harmonic components produced by the test pump.

The experimental values of Z_S thus obtained will be at frequencies which do not correspond to the harmonic frequencies of the pump under test. In order to evaluate the source flow ripple it is necessary to estimate the source impedance at those frequencies. This could be achieved by the following methods:

a) by interpolation between adjacent experimental Z_S results.

b) by application of a suitable mathematical model to the experimental results, minimising the 'sum of squares' error between the results and the model.

The mathematical modelling technique was employed since, provided that the form of the model was chosen so that the correlation between it and the experimental points was good, the technique would have the effect of 'rounding off' the effects of experimental scatter on the Z_S measurements. Also, the model parameters could provide useful information about the effective discharge length and diameter of the pump.

4.3.2. The Secondary Fluid-Borne Noise Source

The pressure ripple produced by this source must satisfy the following criteria:

a) it must have stable harmonic frequencies to permit accurate measurement.

b) it must contain measurable harmonics over a broad frequency band covering the band of pressure ripple generated by the pump under test.

c) it must not be 'swamped' by the pressure ripple from the pump under test.

A number of different types of noise sources were considered. These were:

i) Electromagnetic vibrator and piston mechanism.

This could have the benefit of a high degree of control over the input signal. It would be possible to apply a pure sinusoidal input which could be swept over a frequency band. Alternatively, a random or 'PRBS' (Pseudo-Random Binary Sequence) could be applied. This technique has been used with some success by Henderson *et al* [42]. However, the necessary hardware would be complex and expensive, and the frequency response might be rather limited.

ii) Positive displacement pump or motor.

A 'noisy' pump or motor could be employed as a pressure ripple source. This would have the advantage of simplicity. The pump/motor would need to generate a broad harmonic spectrum; an axial piston unit might be ideal in this respect. A motor would have the advantage of not requiring a separate power supply as it could be driven by the flow from the pump under test; however, a pump would be more versatile as it would not be dependent upon the flow from the test pump.

iii) Pulse generator.

A rotary valve could be constructed to provide a bleed-off from the high pressure line during a small section of its revolution. This would produce a flow ripple consisting of a train of negative pulses of very short duration. Provided the duration of the pulses was very short compared to the cyclic period, the spectrum of such a signal would show a very large number of significant harmonics.

Although the flow ripple would not be particularly controllable, this could be a very simple and effective solution.

Details of the pumps which were tested using the Secondary Source technique are given in appendix 1. The vast majority of pump tests were carried out using an axial piston pump as the secondary source. Pump 'A' was used in most cases as this was known to be especially noisy in terms of its flow ripple [26], with a broad harmonic spectrum, making it ideal in this respect. A spectrum of the pressure ripple produced by this pump in a typical circuit is shown in Fig. 4.4(a). The pump produces a spectrum consisting of reasonably strong and stable harmonics up to a maximum frequency of about 3500 Hz. In addition to the harmonics occurring at multiples of the pumping frequency, however, it can be seen that there are also harmonics at multiples of the shaft rotation frequency, with a fundamental of 25 Hz. These are most noticeable in the range of 1500 Hz to 3000 Hz, and appear to be sidebands of the pumping frequency harmonics. They are caused by small differences between the pumping characteristics of individual cylinders. It was found, however, that these harmonics were not, in general, sufficiently strong or stable for use in the analysis.

When testing pump 'A' itself, pump 'B' was used as the secondary source.

Some tests were also performed using a pulse generator, which is described in appendix 2. The basic principle of operation of this device was to allow a periodic bleed-off from the high pressure line in order to produce a flow pulse of very short duration, occurring once every revolution of the shaft. The pulse generator was driven by a fixed speed electric motor running at 1500 rev/min, producing a fundamental frequency of 25 Hz. A typical pressure ripple spectrum generated using this is plotted in Fig. 4.4(b). As can be seen, there are many significant harmonics, measurable up to about 2000 Hz (80 harmonics). The frequency, amplitude and phase of these was found to be quite stable, except for the highest harmonics, so that accurate harmonic analysis was possible below about 1200 Hz.

The pulse generator was used for measurements in the relatively low frequency band of 25 Hz to 1.2 kHz, and pump 'A' was used for measurements in the higher frequency band of 175 Hz to 3 kHz.

4.3.3. Optimisation of Test Rig Configuration

The potential accuracy of the proposed test is highly dependent upon the pipe length, the positioning of the pressure transducers and the pipe diameter.

4.3.3.1. Pipe Length and Transducer Spacing Optimisation

The longitudinal positioning of the pressure transducers relative to each other is critical to the analysis of the standing wave, and hence to the calculation of ρ_T, ρ_S, Z_S and Q_S. In order to produce good results, the configuration needs to be designed so that the prediction of the above is as insensitive as possible to errors in pressure measurements. Under certain conditions, small experimental errors can lead to large errors in the results, in which case the equations are said to be ill-conditioned. This situation needs to be avoided whenever possible.

For simplicity, consider just two pressure measurements, P_1 and P_2, taken from transducers at positions x_1 and x_2, spaced Δx apart. Ignoring pipe friction,

$$H_{21} = \frac{P_2}{P_1} = \frac{e^{-j\omega x_2/c_0} + e^{-j\omega(2l-x_2)/c_0}}{e^{-j\omega x_1/c_0} + e^{-j\omega(2l-x_1)/c_0}}. \qquad \ldots (4.14)$$

where H_{21} = pressure transfer function between points x_2 and x_1.

If a small experimental error ϵ is introduced into H_{21}, such that

$$H_e = H_{21} + \epsilon \qquad \ldots (4.15)$$

and this produces an error δ in the calculated reflection coefficient ρ_T, such that

$$\rho_{Te} = \rho_T + \delta \qquad \ldots (4.16)$$

then, for small ϵ and δ

$$\frac{\epsilon}{\delta} = \frac{\partial H_{21}}{\partial \rho_T} = \frac{2e^{-2j\omega l/c_0}\sin(\omega \Delta x/c_0)}{[\,e^{-j\omega x_1/c_0} + \rho_T e^{-j\omega(2l-x_1)/c_0}\,]^2} \qquad \ldots (4.17)$$

where $\Delta x = x_2 - x_1$ $\qquad \ldots (4.18)$

$$\text{thus } \left|\frac{\delta}{\epsilon}\right| = \left|\frac{[\,e^{-j\omega x_1/c_0} + \rho_T e^{-j\omega(2l-x_1)/c_0}\,]^2}{2\sin(\omega \Delta x/c_0)}\right|. \qquad \ldots (4.19)$$

A large value of this expression implies that the value of ρ_{Te} is very sensitive to experimental error. It is desirable that the value of the expression is small over the whole range of test conditions.

The denominator of (4.19) tends towards zero when $\omega \Delta x/c_0 \rightarrow n\pi$, where n is an integer. This implies that if the spacing between the transducers is approximately equal to an integer multiple of half a wavelength, large errors will be incurred in the calculation of ρ_T. Such a condition is shown graphically in Fig. 4.5. It is clear that any number of standing wave forms can be superimposed upon the measured pressures.

This condition may be difficult or impossible to avoid when considering a range of test conditions and the broad frequency band involved. There are two possible solutions:

a) Position the transducers close together so that $\omega \Delta x/c_0 < \pi$ over the whole frequency band. However, over the first few harmonics, $\sin(\omega \Delta x/c_0)$ will be small, and so large errors may be introduced at low frequency. This is a problem associated with the 'intensity' method [45].

b) Measure pressure at more than two points, with different spacing between each pair of transducers. By this means, the above condition can be avoided.

Solution (b) was adopted for the experimental apparatus. Five transducers were used initially, the first three being 0.3 m apart and the last three being 0.7 m apart. The overall span of 2 m was chosen so as to be long enough to measure the fundamental frequency characteristics with accuracy, while not being so long as to be unwieldy. The use of more than two transducers has the added advantage of smoothing out the effect of random or calibration error in the experimental results. Thus, more accurate results should be obtainable with several transducers. However, in general it then becomes impossible to fit an exact mathematical curve to the experimental data; because one is attempting to define two complex numbers (F and G) in terms of more than two complex data points, it is necessary to apply some form of 'best fit' so that the modelled standing wave fits the data points as closely as possible. Appendix 3 describes an algorithm for a curve fitting method, which uses the criterion of minimising the sum of the squares of the absolute values of the error between the model and the data points. The reasoning behind providing two groups of equi-spaced transducers is described in section 7.1. In fact most of the later tests were performed using measurements from just three unequally spaced transducers. In this way less data were required and it was found that the decrease in the accuracy of the results was minimal.

4.3.3.2. Pipe Diameter Optimisation

The source impedance of the pump is calculated from the measured reflection coefficient ρ_S using the following equation:

$$Z_S = Z_0 \frac{1+\rho_S}{1-\rho_S}$$

or, putting $z = \frac{Z_S}{Z_0}$, $\rho_S = \frac{z-1}{z+1}$. ...(4.20)

If a small error δ is introduced into the measured value of ρ_S, as in section 4.3.3.1., such that

$$\rho_{Se} = \rho_S + \delta \quad \ldots(4.21)$$

and this produces a relative error ζ in z, where

$$z_e = z(1+\zeta). \quad \ldots(4.22)$$

Differentiating (4.19), one obtains, for small ζ and δ,

$$\frac{\partial \rho_S}{\partial z} = \frac{\delta}{z\,\zeta} = \frac{2}{(z+1)^2} \qquad \ldots (4.23)$$

$$\text{hence } \left|\frac{\zeta}{\delta}\right| = \left|\frac{(z+1)^2}{2z}\right|. \qquad \ldots (4.24)$$

In order to obtain accurate values of Z_S, the ratio $|\zeta/\delta|$ should be as small as possible. This ratio is plotted as a contour map on the complex plane of z in Fig. 4.6. The graph demonstrates that, ideally, $|Z_S/Z_0| = 0$ dB, i.e. $|Z_S| = |Z_0|$, for minimum error in Z_S. Obviously, however, this condition cannot be achieved at all frequencies with several different pumps, so Z_0 was chosen to be approximately equal to the geometric mean of the expected range of Z_S to be encountered.

From results obtained by other researchers [26,32], $|Z_S|$ typically ranges from 165 dB (0 dB = 1 Ns/m^5) to 210 dB. A pipe internal diameter of 20 mm was chosen, for which $|Z_0| \approx 4\times10^9$ Ns/m$^5 \approx 190$ dB for mineral oil.

4.3.4. Description of Hydraulic Circuit

Fig. 4.7 shows a schematic diagram of the hydraulic circuit employed for the testing of pumps 'B', 'C', 'D' and 'E'. The pump under test was driven by a variable speed hydrostatic transmission [47]. The prime mover for this was a 110 kW electric motor with a nominal speed of 1470 rev/min, which drove a large variable capacity axial piston pump, maximum capacity 166 cm^3/rev. The pump swash was controlled using a servoactuator system with a manual demand input from zero to full swash. This pump powered a fixed capacity axial piston motor (78 cm^3/rev) which in turn drove the pump under test. A large Holset viscous damper was mounted on the shaft to help damp out any speed fluctuations in order to improve the accuracy of harmonic pressure ripple measurement. The hydrostatic transmission was run in a simple uni-directional closed loop configuration, with a boost pressure of 17 bar provided by a gear pump driven by a separate 11 kW electric motor. Another gear pump, driven by the same motor, was available to provide a boost supply for the pump under test and the secondary fluid-borne noise source, when necessary. Using the swash control, it was possible to vary the output speed from 0 rev/min to 3,000 rev/min, within about $\pm$15 rev/min.

The working temperature of the oil was controlled by a thermostatic valve in the water

supply to the oil cooler. It was possible to maintain the temperature within $\pm 2^{\circ}$ C of the required value.

4.3.4.1. Measurement Section

The pump under test fed directly into a straight length of tungum alloy pipe. Along the length of this pipe were mounted five pressure transducers, fitted so that their diaphragms were flush with the inside wall of the pipe. This length of pipe and its fitting with the pump under test formed the part of the system where the standing wave was analysed; it was therefore crucial that there were no flow obstructions, side branches or pockets which could affect the results, particularly at the pump-pipe union. Care was taken to prevent the formation of pockets of trapped air.

The loading circuit and the secondary generator were mounted at the other end of the measurement section. Loading was effected using a simple restrictor valve. A relief valve was fitted for safety purposes; the cracking pressure was set well above the normal operating pressure to prevent any stray mechanical oscillations or instability which could adversely affect the results. A pressure gauge was also fitted at this point. Flow from the loading valve then passed through a positive displacement flowmeter and returned to tank through an oil cooler.

Pump 'A' was also fitted at this end of the measurement section, as the secondary generator. It was driven using a 18.5 kW electric motor, running at a nominal fixed speed of 1470 rev/min. This was found to provide an extremely stable shaft speed (within $\pm$ 0.1 % at any operating condition), thus facilitating accurate harmonic measurement of pressure ripple.

A toothed disc with a number of teeth equal to the number of pumping elements was fitted to each pump shaft. In conjunction with magnetic proximity detectors, these provided a pulse signal at a reference frequency equal to the fundamental frequency of the pump.

When testing pump 'A' the configuration was reversed so that pump 'B' was the secondary source.

4.3.5. Instrumentation

A schematic diagram of the instrumentation is shown in Fig. 4.8.

4.3.5.1. Pressure Transducers

The pressure ripple was detected using miniature piezo-electric pressure transducers. These devices have a very small diaphragm, only 4 mm across, such that any pressure variations across them can be considered negligible. The output from these transducers is an electric charge in response to a pressure change, this charge rapidly leaking away in practice, with the result that, in effect, they exhibit the response of a high pass filter and cannot measure mean pressure. This is in fact advantageous as it prevents a large d.c. offset being present on the output due to the mean working pressure of the system. They have a specified natural frequency of 67 kHz, which is well in excess of the frequencies considered.

Each pressure transducer was used in conjunction with a charge amplifier and the connections from transducer to amplifier were kept short, using suitable low-noise cable. The outputs from the charge amplifiers were multiplexed so that any particular signal could be selected, using relays so as not to degrade the signal.

4.3.5.2. Frequency Response Analyser

Harmonic analysis of the pressure ripple signals was initially performed using a digital Frequency Response Analyser ('FRA'). In its normal application, this instrument is used to input a known sinusoidal signal to a system and the system response is recorded. In the measurement of pressure ripple, however, external excitation of the system was not necessary or possible as the pump provided the necessary excitation. In order to operate in this situation, a synchronisation signal was required in order to 'lock' the FRA onto the pressure ripple fundamental frequency. This synchronisation signal was provided by the toothed wheel and proximity detector on each of the pump drive shafts.

The signals from the proximity detectors were multiplexed according to which pump pressure ripple was being analysed, and the resultant passed through a Schmitt trigger, to provide a clean pulse. To provide a more stable trigger frequency for the FRA, this pulse was then passed through a phase-locked loop before it was fed into the FRA synchroniser.

The FRA employed was a dual channel device, capable of analysing either one single signal (ch1 or ch2) or the transfer function between two signals (ch2/ch1). It was found that the transfer function between the pressure signal from two transducers could be measured with greater stability than single channel measurements. This was because any small fluctuations in pump speed or random variations in the pump flow ripple would manifest themselves in the signals to both channels and be cancelled out. One pressure signal was thus routed to channel 1 to act as a reference for transfer function measurements with the other pressure signals, which were multiplexed and routed to channel 2.

In the calculation of ρ_T, Z_T, ρ_S and Z_S, transfer function measurements were sufficient (Eqn (4.11)). However, to calculate Q_S, single channel measurements were necessary. A reference signal was required against which the phase of the signal could be measured; this was derived from the signal obtained from the magnetic pick-offs on the pump shafts. Instead of being passed through the phase-locked loop, however, the signal was passed through a pulse shaper which formed it into a train of very narrow positive pulses. The Fourier transformation of such a signal produces a cosine spectrum where all the harmonics have zero phase over the frequency range of interest. Therefore, by evaluating the phase transfer function between the pressure ripple and the pulse waveform, a cosine spectrum was produced. The phase reference pulse signal was not passed through the phase-locked loop as this was found to give more consistent results; any small, rapid frequency drift in the pressure ripple would also manifest itself in the pulse, thus partially cancelling out any phase error.

The accuracy of the pressure ripple readings was found to be very dependent upon the length of time over which each signal was analysed by the FRA. The optimum analysis period was essentially a compromise governed by the following factors:

a) Frequency selectivity. The capability of the FRA to isolate the required harmonic and reject other components of the signal increased with the analysis period. Provided that the analysis was performed over an integral number of fundamental cycles, any signal components in the same harmonic series as that being analysed would be totally rejected. However, any other components could affect the results.

b) Tolerance of shaft speed variation. Over a long analysis period, any speed variation could cause a loss of synchronisation between the FRA and the system.

It was found experimentally that the best results were obtained by analysing over a large number of cycles for transfer function measurements (typically 200 cycles of the fundamental component, 400 second harmonic cycles, etc.) and a small number of cycles for absolute measurements (typically 10-20 cycles of the fundamental). An integer multiple of the number of pumping elements was taken at all times in order to compensate for any differences between individual pumping element characteristics. Readings at the lower harmonics were found to be much more consistent than readings at the higher harmonics; this was to be expected as:

a) Lower harmonics tended to have higher amplitudes than higher harmonics.

b) Small variations in pump speed may be insignificant at lower harmonics but very important at higher harmonics. For example, a 1 Hz drift in the fundamental frequency would be equivalent to a 16 Hz drift at the 16th harmonic. Over a long analysis period this could produce a significant phase change between the pressure ripple and the synchronisation waveform.

Increased accuracy could also be obtained by taking a number of measurements and calculating the arithmetic mean.

Some problems were encountered with the use of the FRA for the measurement of high frequency harmonics; it was sometimes found difficult or impossible to obtain accurate measurements above about 600 Hz. This was believed to be due to inaccuracies in the synchronisation between the FRA and the shaft reference signal. For this reason, a Digital Spectrum Analyser ('DSA') was used as an alternative to the FRA for a large number of the experimental tests. This was found to give more consistent results for a larger number of measured harmonics.

The DSA was operated in a similar manner to the FRA. Transfer function measurements were employed where possible. The start of the sampling period of the DSA was triggered using the phase reference signal; in this way, single channel phase measurements would automatically be calculated relative to this reference. The DSA had a versatile averaging facility, by which a number of different sets of readings could be averaged in several modes. The 'time averaging' mode was employed in this case, in which the mean of a number of different samples was calculated prior to the Fast Fourier transformation. In this way any signal components not synchronous with the reference

signal would be averaged out, resulting in improved harmonic selectivity.

4.3.6. Computer Control of Data Acquisition

The data acquisition procedure was controlled automatically using a microcomputer. Because of the large amount of data to be acquired, such automatic control was essential; manual control would have been time-consuming and prone to error. The microcomputer performed the following functions.

a) Remote control of the FRA or DSA, via an IEEE 488 General Purpose Instrumentation Bus ('GPIB').

b) Storage of data from the FRA or DSA on disc.

c) Control of the two multiplexers in order to switch the pressure signals and the pulse signals. Although the control signals were binary, they were obtained from Digital-Analogue Converters, since these were the most convenient output from the computer. The DAC's were programmed to output either +5V or -5V. One DAC was used for each control channel; thus three DACs were required to control the five pressure ripple channels (giving a maximum number of signal channels of 8) and one DAC only was required to control the two pulse channels.

The data acquisition stage was found to be very critical to the accuracy of results; hence a precise and systematic data acquisition programme was developed. The test procedure consists of two separate stages; the source impedance and the flow ripple are evaluated from independent tests.

4.3.7. Data Acquisition for Source Impedance Calculation

In order to determine the source impedance of the pump under test, pressure ripple from the secondary generator must be considered. As stated previously, it may or may not be necessary to run the test pump at this stage, but the pressure ripple from the test pump is not considered in this test.

The system was first run at the required operating conditions for at least half an hour, by which time the fluid temperature should have stabilised, and any trapped air should have been flushed out. Transfer function measurements of the pressure ripple from the auxiliary pump were then recorded for the required number of harmonics.

4.3.8. Data Acquisition for Flow Ripple Calculation

For this test, the secondary generator was not required. Single channel harmonic pressure ripple measurements were required to determine the source flow ripple. It should be noted that the termination reflection coefficient is not explicitly required for the pump parameters, but must be calculated in order that the transmission line equation may be solved to find the flow ripple. It could be calculated using the absolute pressure ripple measurements (in a similar way to the source reflection coefficient), but could be calculated more accurately using transfer function measurements. Hence, both transfer function and single channel pressure ripple readings were taken of the pressure ripple from the test pump.

On completion of the test, the data were transferred to a mainframe computer for data reduction.

4.3.9. Modelling the Source Impedance Characteristics of a Positive Displacement Pump or Motor

For the purpose of fluid-borne noise analysis, a positive displacement pump or motor is normally modelled as a source flow ripple in parallel with a source impedance, this being the hydraulic equivalent of Norton's model as used in electrical engineering to model current sources. Both the source flow ripple and the source impedance have a strong effect upon the pressure ripple generated in a system; indeed, the pressure ripple is directly proportional to the source flow ripple. The relationship between the source impedance and the pressure ripple is, however, less simple and is dependent upon the system characteristics. Thus there is no hard and fast rule as to what the source impedance characteristic should be for the pump to be quiet with regard to fluid-borne noise.

The proposed test method requires that an accurate model for Z_S should be developed in order that Q_S can be determined precisely over a wide bandwidth. The source impedance may be dependent upon a number of factors, some of which may be insignificant. These factors include:

a) the geometry of the discharge passageway.

b) the fluid properties (density, bulk modulus and viscosity).

c) the pump leakage.

d) the compliance of the pump casing.

e) air release and/or cavitation effects in the fluid.

It was shown by Edge [32] and Davidson [48] that the main factor affecting the source impedance in the frequency range of interest is the compressibility of the fluid contained within the pump. Thus, Z_S may be considered as a capacitance, i.e.

$$Z_S = \frac{B}{j\omega V}. \qquad \ldots (4.25)$$

Edge [32] and Davidson [48] found that the effective contained volume, inferred from the source impedance, tended to be significantly greater than the volume which could be physically measured by filling the pump discharge port with oil and measuring the capacity. This may be due to pump casing compliance or air relase or cavitation, all of which would tend to reduce the effective bulk modulus of the oil. Such effects tend to be unpredictable, so any attempt to evaluate the source impedance theoretically by measurement of the volume could be highly inaccurate.

At higher frequencies the inertance of the fluid in the discharge passageway becomes significant, and the lumped parameter approximation is no longer valid, so it is necessary to take distributed parameter effects into account. The inertial effect is strongly dependent upon the cross-sectional area of the passageway. In a real case, this cross-sectional area is not constant but there may be several changes in section along the length. In order to obtain a viable model it is necessary to simplify this, and it is proposed that the discharge passageway should be considered as an equivalent length of uniform cross section. Leakage may be assumed to take place at the end of this passageway. Neglecting viscous effects in the fluid, it can be shown that the impedance of such a model is described by the equation

$$Z_S = Z_{0p}\left\{\frac{1+\rho_L e^{-2j\omega l_p/c_0}}{1-\rho_L e^{-2j\omega l_p/c_0}}\right\} \qquad \ldots(4.26)$$

where

$$Z_{0p} = \frac{\rho c_0}{A_p}. \qquad \ldots(4.27)$$

A_p and l_p are the effective cross-sectional area and length respectively.

$$\rho_L = \frac{Z_L - Z_{0p}}{Z_L + Z_{0p}}. \qquad \ldots(4.28)$$

Z_L is the pump leakage impedance. It can be shown (section 6.2.) that Z_L can be estimated by:

$$Z_L = \frac{n\tilde{P}}{\tilde{Q}_{leakage}} \qquad \ldots(4.29)$$

where $n=1$ for laminar leakage flow. For a typical pump under normal operating conditions, $Z_L \approx 100\, Z_{0p}$, in which case $\rho_L \approx +0.98$. Thus leakage is unlikely to have any significant effect upon the source impedance, and may be ignored. Equation 4.26 then simplifies to:

$$Z_S = Z_{0p}\left\{\frac{1+e^{-2j\omega l_p/c_0}}{1-e^{-2j\omega l_p/c_0}}\right\} = \frac{Z_{0p}}{j\tan(\omega l_p/c_0)}. \qquad \ldots(4.30)$$

This model is compared with non-dimensional experimental results obtained by previous researchers [32] on a number of pumps in Fig. 4.9. The correlation between model and experimental results is much better than would be achieved using a lumped parameter model, especially at higher frequencies, though there are still discrepancies, particularly at the 'troughs' (anti-resonances) and 'peaks' (resonances) in the model, where the phase changes from $-90°$ to $+90°$ and vice versa. The experimental points appear to show some rounding of the amplitude and phase curves at these points, indicative of a 'damping' effect.

4.3.9.1. Modified Model Taking Distributed Friction Into Account

In reality the discharge passageway of a pump is not a uniform pipe, but contains bends and changes in section. Frictional losses are likely to be higher than those of an equivalent uniform pipe. A model was developed to take into account distributed viscous losses.

A number of additional assumptions were made in this model. They were:

a) the resistance coefficient is constant along the length of the passageway (i.e. uniformly distributed friction).

b) the resistance coefficient is independent of frequency. In the case of laminar flow in a uniform rigid pipe, the resistance coefficient is in fact strongly dependent on frequency (section 2.2.). However, in this case the passageway is not uniform and the relationship between frequency and resistance is not known.

c) the phase velocity is independent of frequency, i.e. $c = c_0$.

d) leakage effects are ignored.

$$\text{Thus, } Z_S = Z_{0p}\left\{\frac{1+e^{-2\gamma l_p}}{1-e^{-2\gamma l_p}}\right\} = \frac{Z_{0p}}{\tanh(\gamma l_p)} \qquad \ldots (4.31)$$

$$\text{where } \gamma = \frac{j\omega}{c_0} + \alpha \qquad \ldots (4.32)$$

$$Z_{0p} = \frac{\rho c_0}{A_p}\left[1+\frac{\alpha c_0}{j\omega}\right]. \qquad \ldots (4.33)$$

This model has the general form shown in Fig. 4.10. It can be seen that the inclusion of resistance has the required effect of providing 'damping' and rounding off the resonant and anti-resonant points.

At low frequency, provided that α is small,

$$\tanh(\gamma l_p) \approx \gamma l_p$$

in which case, $Z_S \approx \frac{Z_0}{\gamma l_p}$

$$\approx \frac{\rho c_0^2}{A_p j\omega l_p} = \frac{B}{j\omega V_p}. \qquad \ldots (4.34)$$

Hence, at low frequency, the model tends towards a simple capacitance.

A mathematical curve fitting algorithm for applying this model to experimental results is described in appendix 4.

4.3.10. Referral of the Source Flow Ripple within the Pump

It is generally assumed that the fluid-borne noise characteristics of a positive displacement pump or motor can be modelled as a Norton equivalent of a flow ripple in parallel with an impedance. Using this representation, the flow ripple is implicitly assumed to be generated at the outlet of the pump. This is not an accurate model of a real pump, in which the flow ripple generating mechanism is situated some distance inside the pump discharge passageway. The exact position of the source will vary with the type of pump, and in practice the flow ripple may be produced over a finite region rather than a single point. For example, in a gear pump the flow ripple is produced mainly in the meshing region, which is a line extending across the width of the gears. Similarly, for an axial piston pump, the flow ripple is generated in several regions; the backflow (2.1.1.) is generated at the end of the discharge port of the portplate, whereas the kinematic ripple emanates from within each cylinder in the discharge region. If, however, the region of flow ripple generation is small then Q_S can be considered to emanate from a single point. It is assumed here the Q_S is generated at the end of the discharge passageway.

Consider, then, the two pump models shown in Fig. 4.11. Fig. 4.11(a) is the standard 'Norton' representation, whilst Fig. 4.11(b) represents the modified model, in which the flow ripple, Q_S^*, occurs at the end of the discharge passageway. It is assumed that the discharge passageway is represented as in the source impedance model, i.e. as a uniform pipe with friction, with leakage effects ignored.

Now, for the standard model,

$$Q_0 = \frac{Q_S Z_S}{Z_S + Z_E} \qquad \ldots (4.35)$$

where $Z_S = \frac{Z_{0p}}{\tanh \gamma l_p}$. $\qquad \ldots (4.36)$

For the modified model, by applying the transmission matrix (equation (2.55)) to the discharge passageway,

$$\begin{bmatrix} P_{in} \\ Q_S^* \end{bmatrix} = \begin{bmatrix} \cosh \gamma l_p & Z_{0p} \sinh \gamma l_p \\ 1/Z_{0p} \sinh \gamma l_p & \cosh \gamma l_p \end{bmatrix} \begin{bmatrix} P_0 \\ Q_0 \end{bmatrix} \qquad \ldots (4.37)$$

and, since $P_0 = Z_E Q_0$,

$$Q_S^* = Q_0 \left\{ \cosh \gamma l_p + \frac{Z_E}{Z_{0p}} \sinh \gamma l_p \right\}. \qquad \ldots (4.38)$$

Substituting (4.35) and (4.36) into (4.38),

$$Q_S^* = Q_S \cosh \gamma l_p . \qquad \ldots (4.39)$$

Thus there is a direct relationship between the flow ripple modelled at the pump exit and that at the end of the discharge passageway. The factor $\cosh \gamma l_p$ is dependent on the 'equivalent length' of the passageway, and this can be determined directly from the model of the source impedance. Therefore it is possible to refer the flow ripple within the pump without any knowledge of its internal dimensions, provided that a distributed parameter model can be applied to Z_S. The source impedance is the same for both flow ripple representations.

The effect of referring the source flow ripple inside the pump in this way is discussed in section 5.2.1., for typical test results on pump 'A'.

It must be concluded that a more realistic representation of the flow ripple can be achieved if it is referred inside the pump in the above manner. If, however, the pump does not generate significant high frequency flow ripple harmonics, as for example in the case of a gear pump, then the referral will have little effect on the flow ripple.

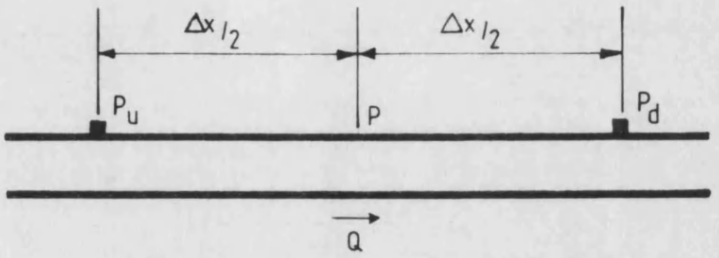

Fig. 4.1 Arrangement of Pressure Transducers for Intensity Measurement

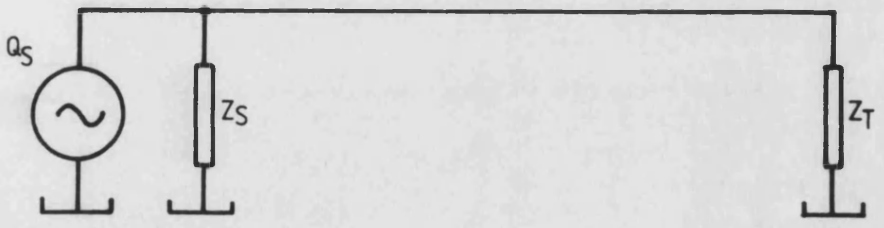

Fig. 4.2 Simple Pump-Pipe-Load Circuit- Impedance Representation

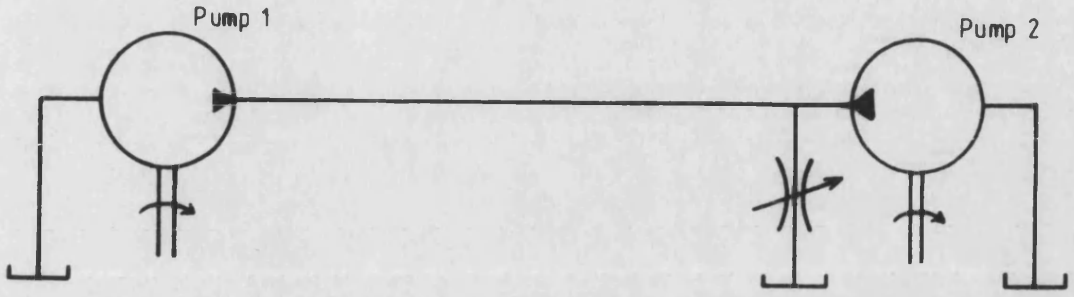

(a) Simple hydrostatic system

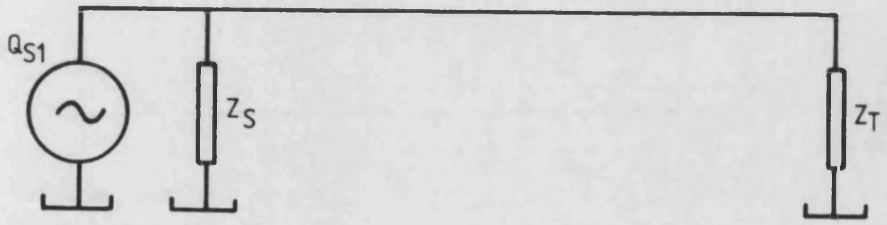

(b) Sub-system (i)

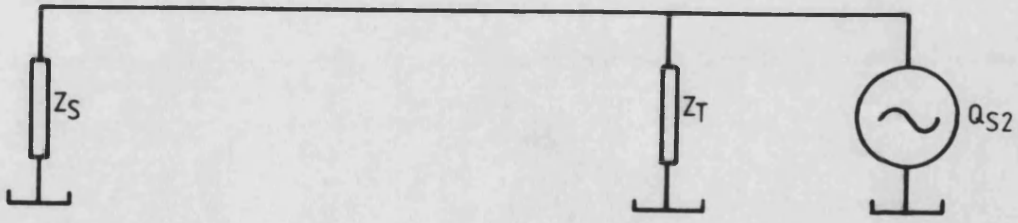

(c) Sub-system (ii)

Fig. 4.3 Analysis of Hydrostatic Transmission System

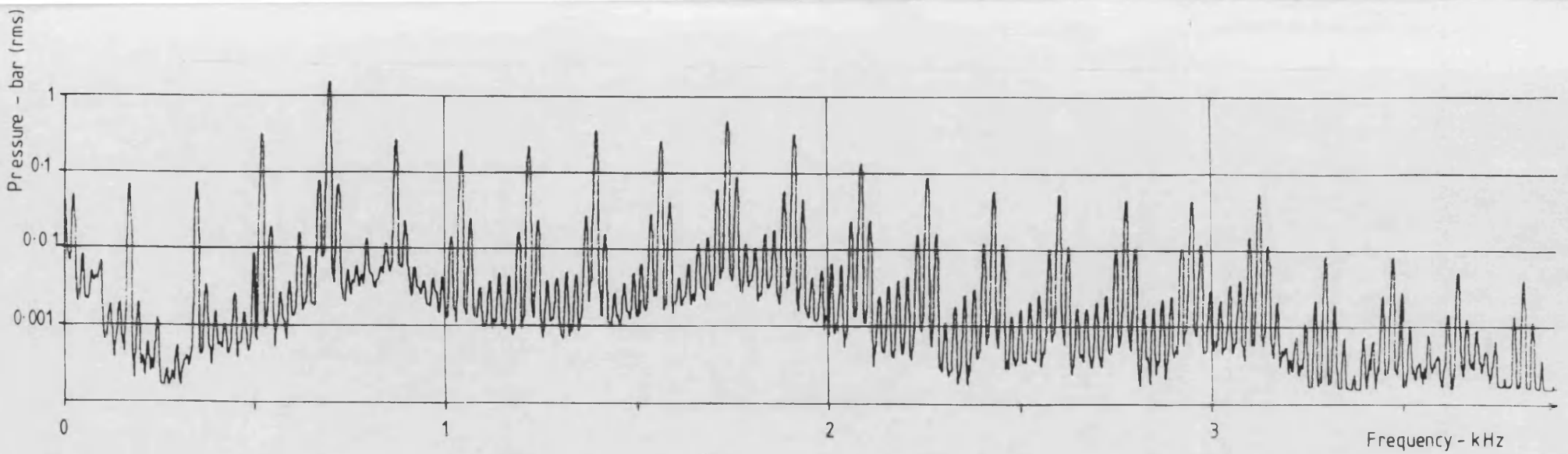

(a) Typical pressure ripple harmonic spectrum from pump 'A'

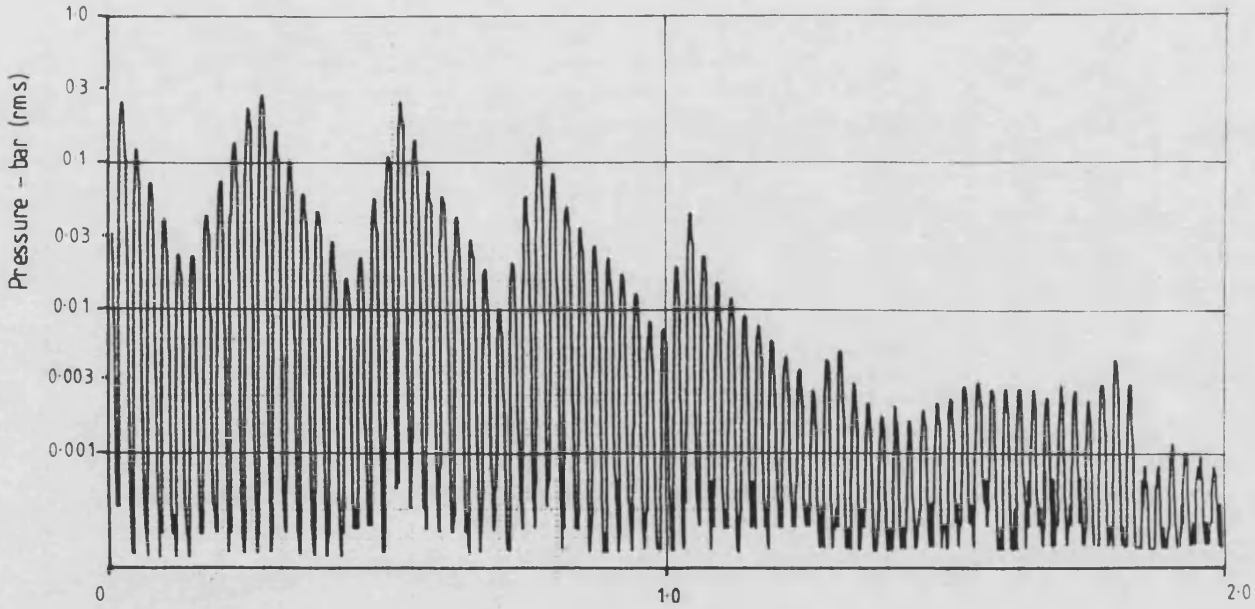

(b) Typical pressure ripple harmonic spectrum from pulse generator

Fig. 4.4 Harmonic Spectra of Pressure Ripple

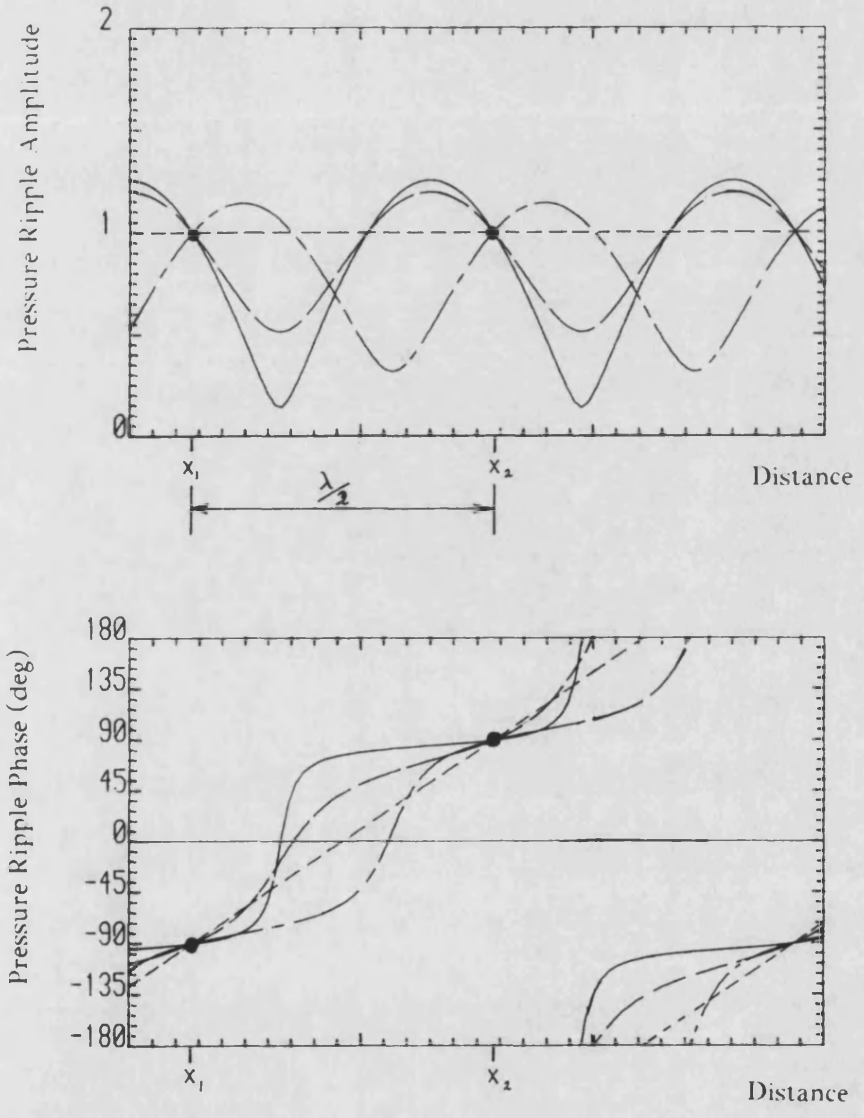

Fig. 4.5 Possible Pressure Standing Wave Profiles Predicted by Pressure Ripple Measurements from Two Transducers Spaced Half a Wavelength Apart

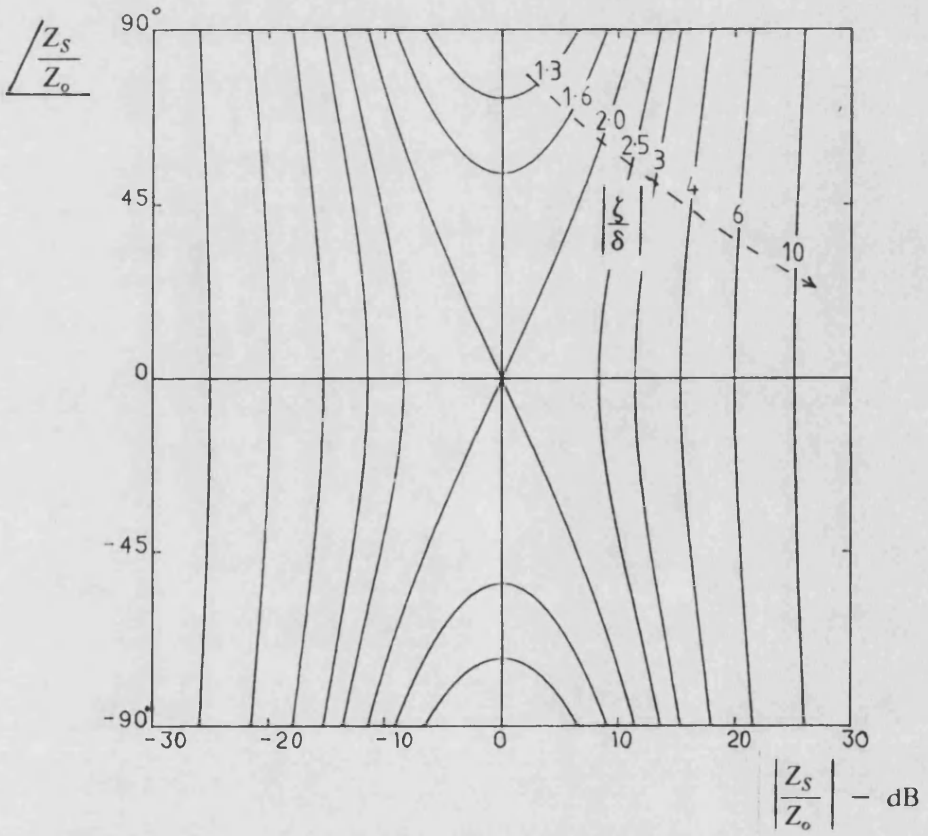

Fig. 4.6 Ratio of Error ζ in Prediction of Z_s to Error δ in ρ_s as a function of Z_s/Z_o

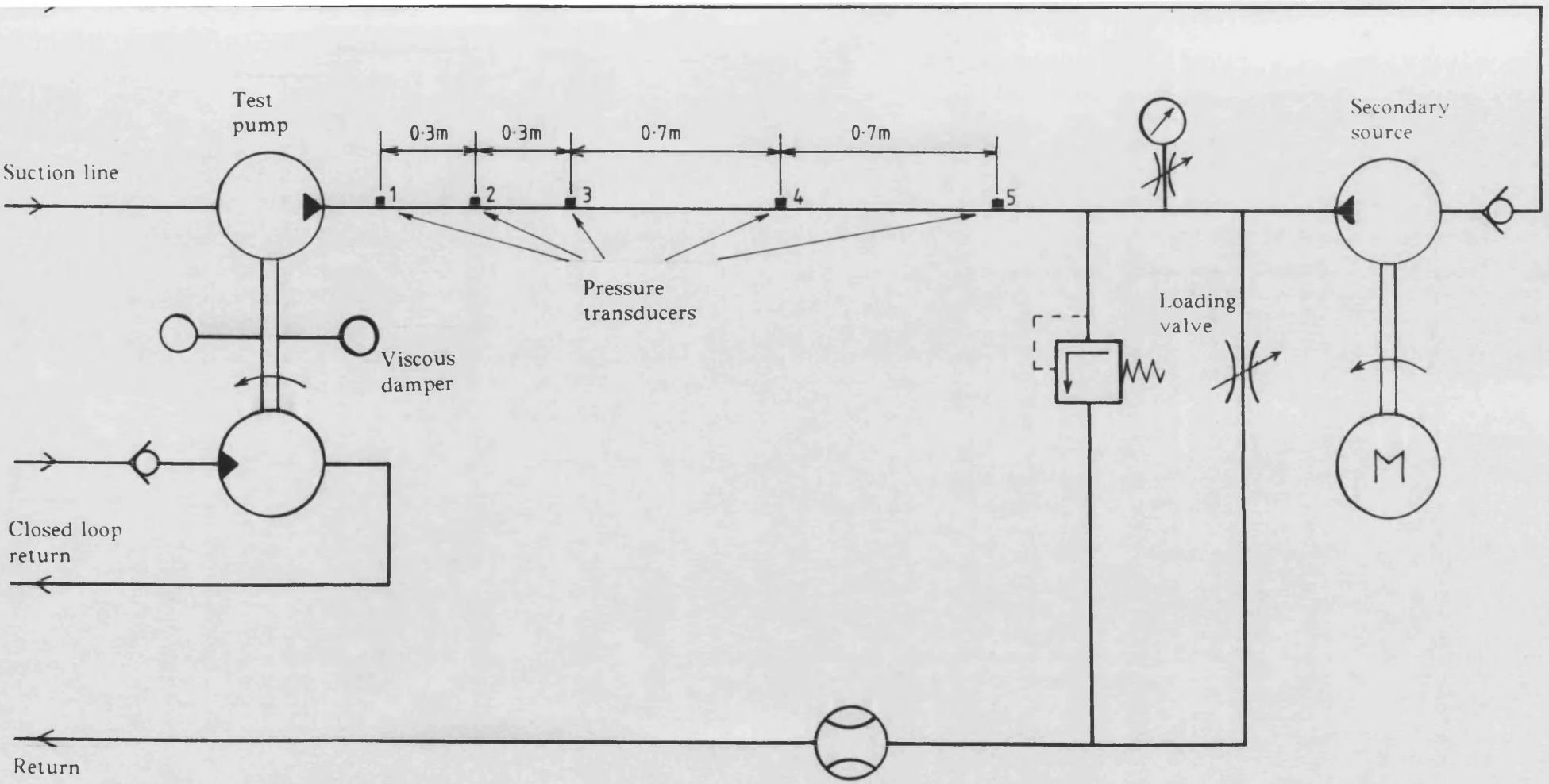

Fig. 4.7 Schematic Diagram of Hydraulic Circuit for Secondary Source Test

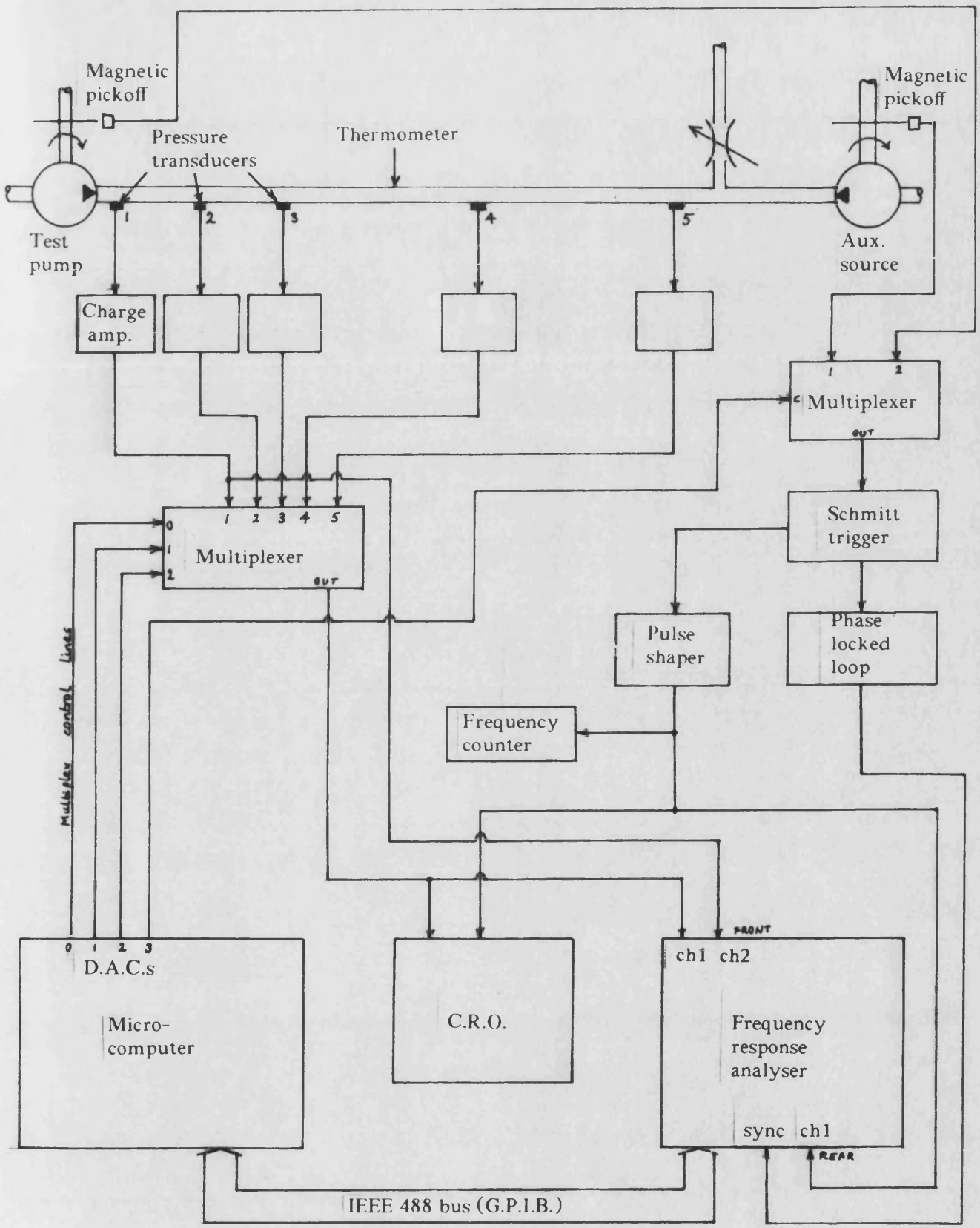

Fig. 4.8 Schematic Diagram of Instrumentation for Secondary Source Technique

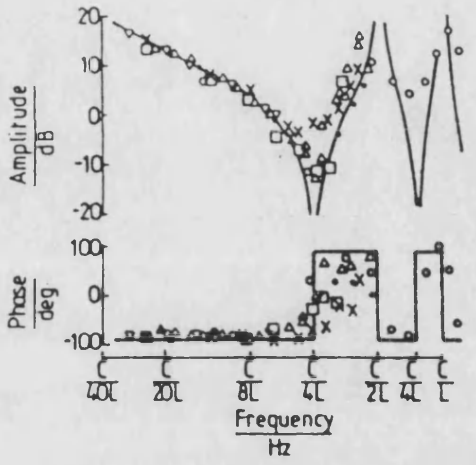

Fig. 4.9 Non-Dimensional Source Impedance Model and Experimental Results (from Edge [32])

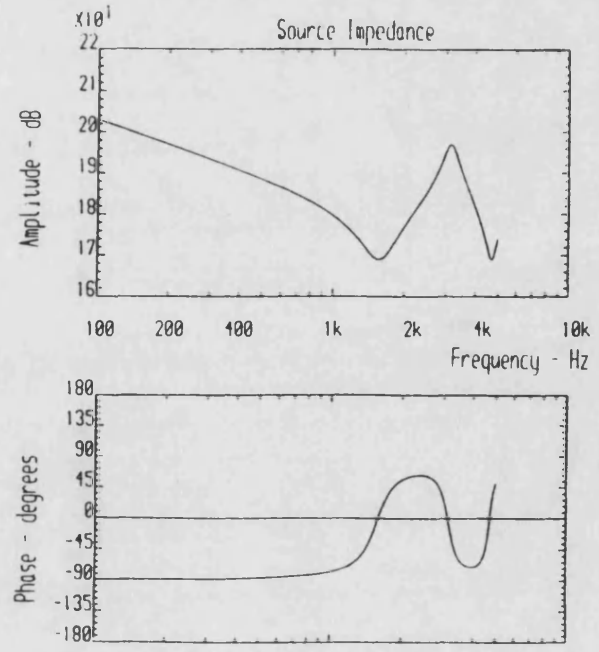

Fig. 4.10 Source Impedance Model with Distributed Friction

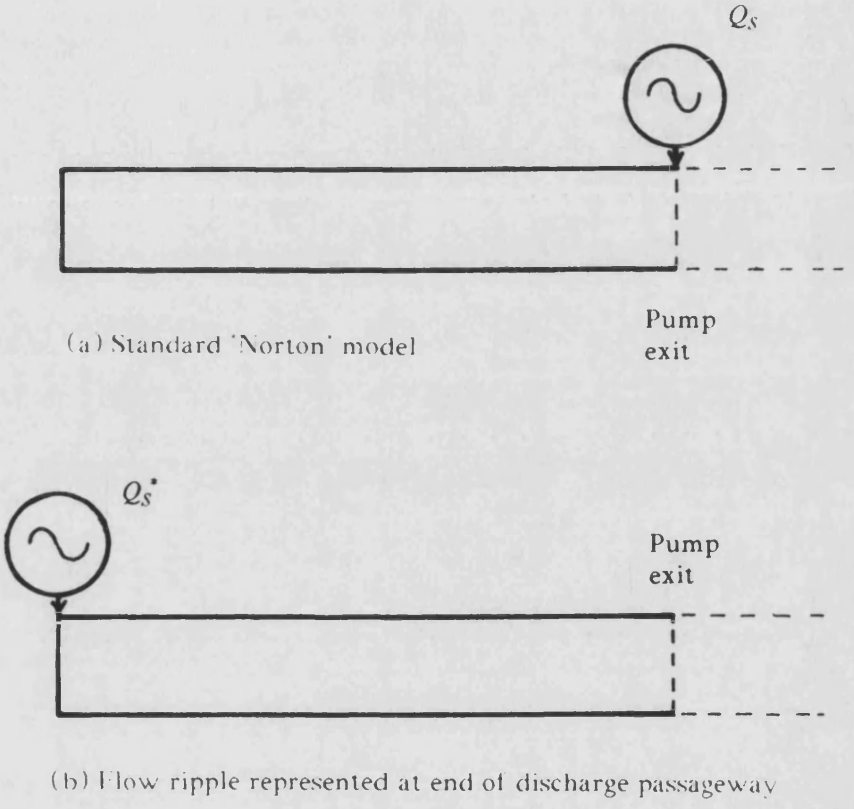

Fig. 4.11 Alternative Representations for Pump Flow Ripple

CHAPTER 5

RESULTS OF PUMP TESTS USING THE 'SECONDARY SOURCE' TECHNIQUE

The 'secondary source' method, as described in chapter 4, was applied to the experimental testing of the fluid-borne noise characteristics of a number of different positive displacement pumps. A wide range of pump types was tested, in order to assess the performance of the test technique over a range of conditions. These included axial piston pumps, external gear pumps and a vane pump. The details of these are listed in appendix 1.

The test method consists of two separate parts, for the measurement of (a) the source impedance and (b) the source flow ripple. In this chapter, the source impedance results for all the pumps tested are presented and discussed first, followed by the source flow ripple results. In all the source flow ripple results it is implicit, unless stated otherwise, that the flow ripple is referred inside the pump using the method described in section 4.3.10. Because of the large number of tests performed, only representative results are included.

5.1. Results of Source Impedance Tests

Except for pump 'A', the pumps under test were driven by the variable speed hydrostatic transmission. Unless otherwise stated, pump 'A' was used as the secondary noise source.

5.1.1. Pump 'B' - Fixed Capacity Axial Piston Pump

Tests were performed on this pump at a wide range of shaft speeds and mean pressures. The pump was fed from a boosted supply, with an inlet pressure of approximately 10 bar.

Some representative source impedance results are presented in Fig. 5.1, at a mean pressure of 100 bar, for a range of shaft speeds. Least squares curve fits, based on a distributed parameter model with friction (section 4.3.9.1.) are superimposed upon the results.

As can be seen, the experimental results show reasonably good correlation with the model, particularly at low frequencies. In each case, below about 1 kHz the impedance is of a capacitive nature, and there is little deviation from the model. An anti-resonance, at which the amplitude of the impedance reaches a minimum and the phase switches from -90° to $+90^{\circ}$, is apparent in each case. The frequency of this anti-resonance shows some variation between the individual test conditions, from approximately 1.4 kHz with the pump running at 1900 rev/min, to 2.1 kHz with the pump stationary. The reason for this variation is not known, but it is believed to be due to cavitation occurring within the pump discharge passageway at the higher pump speeds, reducing the effective bulk modulus and decreasing the effective length of the discharge passageway.

Correlation between the experimental points and the model is less good at high frequencies than at low frequencies. This may be due to experimental error, which is expected to be more severe at high frequencies. However, it may also be due to the assumptions made in the model, in that the complex geometry of the discharge passageway of the pump, while not being significant at low frequency, may have an effect on the measured impedance at high frequency.

Fig. 5.1(d) shows a typical source impedance plot using the pulse generator as the excitation source. In this case the bandwidth of the available harmonic data was such that it was not possible to produce reliable results above about 1 kHz. It can be seen that the results show good correlation with the simple capacitive model.

5.1.2. Pump 'A' - Variable Displacement Axial Piston Pump

In this case pump 'B' was used as the secondary noise source. A typical source impedance result is shown in Fig. 5.2.

The source impedance characteristics of this pump show a marked difference to those of the previous pump (pump 'B'). The same distributed parameter model is applied to the results in this case, and it is apparent that the impedance is almost purely capacitive over the whole of the frequency range. This may be explained by the fact that pump 'A' is very much more compact, such that its effective length is short and the anti-resonant

frequency is high, above the measurable frequency range. The smaller discharge passageway volume in this case means that the amplitude of the source impedance is much higher at low frequencies, being approximately 14 dB higher than that of pump 'B' at any frequency below 1 kHz.

The results for this pump show a considerable degree of scatter. This is due to the fact that pump 'B' was not a particularly good source of noise, because:

a) It was driven by the variable speed hydrostatic transmission, which did not provide a very stable speed.

b) It did not produce such a broad band of fluid-borne noise as pump 'A', so that it was difficult to obtain accurate measurements above 2 kHz.

5.1.3. Pumps 'C' - External Gear Pumps

Tests were performed on a number of similar units. Typical results, for different units at the same operating conditions, are presented in Fig. 5.3. Correlation between the experimental points and the model is considered to be good at low frequency (below 1.5 kHz) and less good above this frequency.

A small but noticeable phase advance, relative to the model, is observed in Fig. 5.3(c) at low frequency. This effect is not apparent in Figs. 5.3(a) and (b), in which the phase remains close to -90°. This pump was found to be faulty and had a low volumetric efficiency. The effect of this was to cause the magnitude of the reflection coefficient at the internal end of the discharge passageway to be significantly less than unity, so that at low frequency the phase of the source impedance tends towards zero.

5.1.4. Pumps 'D' - External Gear Pumps

Two similar units were tested, designated as pump 'D1' and pump 'D2'. The only difference between the two was in the design of the relief grooves in the thrust plates. Typical experimental results are shown in Fig. 5.4. Little overall difference is observable between the impedance characteristics of the two pumps. However, it can be seen that there is a significant degree of scatter between the experimental points and the modelled curves.

At low frequencies the experimental results for both pumps show a distinct phase advance relative to the model. This is similar to the effect observed with the faulty pump 'C', which was due to its high leakage. However, in this case it was found that the leakage flow was far too small for it to have any significant effect on the source impedance. A similar effect can be observed in the results for pump 'A' (Fig. 5.2).

Tests were also performed on pump 'D2' using the pulse generator as the secondary noise source, and a result is presented in Fig. 5.4(c). It can be seen that the data points show very little scatter. The overall correlation between the results obtained using the two different sources is very good. A marked peak in the phase response, with a corresponding trough and peak in the amplitude response, is apparent in Fig. 5.4(c) between 1 kHz and 1.5 kHz. This effect can also be seen on the results obtained using pump 'B' as the auxiliary generator, Fig. 5.4(a) and (b), although it is less clear because of the wider spacing between the data points. This effect cannot be taken into account by the simple distributed parameter model, and may be caused by complexity of the geometry of the discharge passageway, or possibly by mechanical vibration of the internal parts, such as the gears or the thrust plates.

5.1.5. Pump 'E' - Balanced Vane Pump

A typical source impedance characteristic obtained from this pump is shown in Fig. 5.5. Good correlation is apparent between the experimental results and the modelled curve up to 1700 Hz. However, above this frequency correlation was found to be less good. A resonance is apparent in the results at about 3.7 kHz.

5.2. Source Flow Ripple Experimental Results

5.2.1. Pump 'A' - Axial Piston Pump

Experimental tests were performed on this pump at a wide range of load pressures and swash settings. Some typical source flow ripple waveforms, at full swash, for load pressures between 20 bar and 145 bar, are presented in Fig. 5.6. The corresponding harmonic spectra are presented in Fig. 5.7. These results conform well to the form which would be expected from an axial piston pump as described in section 2.1.1., the predominant feature being the sharp backflow which occurs once per pumping cycle. The amplitude of this backflow increases with the load pressure, which is as would be

expected, as the volume of additional fluid necessary to compress the fluid within the cylinder is proportional to the pressure difference across the pump.

An oscillation is apparent in the flow ripple after the backflow spike. It is possible to discern the 'kinematic' ripple which is periodic at twice the pumping frequency, as described in section 2.1.1. It is apparent that this is a small effect, and can only be seen clearly at low load pressures, as it is masked by the effect of the backflow at higher pressures.

Considering the harmonic amplitude spectra shown in Fig. 5.7, it can be seen that this pump produces a large number of significant harmonics. The corresponding phase spectra are shown in Fig. 5.8. At first sight these phase plots appear rather complex. However, the phase in these plots is limited to the range of -180° to $+180^\circ$. If it is 'unwrapped' by removing these constraints then the form of the characteristics can be simplified to a phase advance which increases consistently with frequency, as shown in Fig. 5.9(b). It can be seen that there is an approximately linear relationship between phase and frequency, of the form

$$\phi(\omega) = \pi + \omega\tau + \zeta(\omega) \qquad \ldots (5.1)$$

where ζ represents small deviations from the linear relationship.

$$\text{or, } Q_S(\omega) = |Q_S| e^{j\phi(\omega)} = |Q_S| e^{j\pi} e^{j\omega\tau} e^{j\zeta(\omega)} \qquad \ldots (5.2)$$

The $e^{j\omega\tau}$ term represents a pure time advance τ. This is a function of the angular position of the phase reference and can be ignored without affecting the form of the flow ripple. The phase can then be represented by

$$\phi(\omega) = \pi + \zeta(\omega), \qquad \ldots (5.3)$$

as shown in Fig. 5.9(c). This demonstrates that the phase of the source flow ripple from an axial piston pump, while appearing to be complex, can be greatly simplified by shifting the phase reference. Fig. 5.10 shows the harmonic phase spectra for pump 'A', corresponding to those shown in Fig. 5.8, after shifting the reference in this way.

The above results were obtained using data obtained from three pressure transducers separated by distances of 0.7 m and 1.0 m. The effect on the measured source flow ripple of using just two transducers, spaced 0.3 m apart, can be seen by considering Fig. 5.11(a) and (b). By comparing the harmonic spectra, it is clear that the use of only two transducers leads to large deviations in the region of 2.2 kHz to 2.6 kHz. This is apparent as a large oscillation on the flow ripple waveform. This corresponds to the condition where the transducers are separated by a distance of approximately half of a wavelength (see section 4.3.3.1.).

The effect of referring the source flow ripple to a point inside the pump at the end of the discharge passageway can be seen by comparison of Fig. 5.11(a) with Fig. 5.11(c). In Fig. 5.11(c), in which the flow ripple is not referred inside the pump but is measured at the pump exit, an extreme oscillation is apparent in the waveform with a corresponding peak in the amplitude spectrum at about 2.5 kHz. This peak corresponds to the anti-resonant frequency of the pump source impedance. It is apparent that if the flow ripple is not referred inside the pump then severe distortion can occur in the results.

5.2.2. Pump 'B' - Axial Piston Pump

Tests were performed on this pump at a range of mean load pressures and shaft speeds. Flow ripple waveforms and amplitude spectra are shown in Fig. 5.12 and 5.13 for a range of load pressures at a speed of 1500 rev/min. It can be seen that the source flow ripple of this pump is fundamentally similar to that of pump 'A' and shows all the characteristic features of axial piston pumps, these being a small amplitude kinematic ripple (apparent at low mean pressures), a sharp backflow and an oscillation after the backflow. The oscillation is rather more severe for this pump than for pump 'A'.

For both axial piston pumps 'A' and 'B', the amplitude of the backflow can be seen to increase with pressure. The relationship between the amplitude of the backflow and the mean load pressure is plotted in Fig. 5.14(a) for pump 'A', with the pump at half swash and full swash. It can be seen that there is an approximately linear relationship between the amplitude and the pressure difference across the pump (load pressure − boost pressure). The gradient with the pump at half swash is slightly less than that at full swash. This might be expected as the volume contained in the cylinder at bottom dead centre increases with swash angle. The equivalent graph for pump 'B' at 1500 rev/min is shown in Fig. 5.14(b). Again the relationship is approximately linear.

5.2.3. Pumps 'C' - External Gear Pumps

Several pumps with minor differences in design were tested, as part of a project to assess the effect of a number of modifications on the source flow ripple, in order to develop a low noise pump. Findings from this project were described in detail by Molton [4].

Representative results from two different pumps at 1500 rev/min and 90 bar are shown in Fig. 5.15. Fig. 5.15(a) shows the flow ripple for a 9 tooth pump of 14.8 cm^3/rev displacement, and Fig. 5.15(b) shows it for a 12 tooth pump of 16.1 cm^3/rev displacement. Theoretical waveforms, predicted using equation (2.2), are also shown. It can be seen that there is reasonable correlation between experimental results and theoretical models, particularly in terms of the peak-to-peak values, although there is some distortion of the experimental waveforms. The experimental harmonic amplitude spectra exhibit dominant fundamental components with higher harmonics decaying rapidly and smoothly with frequency.

5.2.4. Pump 'D1' - External Gear Pump

Typical experimental results, at a speed of 1000 rev/min and mean outlet pressures of 25 bar, 50 bar and 100 bar, are shown in Figs. 5.16 and 5.17, together with the flow ripple predicted using the theoretical model. Correlation between the experimental results and the theoretical model is poor. The amplitude of the experimental results is significantly less than that of the model, and the shape of the curves is distorted. Although the peak-to-peak amplitude of the experimental results is less than that of the model, there are increased higher frequency harmonics, which may be undesirable in practice. There appears to be some pressure dependence in the results, with strong oscillations apparent in Fig. 5.16(b).

The deviations from the theoretical model may be due to the non-standard relief groove geometry, which is shown in Fig. 5.18(a). The relief grooves project further towards the centre line than the ideal grooves as used in the model. It is thought that the peripheral chamfers, by causing a sudden pressure increase in the fluid, may cause a backflow effect similar to that encountered with piston pumps, which might partly explain the pressure dependence of the flow ripple.

5.2.5. Pump 'D2' - External Gear Pump

Typical source flow ripple results for this pump are shown in Figs. 5.19 and 5.20. As with pump 'D1', the experimental peak-to-peak values are less than those predicted from the simple model. The results show some pressure dependence, the amplitude increasing with the mean pressure.

The side plate geometry is shown in Fig. 5.18(b). This pump has no peripheral chamfers, and the high frequency 'ringing' which was apparent in the results for pump 'D1' does not occur in this case. There is only one relief groove, which is on the discharge side, and this extends further towards the centre than the 'standard' relief groove on which the model is based. It would be expected that this pump's relief groove design would lead to a flow ripple significantly worse than that predicted by the model. The reason why this pump produces a lower flow ripple than the model is unclear.

5.2.6. Pump 'E' - Balanced Vane Pump

Typical results are presented in Fig. 5.21. for this pump, running at a speed of 1500 rev/min, at different load pressures. Both harmonic amplitude spectra and time domain waveforms are presented.

Considering the harmonic spectra, it can be seen that the first 6 to 8 harmonics are strong, and there is very little information above the tenth harmonic. In all cases, the second harmonic is the strongest.

The flow ripple waveforms show a number of features, the most striking being the narrow negative pulse, the amplitude of which increases with the load pressure. This pulse is caused by the sudden compression of the fluid being pumped as it comes into contact with the high pressure port. This is very similar to the effect which occurs in axial piston pumps due to compression of the fluid in the cylinders.

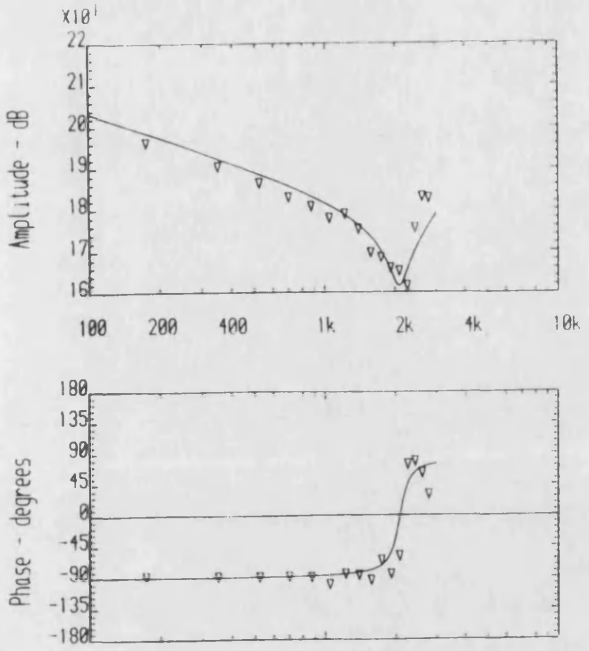

(a) Pump stationary, 100 bar

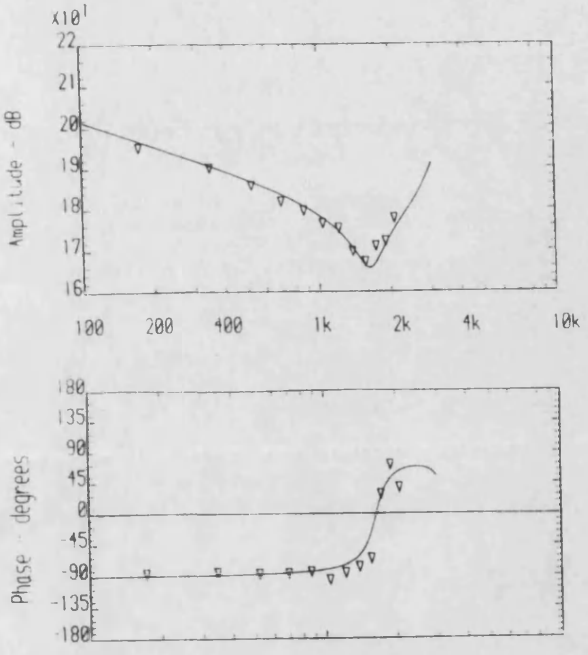

(b) Pump running at 1200 rev/min, 100 bar

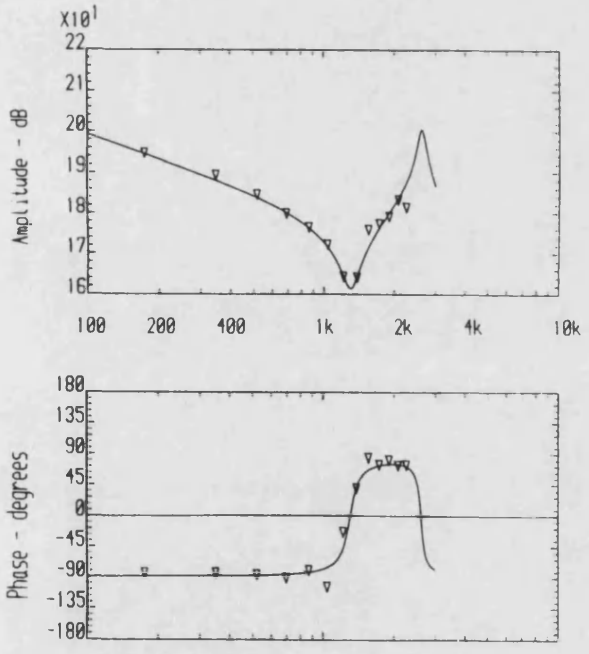

(c) Pump running at 1900 rev/min, 100 bar

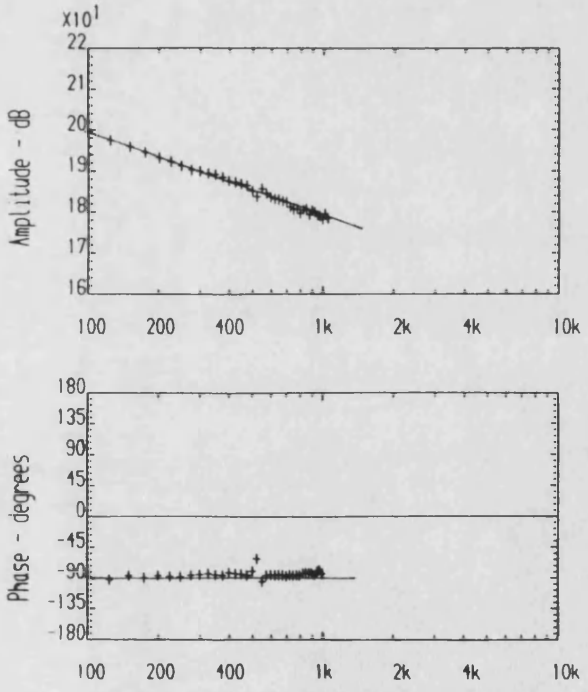

(d) Pump running at 200 rev/min, 100 bar

Fig. 5.1 Source Impedance Results - Pump 'B'

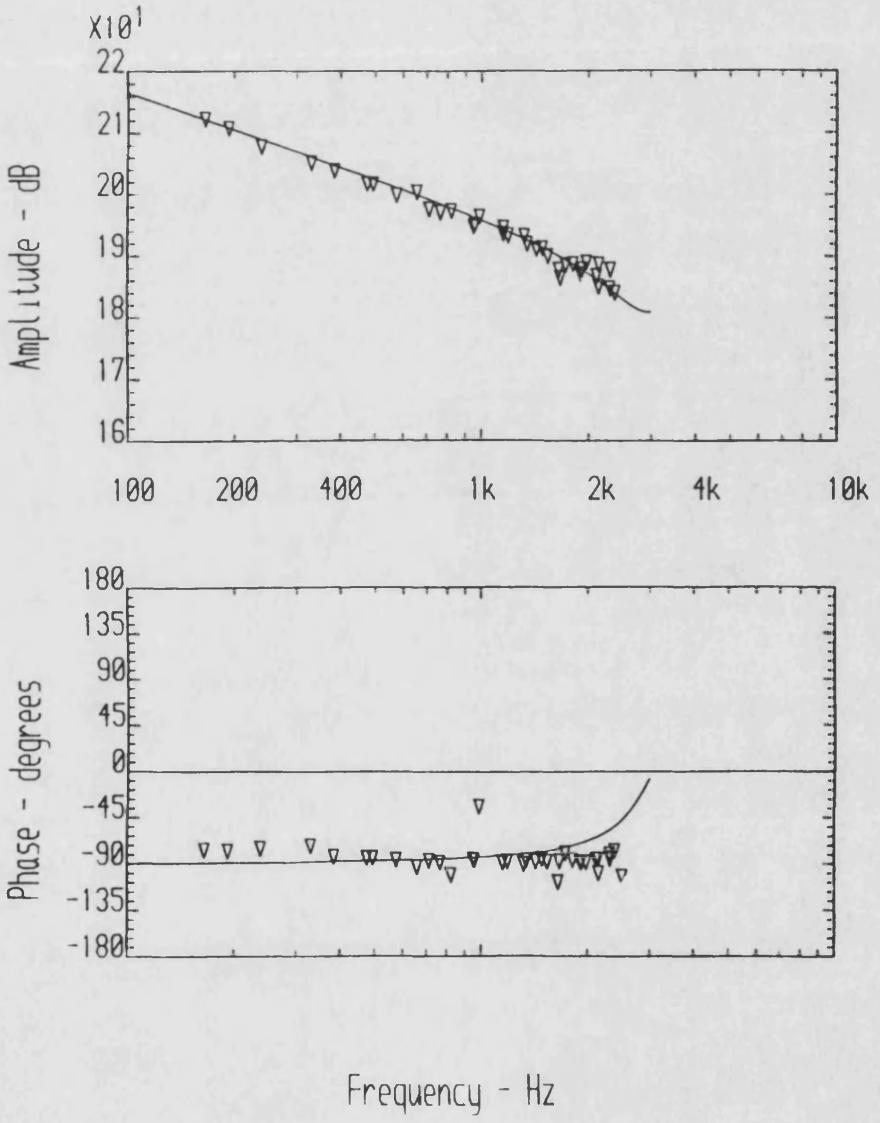

Fig. 5.2 Source Impedance Result - Pump 'A', 1500 rev/min, 100 bar

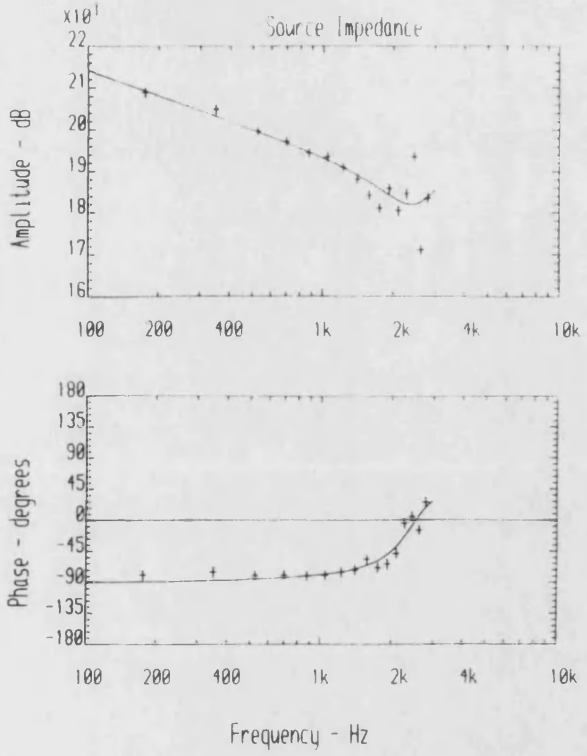

(a) Pump 'C1'

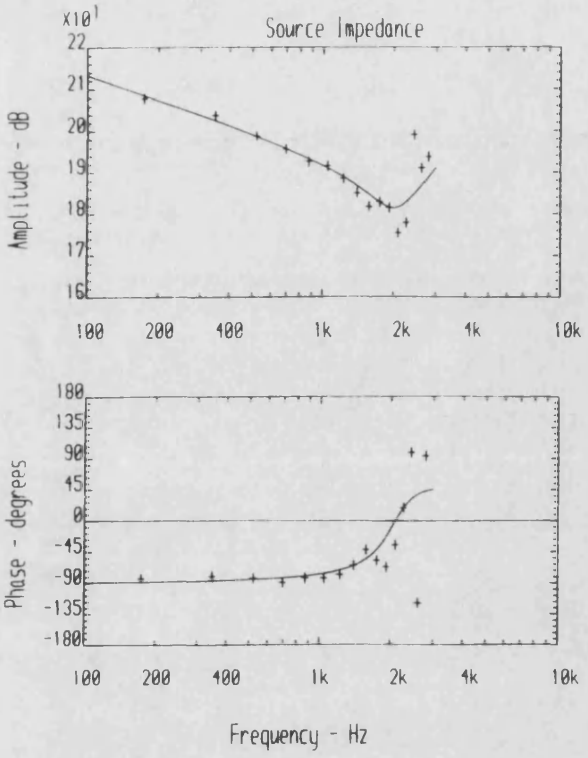

(b) Pump 'C2'

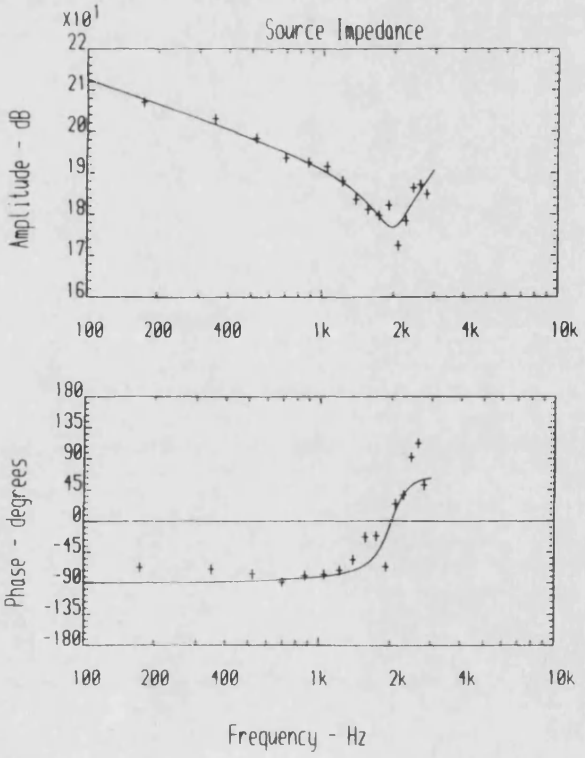

(c) Pump 'C3'

Fig. 5.3 Source Impedance Results - Pumps 'C', 1500 rev/min, 90 bar

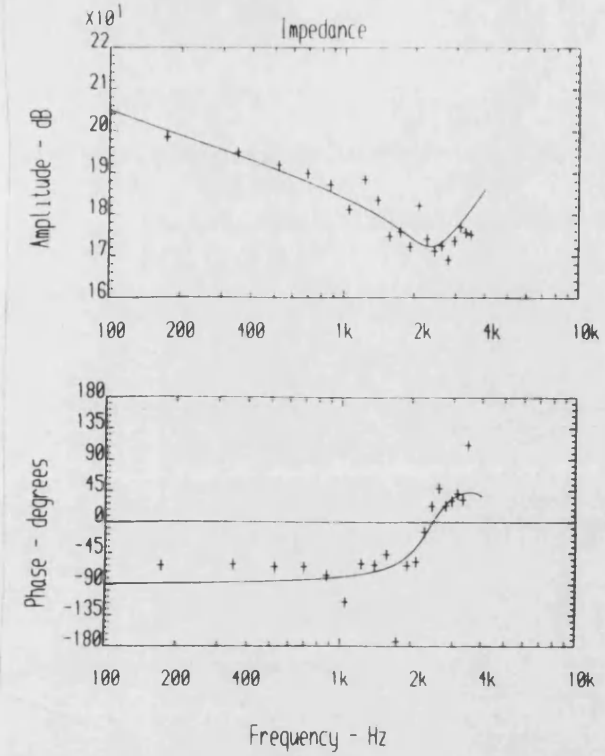

(a) Pump 'D1'

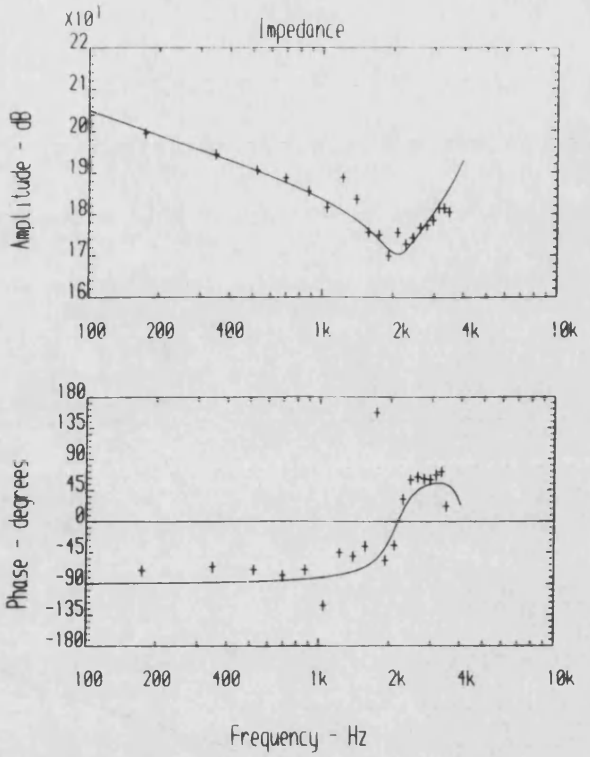

(b) Pump 'D2'

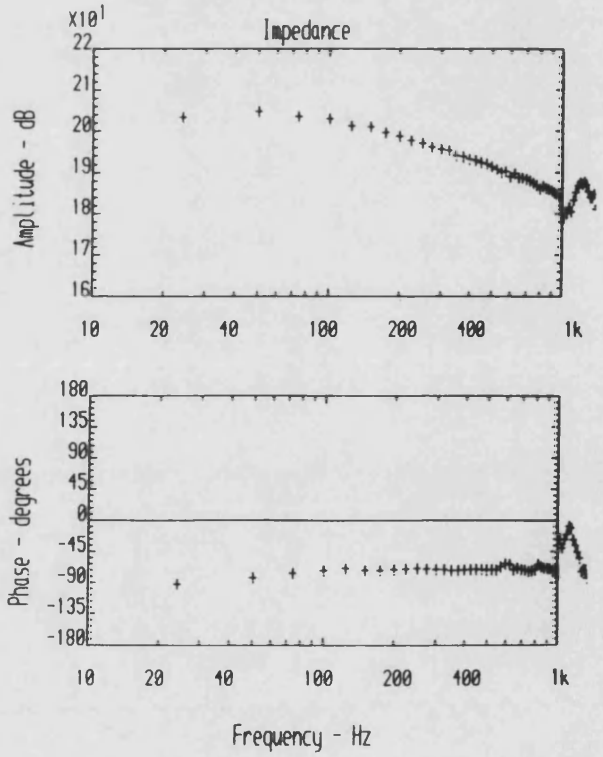

(c) Pump 'D2', using pulse generator

Fig. 5.4 Source Impedance Results - Pumps 'D', 750 rev/min, 100 bar

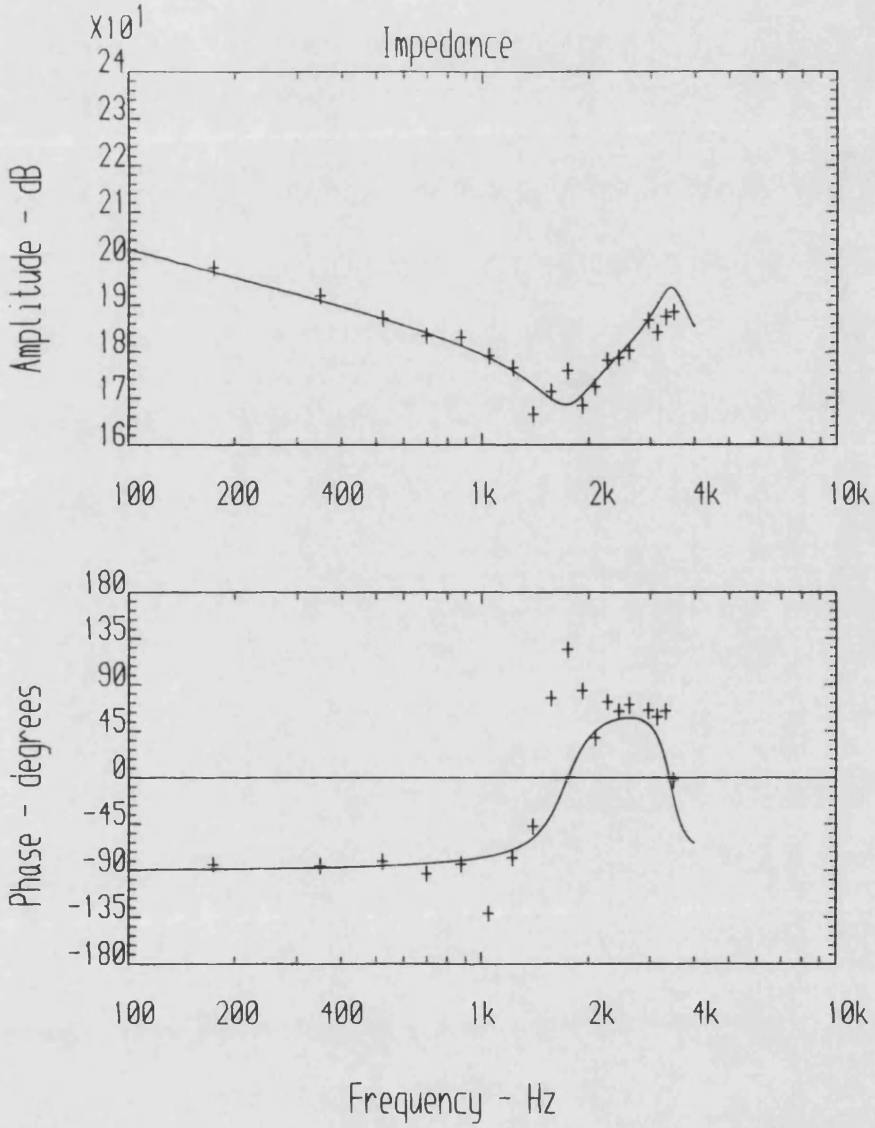

Fig. 5.5 Source Impedance Result - Pump 'E', 750 rev/min, 100 bar

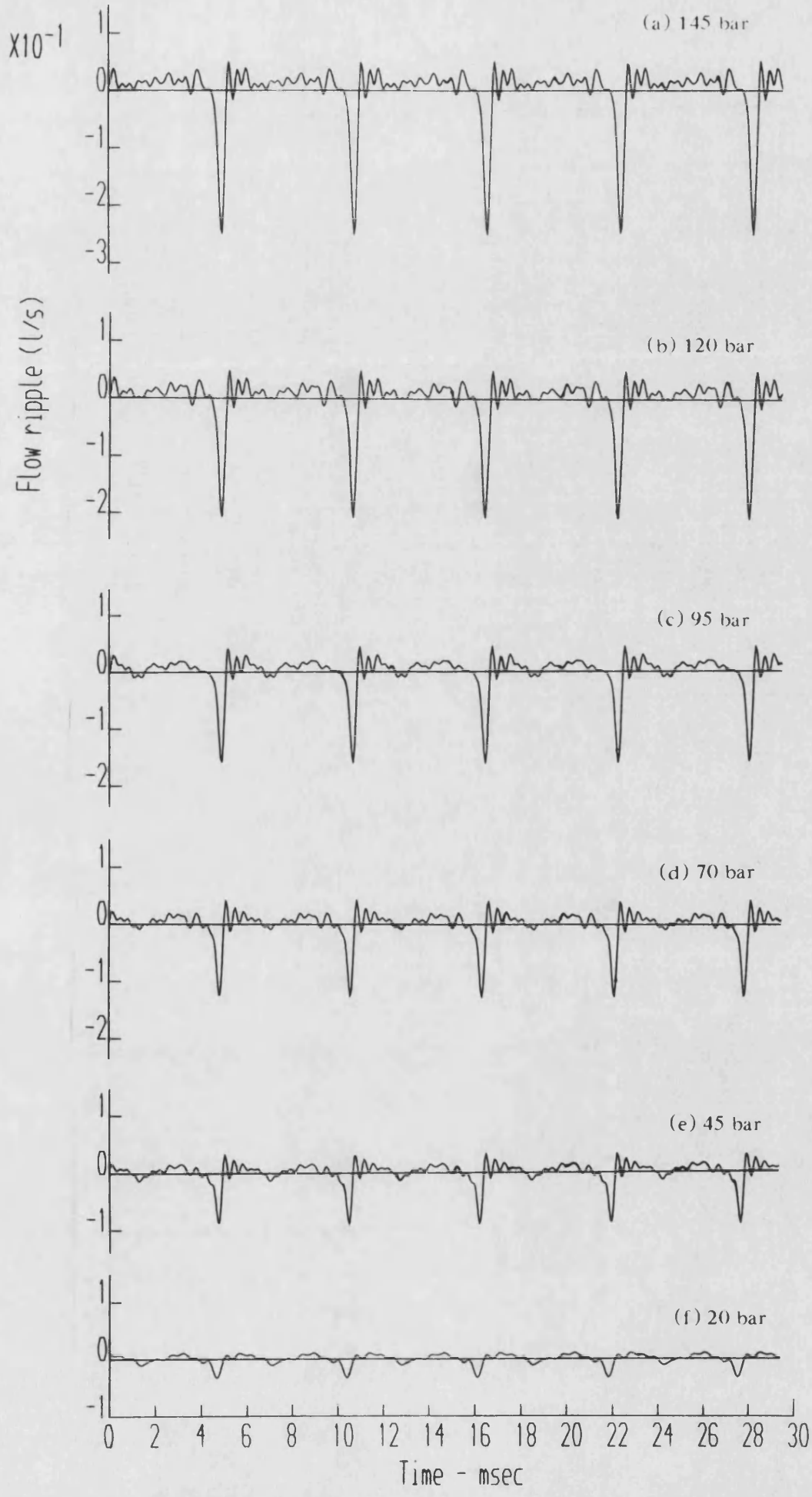

Fig. 5.6 Experimental Source Flow Ripple Waveforms - Pump 'A', 1500 rev/min

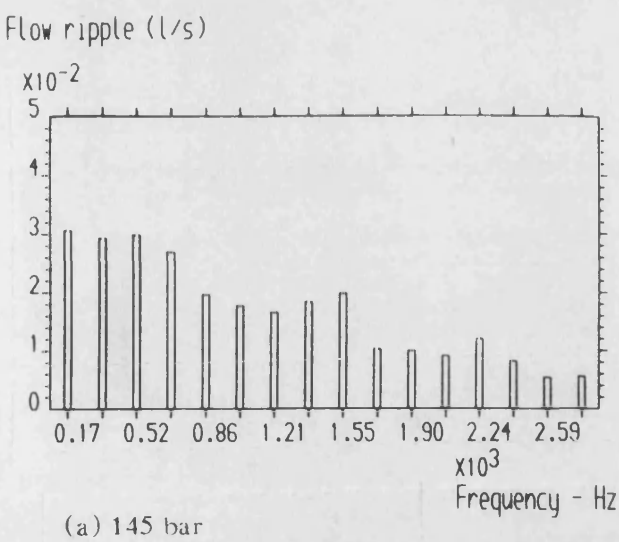

(a) 145 bar

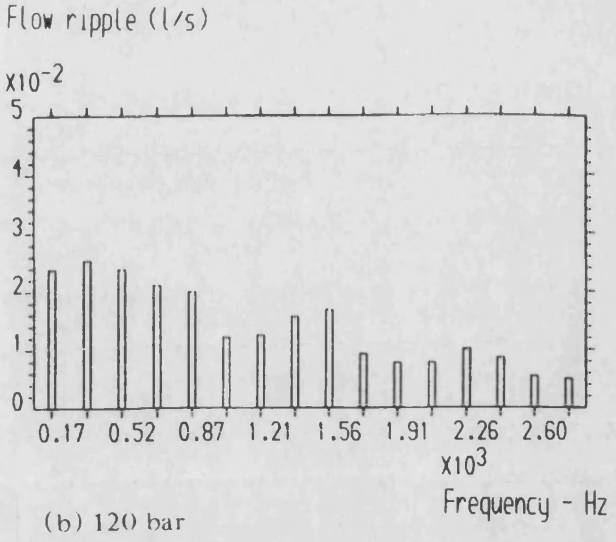

(b) 120 bar

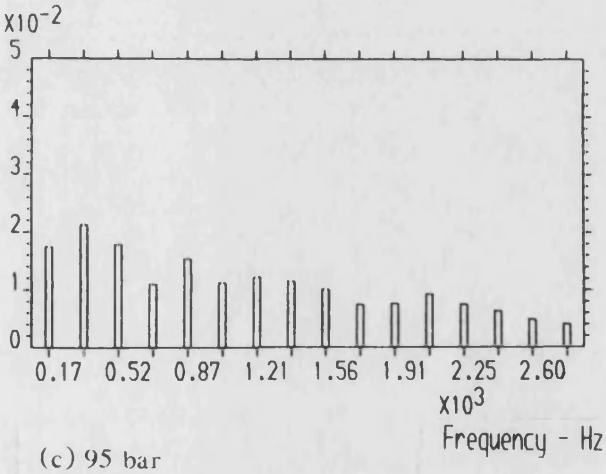

(c) 95 bar

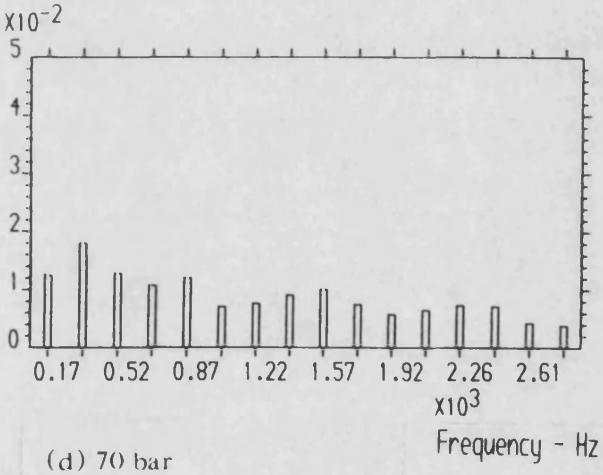

(d) 70 bar

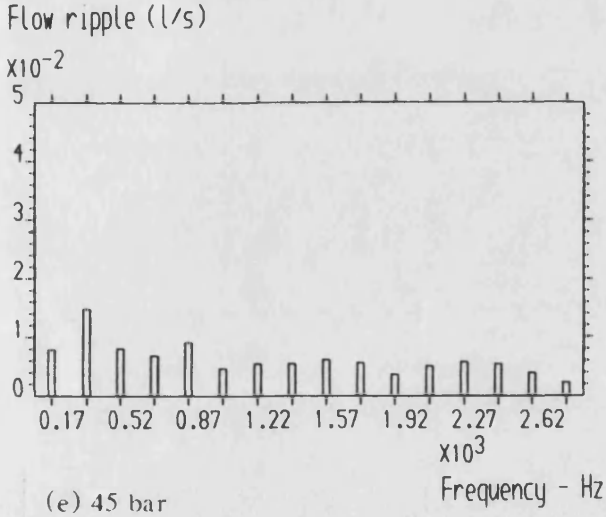

(e) 45 bar

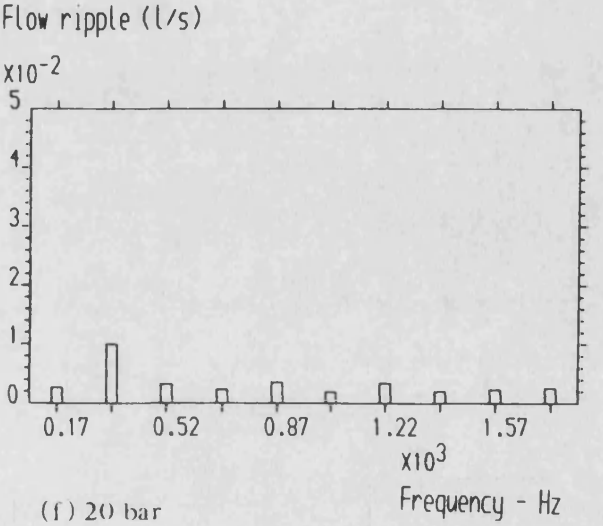

(f) 20 bar

Fig. 5.7 **Experimental Source Flow Ripple Amplitude Spectra - Pump 'A', 1500 rev/min**

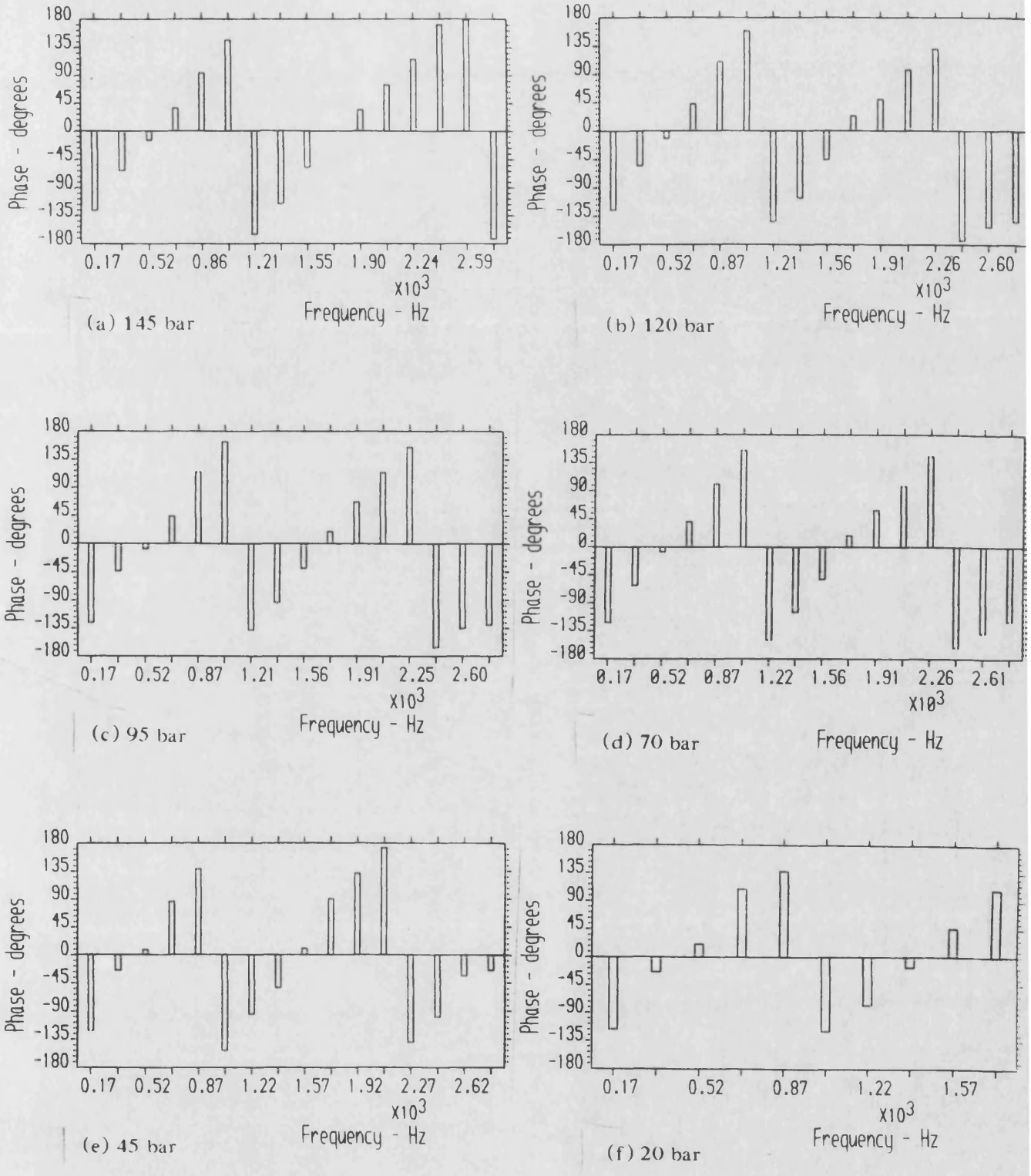

Fig. 5.8 **Experimental Source Flow Ripple Phase Spectra - Pump 'A', 1500 rev/min**

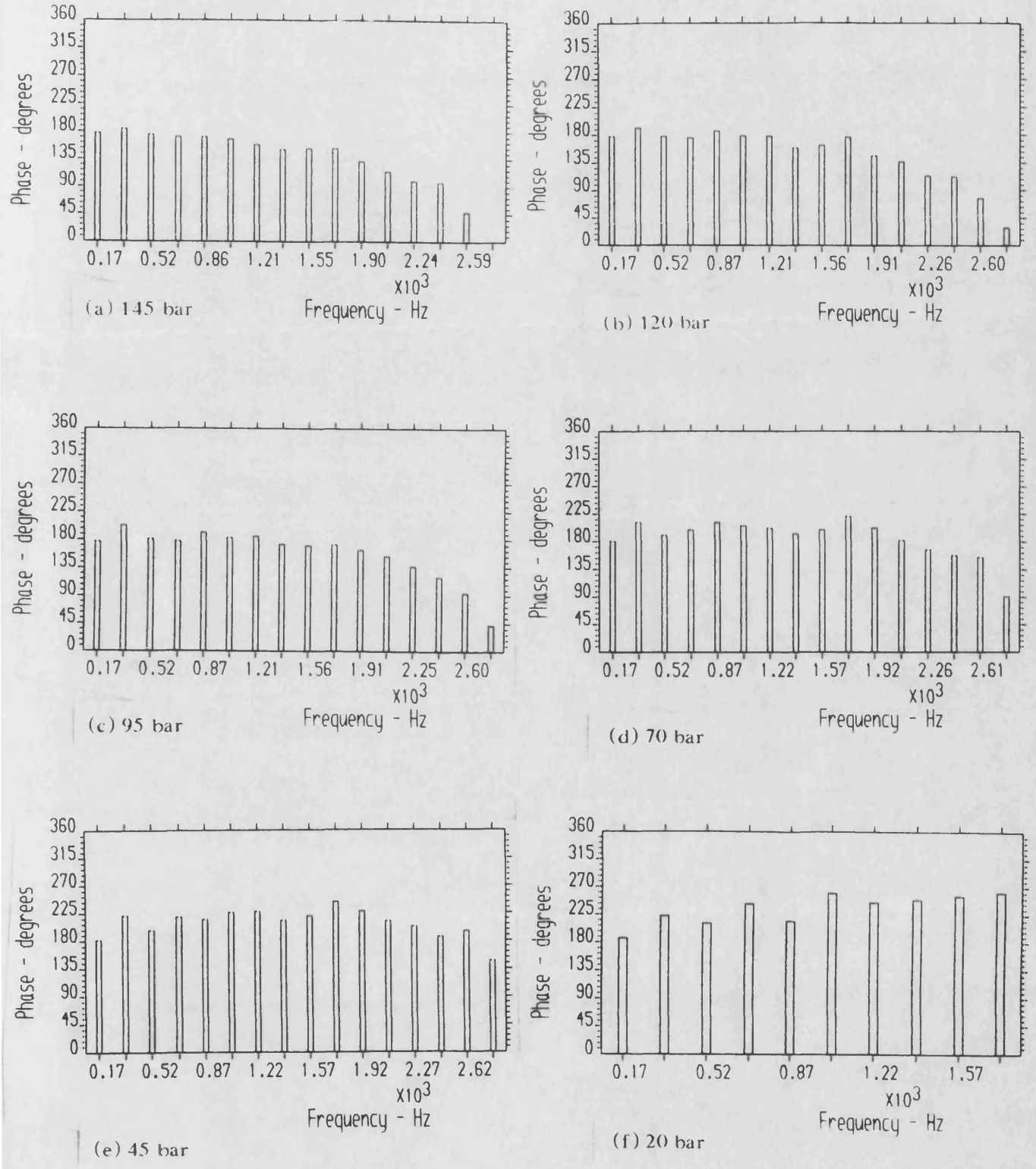

Fig. 5.10 **Simplified Experimental Source Flow Ripple Phase Spectra, Pump 'A', 1500 rev/min**

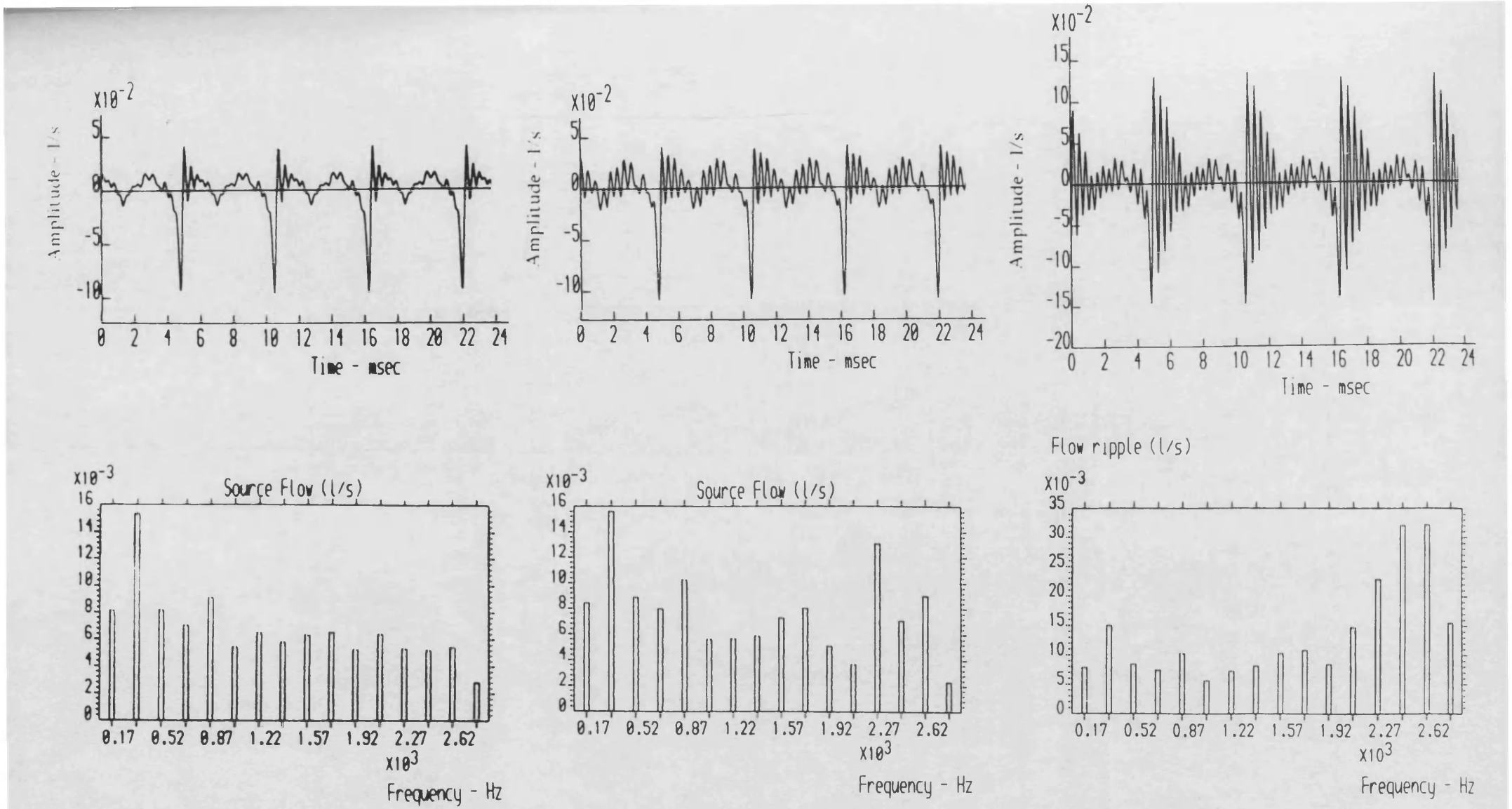

(a) Evaluated using 3 transducers, referred inside pump

(b) Evaluated using 2 transducers spaced 0.3m apart, referred inside pump

(c) Evaluated using 3 transducers, referred to pump exit

Fig. 5.11 **Experimental Flow Ripple, Pump 'A', 100 bar, 1500 rev/min**

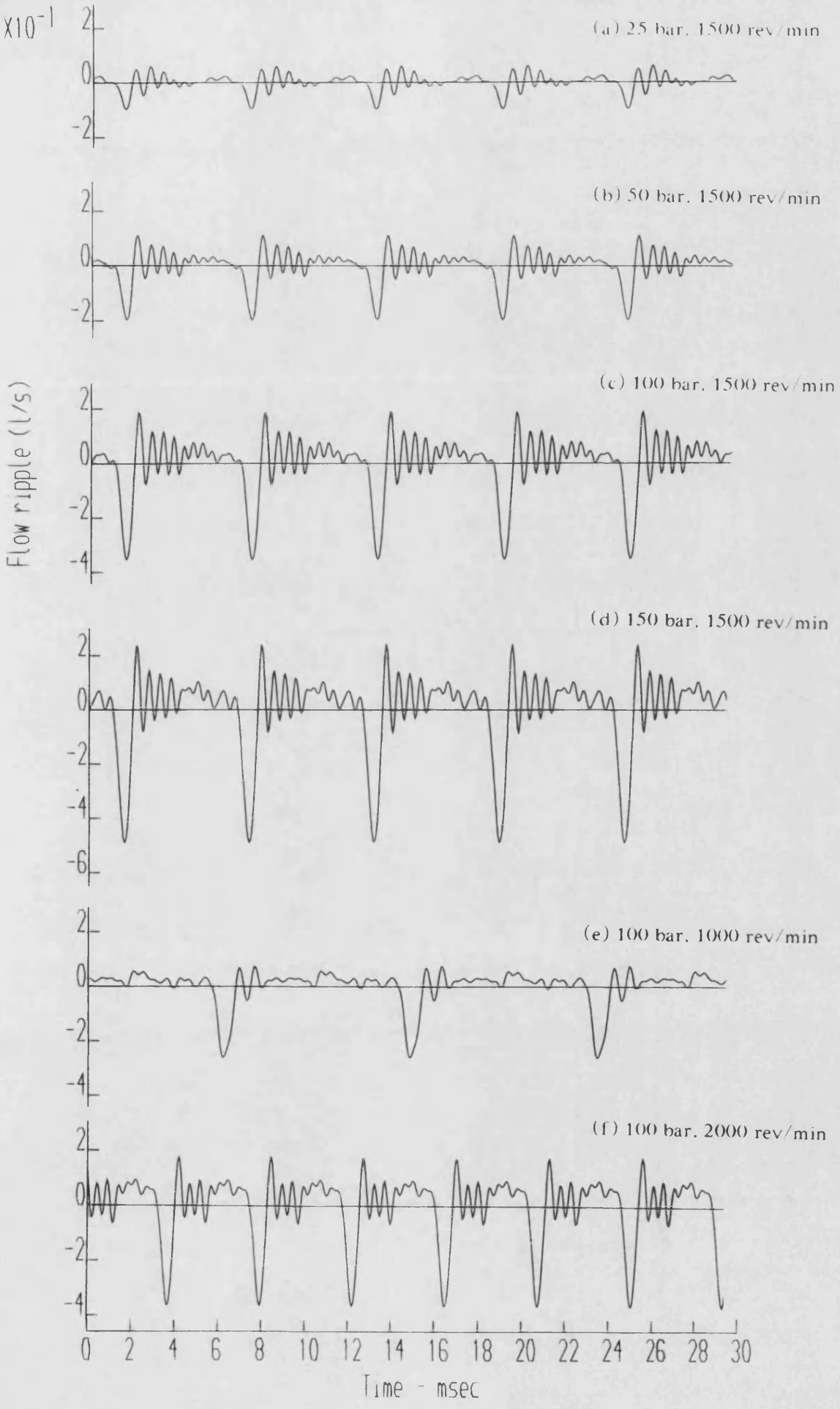

Fig. 5.12 Experimental Source Flow Ripple Waveforms, Pump 'B'

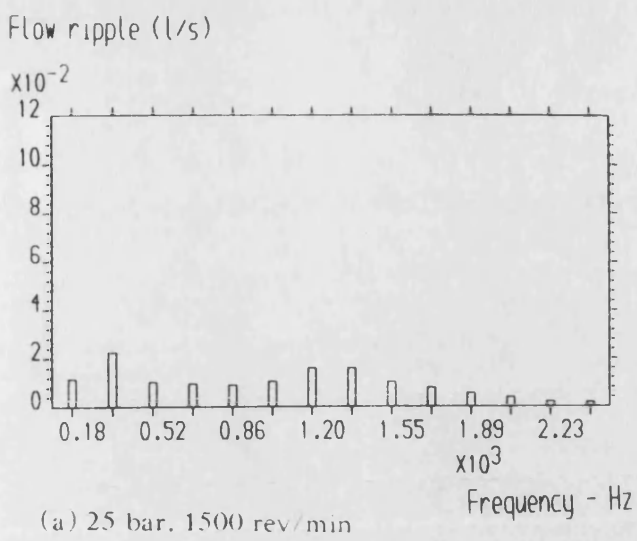

(a) 25 bar, 1500 rev/min

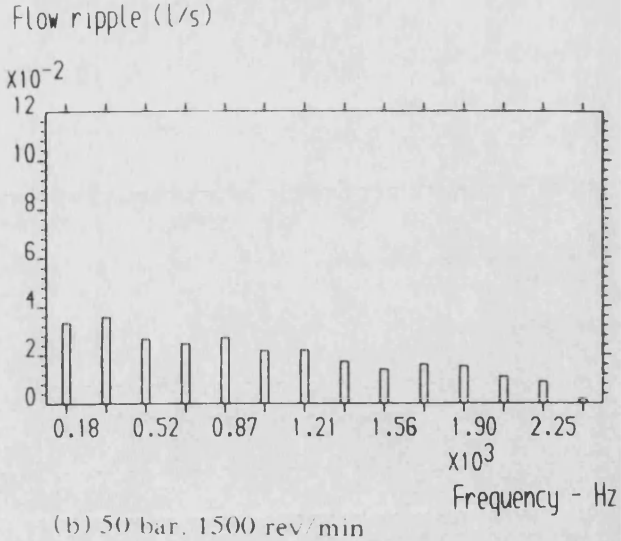

(b) 50 bar, 1500 rev/min

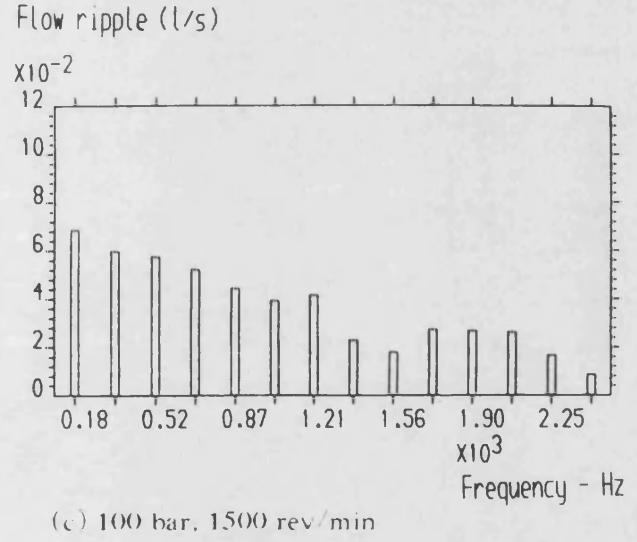

(c) 100 bar, 1500 rev/min

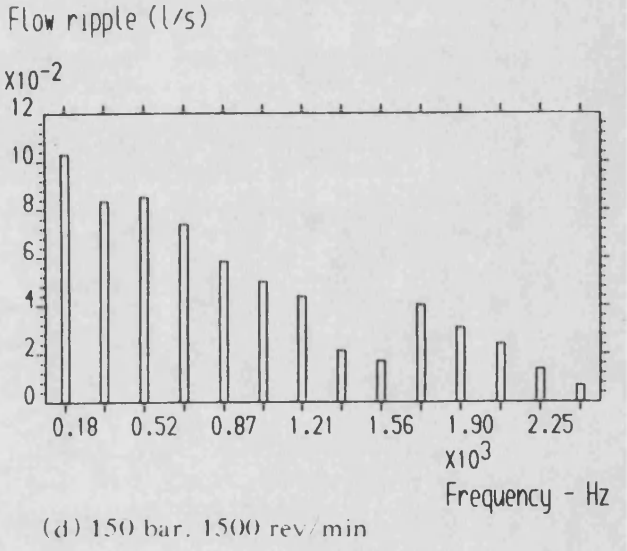

(d) 150 bar, 1500 rev/min

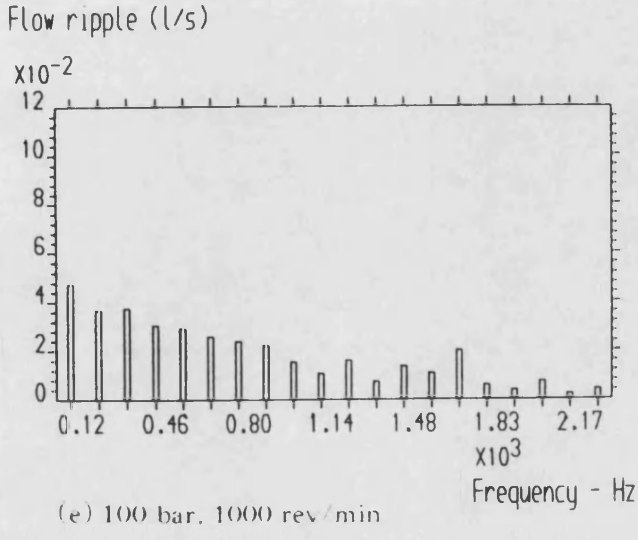

(e) 100 bar, 1000 rev/min

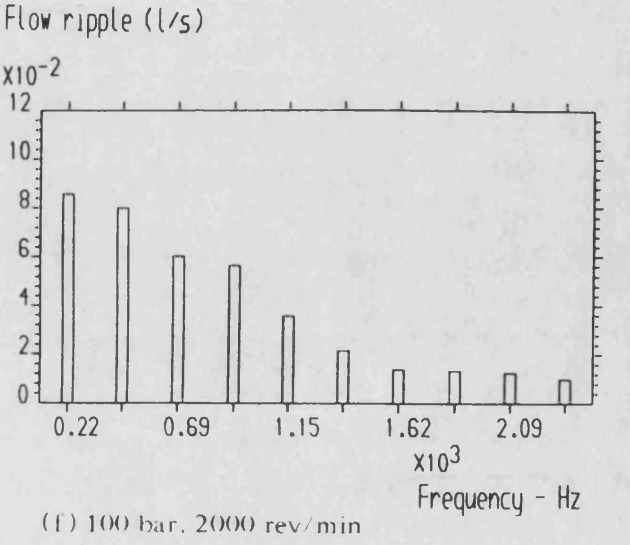

(f) 100 bar, 2000 rev/min

Fig. 5.13 **Experimental Source Flow Ripple Amplitude Spectra, Pump 'B'**

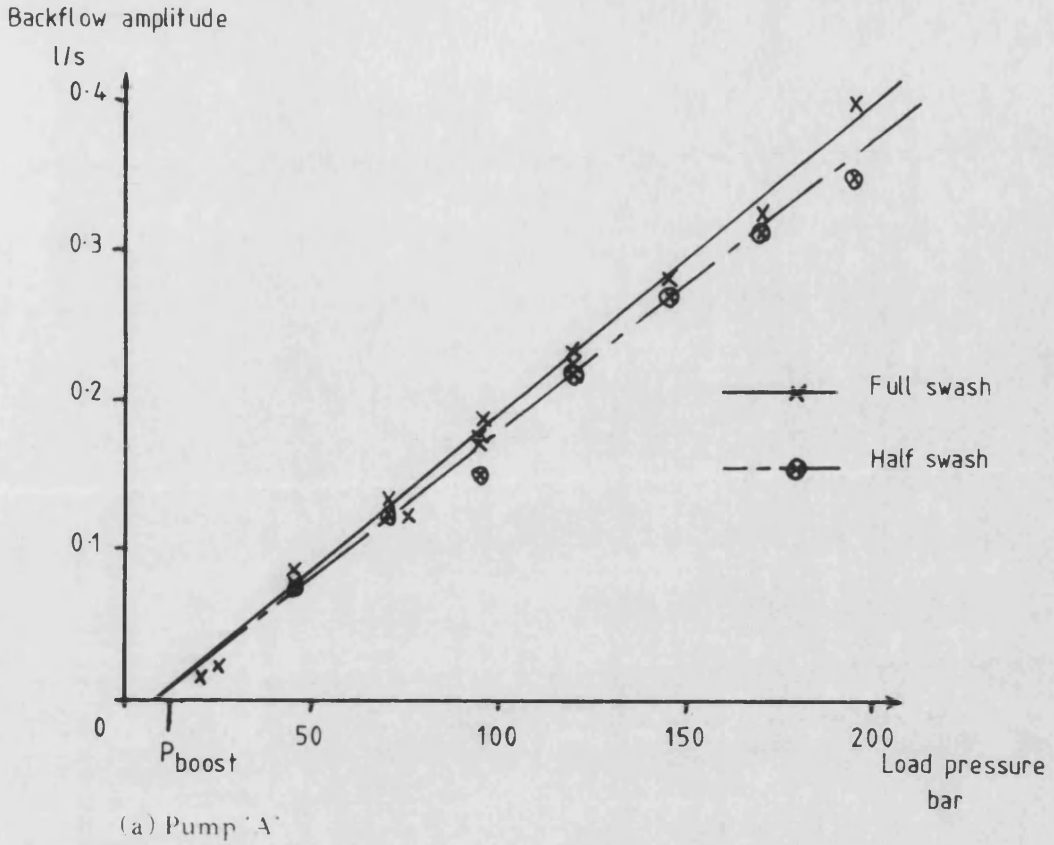

(a) Pump 'A'

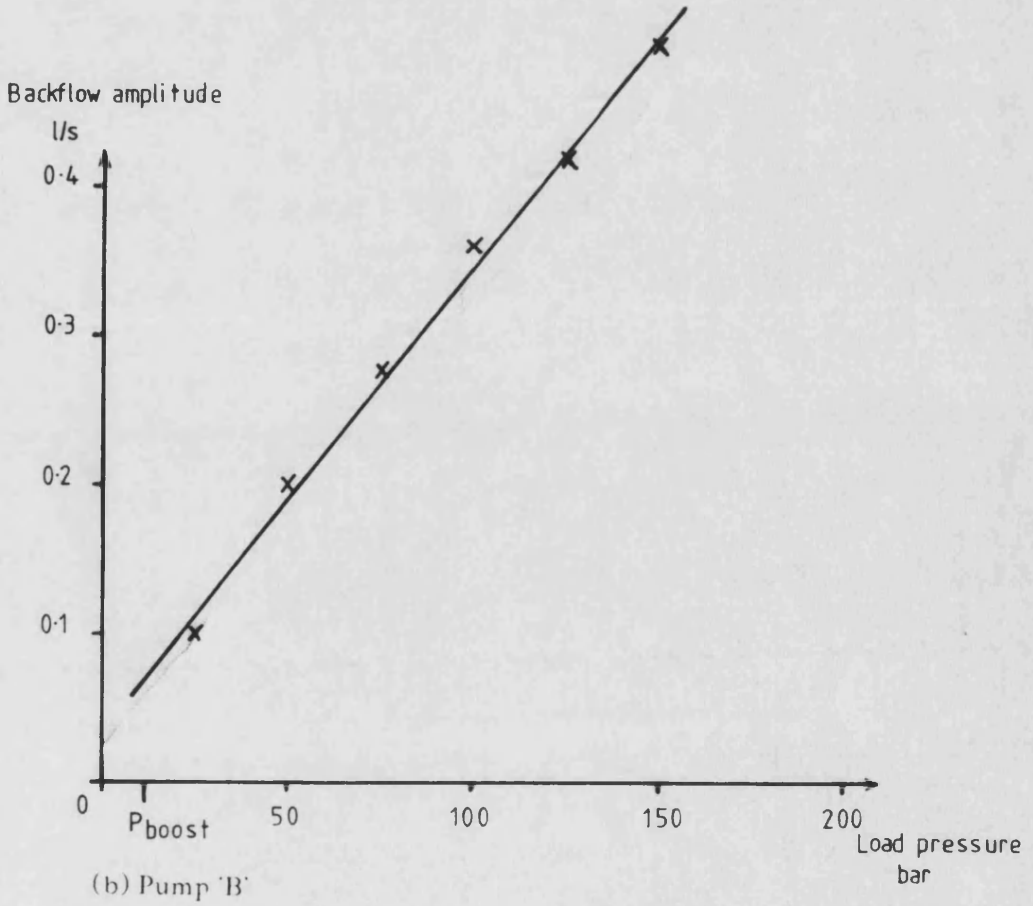

(b) Pump 'B'

Fig. 5.14 Relationship between Backflow Amplitude and Load Pressure

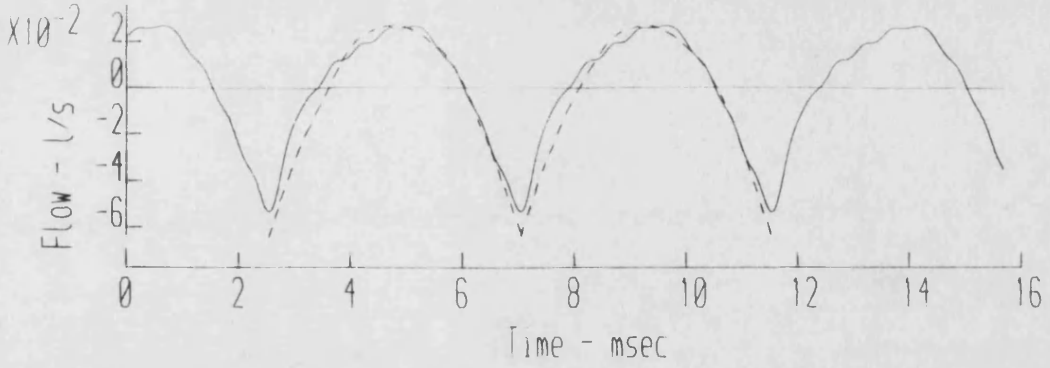

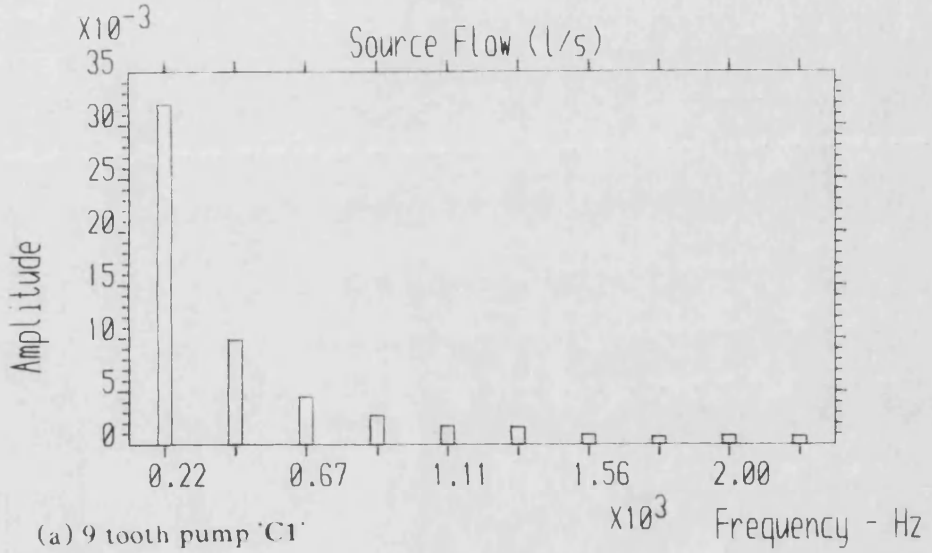

(a) 9 tooth pump 'C1'

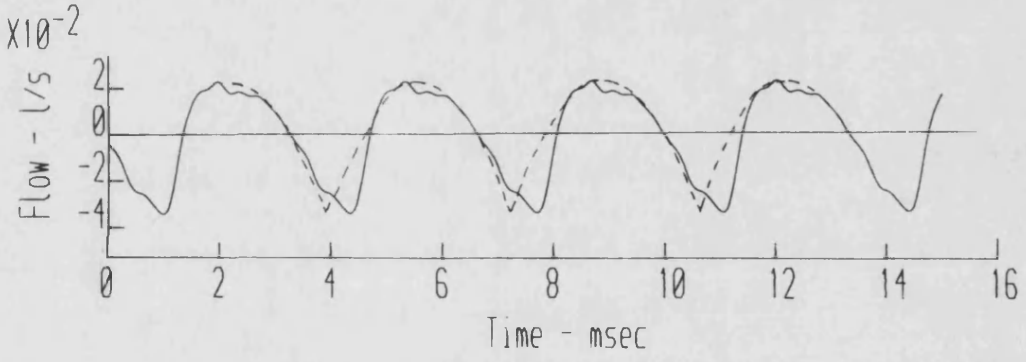

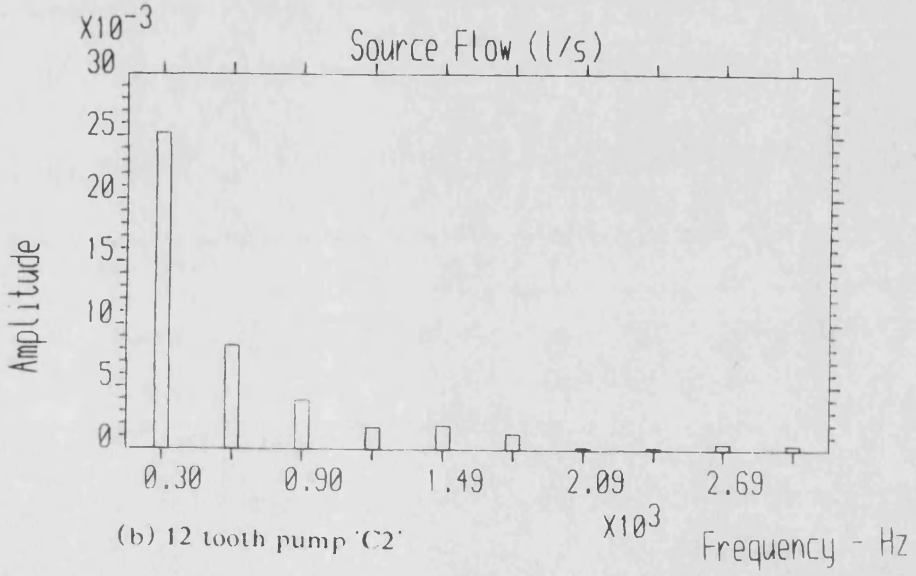

(b) 12 tooth pump 'C2'

Fig. 5.15 **Typical Flow Ripple Waveforms and Amplitude Spectra - Pumps 'C' 90 bar, 1500 rev/min (theoretical waveforms shown as dotted lines)**

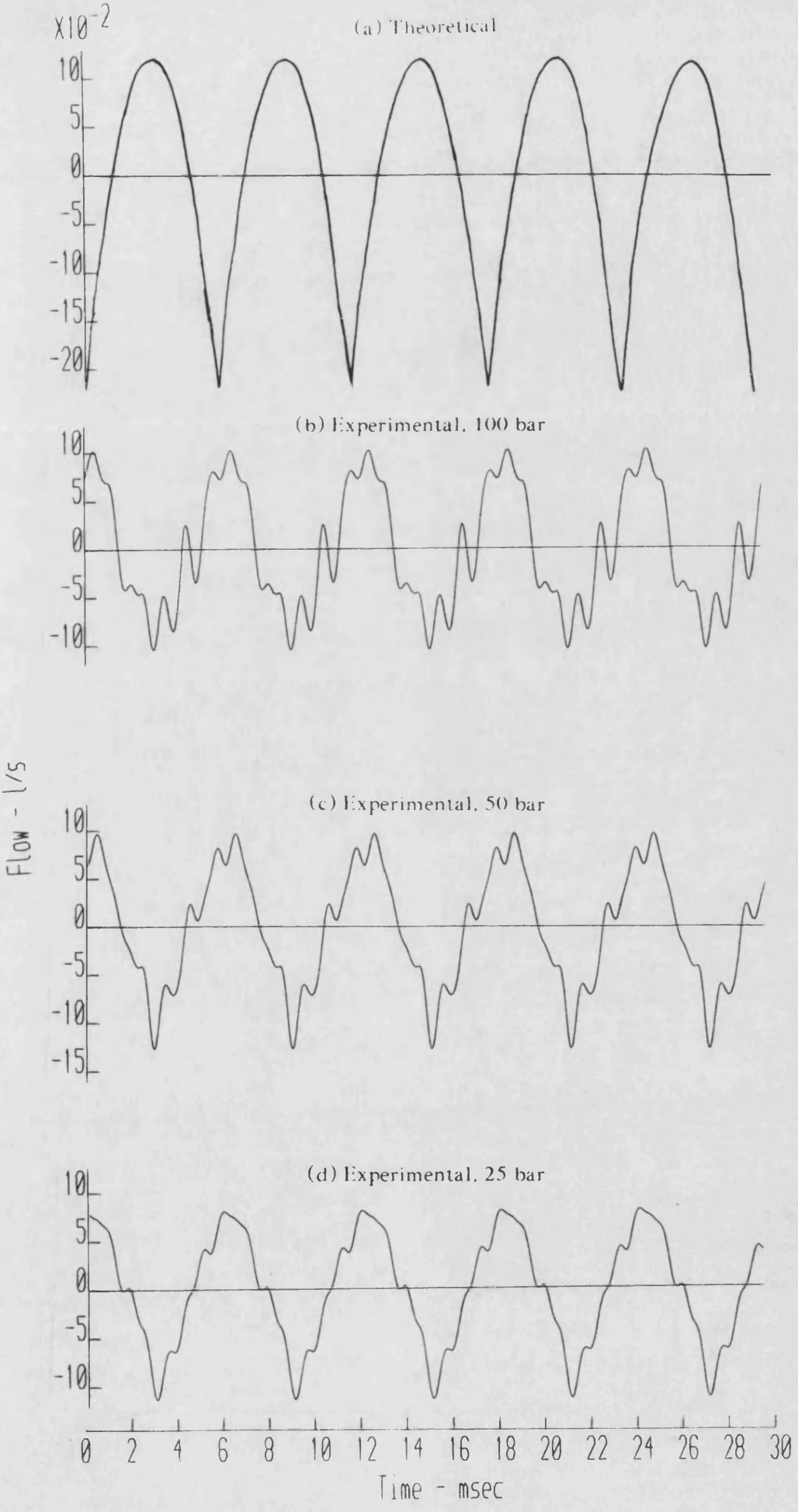

Fig. 5.16 **Flow Ripple Waveforms - Pump 'D1', 1000 rev/min**

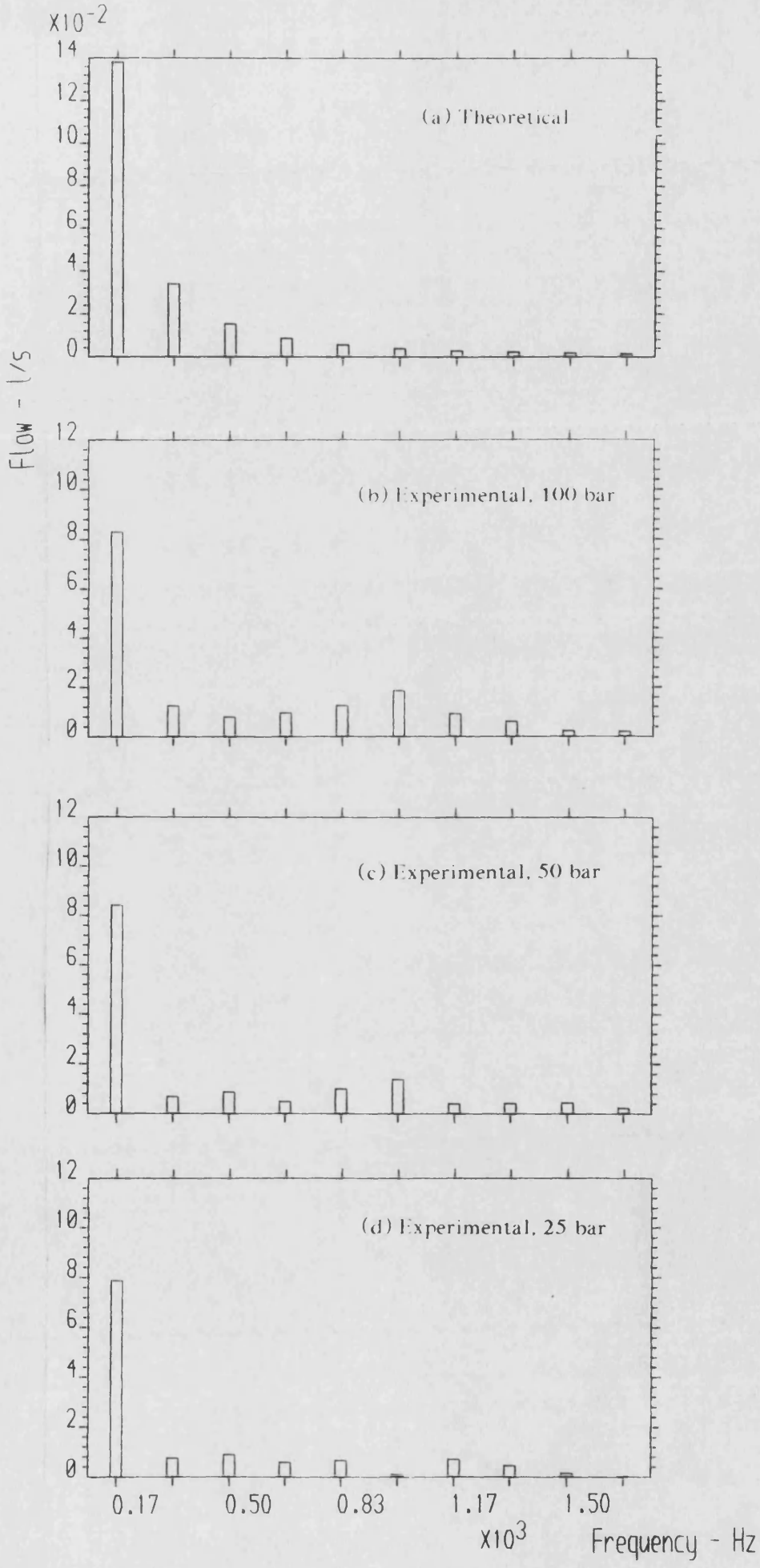

Fig. 5.17 Flow Ripple Amplitude Spectra - Pump 'D1', 1000 rev/min

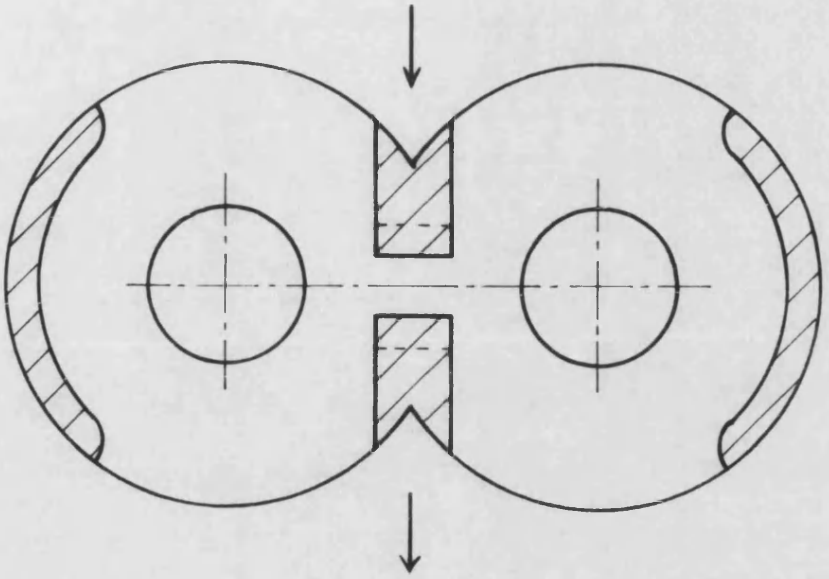

(a) Pump 'D1'

Recessed areas

Extent of theoretical relief grooves

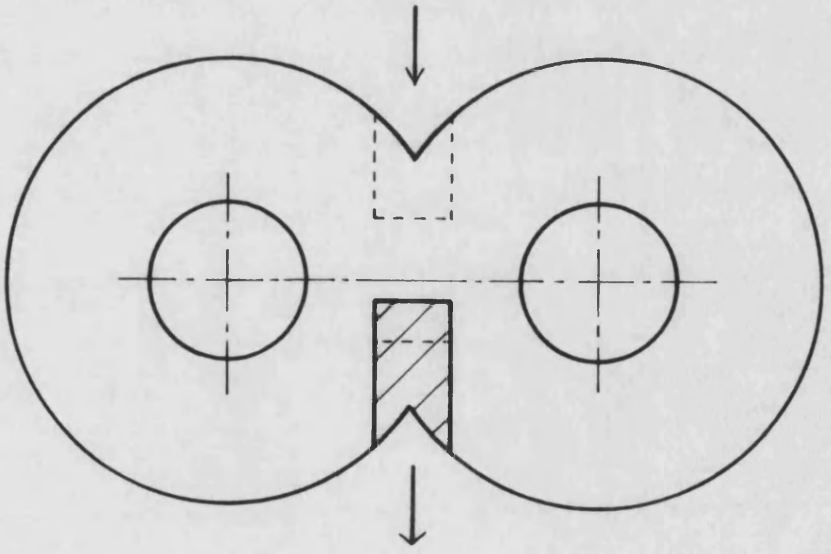

(b) Pump 'D2'

Fig. 5.18 Gear End Plate Design, Pumps 'D'

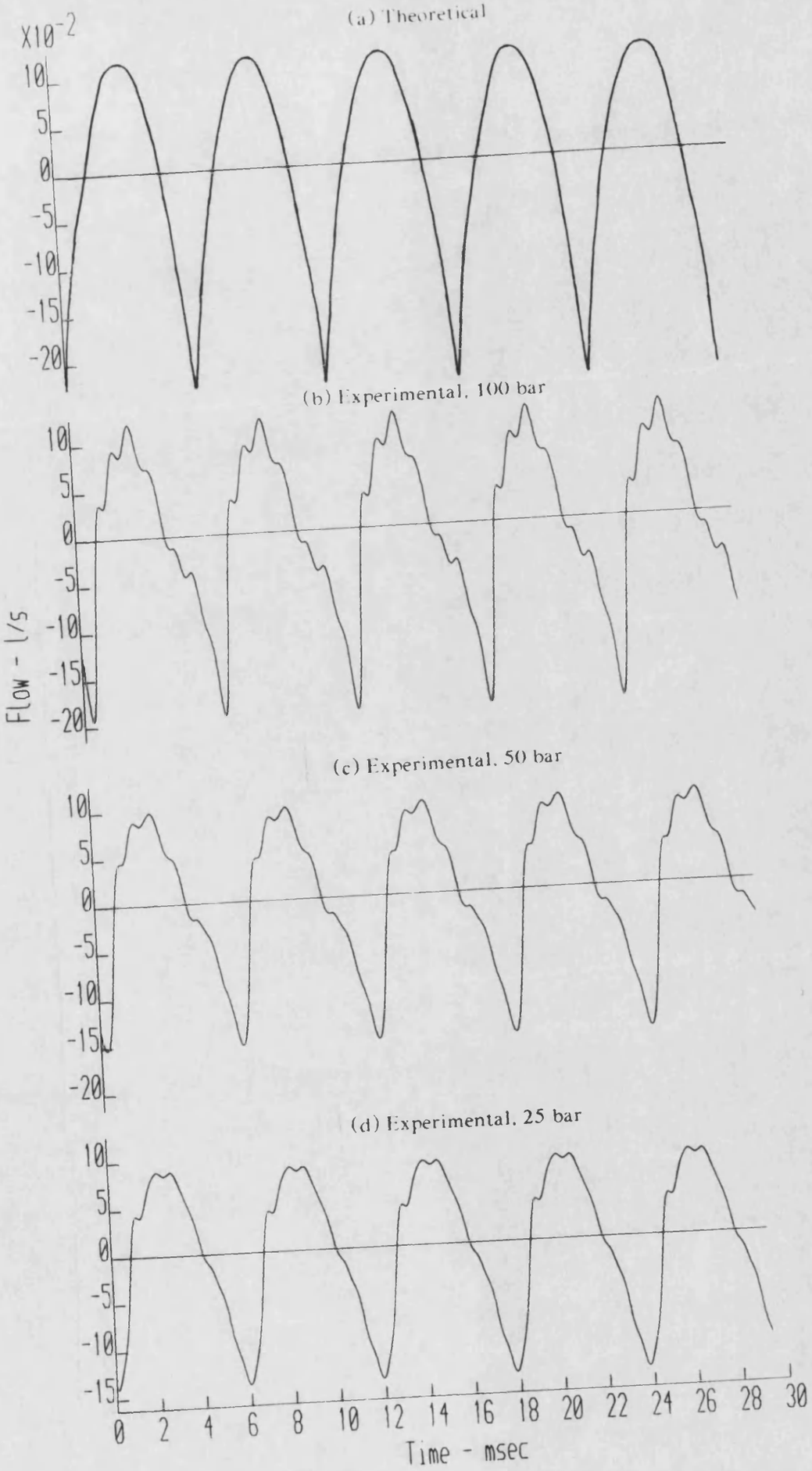

Fig. 5.19 Flow Ripple Waveforms - Pump 'D2', 1000 rev/min

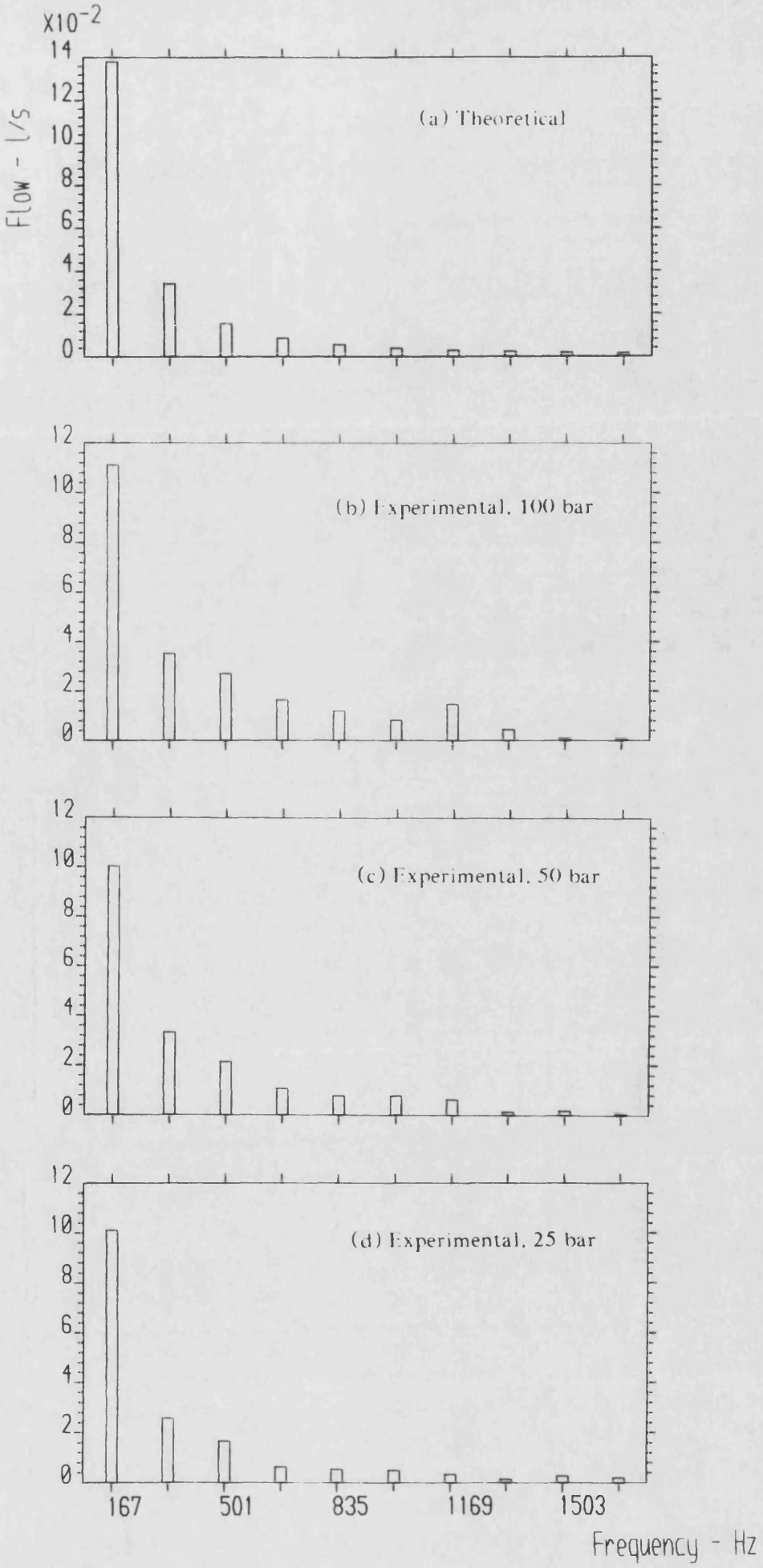

Fig. 5.20 Flow Ripple Amplitude Spectra - Pump 'D2', 1000 rev/min

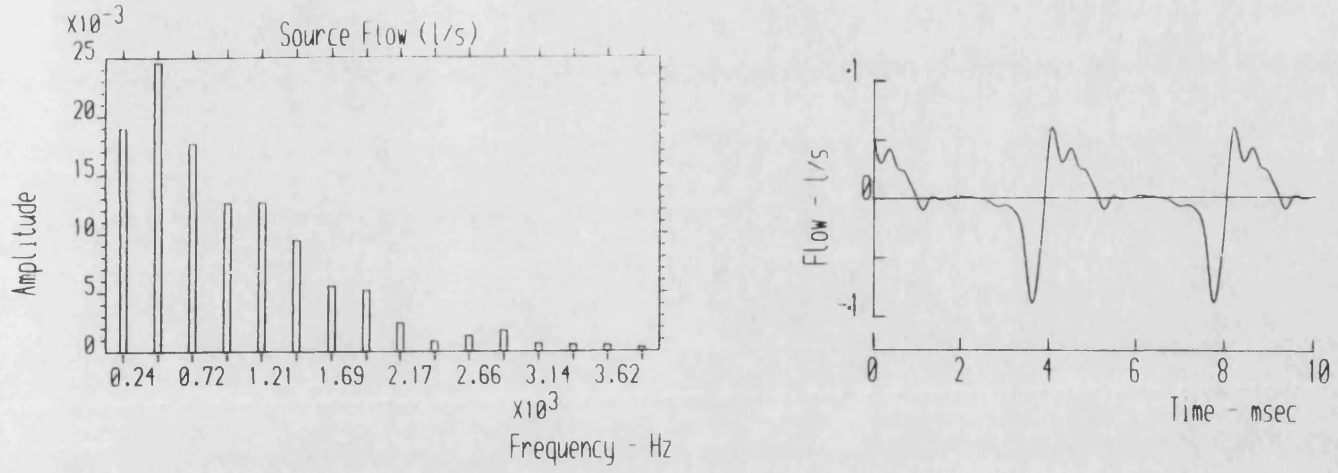

(a) 50 bar

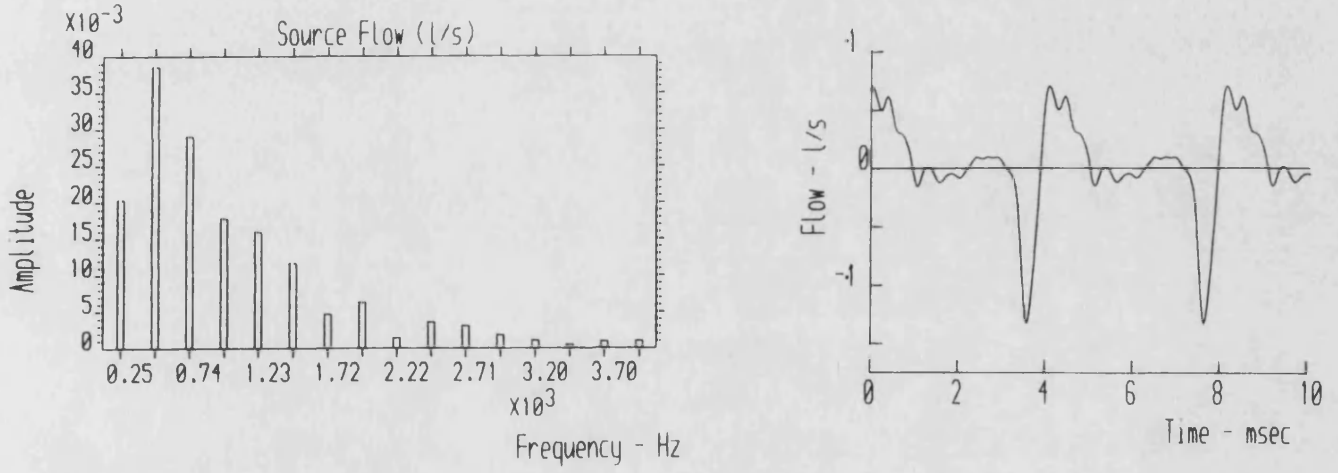

(b) 100 bar

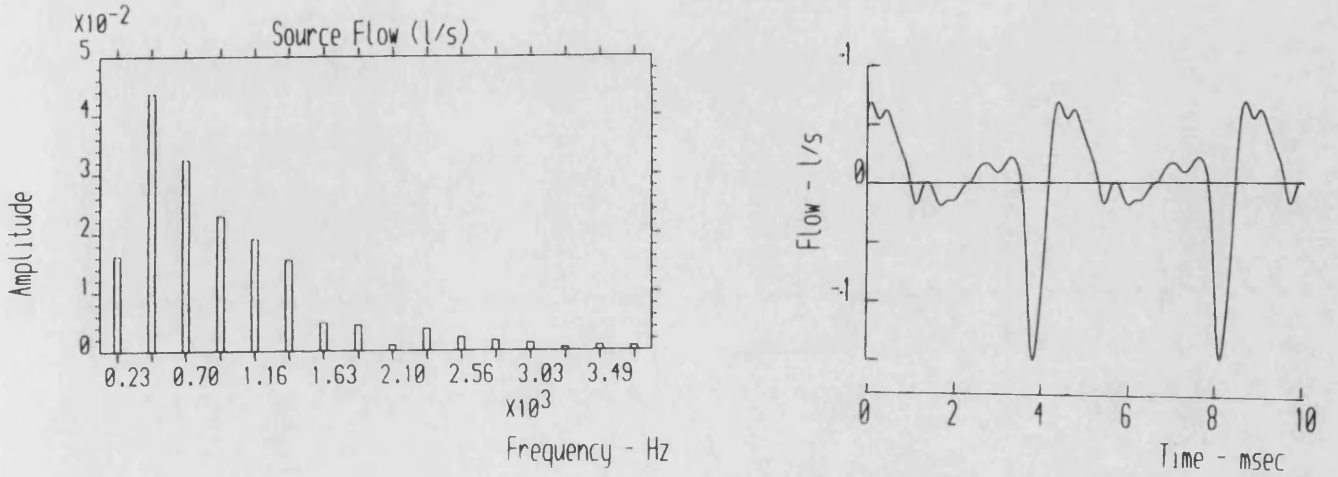

(c) 150 bar

Fig. 5.21 **Experimental Flow Ripple Amplitude Spectra and Waveforms Pump 'E', 1500 rev/min**

CHAPTER 6

RESULTS OF IMPEDANCE TESTS ON PASSIVE COMPONENTS

The technique described in chapter 4 for the evaluation of the source impedance of positive displacement pumps can also be applied to the measurement of the impedance characteristics of other components such as valves and accumulators.

6.1. Accumulator Impedance Tests

Tests were performed in order to measure the impedance characteristics of a bladder type accumulator. This had a capacity of 1.14 litres and is shown diagrammatically in Fig. 6.1(a).

6.1.1. Theoretical Impedance

At low frequency, an accumulator behaves as a compressible volume, in which case its impedance is capacitive, i.e.

$$Z_a = \frac{1}{j\omega C_a} \qquad \ldots (6.1)$$

It is reasonable to ignore the compressibility of the contained oil in the analysis: the oil stiffness is very much greater than that of the nitrogen contained in the bladder. The stiffness of the rubber bladder is also neglected.

Since we are considering small, rapid pressure changes about a mean, then adiabatic conditions can be assumed, in which case

$$pv^{\gamma} = \tilde{P}\tilde{V}^{\gamma} \qquad \ldots (6.2)$$

where $\tilde{P}$ is the mean pressure, and $\tilde{V}$ is the volume of the gas in the bladder at that pressure. γ is the ratio of the specific heats, which for nitrogen is approximately 1.5. For small perturbations about the mean condition,

$$\frac{\partial v}{\partial p} = -\frac{\tilde{V}}{\gamma \tilde{P}} \qquad \ldots (6.3)$$

The mean volume $\tilde{V}$ can be calculated from the precharge conditions. Assuming an isothermal (slow) compression from the precharge condition to the mean condition,

$$\tilde{P}\tilde{V} = P_{PC} V_{PC} \qquad \ldots (6.4)$$

where P_{PC} is the precharge pressure, and V_{PC} is the accumulator capacity.

$$\text{Therefore } \tilde{V} = \frac{V_{PC} P_{PC}}{\tilde{P}} \qquad \ldots (6.5)$$

Hence, substituting equation (6.5) into (6.3),

$$\frac{\partial v}{\partial p} = -\frac{V_{PC} P_{PC}}{\gamma \tilde{P}^2} \qquad \ldots (6.6)$$

The accumulator impedance is given by the equation $Z_a = \frac{\partial P}{\partial Q}$, where $Q = -\frac{\partial v}{\partial t}$.

$$\text{Thus } Z_a = \frac{\gamma \tilde{P}^2}{j \omega P_{PC} V_{PC}} \qquad \ldots (6.7)$$

Therefore the capacitance of the accumulator will be dependent on the precharge pressure P_{PC} and the working pressure $\tilde{P}$.

At higher frequencies, the inertance of the fluid contained within the neck of the accumulator will become significant. Ignoring wave propagation effects, this can be considered to act in series with the capacitance. Thus the impedance can be defined by the equation [49]:

$$Z_a = \frac{1}{j \omega C_a} + R_a + j \omega L_a \qquad \ldots (6.8)$$

where $C_a = \dfrac{P_{PC} V_{PC}}{\gamma \tilde{P}^2}$ ...(6.9)

R_a is a resistance term which may be present due to any energy losses in the accumulator, such as viscous losses in the neck or hysteresis in the rubber bladder. The 'inductance' L_a is due to the inertia of the fluid in the neck and may be difficult to measure because of the complexity of the flow passageway. It should, however, be virtually independent of operating conditions, being a function solely of the accumulator geometry and fluid density.

The impedance will thus exhibit an anti-resonance at which its amplitude will be at a minimum. The natural (anti-resonant) frequency is given by the equation

$$\omega_n = 2\pi f_n = \frac{1}{\sqrt{L_a C_a}} \quad \ldots(6.10)$$

$$\text{or } f_n^2 = \frac{1}{4\pi^2} \frac{\gamma \tilde{P}^2}{L_a P_{PC} V_{PC}} \quad \ldots(6.11)$$

Below this frequency, the impedance will be asymptotic to a line with a gradient of -20 dB/decade and a phase of $-90°$, and above this frequency it will be asymptotic to a line with a gradient of +20 dB/decade and a phase of $+90°$. Thus, assuming that L_a and γ are constant, there should be a linear relationship between f_n^2 and $\tilde{P}^2/P_{PC}$.

6.1.2. Experimental Technique

The test circuit is shown diagrammatically in Fig. 6.1(b). The accumulator was mounted horizontally on the end of the standing wave measurement pipe. A small diameter bleed valve was situated in parallel with the accumulator; this had the double purpose of permitting the bleed-off of any trapped air, and of allowing a small mean flow in the pipe, necessary for the control of the temperature of the oil in the pipe. Provided that the bleed flow and the side branch volume were small, the effect on the measured impedance would be insignificant.

The fluid-borne noise source was situated at the other end of the pipe. Tests were performed using both pump 'A' and the pulse generator as sources. Pressure ripple was measured at three points, in the form of transfer function measurements. The impedance was referred to the end face of the accumulator neck.

6.1.3. Results

Typical results obtained using pump 'A' as the source are presented in Fig. 6.2. Fig. 6.2(a) shows the impedance where the system pressure is below the precharge pressure, so that the poppet valve in the accumulator is closed. It can be seen that the impedance corresponds roughly to that of a compressible volume, which is probably due to the oil contained within the neck. Discrepancies at low frequency may be caused by experimental error (since $|Z_T| >> |Z_0|$), or they may be due to mechanical vibration (see section 6.2.1.). Higher frequency discrepancies may be caused by distributed parameter effects.

As the mean pressure becomes greater than the precharge pressure, the accumulator becomes functional and there is a sudden change in its characteristics. In practice this was noticeable as a distinct change in the tone of the air-borne noise emanating from the system. Fig. 6.2(b) shows an impedance characteristic measured at a mean pressure higher than the precharge pressure. As can be seen, the impedance now shows an inductive characteristic, being small at low frequency and increasing with frequency at 20 dB/decade. Above 2.5 kHz, there appears to be some discrepancy between the experimental points and inductance model; this is presumably due to distributed parameter effects. It is not possible to discern any capacitive effects at the lower frequencies since the experimental frequencies are too high. For this reason, tests were also performed using the pulse generator as a FBN source, in which case mean pressure and flow were supplied by another pump.

Experimental impedance results obtained using the pulse generator are plotted in Fig. 6.3(a-d), for different mean and precharge pressures, where in each case the mean pressure exceeded the precharge pressure. A least-squares curve fit in the form of equation (6.8) is superimposed upon the results. In each case, the capacitive, resistive and inductive effects are clearly visible. At high frequencies the impedance tends toward the same characteristic in each case; this implies that the inductance is independent of operating conditions, as would be expected from theory. The capacitance, however, is strongly dependent upon the operating conditions. A theoretical capacitive impedance characteristic, based upon equation (6.9) is also superimposed upon the experimental results as a dotted line. It can be seen that the model fitted to the experimental impedance points shows very good correlation with this theoretical characteristic.

Fig. 6.4 shows a graph of the square of the measured natural frequencies of the accumulator, f_n^2, as a function of $\tilde{P}^2/P_{PC}$. The natural frequency is obtained from the curve fit to the experimental results. It can be seen that the relationship is a straight line, passing through the origin. This is as would be expected from theory.

It can therefore be concluded that the model described provides a very good representation of an accumulator. From the above results it can be seen that the capacitive effects are significant only at frequencies which lie below the range normally considered in FBN analysis. Therefore, the impedance characteristics of an accumulator can be modelled as a pure inductance. A major difficulty, however, lies in the estimation of the value of this inductance. This is probably best obtained empirically from experimental results, because of the difficulty of its theoretical prediction. The resistance is a minor effect and under most circumstances may be ignored.

From Fig. 6.3 it can be seen that reasonably accurate impedance results were obtained around the anti-resonant frequency. This is perhaps surprising as in this region the accumulator impedance is very small, typically 30 dB smaller than the pipe characteristic impedance (section 4.4.3.2.). Furthermore, the frequency is low, so that the transducer spacing is very small compared to the wavelength (section 4.4.3.1.). Under such circumstances it would normally be expected that the predicted impedance values would be highly inaccurate. The unexpected accuracy of the results may be explained by considering Fig. 6.5, which shows the pressure ripple transfer function measurements along the pipe together with the modelled standing wave profile. Firstly, it can be seen that the experimental points show very good correlation with the model. Secondly, considering Fig. 6.5(a), which shows the first harmonic, it can be seen that there is a node very close to the accumulator. Thus there are significant changes in both amplitude and phase along the length of the pipe. Fig. 6.6 shows the equivalent pressure ripple transfer function measurements and modelled standing wave for the case where the system pressure is below the accumulator precharge pressure, so that the accumulator acts as a closed end. It can be seen that, for the first harmonic, there is very little change in the standing wave amplitude and phase along the length of pipe. Small transducer calibration errors or experimental scatter could cause a large error in the prediction of the accumulator impedance, and it was found in practice that it was impossible to obtain accurate low frequency results in this case.

The above results show that the standing wave analysis at low frequency, where the pressure ripple wavelength is much greater than the length over which measurements are taken, can produce accurate impedance results provided that measurements are taken at or near a node. If, however, the measurements are taken at or near an anti-node, the results are likely to be seriously error-prone.

6.2. Restrictor Valve Impedance Tests

In previous FBN analysis [20], it has been assumed that the impedance of a simple restrictor valve can be modelled as a simple resistance, derived from the steady state characteristics.

The general pressure-flow characteristic for a restrictor can be given by the equation

$$\Delta\tilde{P} = k\tilde{Q}^n \qquad \ldots(6.12)$$

where $\Delta\tilde{P}$ is the steady state pressure drop across the valve, and $\tilde{Q}$ is the mean flow rate.

For small perturbations about the mean condition, the resistance is given by the equation

$$R_v = \frac{\partial(\Delta\tilde{P})}{\partial\tilde{Q}} = \frac{n\,\Delta\tilde{P}}{\tilde{Q}} \qquad \ldots(6.13)$$

For laminar flow, the restrictor would have a linear pressure-flow characteristic, in which case the exponent n = 1.0. For fully developed turbulent flow, the restrictor would have a parabolic pressure-flow characteristic, with an exponent n = 2.0. In general, the characteristic of a restrictor valve will have an exponent between 1.0 and 2.0.

Some experimental impedance measurements were performed on a restrictor valve by Wing [26], using the 'Hydraulic Trombone'. It was found that the correlation between the experimental results and the simple model above was poor; the results showed some variation of the amplitude and phase with frequency.

A large number of tests were performed on a restrictor valve, with the aim of identifying the reasons for the deviations from the model, so that it might be possible to develop a more comprehensive model for such a valve.

6.2.1. Experimental Technique

The method was similar to that used in the measurement of the impedance of an accumulator (section 6.1.2.). A length of flexible hose was situated downstream of the valve, followed by a positive displacement flowmeter. The valve under test was a 3/4" needle valve, described in appendix 1.

Some typical results using pump 'A' as the source of FBN are presented in Fig. 6.7. As can be seen, there are significant deviations from the idealised resistance model described above, in terms of both amplitude and phase. For the case of zero mean flow, Fig. 6.7(a), the impedance seems to be close to that of a pure capacitance, with the amplitude reducing at a rate of 20 dB/decade, and the phase about $-90°$. With flow through the valve, as in Fig. 6.7(b-d), the impedance characteristics tend towards a constant amplitude and zero phase at low frequency, with a capacitive effect predominant at higher frequency. The capacitive effect can be explained by the volume of fluid contained in the upstream chamber of the valve; the impedance was measured at the end of the valve casing, and there was a significant volume of fluid between this point and the restrictor itself. This would tend to act in parallel with the valve resistance, giving an impedance of the form

$$Z_v = \frac{R_v}{1+\frac{R_v V_v}{B} j\omega} \qquad \ldots (6.14)$$

i.e. a first order lag. However there appear to be some deviations from this simple model, in particular at the 5th harmonic (875 Hz), where the amplitude shows a noticeable reduction.

It is possible to remove the capacitive part of the valve impedance by shifting the point at which the impedance is measured inside the valve, such that the effective volume is zero. Impedance results measured at this point are shown in Fig. 6.8. As can be seen, although the results are closer to the simple resistance model, there are still discrepancies, which may be attributed to a number of possible factors other than experimental error, outlined below.

a) Longitudinal mechanical vibration of the valve and pipe. This may cause a 'piston' action on the fluid. This will act in parallel with the valve impedance and have most effect if the valve impedance is high.

b) The entry impedance of the system downstream of the valve. This will tend to act in series with the valve impedance, and be most significant when the valve impedance is low.

c) The orifice itself may not act as a pure resistance but may also exhibit some inductive effect, due to the high fluid velocity at that point.

Factors (a) and (b) are not properties of the valve, but are dependent upon the connected system. In order to isolate the impedance of the valve alone, these effects need to be removed.

A more comprehensive valve impedance model was developed to take the above effects into account. This model is shown schematically in Fig. 6.9. The following assumptions were made.

a) Dimensions are small so that wave propagation effects can be ignored.

b) The body of the valve vibrates as a rigid unit.

c) The orifice area is insignificant compared to the pipe cross sectional area.

Considering continuity upstream of the orifice,

$$Q_{IN} = \frac{j\omega V}{B} P_{IN} + Q_v + AU \qquad \ldots (6.15)$$

The impedance of the valve, Z_v, is given by

$$Z_v = \frac{P_{IN} - P_{OUT}}{Q_v} \qquad \ldots (6.16)$$

Substituting (6.15) into (6.16),

$$Z_v = \frac{1-\frac{P_{OUT}}{P_{IN}}}{\frac{Q_{IN}}{P_{IN}} - \frac{j\omega V}{B} - \frac{AU}{P_{IN}}} \qquad \ldots (6.17)$$

Thus the effect of the entry impedance downstream of the valve can be taken into account by measuring the pressure ripple at the valve outlet.

A number of ways are possible for removing the effect of vibration:

a) By mounting the valve rigidly on a large mass. This should have the effect of making any vibration insignificant.

b) By measuring the vibration of the valve, using an accelerometer. By integration of the acceleration, the velocity U could be calculated and taken into account in equation (6.17).

c) By measuring the impedance of the valve when shut, Z_{shut}. If one assumes that the vibration is a function of the upstream pressure P_{IN} alone (This is not strictly true; it may also be dependent on the downstream pressure, P_{OUT}, as well as any other vibrations elsewhere in the system), we can then define a 'mechanical impedance' Z_{mech}, where

$$Z_{mech} = \frac{P_{IN}}{AU} \qquad \ldots (6.18)$$

If the valve is shut, then $Z_v = \infty$. Hence, from equation (6.17),

$$\frac{1}{Z_{shut}} = \frac{j\omega V}{B} + \frac{1}{Z_{mech}} \qquad \ldots (6.19)$$

The value of Z_{shut} can then be substituted into equation (6.17) in order to find the valve impedance at any other condition;

$$Z_v = \frac{1-\frac{P_{OUT}}{P_{IN}}}{\frac{Q_{IN}}{P_{IN}} + \frac{1}{Z_{shut}}} \qquad \ldots (6.20)$$

Method (c) was found to give satisfactory results in practice. It was applied to the experimental results shown in Fig. 6.7, as shown in Fig. 6.10 (note: downstream effects were ignored, and P_{OUT} was not measured in this case). It can be seen that there is a significant improvement in the uniformity of the results. The resistance value predicted by the turbulent flow model $R_v = 2\tilde{P}/\tilde{Q}$ is also shown on the plots. In most cases this is quite close to the experimental results, within ± 2 dB except at the higher frequencies. A phase advance is apparent on the results, particularly Fig. 6.10(b) and (c). It is thought that this is an inductive effect due to the inertia of the fluid in the restrictor.

Results in which the vibration of the valve was allowed for using method (b) are presented in Fig. 6.11. As can be seen when compared to the uncorrected results in Fig. 6.7, the effect is to reduce any discrepancies so that the experimental points conform closely to the form of a first order lag, except for Fig. 6.11(a) in which the form of the results is very close to that of a pure capacitance.

6.2.2. Variation of Resistance with Mean Pressure Drop and Flow Rate

Further tests were carried out in order to investigate the behaviour of the restrictor valve impedance in detail over a wide range of conditions. In particular, the behaviour of the impedance at very low mean flow rates and pressure drops was studied.

The experimental tests were carried out by varying the flow through the valve, while retaining the valve opening at a constant setting. The experimental rig is shown in Fig. 6.12. The mean pressure upstream of the valve under test was maintained at a constant value using the relief valve. The flow through and the pressure drop across the valve were then varied by adjusting the valve downstream of the valve under test. By this means it was possible to produce the condition of zero mean flow and pressure drop, while maintaining the system pressure. Mean pressure was measured both upstream and downstream of the valve. The impedance analysis procedure was as described above, pressure ripple being measured downstream of the valve in order that the entry impedance of the system downstream could be allowed for. The effects of vibration and contained volume were allowed for by substitution into equation (6.20) of the impedance of the valve when shut. The tests were repeated for a range of different valve openings.

Typical impedance results are shown in Fig. 6.13, for different pressure drops and flow rates, at the same valve opening. An inductive effect is apparent, with a phase advance and increase in amplitude at high frequencies, particularly in Fig. 6.13(a) and (b). Superimposed upon the experimental points is a mathematical model of the form:

$$Z_v = R_v + j\omega L_v \qquad \ldots (6.21)$$

This is intended to represent the resistive and inductive components of the impedance of the restriction. The parameters R_v and L_v were determined by means of a least squares curve fitting procedure. A certain amount of deviation of the experimental points from the mathematical model is apparent, in particular between 800 Hz and 1 kHz. It was intended that, in the estimation of the resistance and inductance, the mathematical model should average out the effects of these variations.

It can be seen that the resistance varies with the mean flow and pressure drop, being highest at high mean flow rate. At the lower flow rates, the inductive effect is clearly apparent as a phase advance and increase in amplitude. In fact the modelled value of inductance is virtually independent of the mean flow, but its effect is more noticeable where the resistance is low. The inductance is a function of the fluid density and valve geometry (as with the accumulator, section 6.1.1.); thus it would not be expected to change with the mean flow rate or pressure drop. Furthermore, it was found that the inductance did not change significantly for different valve openings.

The resistance R_v is often assumed to be a function of the steady state characteristic of the valve, which is described by the equation

$$\tilde{Q} = c_Q A_v \left| \frac{2\Delta\tilde{P}}{\rho} \right|^{1/2} \qquad \ldots (6.22)$$

$$\text{or } \Delta\tilde{P} = \frac{\rho\tilde{Q}^2}{2c_Q^2 A_v^2} \qquad \ldots (6.23)$$

Differentiating (6.23), and linearising for small perturbations around the operating point,

$$R_v = \frac{\partial(\Delta\tilde{P})}{\partial\tilde{Q}} = \frac{\rho\tilde{Q}}{c_Q^2 A^2} \qquad \ldots (6.24)$$

This assumes that c_Q is constant and independent of the mean flow. Thus the resistance R_v would be expected to be proportional to $\tilde{Q}$, for a particular orifice area A_v. Fig. 6.13(a) shows the impedance characteristics at zero mean flow and pressure drop. As can be seen, the valve has a finite resistance at this condition; this does not conform to equation (6.24), which predicts that $R_v = 0$ when $\tilde{Q} = 0$.

Experimental resistance values R_v, obtained by applying the model of equation (6.21) to the experimental results, are plotted in Fig. 6.14 over the range of mean flow conditions tested at different valve openings. It can be seen from Fig. 6.14(a) that, for a valve lift of 0.11 mm, there is little variation in the resistance with mean flow. As the valve opening is increased (Figs 6.14(b),(c) and (d)), the variation of R_v with $\tilde{Q}$ become more marked, but in no case is the resistance proportional to the mean flow.

Two possible reasons for this deviation from the simple model of equation (6.24) were considered:

a) at low mean flow rates the magnitude of the flow ripple may be significant compared to $\tilde{Q}$. In such a situation, the linearisation of equation (6.23) may be invalid, and the instantaneous resistance might change significantly due to the flow fluctuations. This effect would tend to increase the measured resistance at low values of $\tilde{Q}$. However, further analysis showed that this effect, because of the low magnitude of the flow ripple through the valve, would not be sufficiently great to explain the observed discrepancies. Tests were performed, with zero mean flow, at different mean inlet pressures, in order to vary the pump flow ripple amplitude and hence the flow ripple amplitude through the valve. This was found not to have a significant effect on the measured valve resistance. Therefore, this explanation can be discounted from being a major source of the discrepancy.

b) at low mean flow rates, the Reynold's number N_R through the valve is low. In such a situation, the value of c_Q shows significant variation with N_R as the flow regime in the valve changes from turbulent to laminar [50,51]. For laminar flow, the steady state pressure/flow characteristic would be linear, so that R_v would be finite at the zero mean flow condition.

6.2.3. Correlation between Steady State Characteristics and Dynamic Resistance

In order to investigate the validity of the assumption that the dynamic resistance of the valve is equal to the rate of change of mean pressure drop with respect to the mean flow rate, the steady state characteristics of the valve were also measured. If the assumption

is true, it follows that:

$$\Delta\tilde{P} = \int_0^{\tilde{Q}} R_v \, dQ. \qquad \ldots (6.25)$$

This integral was evaluated from the measured dynamic resistance characteristics, using the trapezoidal method (note: because of experimental scatter, it is more accurate to integrate the resistance characteristics in order to predict the steady state characteristics than to differentiate the steady state characteristics to predict the resistance). This integral is plotted together with the steady state characteristics in Fig. 6.15. As can be seen, there is reasonably good correlation between the measured and predicted characteristics, though the prediction from the dynamic resistance is consistently higher by approximately 10%. It can be concluded, therefore, that the postulation that $R_v = \partial(\Delta\tilde{P})/\partial\tilde{Q}$ is valid.

It is apparent from Fig. 6.15, and Fig. 6.15(a) in particular, that the steady state characteristic approaches a linear form at low flow rate. In this region, the flow through the valve behaves in a laminar fashion. In order to investigate this further, it was attempted to study the relationship between the flow coefficient c_Q and the Reynold's number.

6.2.4. Variation of the Flow Coefficient with Reynold's Number

The Reynold's number at the valve orifice is given by the formula:

$$N_R = \frac{\tilde{V} d_H}{\nu} \qquad \ldots (6.26)$$

where $\tilde{V}$ = mean velocity through orifice = $\dfrac{\tilde{Q}}{A_v}$

and d_H = hydraulic mean diameter = $4\dfrac{\text{flow section area}}{\text{flow section perimeter}}$ $\qquad \ldots (6.27)$

Thus, $N_R = \dfrac{\tilde{Q}}{A_v}\dfrac{4A_v}{h}\dfrac{1}{\nu}$ $\qquad \ldots (6.28)$

For small valve lifts, the perimeter $h \approx 2\pi d_v$ ...(6.29)

where d_v = diameter of valve seat

thus $N_R = \frac{2\tilde{Q}}{\pi d_v \nu}$ ...(6.30)

The flow coefficient is given directly from equation (6.30) as:

$$c_Q = \frac{\tilde{Q}}{A_v}\left(\frac{\rho}{2\Delta\tilde{P}}\right)^{1/2} \quad \ldots(6.31)$$

Results are plotted in Fig. 6.16. As can be seen, for $N_R < 400$ there is a marked drop in the flow coefficient. There is some scatter on the results which may be attributed to inaccuracies in the measurement of the pressure drop, flow rate and valve opening. The relationship between c_Q and N_R appears to show little dependency upon the valve opening. At high values of N_R, c_Q tends towards a value of about 0.8.

These results show good correlation with measurements of c_D for long orifices by Lichtarowicz *et al* [51] if the length/diameter ratio is chosen to be 2 or 4, as shown. For a long orifice, the vena contracta occurs within the length of the orifice. As the downstream pressure was measured by Lichtarowicz *et al* at the end of the orifice, then this is likely to be beyond the vena contracta, in which case the flow coefficient c_Q and the discharge coefficient c_D will be approximately equal. Therefore, although the internal geometry of a needle valve is rather more complicated than that of a long orifice, it may be possible to model the characteristics of a needle valve as such.

6.3. Results of Tests on Pressure Compensated Flow Control Valve 'V2'

Tests were performed on a pressure compensated flow control valve (appendix 1). The impedance was measured for a range of mean pressure drops and flow rates, in a similar way to the tests on the restrictor valve.

Fig. 6.17 shows a simplified schematic diagram of the valve. As can be seen, this valve is much more complex than the restrictor valve tested previously, and it is likely that its impedance characteristics will be more complex. No attempt was made to allow for the effects of the system downstream of the valve. Similarly, no allowance was made for the vibration of the valve; however, as it was relatively large and massy, vibration effects were unlikely to be significant.

Typical results are presented in Fig. 6.18. As can be seen, they bear a close resemblance to the form of the source impedance of a positive displacement pump (chapter 5). The results exhibit an anti-resonance between 1 kHz and 2 kHz in each case, and a resonance is apparent between 2 kHz and 3 kHz. Considering Fig. 6.18(b), (c) and (d), it can be seen that at low frequency the results deviate from the source impedance model in that the phase approaches 0°, and the amplitude curve flattens out. This effect is due to the impedance tending toward the steady state resistance of the valve at low frequency.

This characteristic can be explained by considering the valve to behave as a long passageway terminated by a simple resistance. If the passageway is assumed to be frictionless and uniform, then the valve impedance can be represented by the equation

$$Z_v = Z_0 \left\{ \frac{1+\rho_v e^{-2j\omega l/c_0}}{1-\rho_v e^{-2j\omega l/c_0}} \right\} \qquad \ldots (6.32)$$

where the reflection at the end of the passageway, ρ_v, is given by

$$\rho_v = \frac{R_v - Z_0}{R_v + Z_0} \qquad \ldots (6.33)$$

This model predicts that the impedance will exhibit a resonance at twice the frequency of the first anti-resonance, and another anti-resonance at three times the frequency, and so on. However, by studying Fig 6.18, it is clear that this is not the case, and in all cases the ratio of the resonant frequency to the anti-resonant frequency is significantly less than 2.0.

This effect can be explained by the fact that the assumption of a uniform cross section for the valve passageway is not an accurate representation of the actual geometry. In practice, the passageway is far more complex, with side branches, bends and changes in cross sectional area. At low frequency the simple model is valid, but at higher frequencies the impedance may be greatly affected by the geometry.

A 'standard' source impedance model (section 4.3.9.1.) applied to experimental results for this valve is shown in Fig. 6.19. It can be seen that the correlation between the model and the experimental points is very good; in this case the steady state resistance is high so there is little deviation from the model at low frequency. However, there is no resonance within the frequency range and so the simple model is sufficient. Consider, however, Fig 6.20(a). In this case a resonance is apparent in the results. The resonant frequency is significantly less than twice the anti-resonant frequency and the simple model is unable to produce a good fit, even though there is little experimental scatter in the results. Fig. 6.20(b) shows a situation where two anti-resonances are clearly defined. Again the degree of fit of the model is very poor.

The accuracy of any impedance model under these situations depends on the number of variables or 'degrees of freedom' of the model. The simple model above has three degrees of freedom. One of these defines the mean level of the impedance, one the 'damping', and one the anti-resonant frequency, subsequent resonances and anti-resonances being integer multiples of this. In order to define the first resonant frequency independently of the anti-resonant frequency, it is necessary to include another degree of freedom. This was done by including a step change in the diameter of the passageway, half way along the length of the passageway, as shown in Fig. 6.21. If friction is neglected, then the model equation becomes:

$$Z = \frac{Z_{02}}{j \tan\left[\omega l / 2c_0 + \tan^{-1}(r \tan \omega l / 2c_0)\right]} \qquad \ldots (6.34)$$

$$\text{where } r = \frac{Z_{02}}{Z_{01}} = \frac{A_1}{A_2} \qquad \ldots (6.35)$$

Fig. 6.21 shows the typical form of this model for $r < 1$ ($A_2 > A_1$) and $r > 1$ ($A_2 < A_1$). It can be seen that the frequency of the first anti-resonance varies with the value of r. The resonant frequency, however, is independent of r. From equation (6.34), it can be shown that the anti-resonant frequency is given by

$$f_a = \frac{c_0}{\pi l}(\tan^{-1} 1/r)^2 \qquad \ldots (6.36)$$

Fig. 6.22 shows this model applied to the same results as in Fig. 6.20. It can be seen that the closeness of fit in this case is very good over the whole frequency range. The model, however, is rather more complicated than the previous one and is therefore much more difficult to apply.

It can be seen from Figs. 6.18, 6.19 and 6.21 that there is a distinct variation in the anti-resonant and resonant frequencies between the tests. Also, there is a variation in the effective volume. This was rather unexpected. Two possible reasons for this effect were considered:

a) the valve presents two restrictions in series to the flow, at spools 'A' and 'B'. The operation of the valve is such that the pressure drop across restrictor 'B' is held constant, independently of the mean flow. At low system pressure, the pressure drop across 'A' may be small in which case the fluid volume between 'A' and 'B' may be important. However, under the conditions considered, the impedance of restrictor 'A' will, in fact, be large enough for the volume downstream of it to be of little significance.

b) a pocket of air may have been trapped within the valve, perhaps in the branch line to the non-return valve. This would tend to increase the effective volume, particularly at low pressure. A graph of the effective volume against mean pressure is shown in Fig. 6.23(a), from which it is apparent that the effective volume is indeed greatest at low pressure. Fig. 6.23(b) shows a plot of the first anti-resonant and resonant frequencies against mean pressure. It can be seen that both frequencies increase with pressure. Hence the effective length of the discharge passageway is greatest at low pressure.

6.4. Results of Impedance Tests on Relief Valves

Tests were performed to measure the impedance characteristics of three different types of relief valve, these being:

a) valve 'V3'- a single stage cartridge relief valve

b) valve 'V4'- a pilot operated cartridge relief valve

c) valve 'V5'- a pilot operated relief valve.

A similar technique to that used in the restrictor valve tests was used in each case. Pressure was measured downstream of the valves in order to remove the effect of the downstream characteristics. Tests were carried out at various mean flow rates and pressure drops.

6.4.1. Valve 'V3' - Single Stage Cartridge Relief Valve

Pump 'A' was employed as the FBN source. Typical experimental overall impedance characteristics are presented in Fig. 6.24. As can be seen, there is a large degree of frequency dependence in the results, in particular at the low mean pressure conditions (Fig. 6.24(a) and (b)). The respective downstream impedance measurements are plotted in Fig. 6.25. Little variation between the downstream entry impedance characteristics is apparent at the different operating conditions. It can be seen by comparison with the overall impedance measurements that the downstream impedance is of a similar order of magnitude to the overall impedance, and hence will be a significant factor affecting the results.

The equivalent results, after allowing for the effects of vibration, contained volume and the downstream circuit, are plotted in Fig. 6.26. It can be seen that the removal of these effects greatly simplifies the form of the results, so that they correspond very closely to those obtained from the tests on the restrictor valve. Both resistive and inductive effects are apparent, and the resistive component corresponds very well to the value predicted using the equation $R_v = 2\Delta\tilde{P}/\tilde{Q}$.

These results indicate that, when considering FBN, the behaviour of this valve is very similar to that of a simple restrictor. This implies that there is insignificant vibration of the internal parts, so that, at the frequencies considered, the valve is acting as a fixed orifice. This may be due to coulomb friction effects between the valve spool and the casing, as the pressure perturbations are likely to be too small to overcome this friction.

6.4.2. Valve 'V4' - Two Stage Cartridge Relief Valve

Under certain conditions this valve was found to be unstable, with severe oscillations occurring at about 150 Hz. The effect was strongly audible, and was apparent on the measured pressure ripple waveforms. Some typical pressure ripple traces measured upstream and downstream of the valve are shown in Fig. 6.27. The conditions of Fig. 6.27(a) were such that the valve showed no signs of instability. It can be seen that a significant amount of the pressure ripple is transmitted through the valve. A high degree of high frequency noise is also apparent on this trace, due to cavitation and/or turbulence from the valve. In Fig. 6.27(b) the valve was in an unstable state. It can be seen that the upstream waveform is somewhat distorted in that there are observable differences between successive cycles. Downstream of the valve a large amplitude ($\approx$ 10 bar peak-to-peak) oscillation is apparent on the signal with a frequency of 150 Hz.

Some typical measured impedance characteristics are shown in Fig. 6.28, for different mean pressures and flows. In Figs 6.28(a) and (b), the valve was at a stable condition. The amplitude results show fair correlation with the resistance model over most of the frequency range, except for the second harmonic (350 Hz). However, the phase shows large deviations from this model, especially below 1 kHz. In all cases the phase lies between -90° and $+90^\circ$.

In Fig's 6.28(c) and (d), the valve was in an unstable state. The amplitude in these cases shows considerable deviation from the simple model, in particular in Fig. 6.28(d). The phase shows a significant advance at low frequencies. In Fig. 6.28(d) the phase at certain harmonics (175 Hz and 2100 Hz) lies well outside the range of -90° to $+90^\circ$, implying that the resistance of the valve at these harmonics is negative. This effect was observed under several other test conditions not presented here, and so is unlikely to be due to experimental error. It may instead be attributed to the instability.

A negative real part of the impedance implies a negative resistance and may cause a reflection coefficient of greater than unity (section 2.7.). Under certain conditions this may then cause instability in the system. In order to analyse this effect, the system may be represented as a block diagram, as shown in Fig. 6.29. This block diagram has one closed loop, which represents the effect of multiple reflections in the pipe. Considering this loop alone, its open loop transfer function is given by the equation:

$$GH = -\rho_S \rho_T e^{-2\gamma l} \qquad \ldots (6.37)$$

Classical control theory states that if this function encloses the (-1,0) point on the complex plane the system is unstable. If $|\rho_S| \leqslant 1$, this condition can only be attained where $|\rho_T| > 1$. Thus a negative real part of the termination impedance may cause instability, although this is dependent upon the value of $\rho_S e^{-2\gamma l}$ at that frequency. This implies that such a valve may be perfectly stable when connected to one pipe length, but unstable at the same pressure/flow conditions when connected to a different pipe length.

6.4.3. Valve 'V5' - Two Stage Relief Valve

Some representative experimental impedance results for this valve are presented in Fig. 6.30. In Figs. 6.30(a) and (c), the pulse generator was used as the fluid-borne noise source, and in Figs. 6.30(b) and (d) pump 'B' was used.

By comparison of Fig. 6.30(a) and (b), it can be seen that the correlation between the corresponding results obtained under the same test condition using the two different sources is good, being within about 1 dB and 3° in most cases. Similarly, the overall correlation is good between the results at the test condition shown in Fig. 6.30(c) and (d). However, at certain harmonics there are significant deviations between the two sets of results, in particular between 500 Hz and 700 Hz, where differences of 5 dB and 15° are apparent. It is thought that these deviations may be caused by non-linear characteristics of the valve, such as coulomb friction or stick-slip friction, so that the valve exhibits a different impedance characteristic in response to different excitations.

In terms of both amplitude and phase the correlation between the measured impedance results and the simple resistive model is very poor. Below about 1 kHz, a predominantly inductive characteristic is apparent, the amplitude increasing with frequency and the phase being positive. A resonant peak is apparent at 1 kHz for both test conditions, and at higher frequencies the phase becomes negative and the amplitude appears to remain fairly constant.

Considering Fig. 6.30(a) and (c), below 100 Hz the results show a large degree of variation with frequency. This may be a characteristic of the valve, but it may also be due to the long wavelengths at these frequencies which may cause difficulty in the accurate measurement of the impedance.

Comparison with the results of tests on two stage relief valve 'V4' yields little correlation between the two. The only observable similarity is the phase advance at frequencies below 1 kHz. Both sets of results show that the fluid-borne noise characteristics of two-stage relief valves, and presumably of many other types of pilot-operated devices, cannot be represented adequately by a simple resistive model.

6.5. Simulation of the Impedance Characteristics of Two-Stage Relief Valves

In order to obtain a more realistic model of the impedance characteristics of a two-stage relief valve than the simple resistive model, it is necessary to take into account the detailed internal structure of the valve and to consider vibration of the main stage and pilot stage components. By considering flow continuity and force balance at the pertinent points within the valve, a number of differential equations can be derived [52]. By linearisation of these equations and transformation into the frequency domain, they can be solved simultaneously and the valve impedance obtained.

The following assumptions were made in the formulation of the model:

a) perturbations were assumed to be small so that the orifice characteristics could be linearised around the mean point.

b) discontinuous effects, such as stick-slip friction and coulomb friction, were ignored.

c) fluid inertia effects were ignored, except in long 'capillary' orifices.

d) cavitation and air release effects were ignored, so that the effective bulk modulus of the fluid inside the valve was assumed to be constant.

The internal configurations of valves 'V4' and 'V5' were found to be different, so it was necessary to develop a slightly different set of equations for each valve.

6.5.1. Derivation of Mathematical Model of Valve 'V5'

A schematic diagram of the internal configuration of this valve is shown in Fig. 6.31. The measured dimensions and parameters are listed in Table 6.1.

In the following analysis, the absolute values of the state variables are represented by lower case characters (x, p_{IN} etc). The Fourier transformed variables for small perturbations about the mean condition are represented by upper case characters (X, P_{IN} etc), and the mean values at the operating point are represented by upper case characters with tildes ($\tilde{X}$, $\tilde{P}_{IN}$ etc).

1) Main stage force balance

$$m_{eff\,1}\frac{d^2x}{dt^2}+b_{eff\,1}\frac{dx}{dt}+k_{eff\,1}x = p_{IN}A_1-p_3A_p-F_1 \qquad \ldots(6.38)$$

where

x = main stage poppet lift

$m_{eff\,1}$ = effective mass of main stage poppet. This was assumed to be equal to the mass of the poppet plus one third of the spring mass.

$b_{eff\,1}$ = effective damping coefficient of main stage poppet

$k_{eff\,1}$ = effective spring stiffness, including flow force effects

$$= k_{s\,1}+\pi d_1(p_{IN}-p_3)\sin 2\theta_1\,(c_Q-1/2) \qquad \ldots(6.39)$$

$k_{s\,1}$ = spring stiffness

θ_1 = main stage poppet angle

F_1 = precompression of spring with poppet closed

2) Flow continuity equation at inlet

$$\frac{V_1}{B}\frac{dp_{IN}}{dt} = q_{IN} - q_1 - q_L - A_1\frac{dx}{dt} \qquad \ldots(6.40)$$

where

$$q_1 = \pi c_Q d_1 x \sin\theta_1 \left\{\frac{2(p_{IN} - p_{OUT})}{\rho}\right\}^{1/2} \qquad \ldots(6.41)$$

It is assumed here that the outlet pressure p_{OUT} is zero.

The steady state flow rate q_L is given by the equation

$$q_L = c_{Q1} A_3 \left\{\frac{2(p_{IN} - p_2)}{\rho}\right\}^{1/2} \qquad \ldots(6.42)$$

where the flow coefficient c_{Q1} is a function of the Reynold's number through the orifice, and of the length to diameter ratio of the orifice [51].

In the dynamic analysis, however, the fluid inertia in the long orifice must also be considered. This can be represented by an inductive term, such that

$$p_{IN} - p_2 = \frac{\rho q_L^2}{2c_{Q1}^2 A_3^2} + \frac{\rho l_3}{A_3}\frac{dq_L}{dt} \qquad \ldots(6.43)$$

3) Flow continuity equation at rear end of main stage poppet

$$\frac{V_3}{B}\frac{dp_3}{dt} = A_p\frac{dx}{dt} - q_3 \qquad \ldots(6.44)$$

The mean value of q_3 is zero, so laminar flow is assumed through the long orifice. Considering fluid inertia in the orifice, the pressure drop is described by the equation:

$$p_3 - p_2 = \frac{128\mu l_4}{\pi d_4^4} q_3 + \frac{4\rho l_4}{\pi d_4^2}\frac{dq_3}{dt} \qquad \ldots(6.45)$$

4) Flow continuity equation for pilot stage

$$\frac{V_2}{B}\frac{dp_2}{dt} = q_L + q_3 - q_2 - A_2\frac{dy}{dt} \qquad \ldots (6.46)$$

where

y = pilot stage poppet lift.

θ_2 = pilot stage poppet angle.

$$q_2 = \pi c_Q d_2 y \sin\theta_2 \left\{\frac{2(p_2 - p_{OUT})}{\rho}\right\}^{1/2} \qquad \ldots (6.47)$$

5) Force balance equation for pilot stage

$$m_{eff\,2}\frac{d^2y}{dt^2} + b_{eff\,2}\frac{dy}{dt} + k_{eff\,2}y = (P_2 - P_{OUT} - P_{cr})A_2 \qquad \ldots (6.48)$$

where

$m_{eff\,2}$ = effective mass of pilot stage poppet.

$b_{eff\,2}$ = effective damping coefficient of pilot stage poppet.

$k_{eff\,2}$ = effective spring stiffness, including flow force effects

$$= k_{s2} + \pi d_2(p_2 - p_3)\sin 2\theta_2\,(c_Q - 1/2) \qquad \ldots (6.49)$$

k_{s2} = spring stiffness.

P_{cr} = cracking pressure of valve.

In order to solve the above equations, it is necessary to linearise them for small perturbations about the operating point. Applying the Fourier transformation $d/dt = j\omega$, the dynamic equations become:

From equation (6.38):

$$(-m_{eff\ 1}\omega^2+b_{eff\ 1}j\omega+k_{eff\ 1})X = P_{IN}A_1 \qquad \ldots (6.50)$$

From equation (6.40):

$$A_1 j\omega X - Q_{IN} + Q_1 + Q_L = 0 \qquad \ldots (6.51)$$

From equation (6.43):

$$P_{IN} - P_2 = \left[\frac{\rho\tilde{Q}_L}{c_{D1}^2 A_3^2} + \frac{\rho l_3}{A_3} j\omega\right] Q_L \qquad \ldots (6.52)$$

From equation (6.41):

$$Q_1 = c_1 X + c_2 P_{IN} \qquad \ldots (6.53)$$

$$c_1 = \frac{\partial q_1}{\partial x} = \pi c_Q d_1 \sin\theta_1 \left\{\frac{2\tilde{P}_{IN}}{\rho}\right\}^{1/2} \qquad \ldots (6.54)$$

$$c_2 = \frac{\partial q_1}{\partial p_{IN}} = \pi c_Q d_1 \tilde{X} \sin\theta_1 \left\{\tilde{P}_{IN}\rho\right\}^{-1/2} \qquad \ldots (6.55)$$

From equation (6.44):

$$A_p j\omega X - Q_3 - \frac{V_3}{B} j\omega P_3 = 0 \qquad \ldots (6.56)$$

From equation (6.45):

$$P_3 - P_2 = \left[\frac{128\mu l_4}{\pi d_4^4} + \frac{4\rho l_4}{\pi d_4^2} j\omega\right] Q_3 \qquad \ldots (6.57)$$

From equation (6.46):

$$\frac{V_2}{B} j\omega P_2 = Q_L + Q_3 - Q_2 - A_2 j\omega Y \qquad \ldots (6.58)$$

From equation (6.47):

$$Q_2 = c_3 Y + c_4 P_2 \qquad \ldots (6.59)$$

$$c_3 = \frac{\partial q_2}{\partial y} = \pi c_Q d_2 \sin\theta_2 \left\{ \frac{2\tilde{P}_2}{\rho} \right\}^{1/2} \qquad \ldots (6.60)$$

$$c_4 = \frac{\partial q_2}{\partial p_2} = \pi c_Q d_2 \tilde{Y} \sin\theta_2 \left\{ \tilde{P}_2 \rho \right\}^{-1/2} \qquad \ldots (6.61)$$

From equation (6.48):

$$(-m_{eff\,2}\omega^2 + b_{eff\,2} j\omega + k_{eff\,2}) Y = P_2 A_2 \qquad \ldots (6.62)$$

The steady state values of the variables need to be determined before the above equations can be solved. These values can be calculated from equations (6.38) to (6.49) by ignoring dynamic terms (those containing $j\omega$ or $(j\omega)^2$).

Thus, in the steady state, from equation (6.41):

$$\tilde{Q}_1 = \pi c_Q d_1 \tilde{X} \sin\theta_1 \left\{ \frac{2\tilde{P}_{IN}}{\rho} \right\}^{1/2} \qquad \ldots (6.63)$$

from equation (6.40):

$$\tilde{Q}_1 = \tilde{Q}_{IN} - \tilde{Q}_L \qquad \ldots (6.64)$$

from equation (6.38):

$$k_{eff\,1}\tilde{X} = \tilde{P}_{IN} A_1 - \tilde{P}_3 A_p \qquad \ldots (6.65)$$

from equation (6.44):

$$\tilde{Q}_3 = 0, \text{ hence } \tilde{P}_3 = \tilde{P}_2 \qquad \ldots (6.66)$$

from equation (6.42):

$$\tilde{Q}_L = c_{Q1} A_3 \left\{ \frac{2(\tilde{P}_{IN} - \tilde{P}_2)}{\rho} \right\}^{1/2} \qquad \ldots (6.67)$$

where c_{Q1} is a function of the Reynold's number through the orifice, and hence of the flow rate $\tilde{Q}_L$.

From equations (6.46) and (6.47):

$$\tilde{Q}_2 = \tilde{Q}_L = \pi c_Q d_2 \tilde{Y} \sin\theta_2 \left\{ \frac{2\tilde{P}_2}{\rho} \right\}^{1/2} \qquad \ldots (6.68)$$

An iterative method was used for the solution of the steady state simultaneous equations (6.63) to (6.68). The dynamic equations (6.50) to (6.62) were then solved simultaneously using the method of Gaussian elimination, and the impedance calculated as the ratio p_{IN}/q_{IN}. This was performed for a range of frequencies. The damping factors for the main and pilot stages, $b_{eff\,1}$ and $b_{eff\,2}$, could not be measured easily and were ignored in the simulations. The upstream volume V_1 was assumed to be zero, to correspond to the experimental results where the impedance was referred inside the valve.

6.5.2. Simulation Results for Valve 'V5'

Simulated valve impedance results, using the parametric data listed in table 1, are compared with experimental results in Fig. 6.32. Qualitatively, the experimental results and the simulations show some similar features. At low frequencies, the impedance increases with frequency with a phase advance, and there is a resonance at about 1 kHz above which the amplitude falls and the phase becomes negative. Quantitatively, however, the correlation is less good, with errors of up to 10 dB and 60°.

6.5.3. Simulation Results for Valve 'V4'

The internal configuration of this valve differed slightly from that of valve 'V5', and is shown schematically in Fig. 6.33. This gave rise to a different set of describing equations, but the simulation technique was the same and will not be described in detail.

Simulation results are compared with the corresponding experimental results in Fig. 6.34. As can be seen, the correlation is rather poor, in terms of both the amplitude and phase. At high frequency, between 3 kHz and 4 kHz, a sharp anti-resonant trough is apparent in the simulated impedance amplitude in each case. Corresponding to this trough, the simulated phase exceeds the bounds of -90° to $+90^{\circ}$ in this region, indicating possible instability at this point. Insufficient high frequency data were available to see this feature experimentally. However, a similar effect can be observed in Fig. 6.34(d) at the lower frequency of 2 kHz.

6.5.4. Relief Valve Mathematical Modelling - Conclusions

It can be seen from the above results that, even with the detailed dynamic valve model described, it is very difficult or impossible to obtain good correlation between experiment and theory. The experimental results seem to exhibit a more complicated frequency response, in particular at low frequency. It is thought that this discrepancy may be due, to a large extent, to discontinuities such as stick-slip friction or coulomb friction on the poppets. Further work would be necessary in order to analyse the dynamic characteristics of pilot-operated relief valves in greater detail, in which it would be desirable to record the experimental pressures in the internal chambers of the valve, as well as the movement of the poppets.

		Main Stage	Pilot Stage
Poppet mass		65 g	4 g
Spring mass		8 g	10 g
Effective mass	m_{eff}	68 g	7 g
Damping constant	b_{eff}	0	0
Spring stiffness	k_s	10.4 kN/m	270 kN/m
Seat diameter	d	20 mm	5 mm
Bore diameter	d_p	22 mm	
Seat angle	θ	30°	20°
Orifice length	l_3, l_4	4 mm	
Orifice diameter	d_3, d_4	1.0 mm	
Volume	V_1	0	
Volume	V_2	0.5 cm^3	
Volume	V_3	3.2 cm^3	
Bulk Modulus	B	10,000 bar	

Table 6.1 Two Stage Relief Valve 'V5' - Physical Parameters

		Main Stage	Pilot Stage
Effective mass	m_{eff}	15 g	6 g
Damping constant	b_{eff}	0	0
Spring stiffness	k_s	10 kN/m	42 kN/m
Seat diameter	d	20 mm	5 mm
Bore diameter	d_p	22 mm	
Seat angle	θ	40°	34°
Orifice length	l_3	2 mm	
Orifice diameter	d_3	0.4 mm	
Orifice length	l_4	2 mm	
Orifice diameter	d_4	0.4 mm	
Volume	V_1	0	
Volume	V_2	2.0 cm^3	
Bulk Modulus	B	10,000 bar	

Table 6.2 Two Stage Relief Valve 'V4' - Physical Parameters

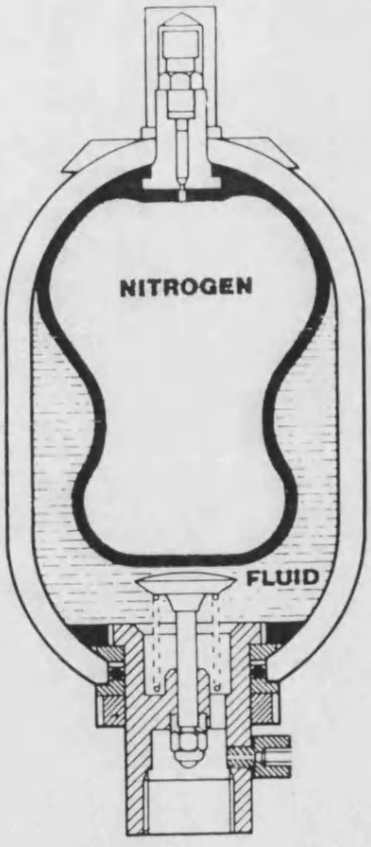

Fig. 6.1 (a) Cross Section of Accumulator

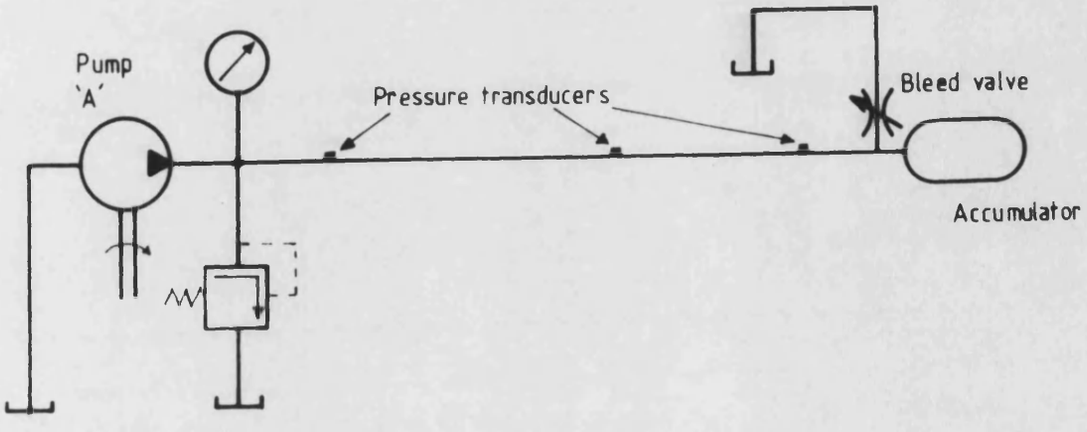

Fig. 6.1 (b) Experimental Circuit used in Accumulator Tests

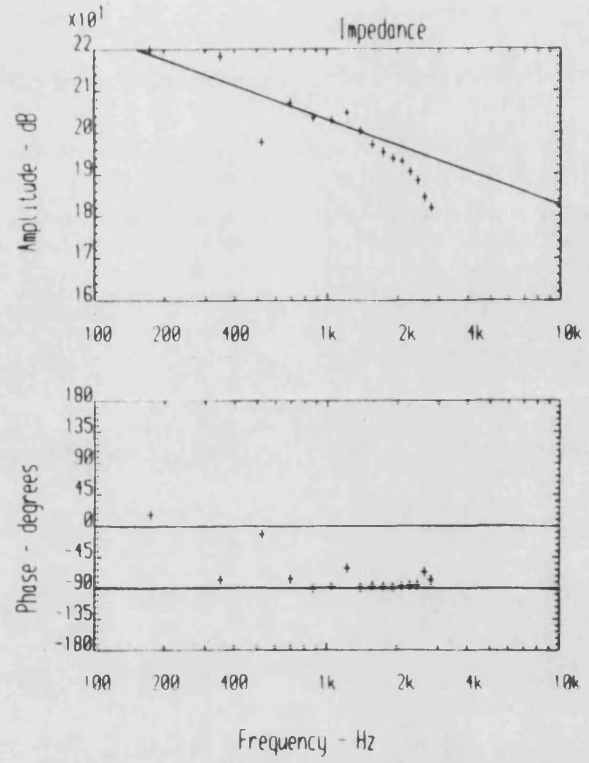

(a) Below precharge pressure

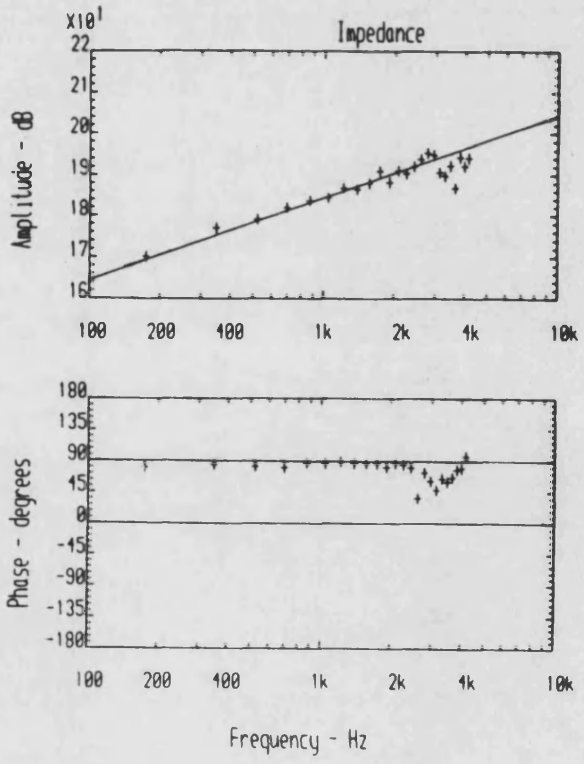

(b) Above precharge pressure

Fig. 6.2 Experimental Accumulator Impedance Results using Pump 'A' as Source of FBN

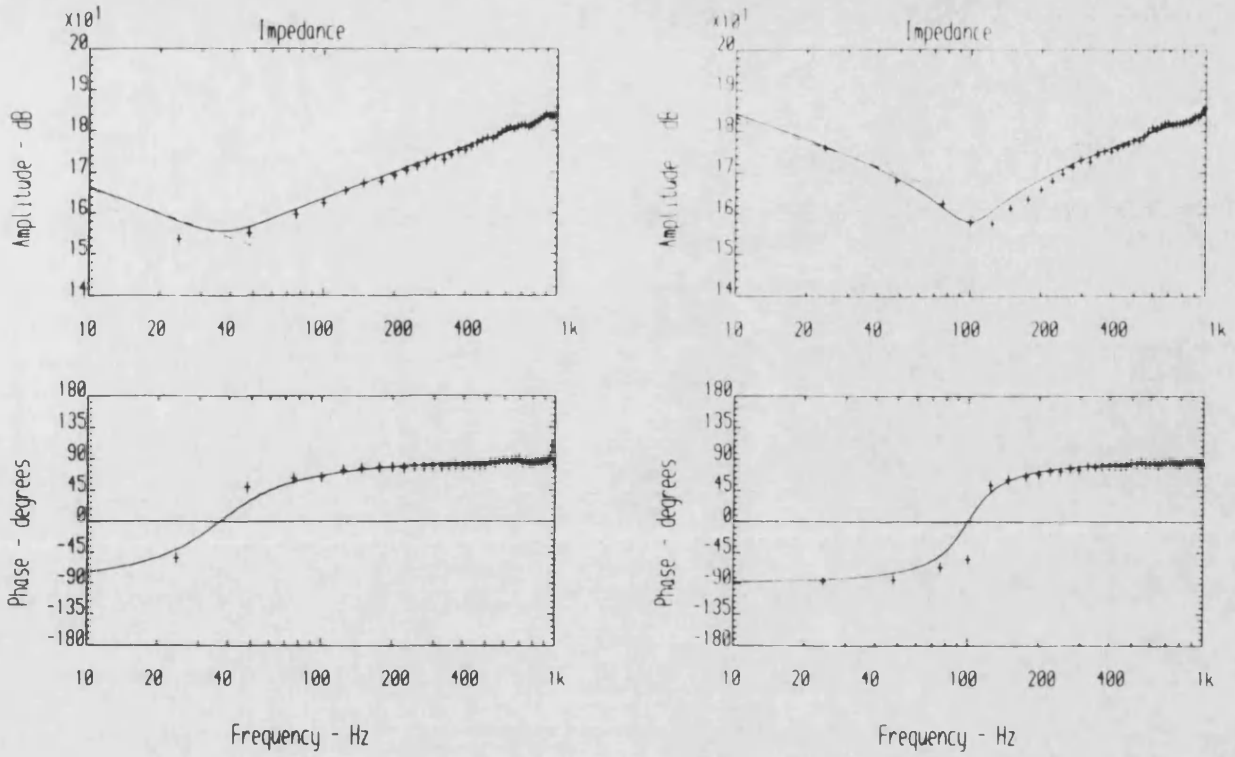

(a) $\tilde{P}$ =45bar; P_{Pc} =22bar

(b) $\tilde{P}$ =115bar; P_{Pc} =22bar

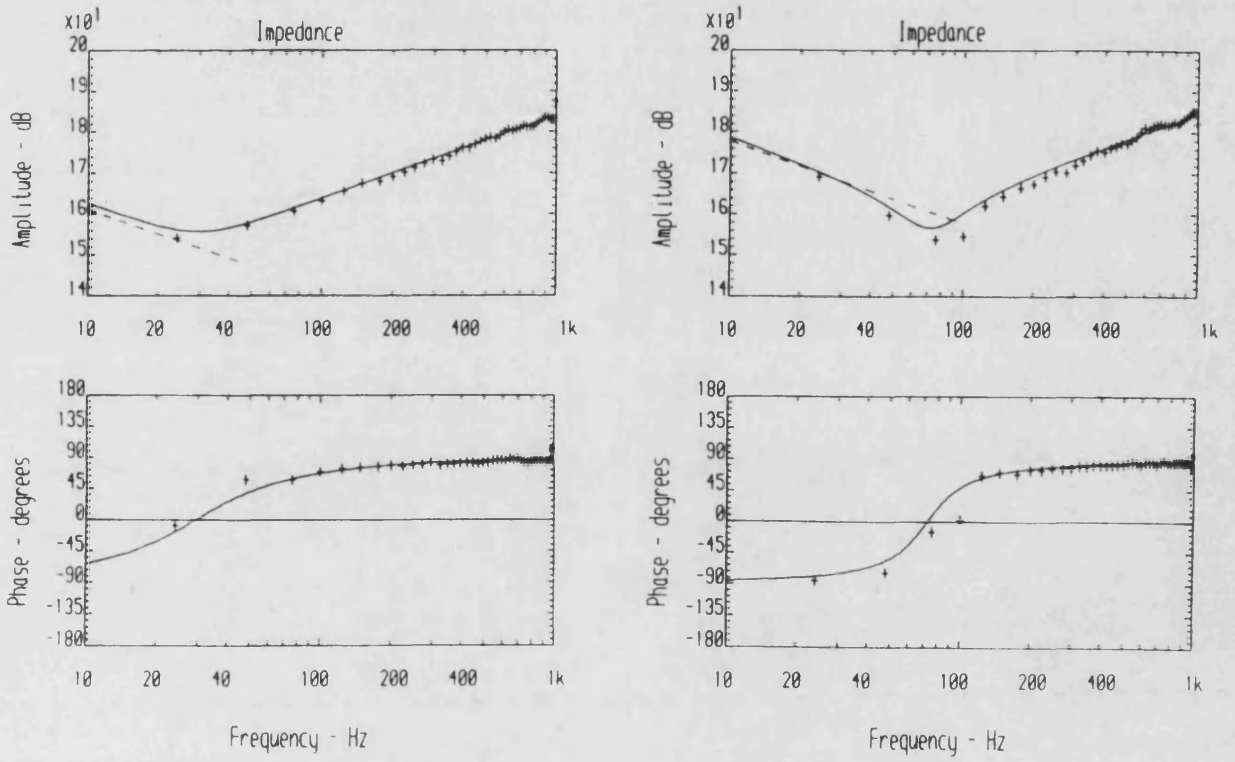

(c) $\tilde{P}$ =45bar; P_{Pc} =40bar

(d) $\tilde{P}$ =111bar; P_{Pc} =40bar

– – – – – Theoretical capacitive impedance

Fig. 6.3 Experimental Accumulator Impedance Results using Pulse Generator as Source of FBN

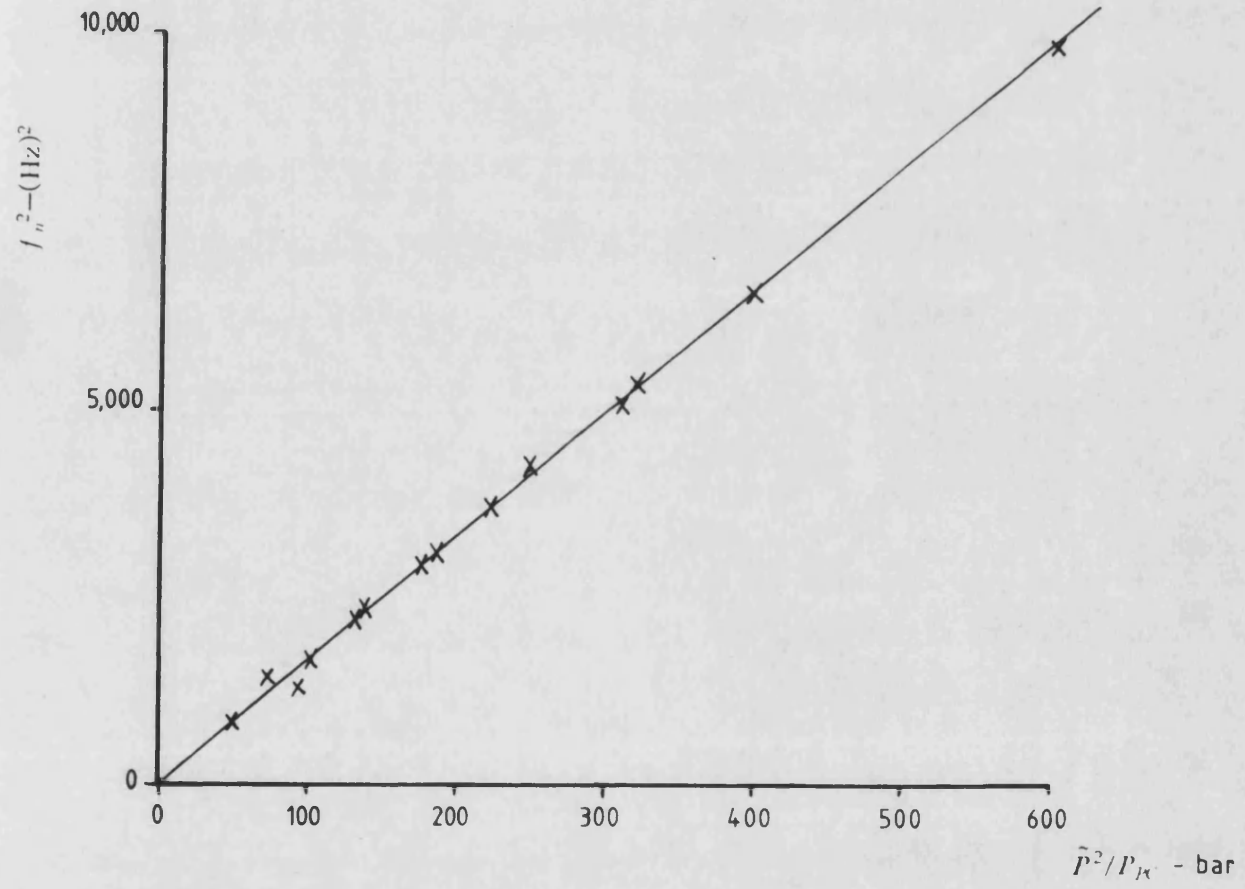

Fig. 6.4 Relationship between (natural frequency)^2 and $\tilde{P}^2/P_{jx}$ for Accumulator

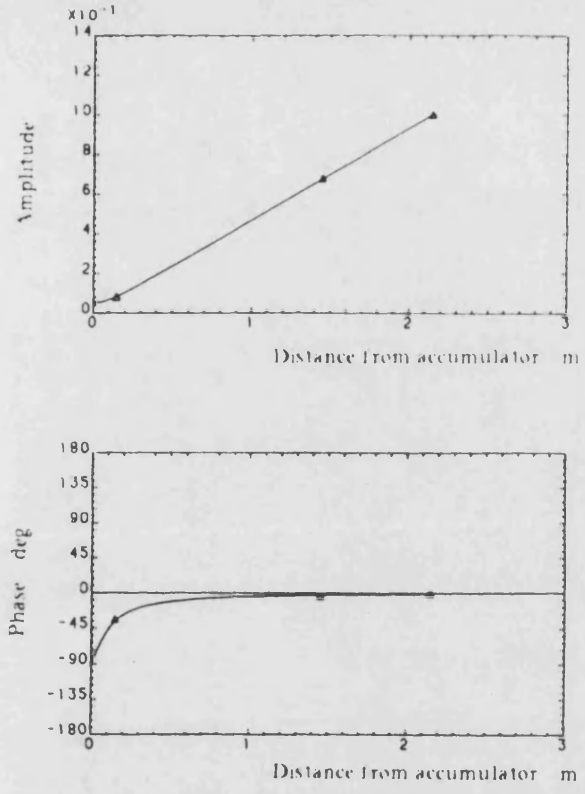

(a) Harmonic no. 1: 25 Hz

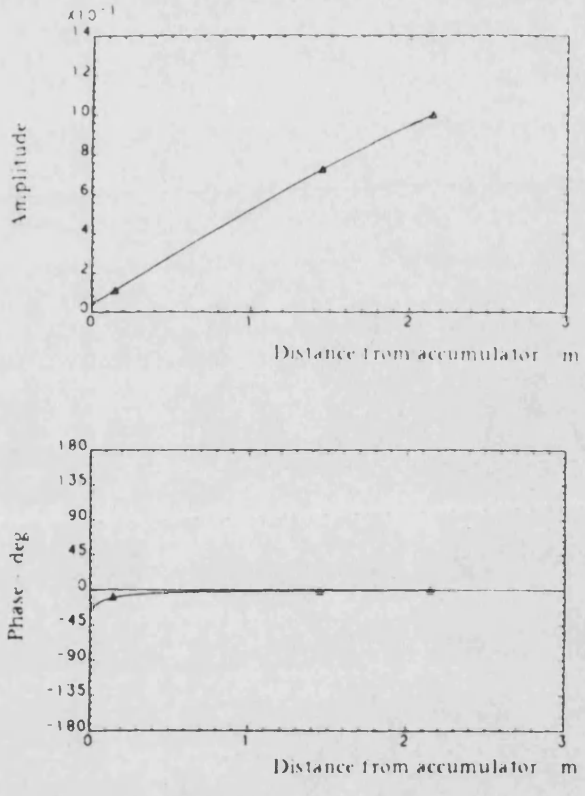

(b) Harmonic no. 3: 75 Hz

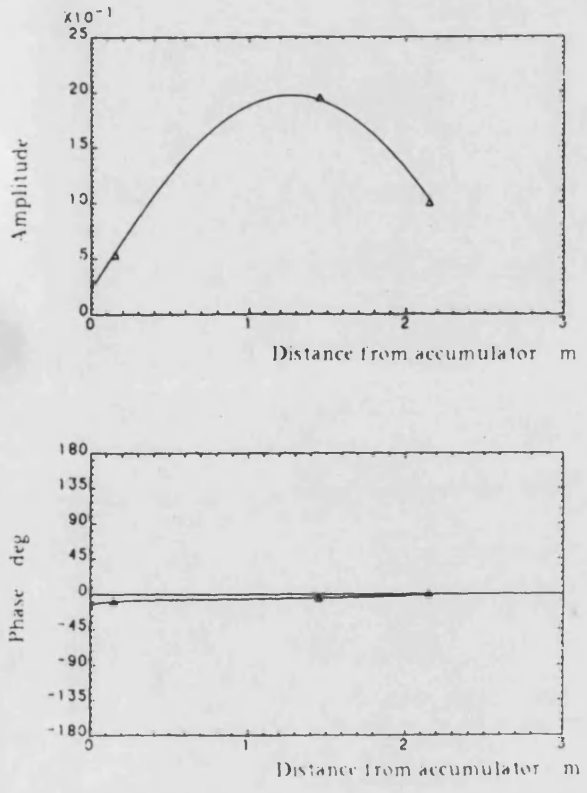

(c) Harmonic no. 10: 250 Hz

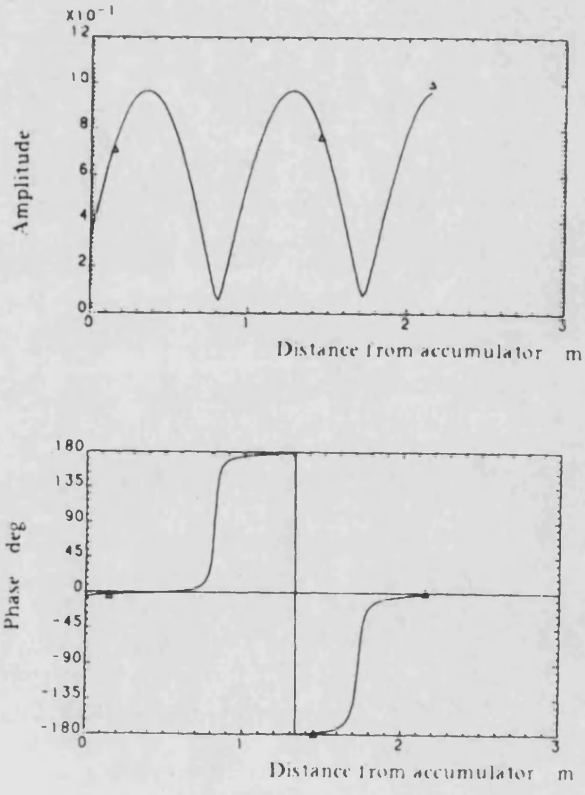

(d) Harmonic no. 30: 750 Hz

Fig. 6.5 Representative Pressure Ripple Transfer Function Measurements and Standing Wave Profiles, Mean Pressure above Precharge Pressure

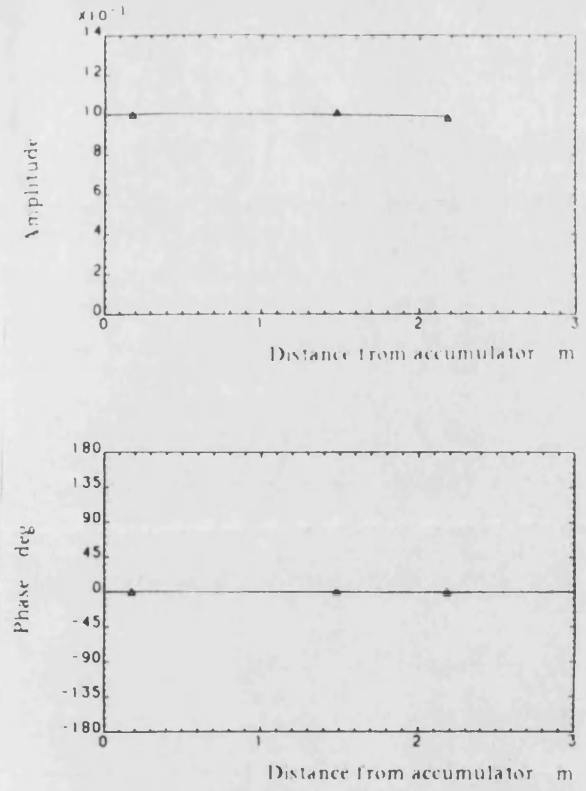

(a) Harmonic no. 1: 25 Hz

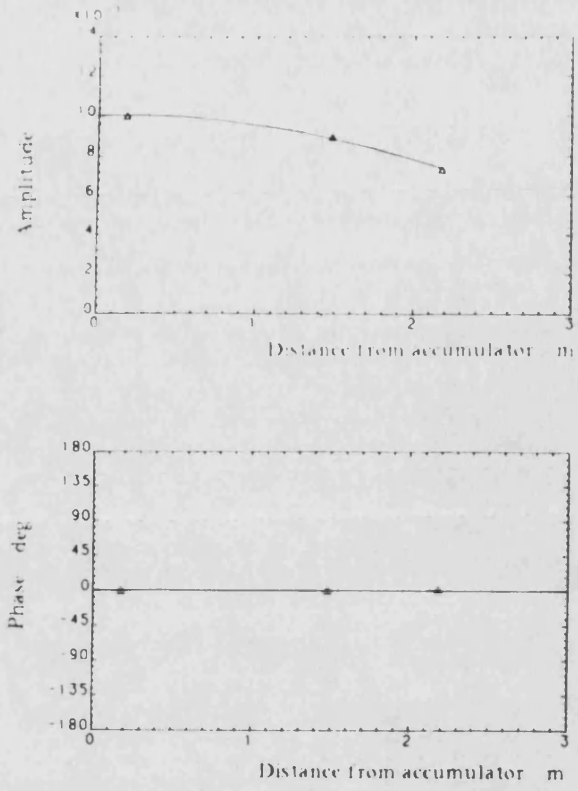

(b) Harmonic no. 3: 75 Hz

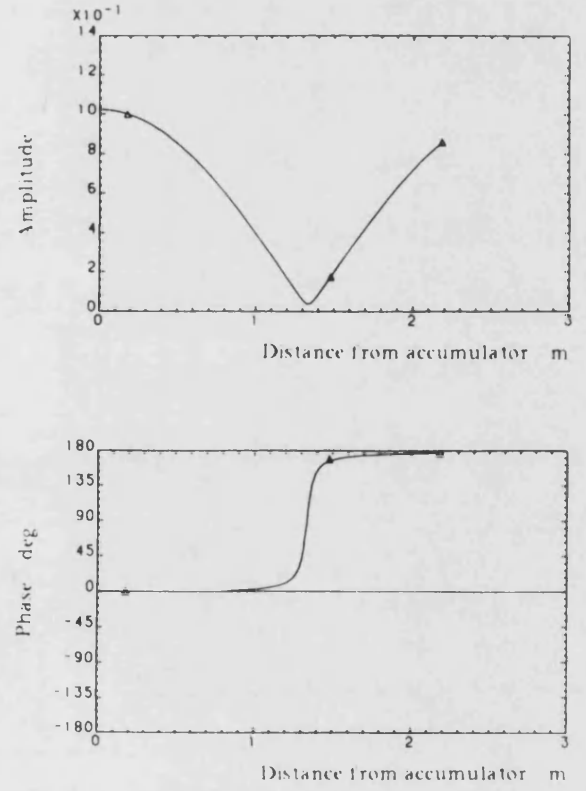

(c) Harmonic no. 10: 250 Hz

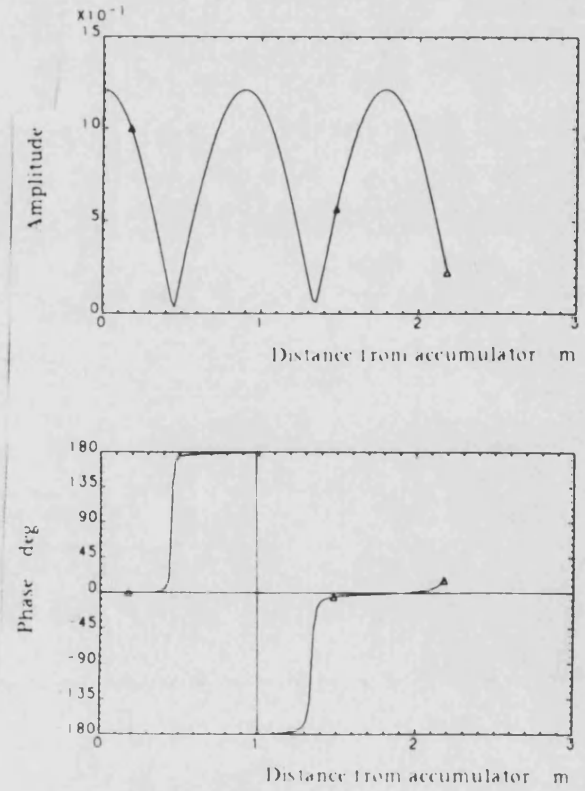

(d) Harmonic no. 30: 750 Hz

Fig. 6.6 **Representative Pressure Ripple Transfer Function Measurements and Standing Wave Profiles, Mean Pressure below Precharge Pressure**

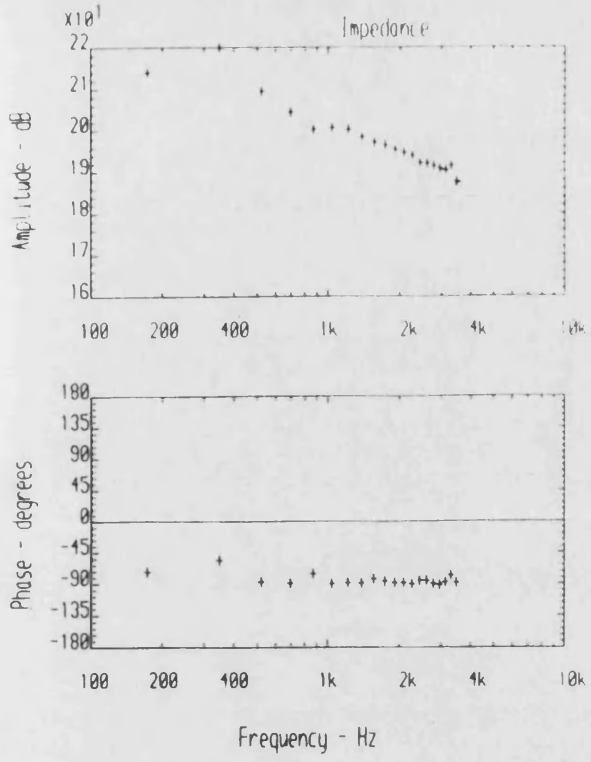

(a) 100 bar 0.0 l/s

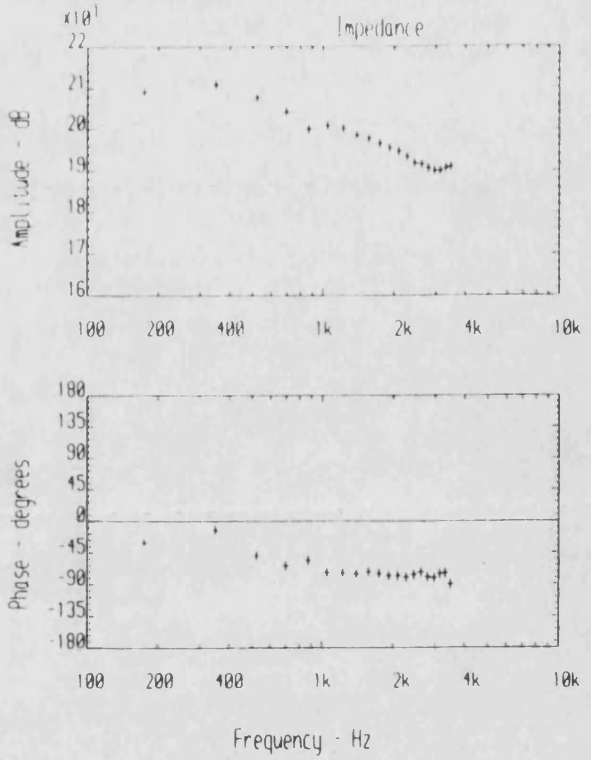

(b) 100 bar 0.4 l/s

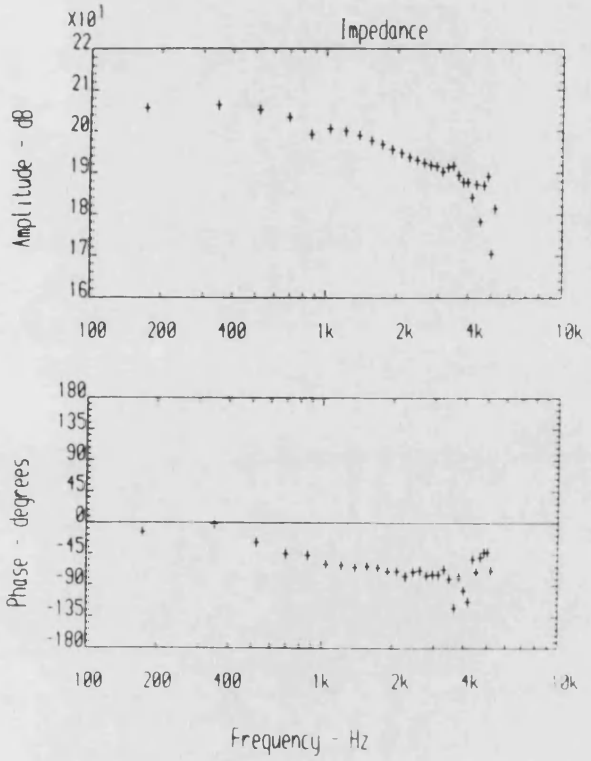

(c) 100 bar 0.8 l/s

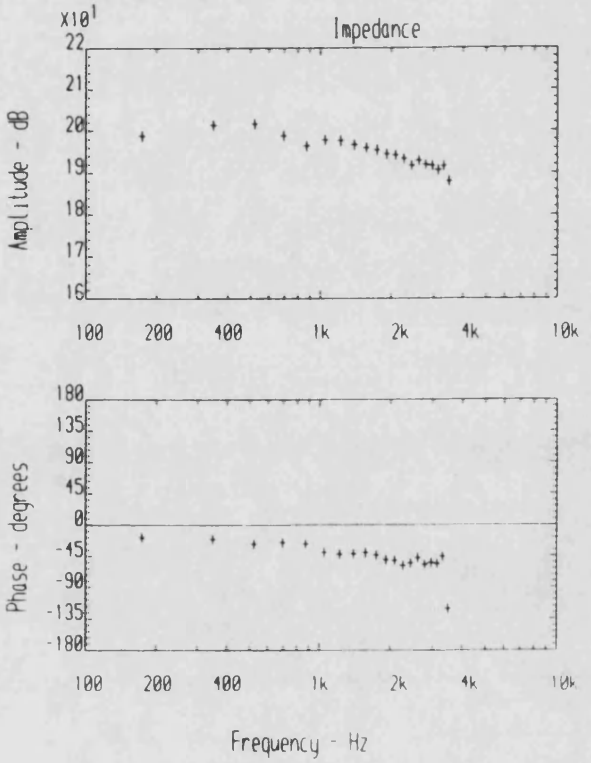

(d) 50 bar 0.8 l/s

Fig. 6.7 Experimental Impedance Characteristics - Needle Valve 'V1'

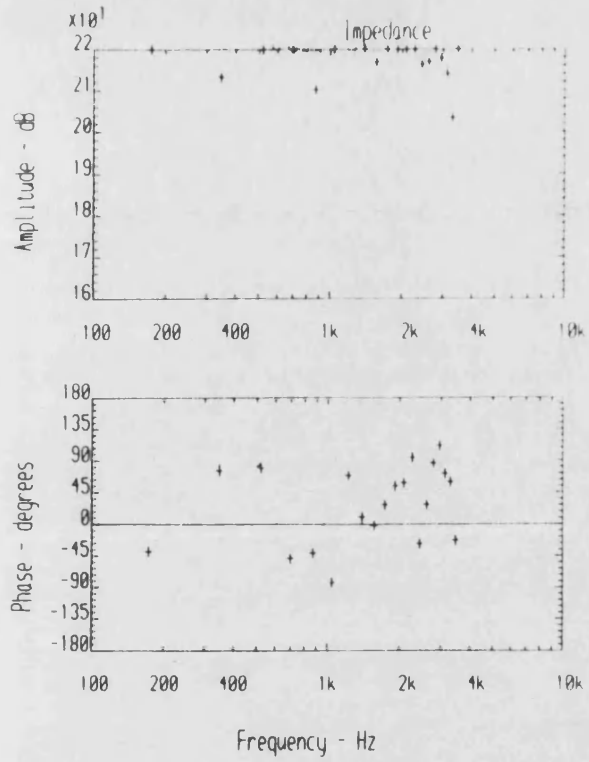

(a) 100 bar 0.0 l/s

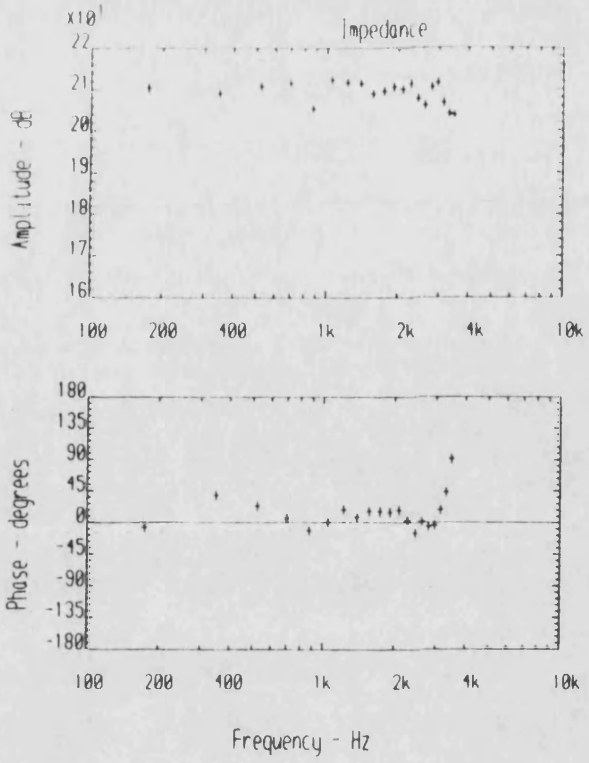

(b) 100 bar 0.4 l/s

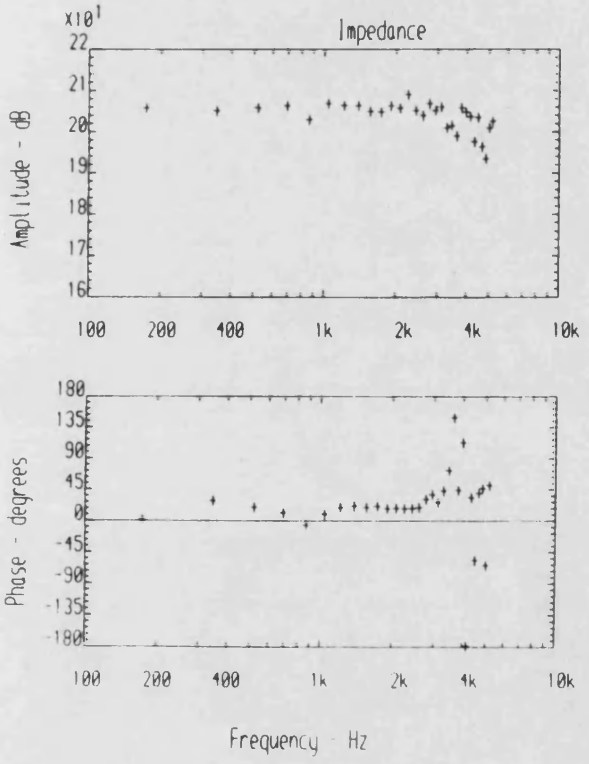

(c) 100 bar 0.8 l/s

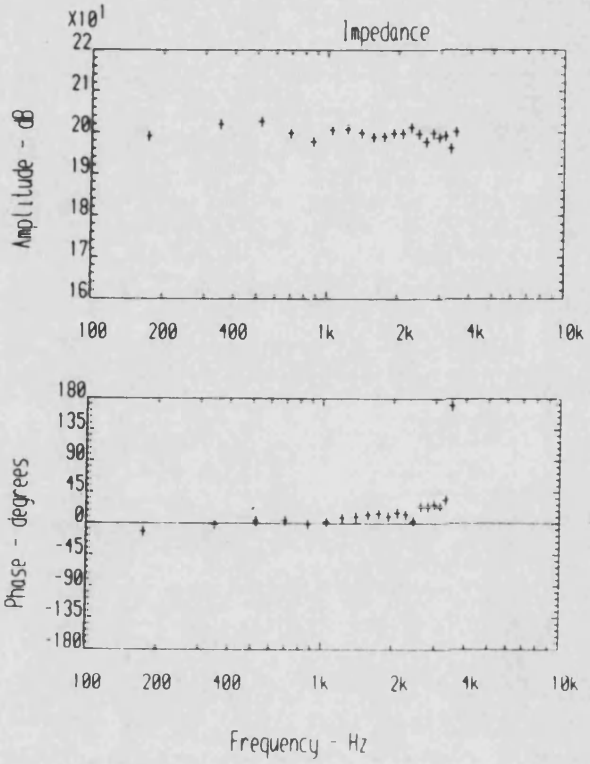

(d) 50 bar 0.8 l/s

Fig. 6.8 **Experimental Impedance Characteristics - Needle Valve 'V1', Zero Effective Volume**

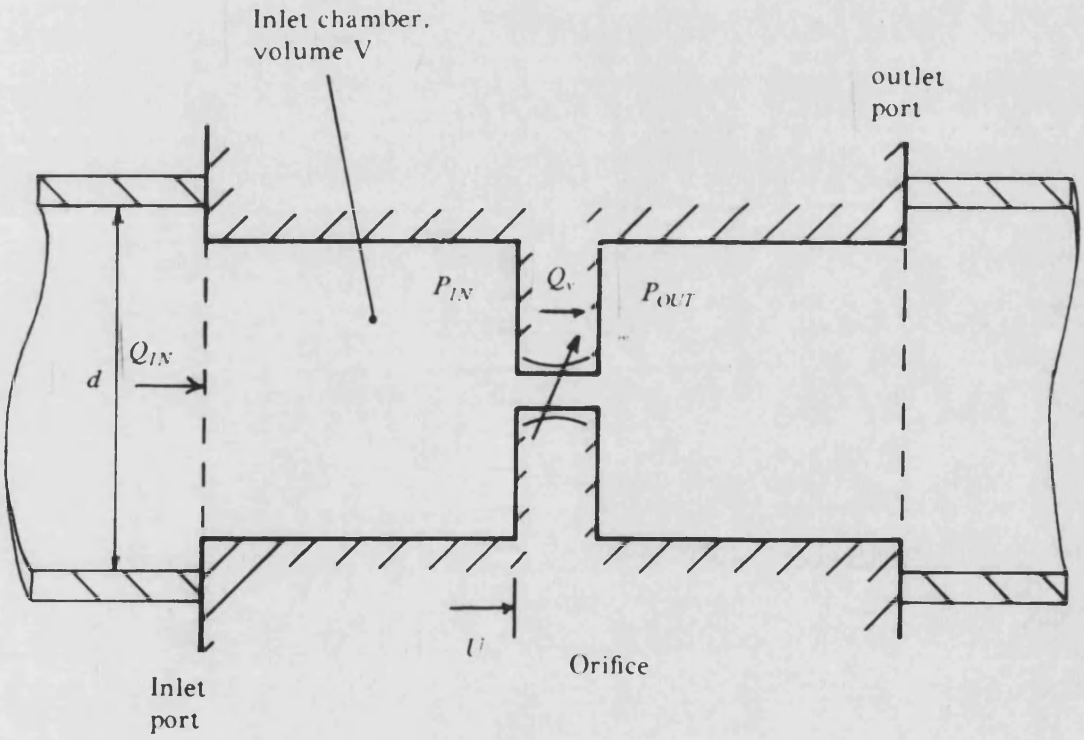

Fig. 6.9 Comprehensive Restrictor Valve Model

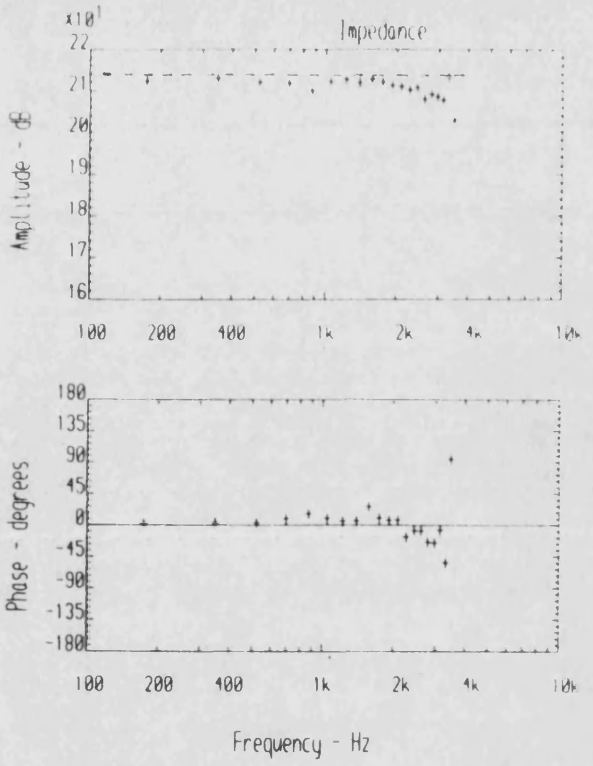

(a) 100 bar 0.4 l/s

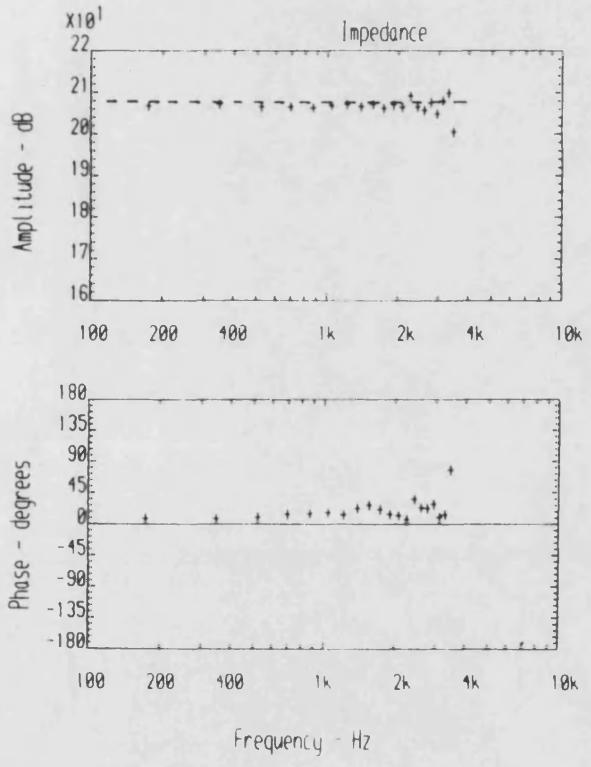

(b) 100 bar 0.8 l/s

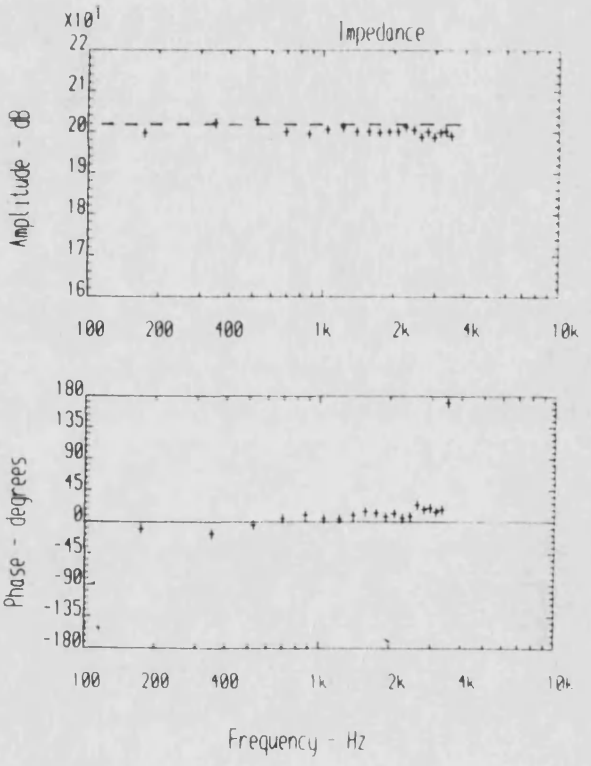

(c) 50 bar 0.8 l/s

- - - - - - steady state resistance (= $2\Delta\tilde{P}/\tilde{Q}$)

Fig. 6.10 Experimental Impedance Characteristics - Needle Valve 'V1', Impedance of Closed Valve Subtracted from Results

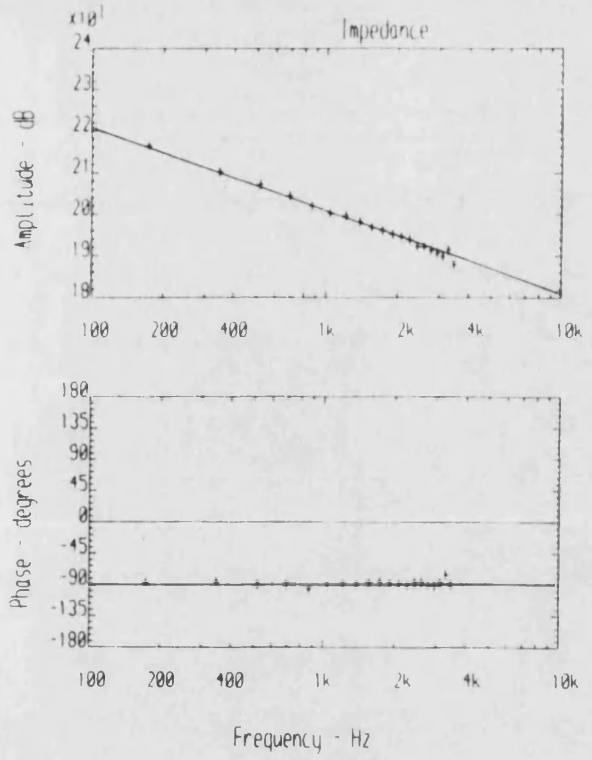

(a) 100 bar 0.0 l/s

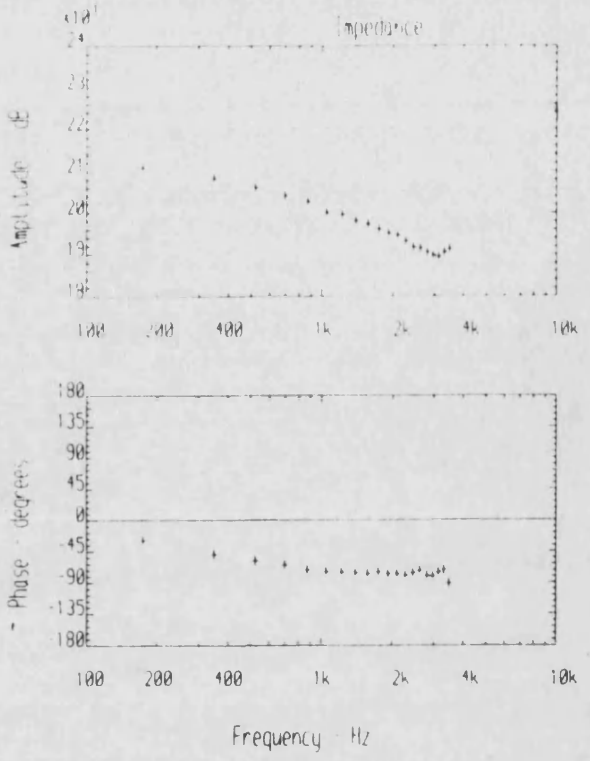

(b) 100 bar 0.4 l/s

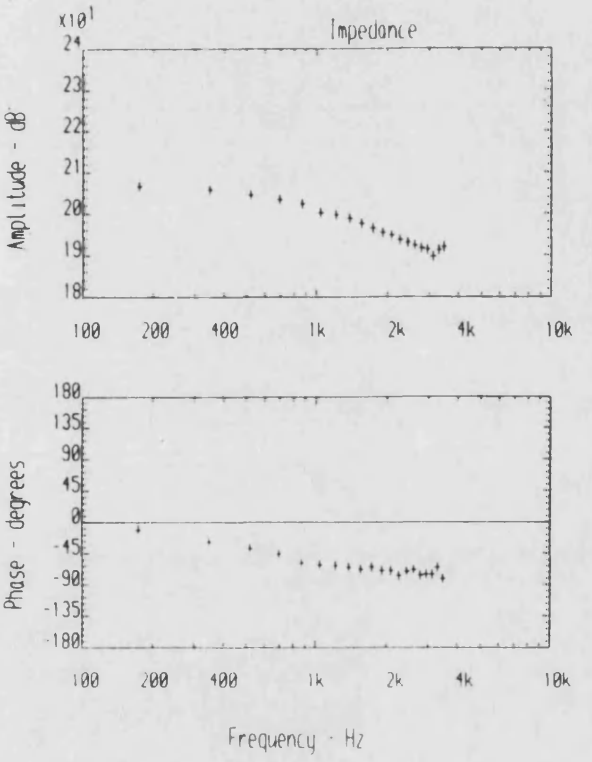

(c) 100 bar 0.8 l/s

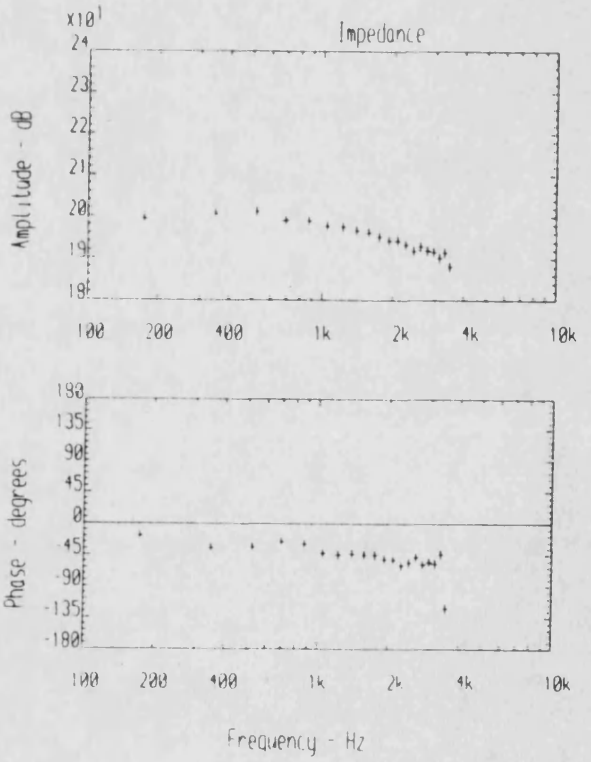

(d) 50 bar 0.8 l/s

Fig. 6.11 **Experimental Impedance Characteristics - Needle Valve 'V1', Vibration Measured and Allowed for**

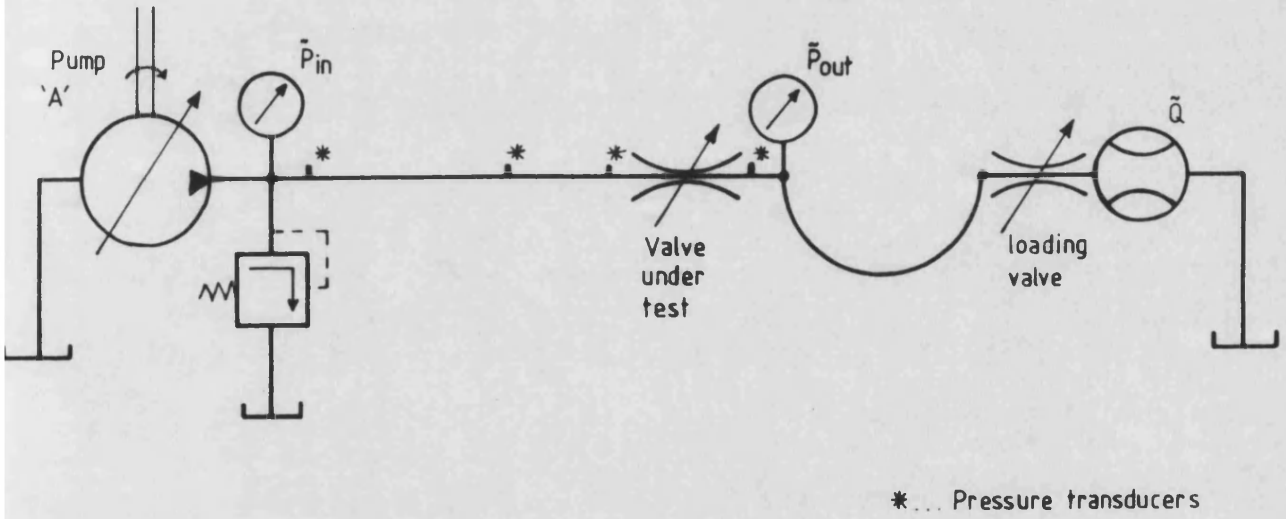

Fig. 6.12 Experimental Circuit for Measuring Valve Characteristics under Low Flow/Pressure Drop Conditions

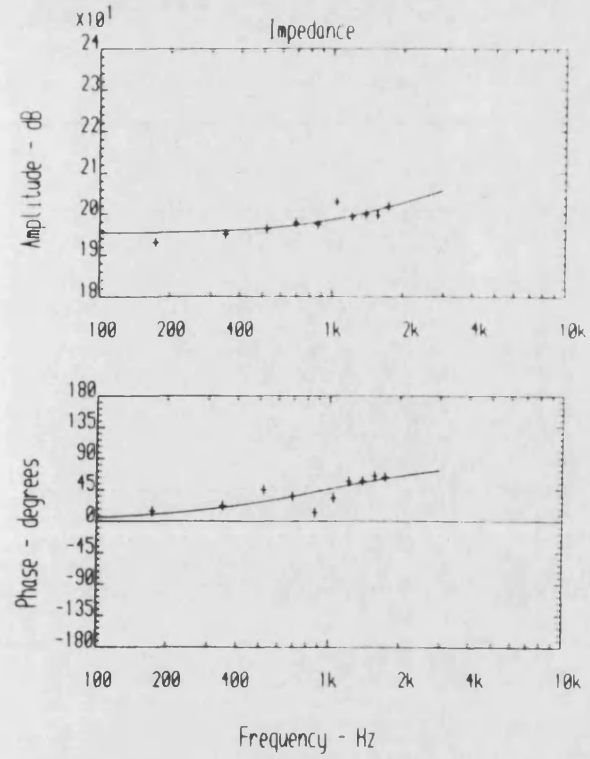

(a) 0 bar pressure drop, 0.0 l/s

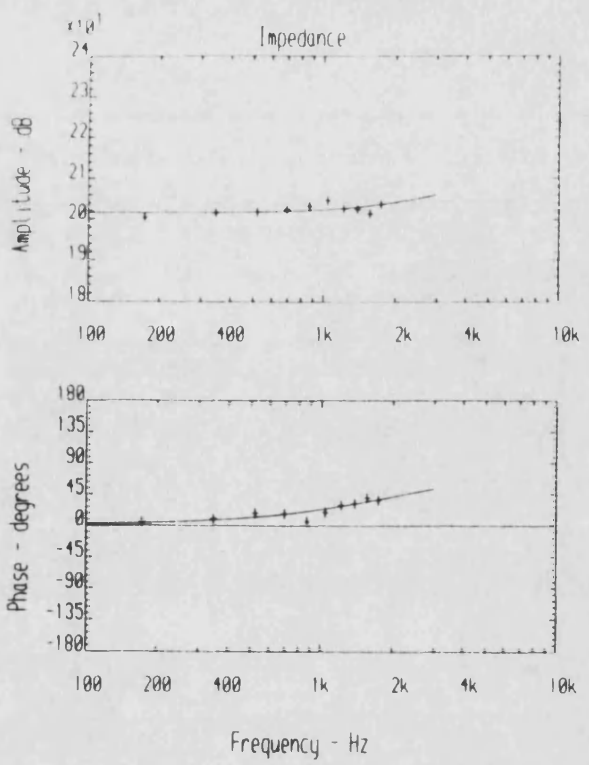

(b) 17 bar pressure drop, 0.23 l/s

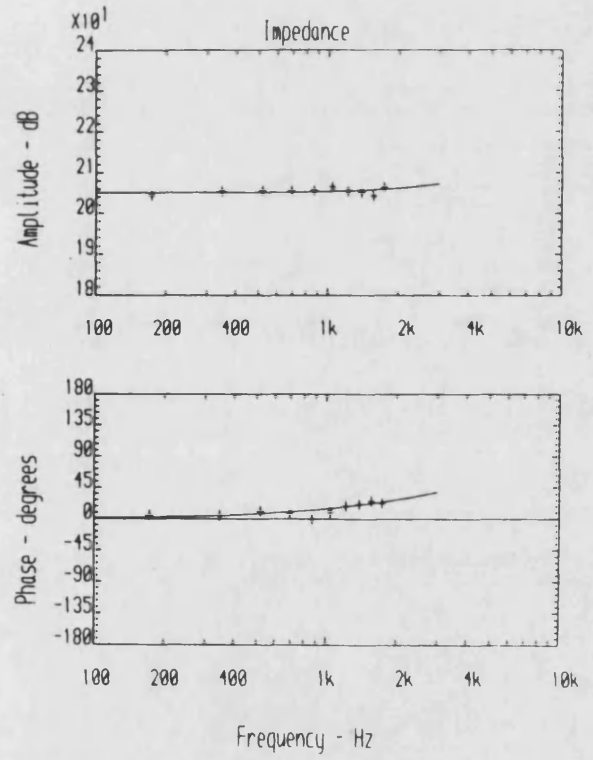

(c) 45 bar pressure drop, 0.44 l/s

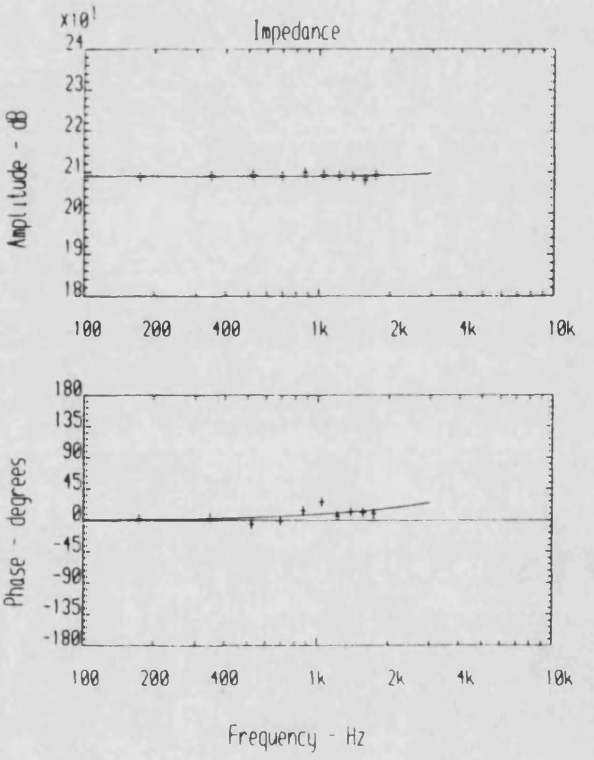

(d) 86 bar pressure drop, 0.64 l/s

Fig. 6.13 **Typical Needle Valve Impedance Characteristics at a Constant Valve Opening**

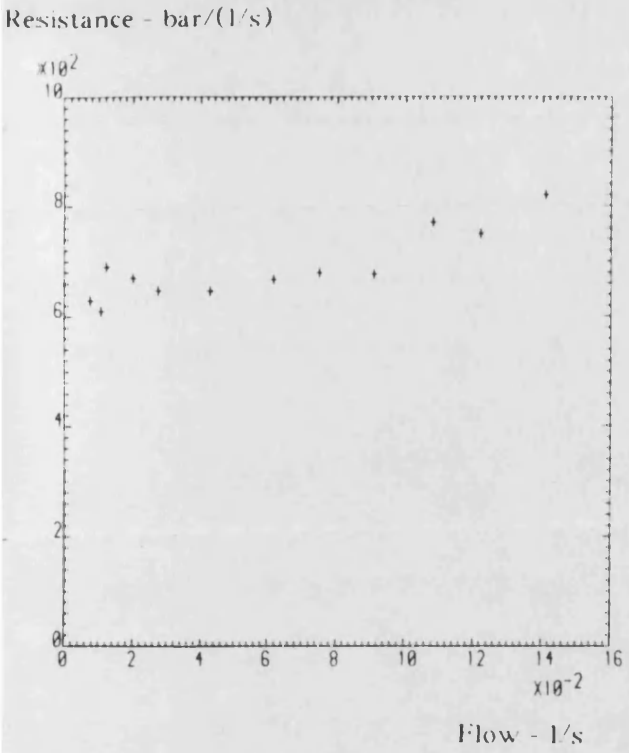

(a) Valve lift = 0.11 mm

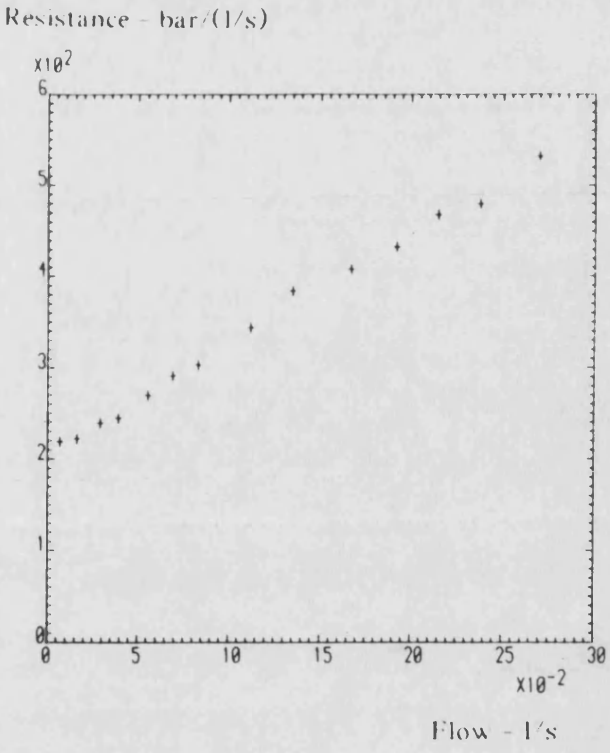

(b) Valve lift = 0.18 mm

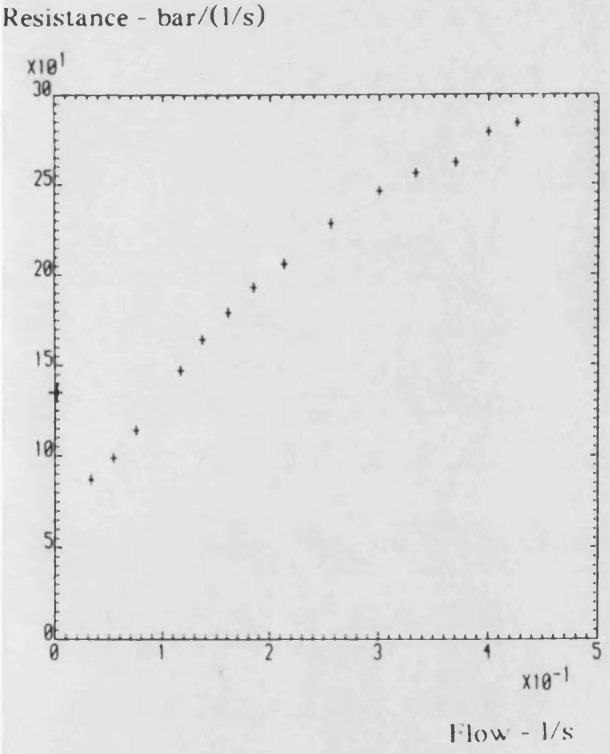

(c) Valve lift = 0.24 mm

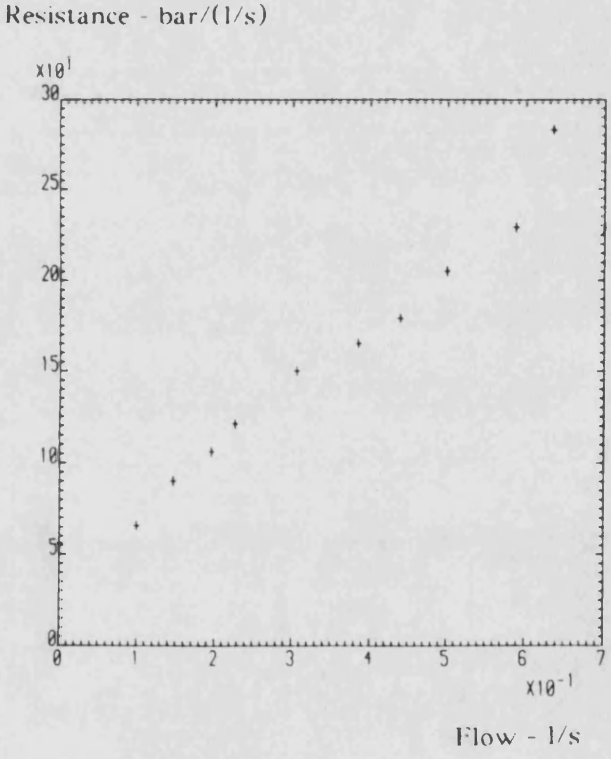

(d) Valve lift = 0.36 mm

Fig. 6.14 Relationships between Measured Valve Resistance and Flow Rate

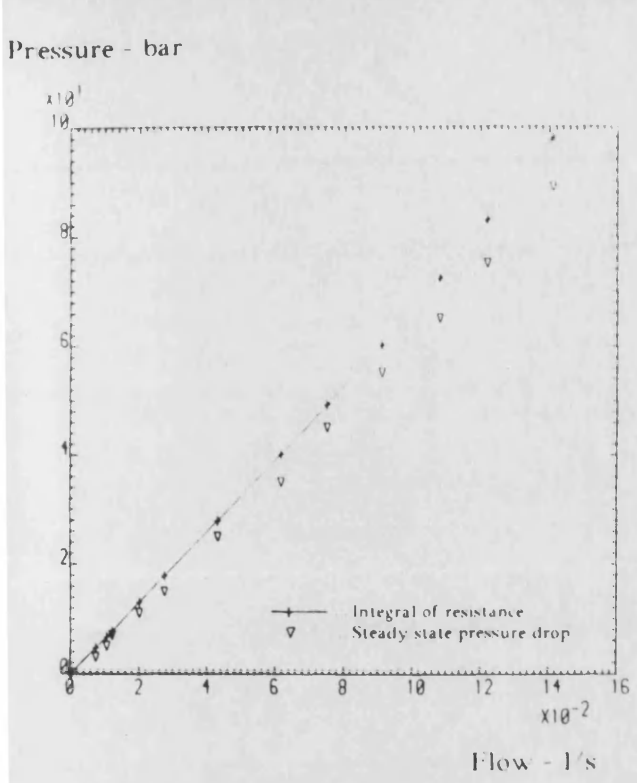

(a) Valve lift = 0.11 mm

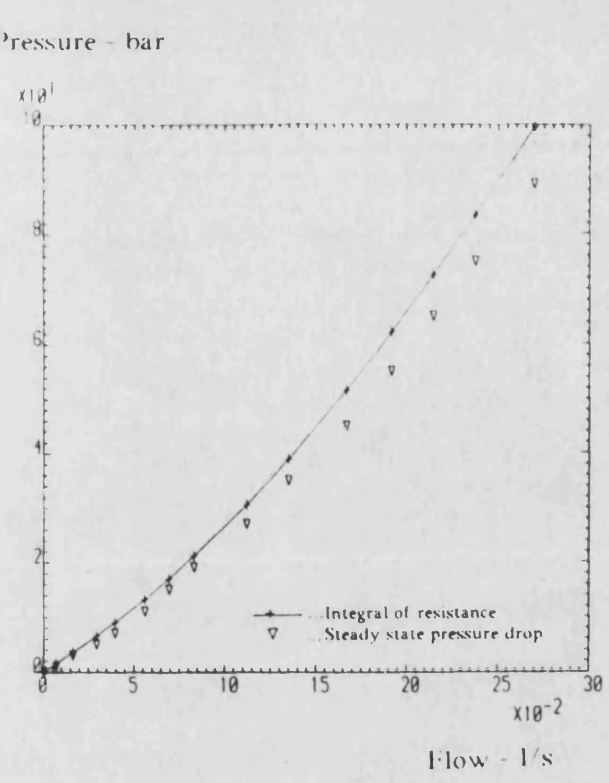

(b) Valve lift = 0.18 mm

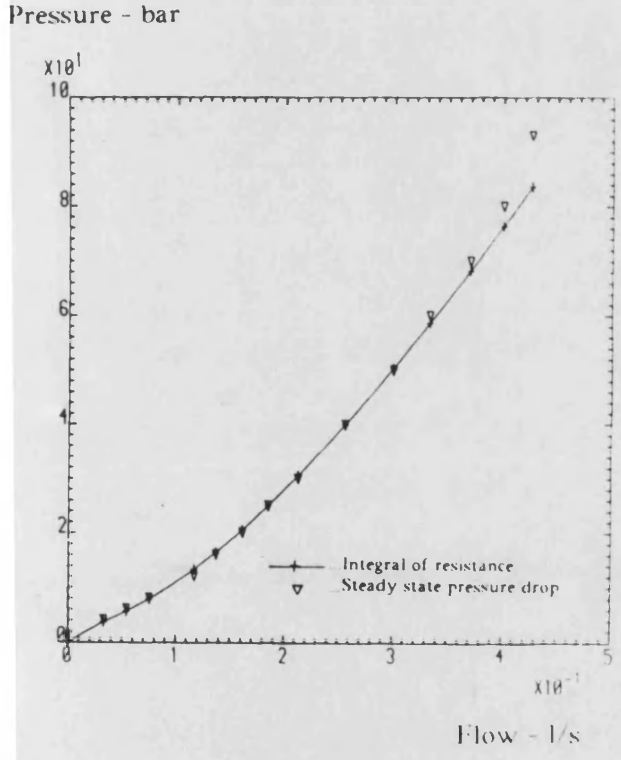

(c) Valve lift = 0.24 mm

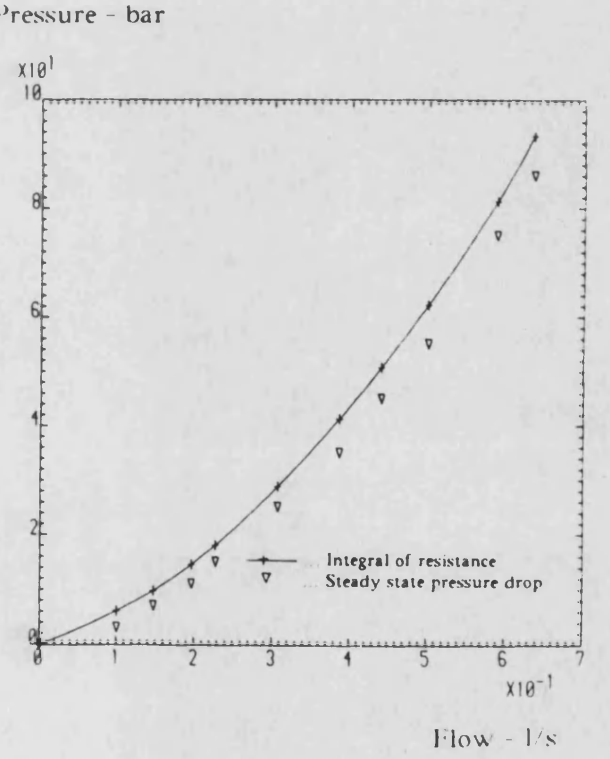

(d) Valve lift = 0.36 mm

Fig. 6.15 **Steady State Characteristics of Valve, showing Correlation with 'Integral of Dynamic Resistance'**

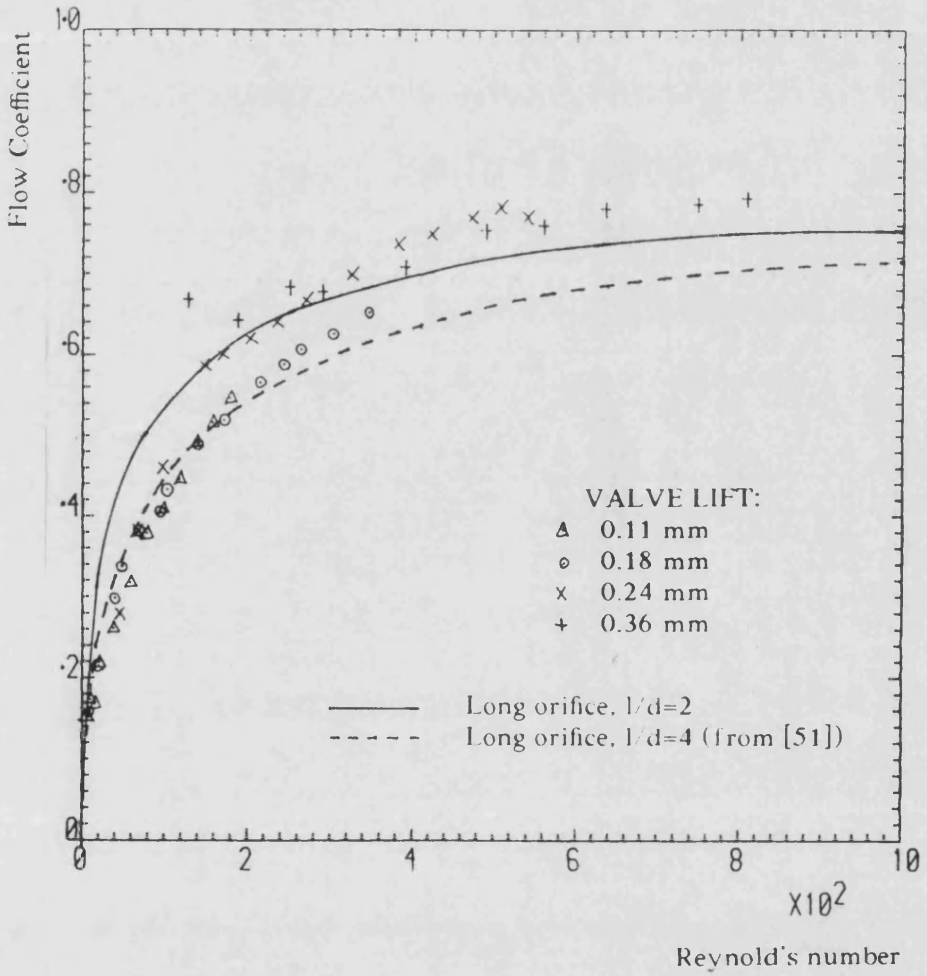

Fig. 6.16 Relationship between Flow Coefficient and Reynold's Number for Needle Valve

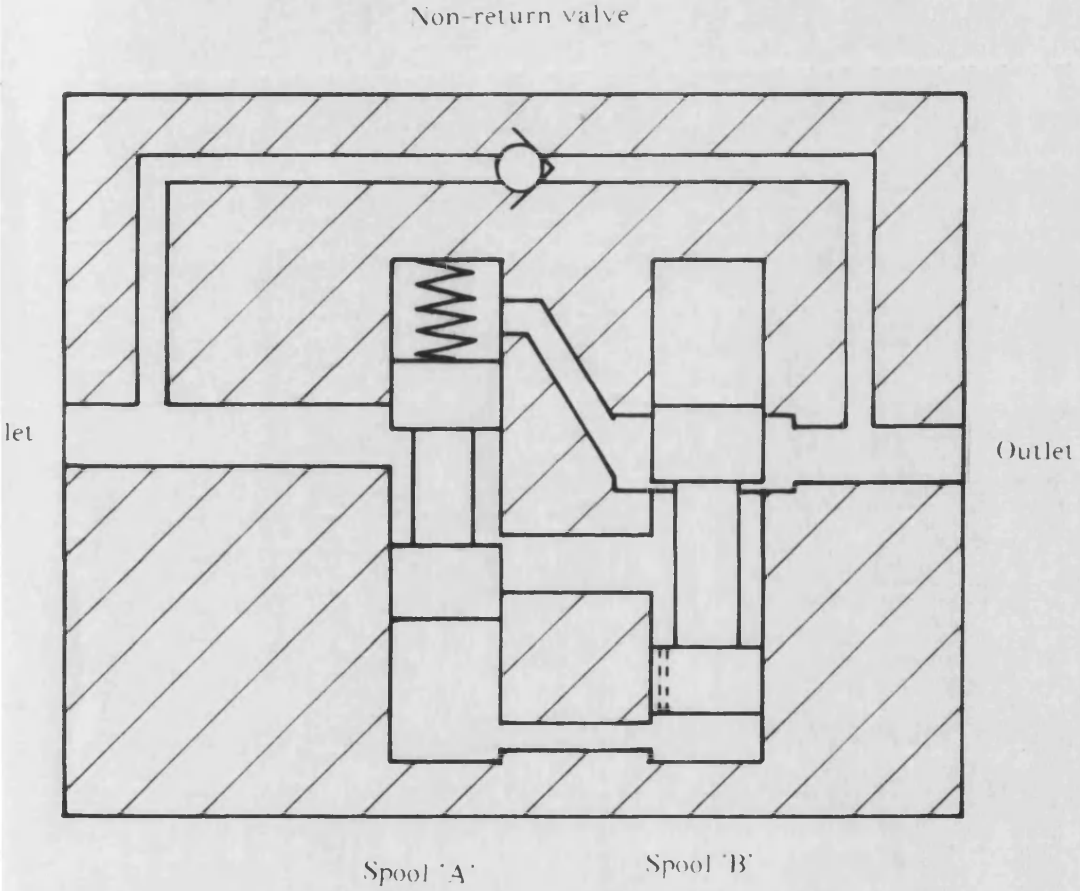

Fig. 6.17 Schematic Diagram of valve 'V2'

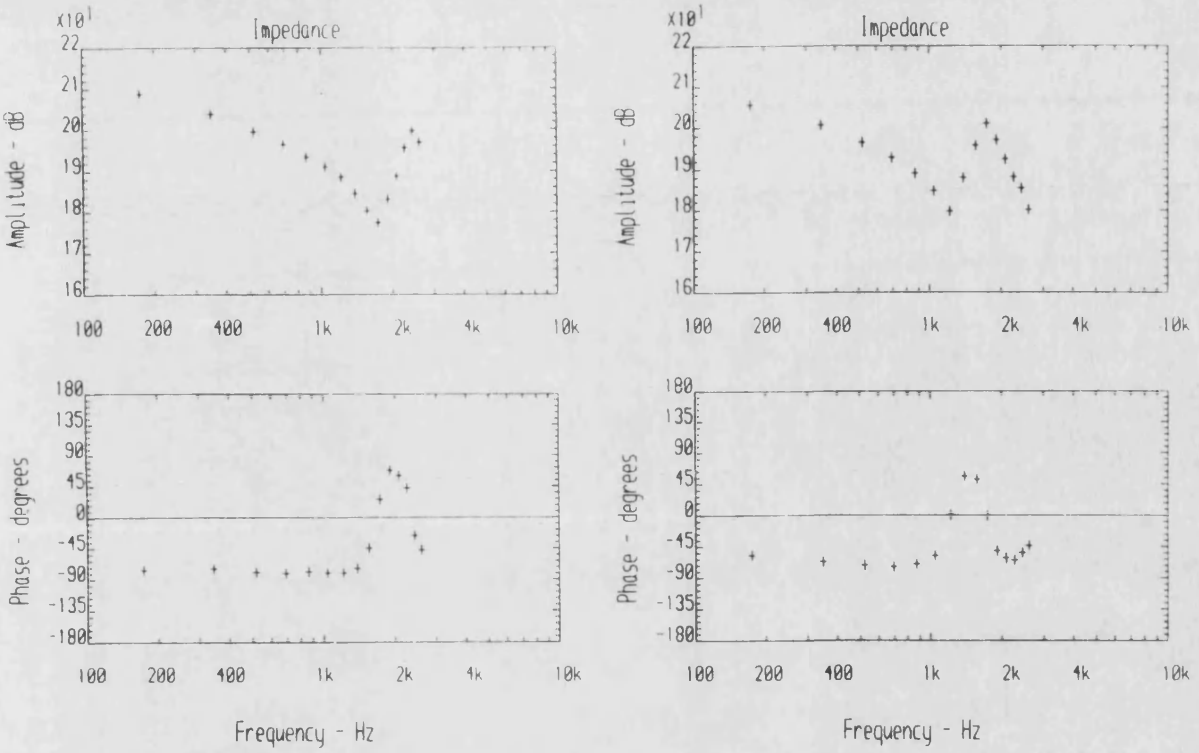

(a) 100 bar 0.17 l/s

(b) 50 bar 0.19 l/s

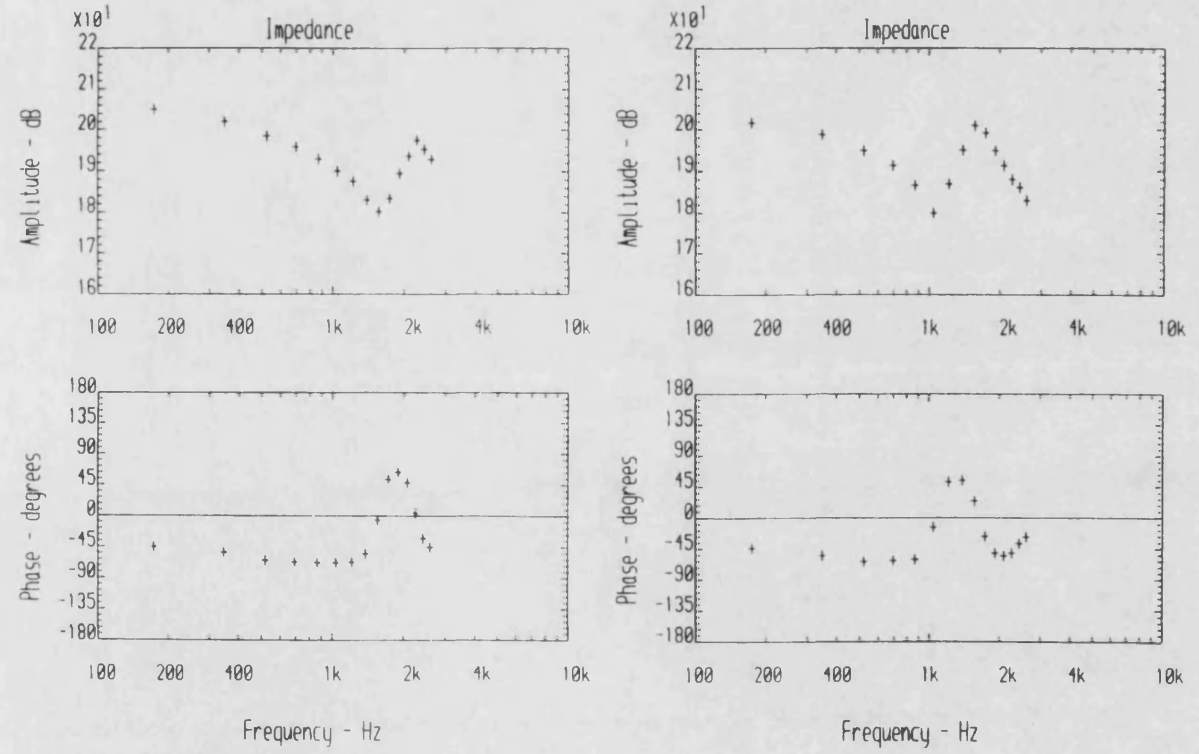

(c) 100 bar 0.71 l/s

(d) 50 bar 0.40 l/s

Fig. 6.18 Measured Impedance Characteristics, Valve 'V2'

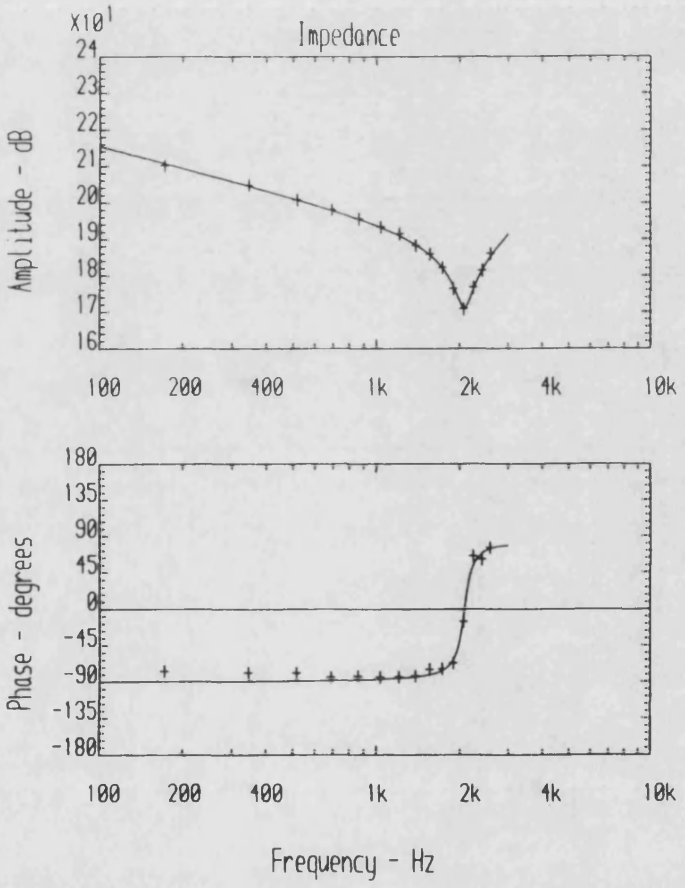

150 bar, 0.19 l/s

Fig. 6.19 Source Impedance Model Applied to Valve 'V2' Impedance Results

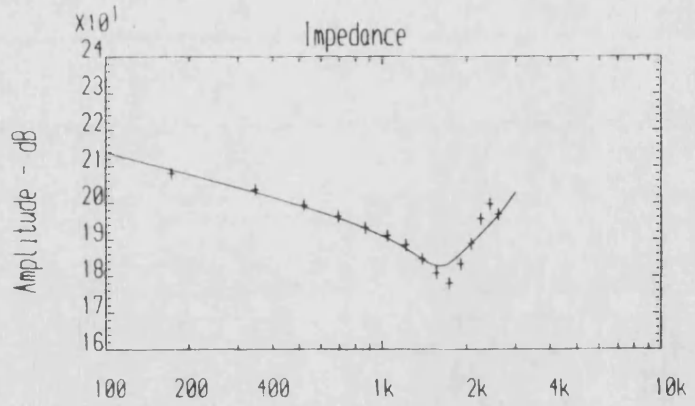

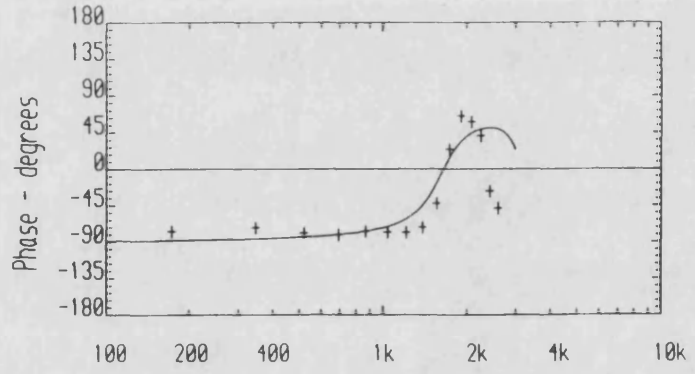

(a) 100 bar, 0.17 l/s

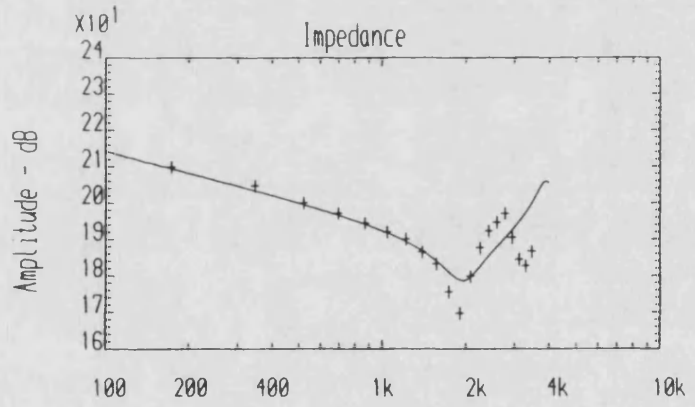

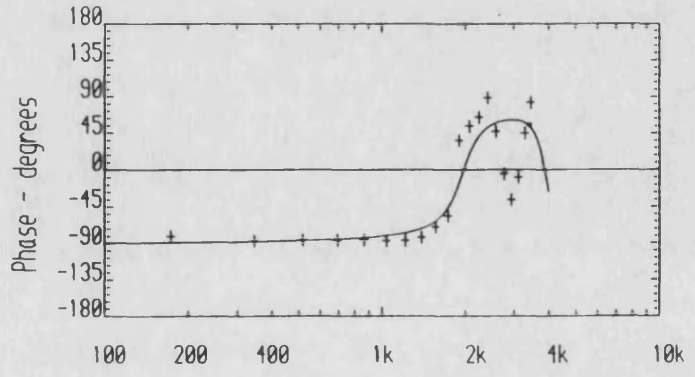

(b) 100 bar, 0.0 l/s

Fig. 6.20 Source Impedance Model Applied to Valve 'V2' Impedance Results

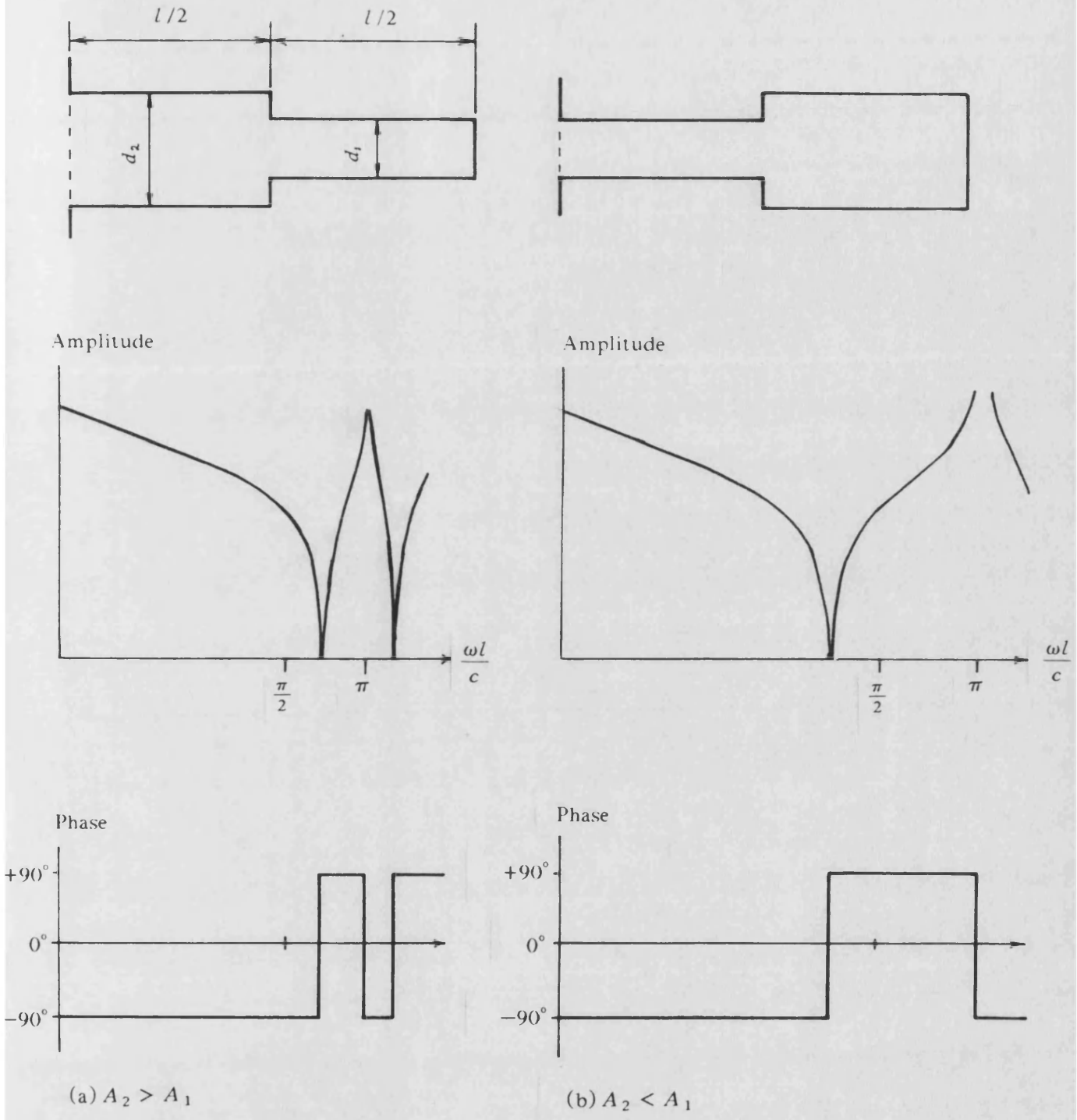

Fig. 6.21 Modified Source Impedance Model - Effect of Diameter Changes

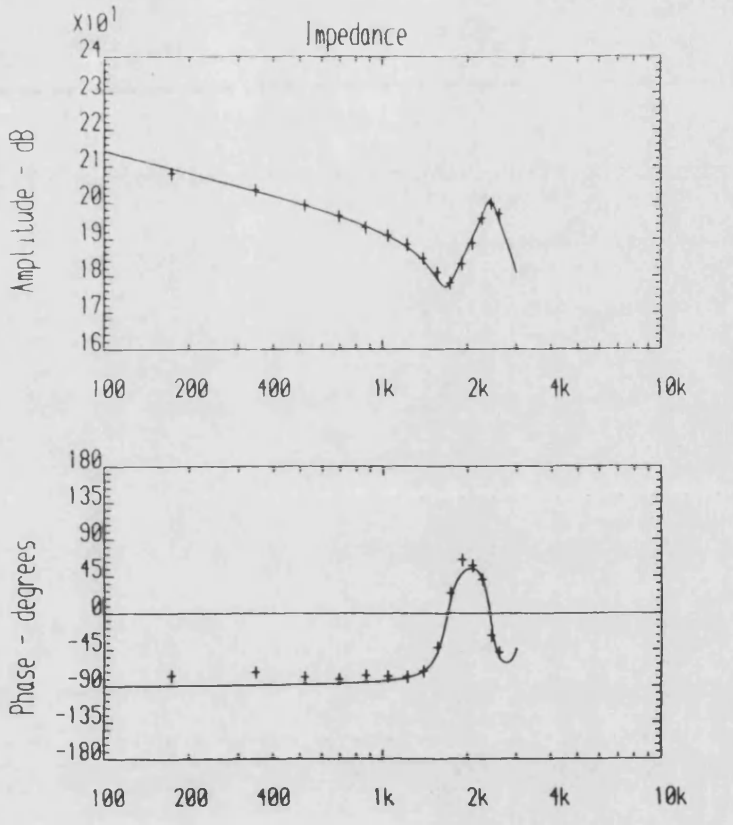

(a) 100 bar, 0.17 l/s

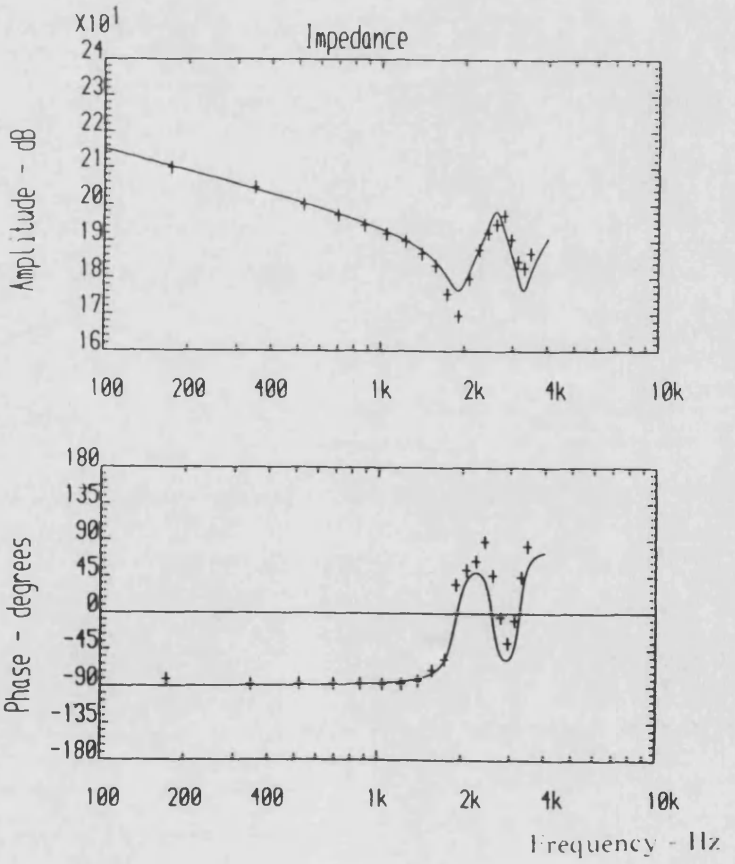

(b) 100 bar, 0.0 l/s

Fig. 6.22 **Modified Source Impedance Model Applied to Valve 'V2' Impedance Results**

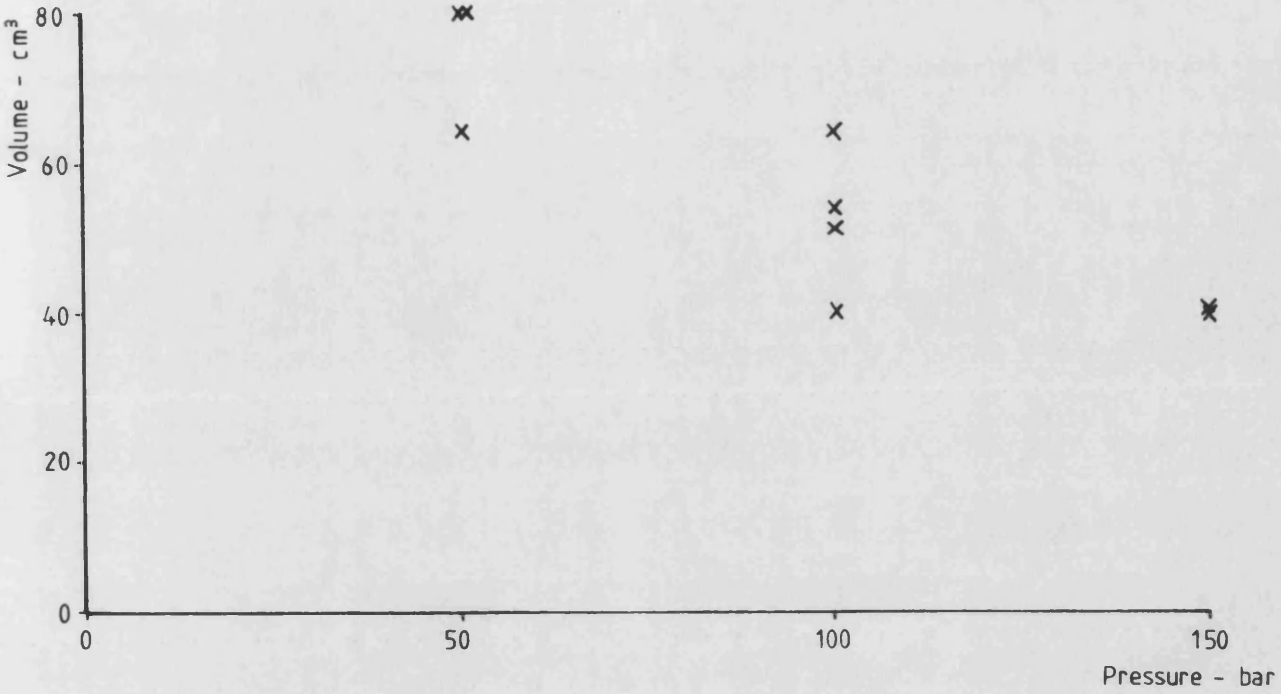

(a) Effective volume

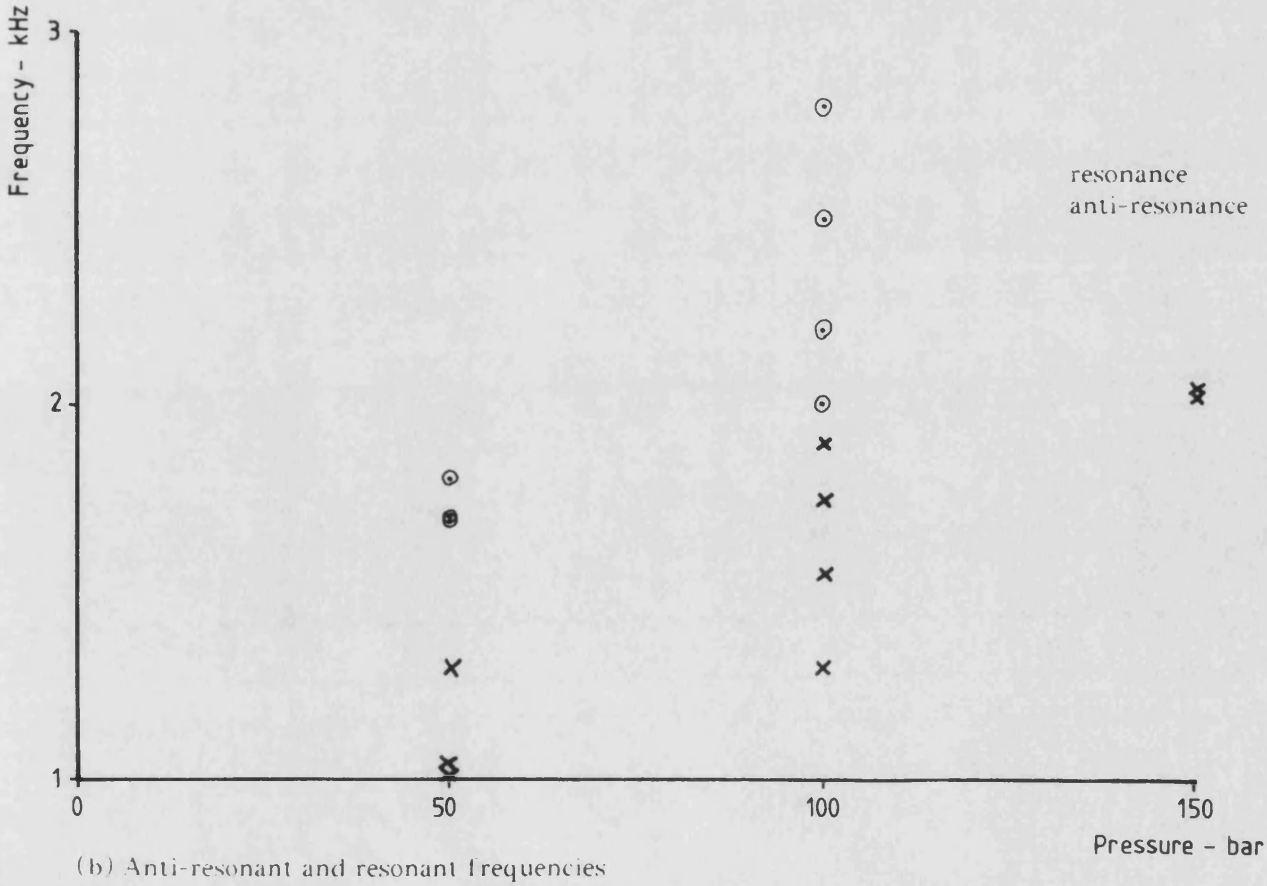

(b) Anti-resonant and resonant frequencies

Fig. 6.23 Graphs showing the Variation with Pressure of Effective Volume and Anti-Resonant and Resonant Frequencies

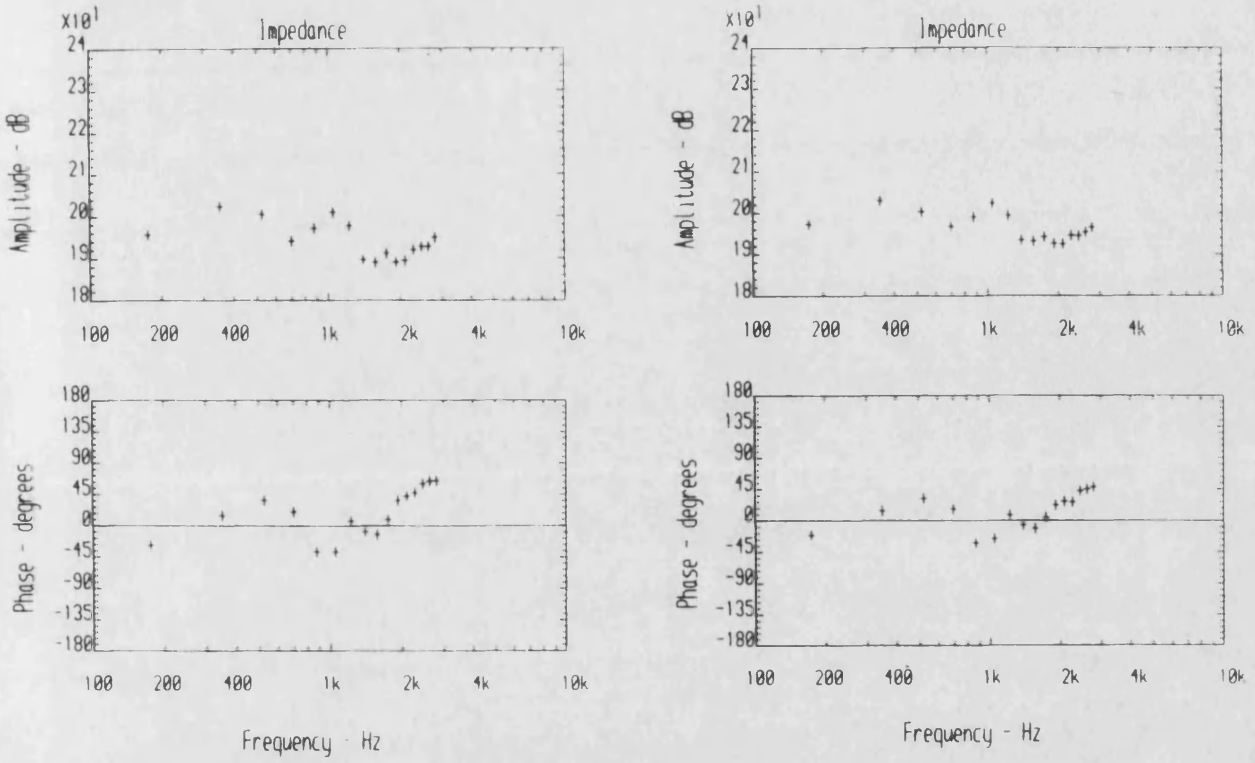

a) 10 bar, 0.8 l/s

b) 20 bar, 0.8 l/s

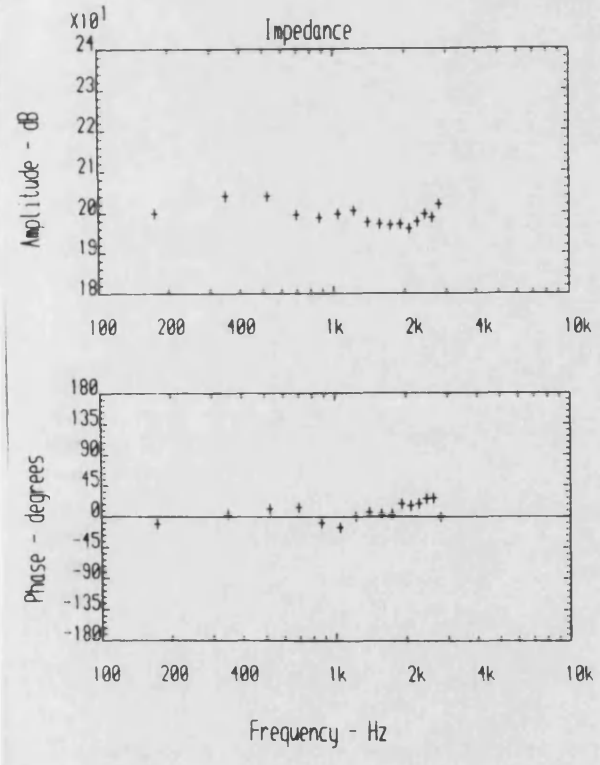

c) 30 bar, 0.8 l/s

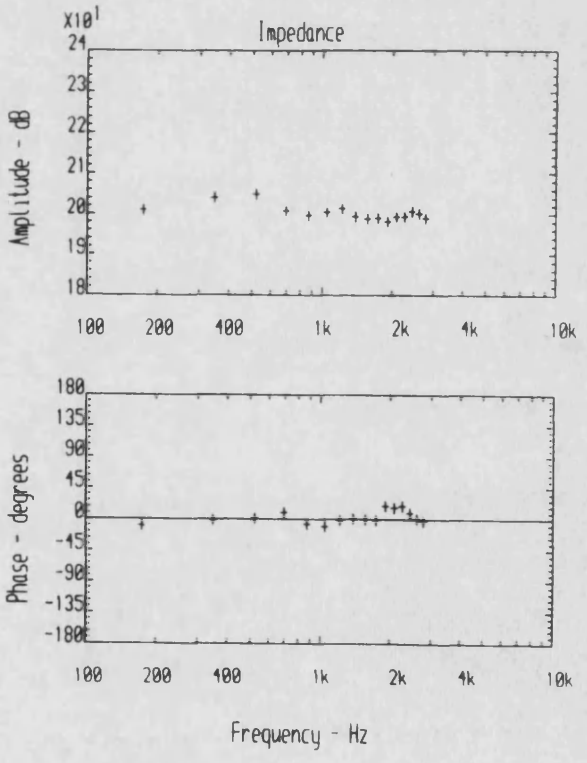

d) 40 bar, 0.8 l/s

Fig. 6.24 Experimental Impedance Results, Single Stage Relief Valve 'V3'

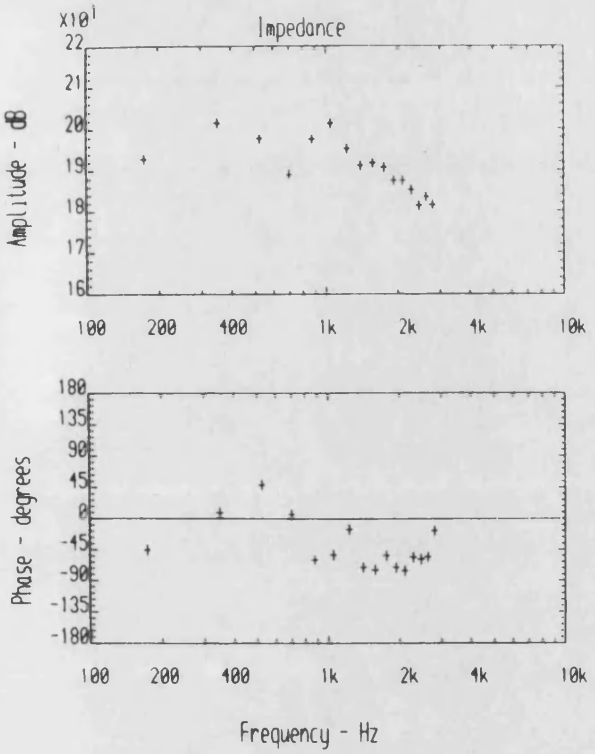

a) 10 bar, 0.8 l/s

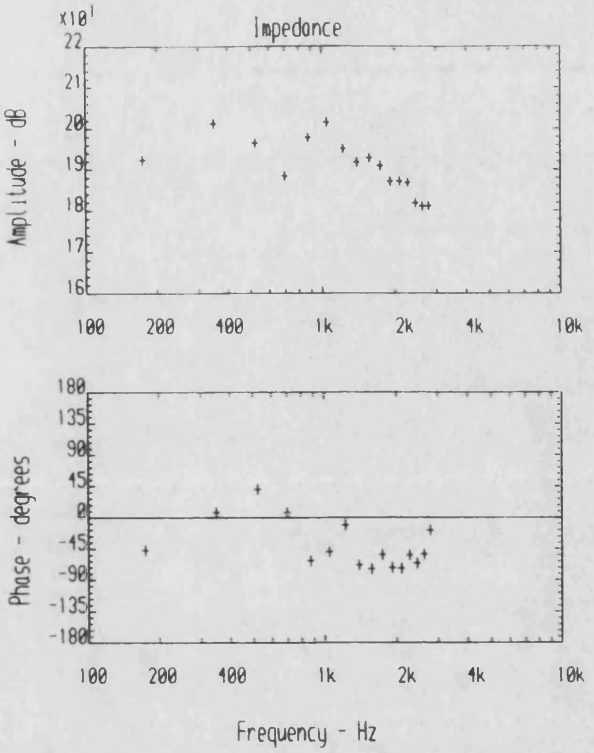

b) 20 bar, 0.8 l/s

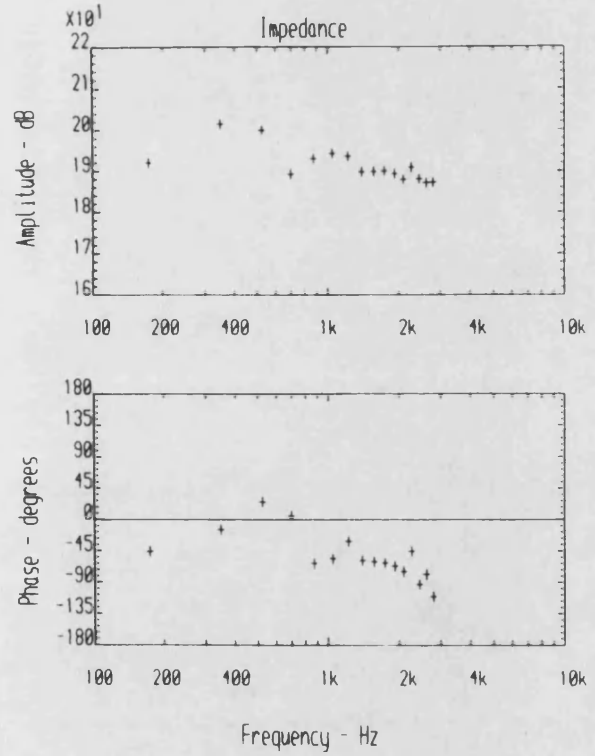

c) 30 bar, 0.8 l/s

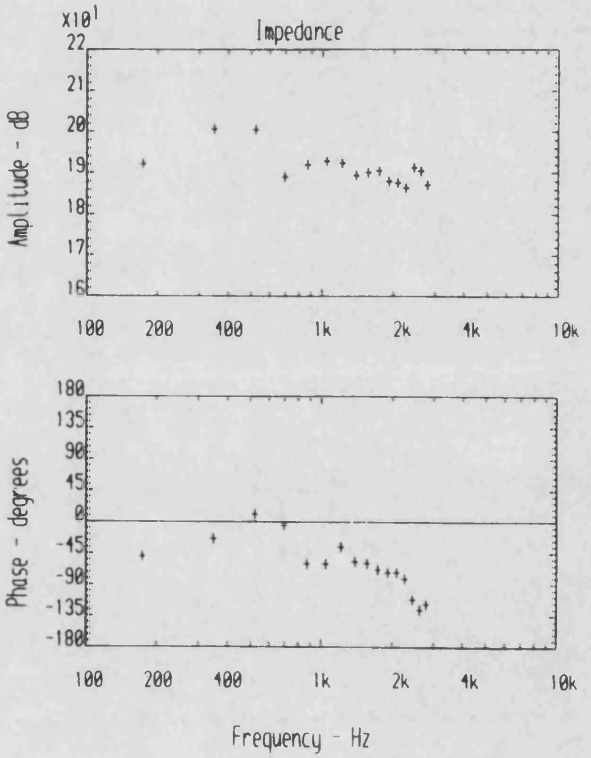

d) 40 bar, 0.8 l/s

Fig. 6.25 Measured Entry Impedance Downstream of Valve 'V3'

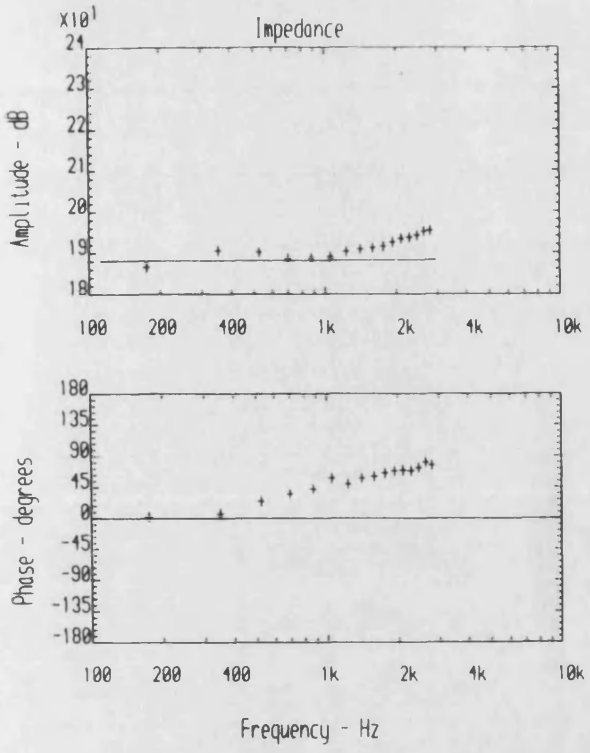

a) 10 bar, 0.8 l/s

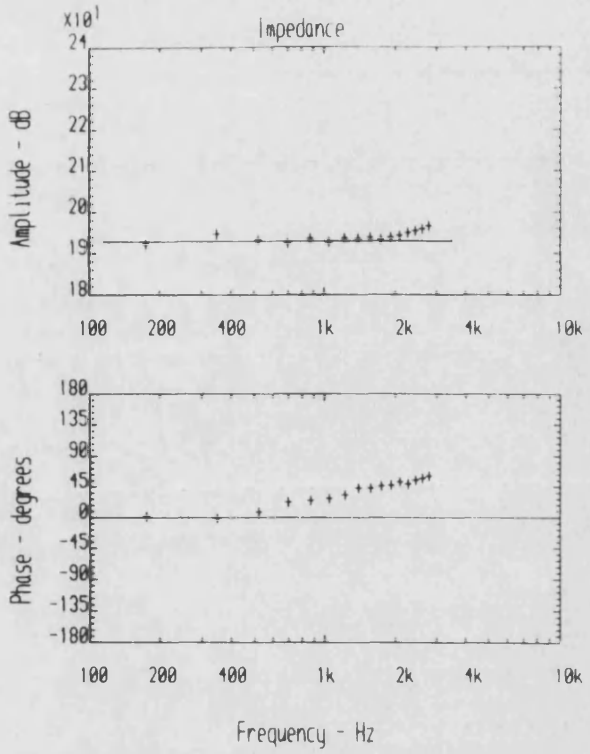

b) 20 bar, 0.8 l/s

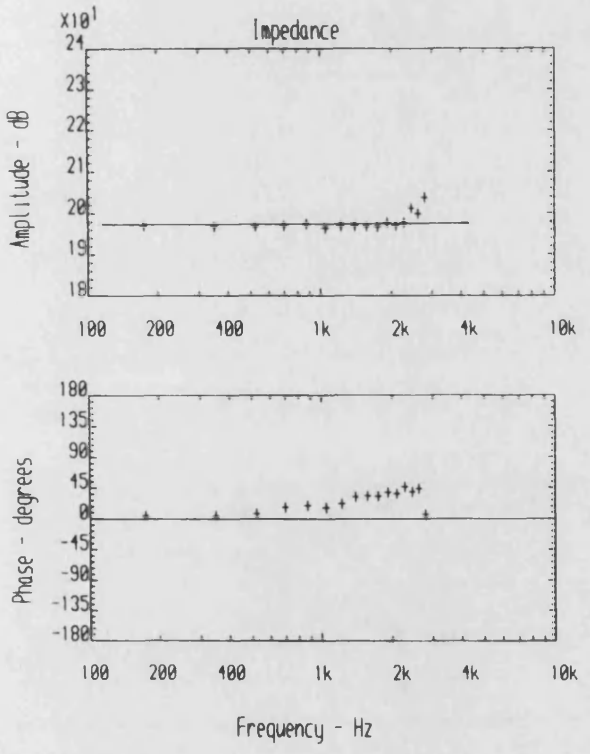

c) 30 bar, 0.8 l/s

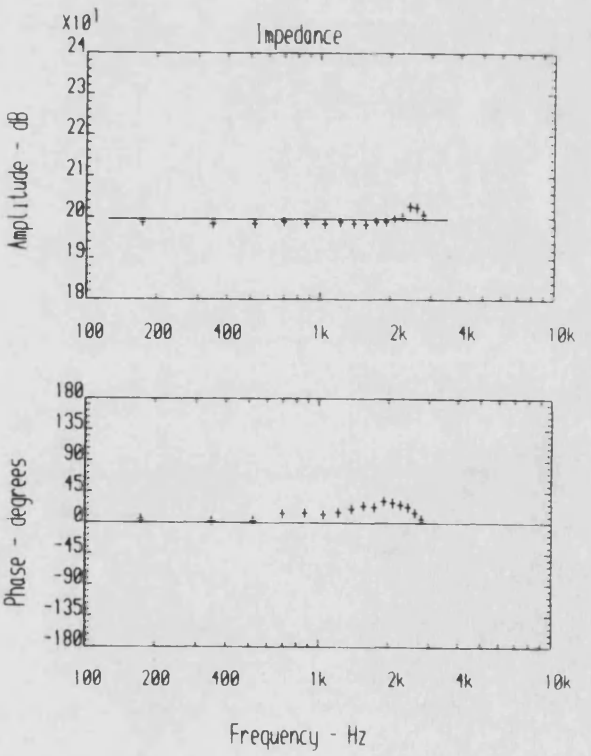

d) 40 bar, 0.8 l/s

Fig. 6.26 **Measured Impedance results, Valve 'V3', Allowing for Vibration, Contained Volume and Downstream Impedance**

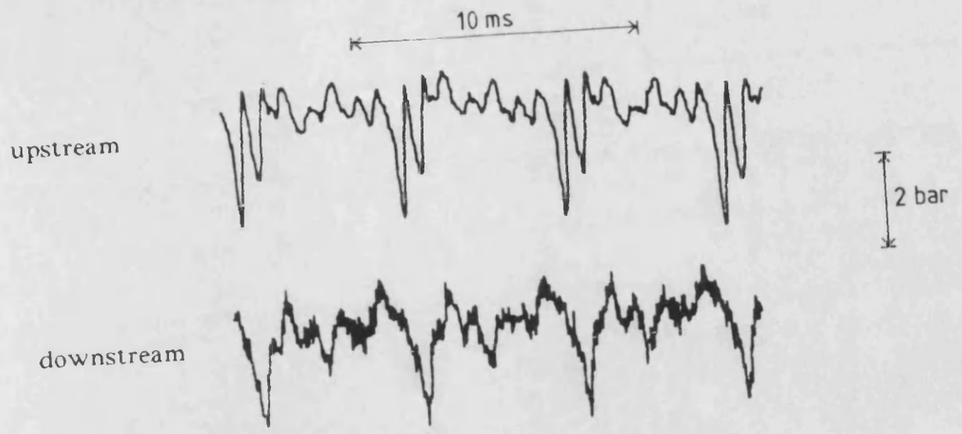

(a) 40 bar, 0.8 l/s

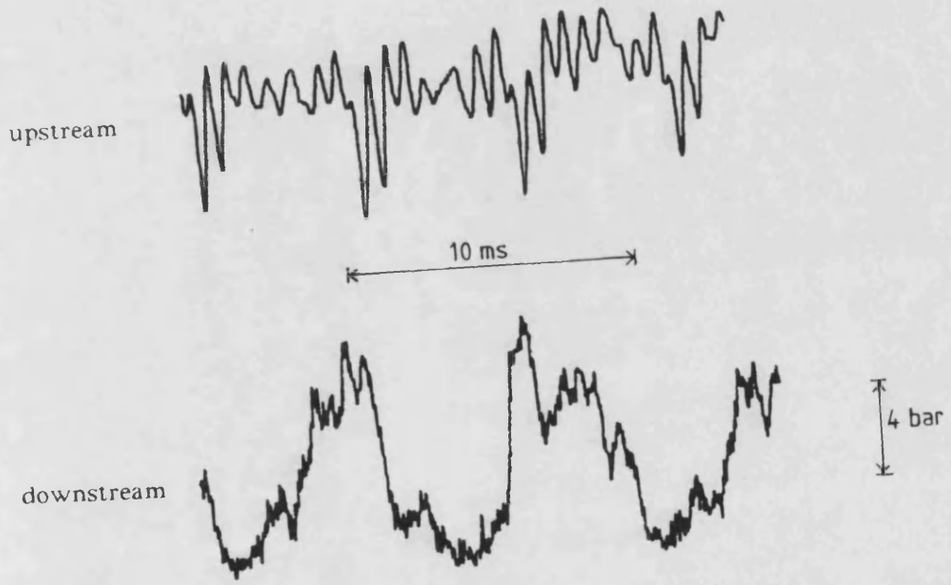

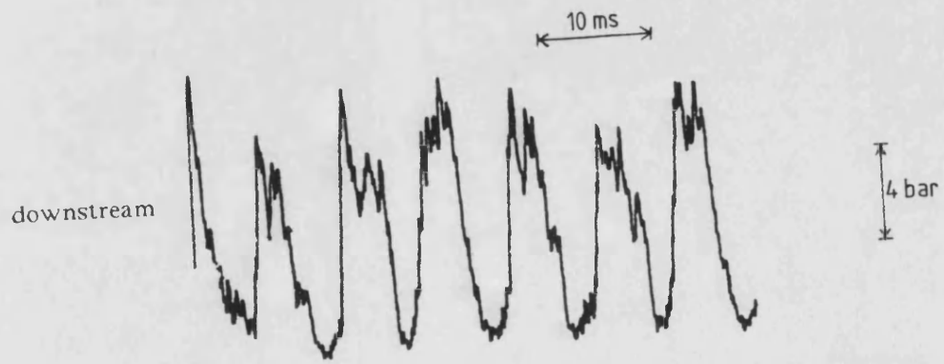

b) 90 bar, 0.8 l/s

Fig. 6.27 **Measured Pressure Ripple Traces, Valve 'V4'**

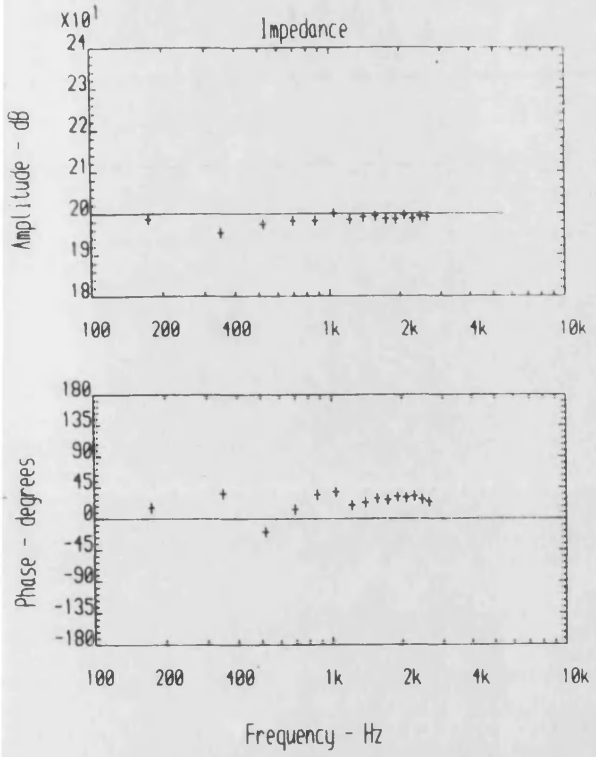

a) 40 bar, 0.8 l/s

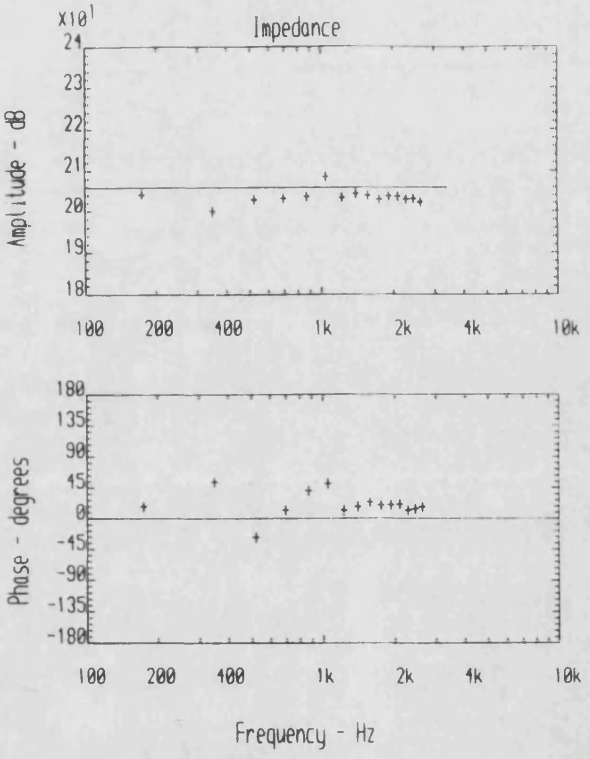

(b) 40 bar, 0.4 l/s

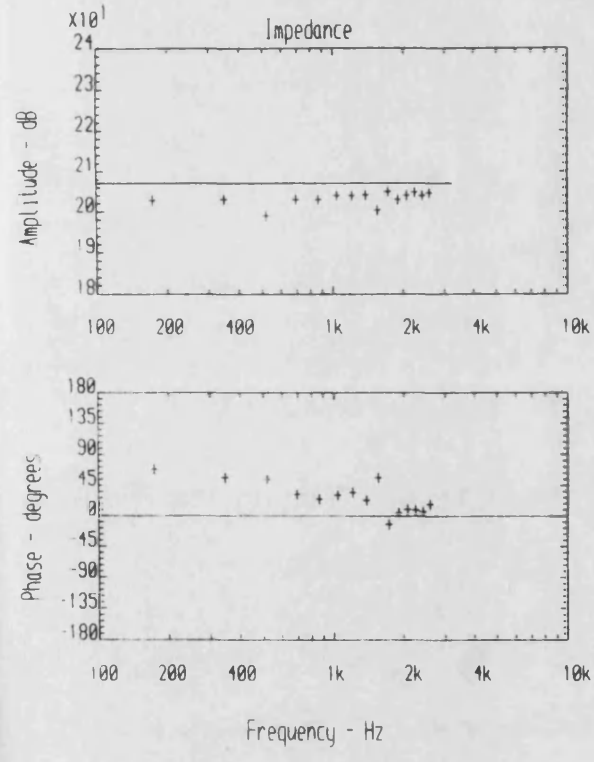

(c) 90 bar, 0.8 l/s

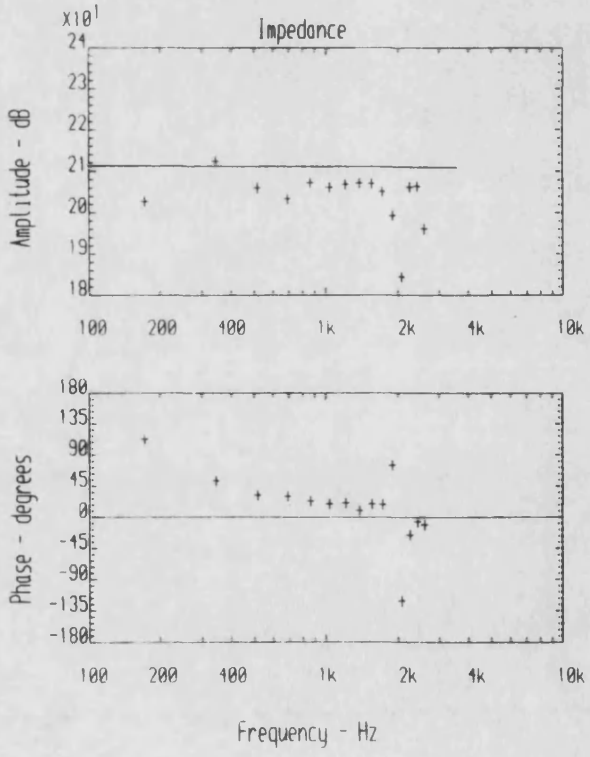

(d) 140 bar, 0.8 l/s

Fig. 6.28 Experimental Impedance Results - Two Stage Relief Valve 'V4'

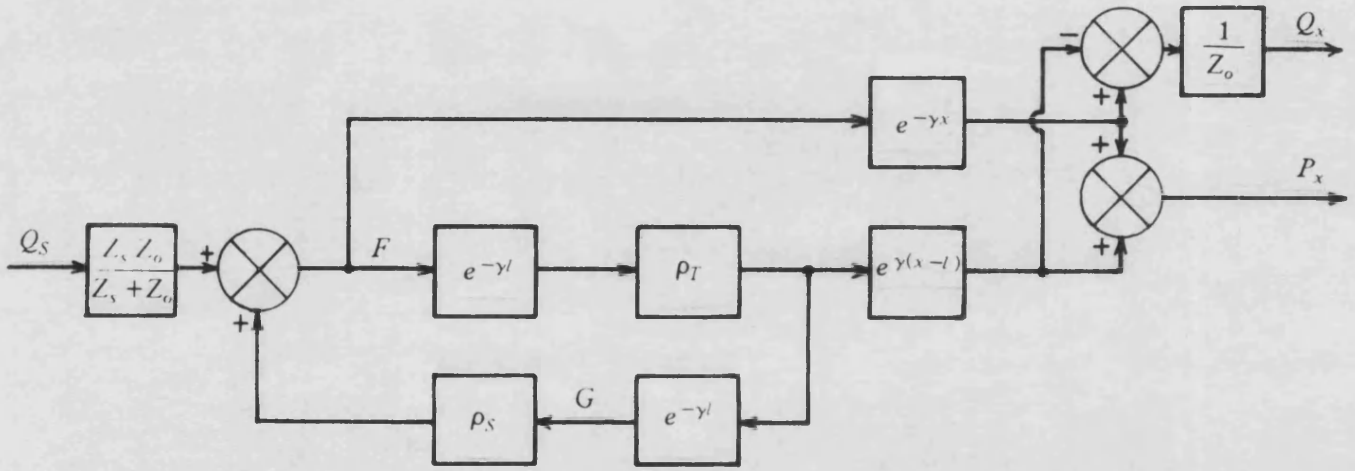

Fig. 6.29 Block Diagram of Simple Pump-Pipe-Termination System

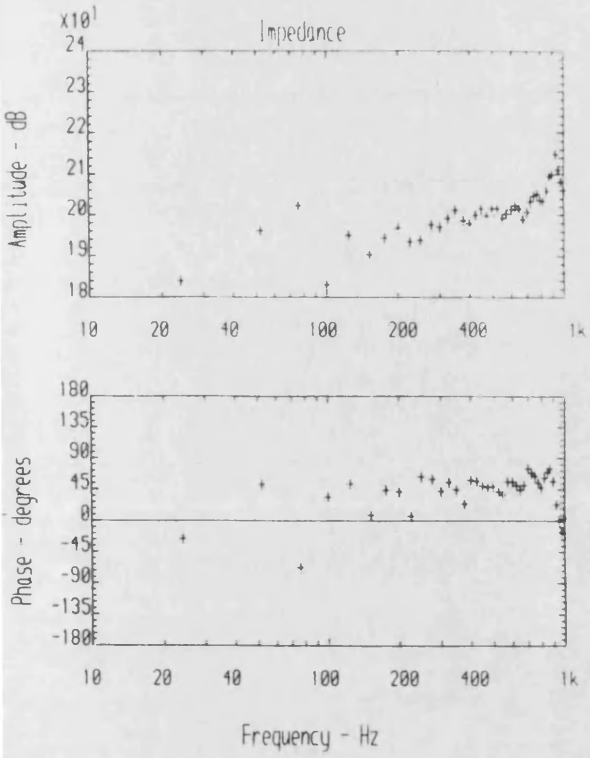

(a) 0.47 l/s, 75 bar

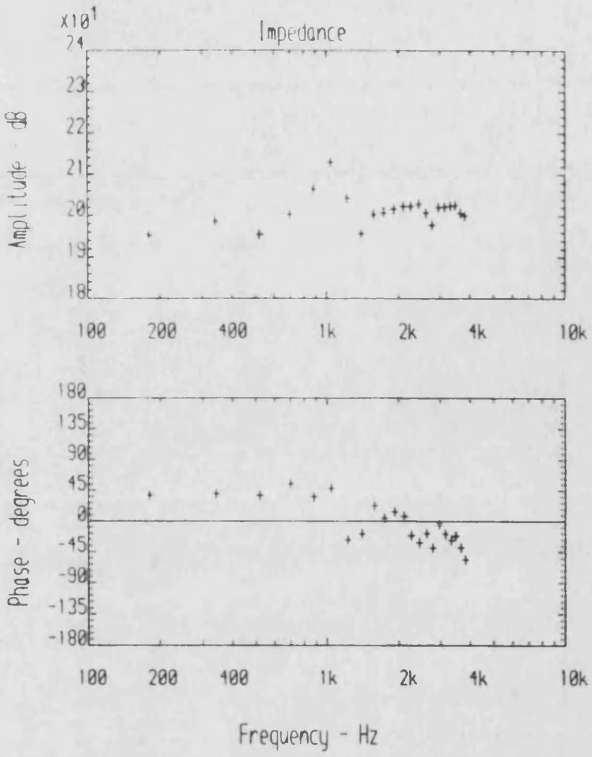

(b) 0.47 l/s, 75 bar

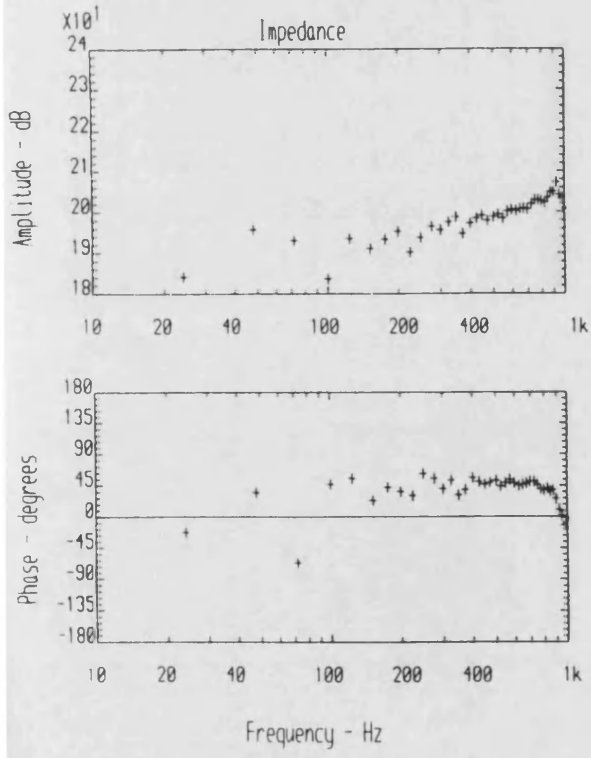

(c) 0.80 l/s, 75 bar

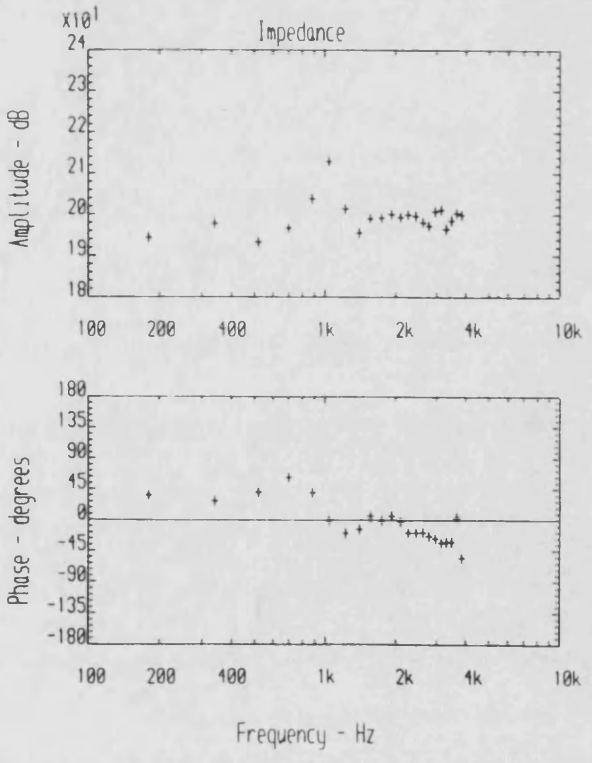

(d) 0.80 l/s, 75 bar

Fig. 6.30 Experimental Impedance Results - Two Stage Relief Valve 'V5'

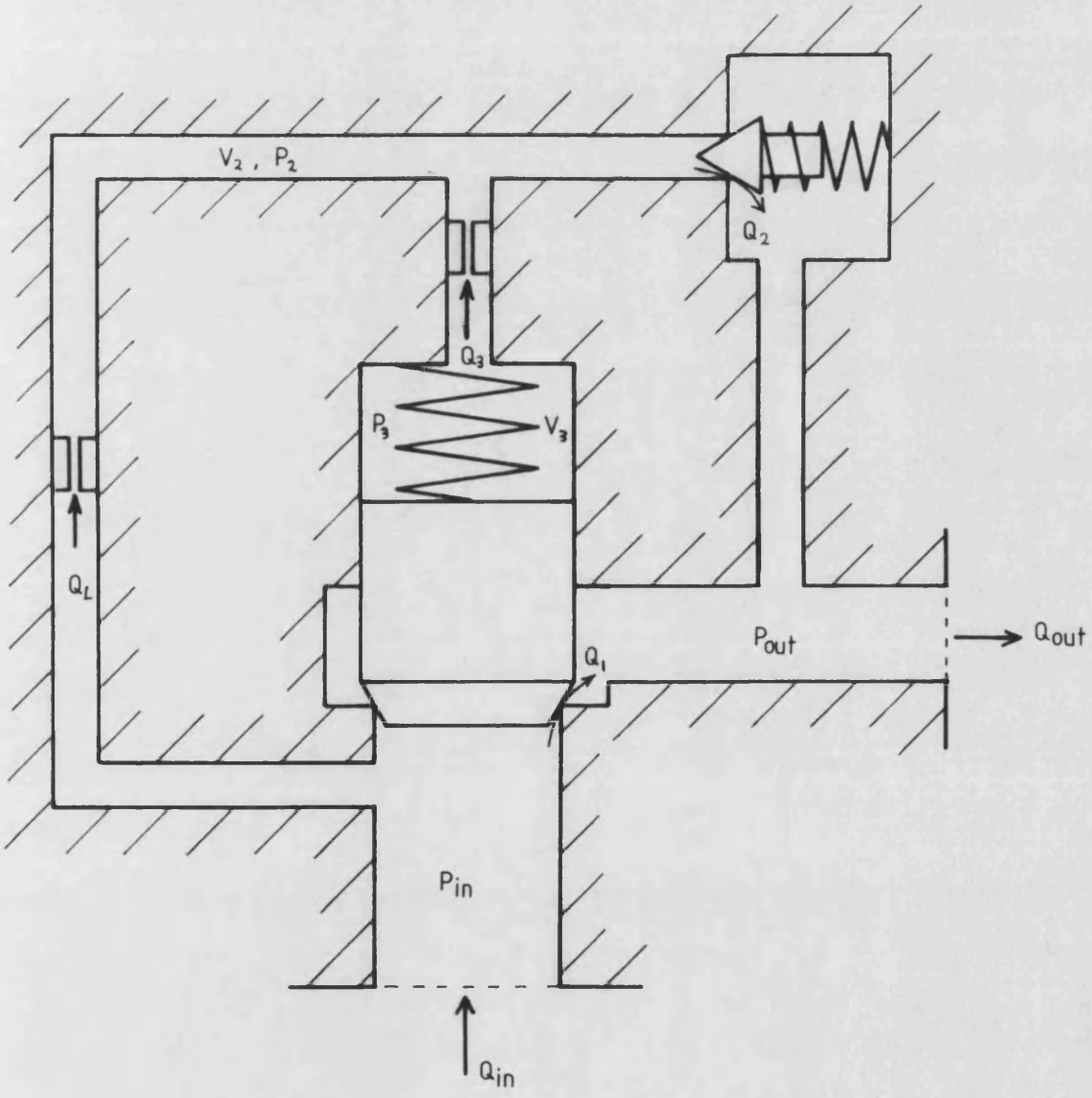

Fig. 6.31 Schematic Diagram of Valve 'V5'

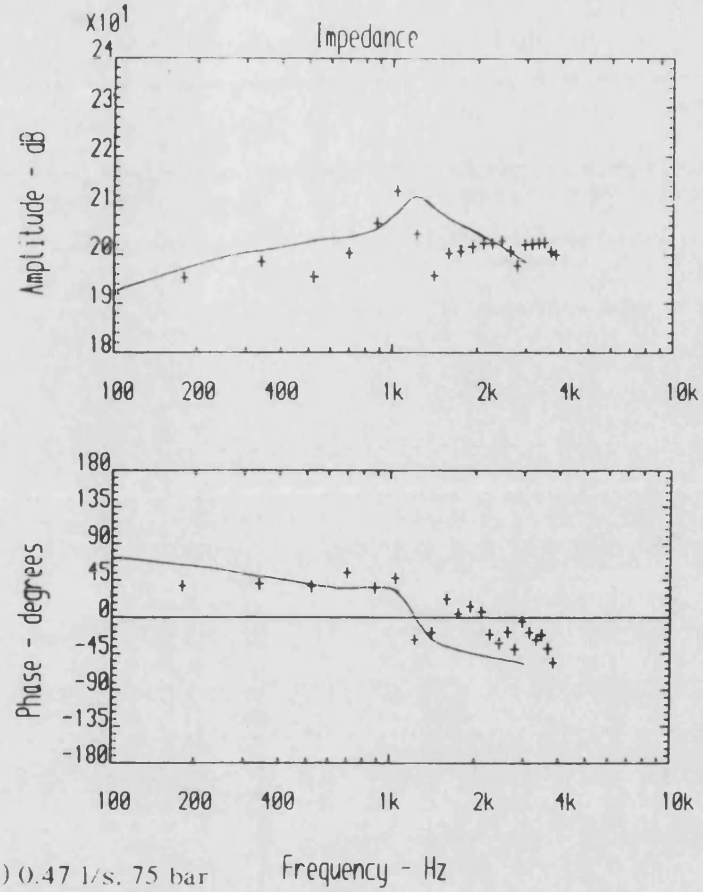

(a) 0.47 l/s, 75 bar

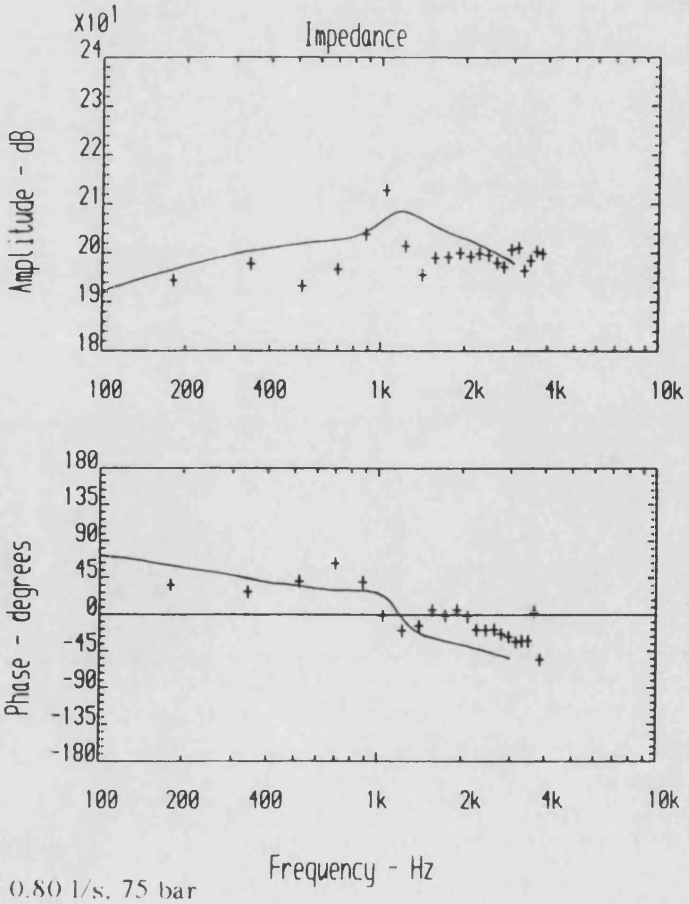

(b) 0.80 l/s, 75 bar

Fig. 6.32 **Valve 'V5' - Experimental and Simulated Impedance Results**

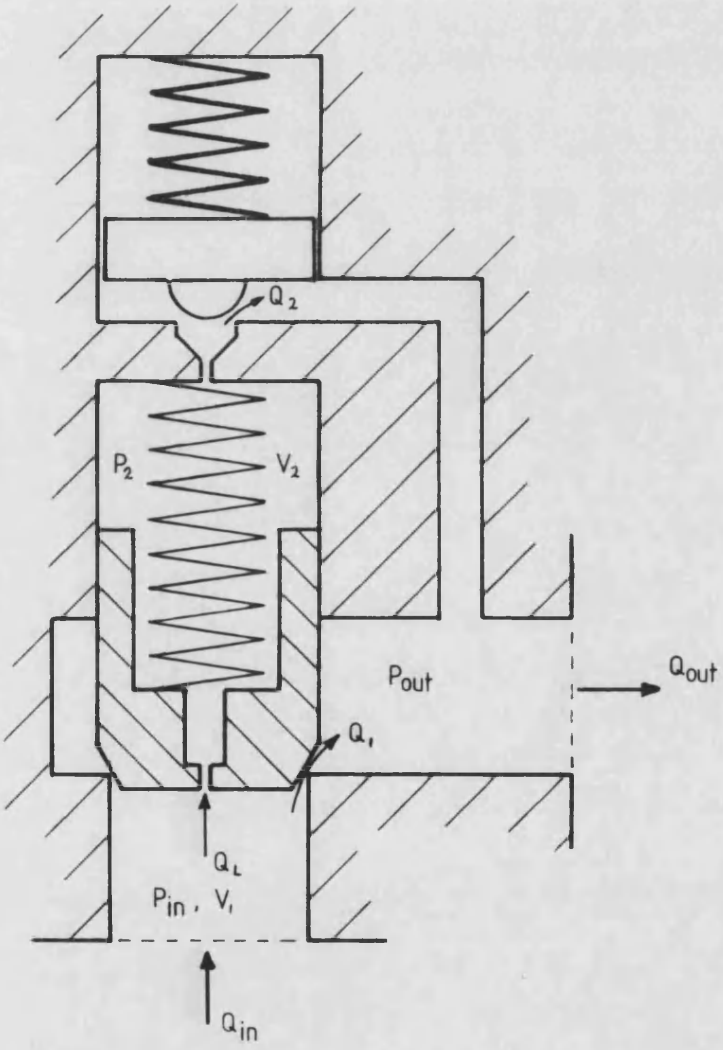

Fig. 6.33 Schematic Diagram of Valve 'V4'

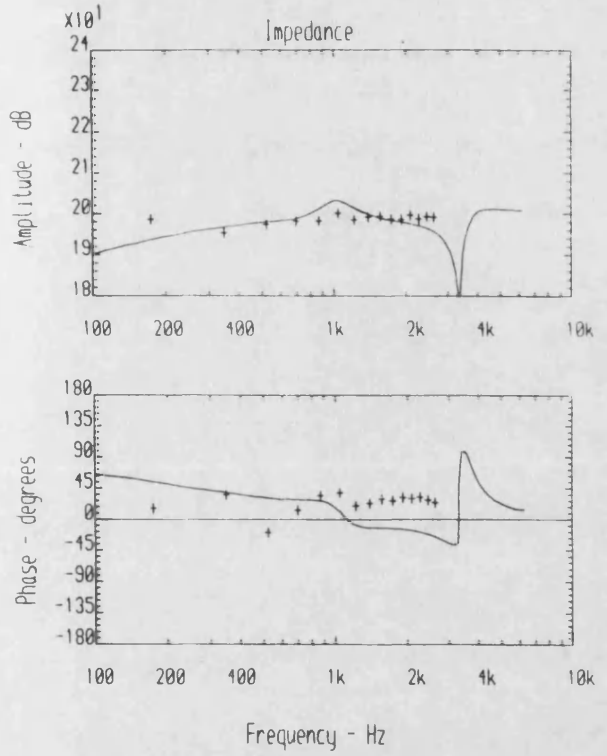

(a) 40 bar, 0.8 l/s

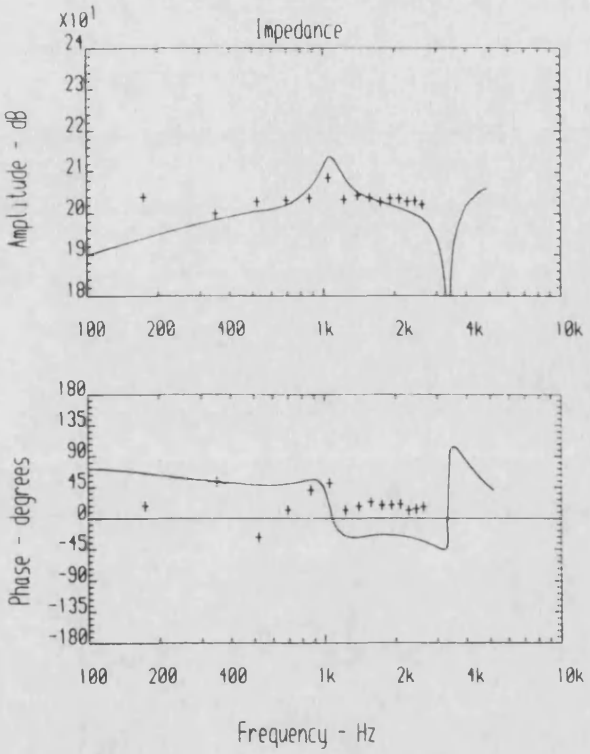

(b) 40 bar, 0.4 l/s

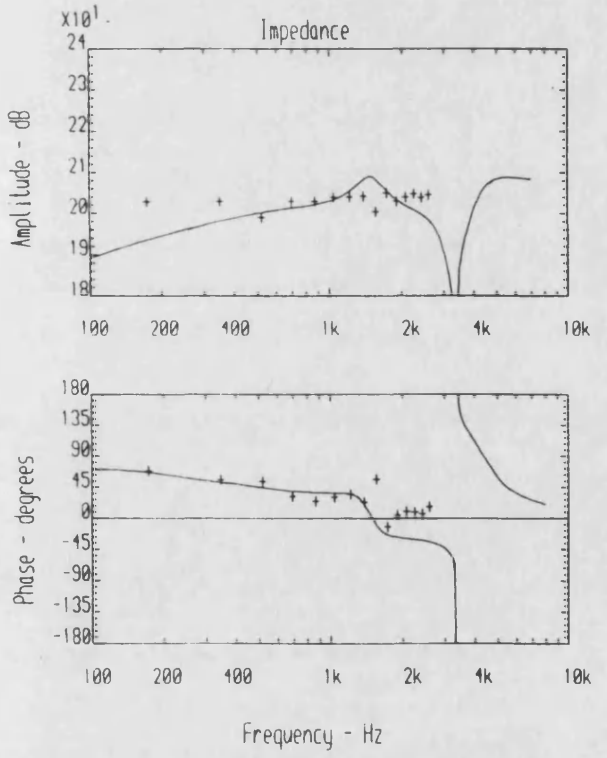

(c) 90 bar, 0.8 l/s

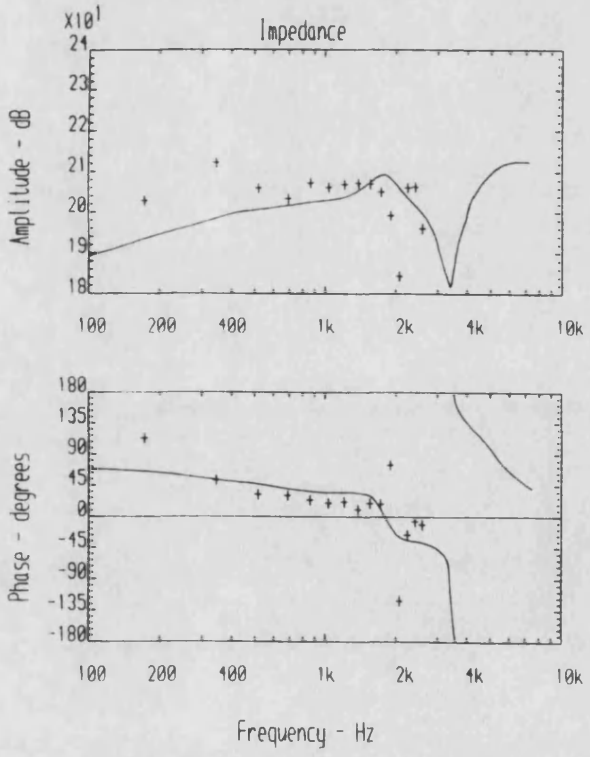

(d) 140 bar, 0.8 l/s

Fig. 6.34 **Valve 'V4' - Experimental and Simulated Impedance Results**

CHAPTER 7

EXPERIMENTAL DETERMINATION OF THE WAVE PROPAGATION CHARACTERISTICS OF A HYDRAULIC LINE

7.1. Evaluation of the Speed of Sound

The speed of sound in a fluid is a function of the fluid density and the effective bulk modulus:

$$c_0 = \sqrt{B_{eff}/\rho} \qquad \ldots(7.1)$$

In previous studies of fluid-borne noise and water hammer, it was assumed that c_0 can be determined analytically by calculation of ρ and B_{eff} from the fluid manufacturer's data. The value of ρ can normally be predicted with a high degree of accuracy. However, as stated in section 2.2., B_{eff} may be difficult to predict as it can be affected by the characteristics of the pipe wall and by entrained air in the fluid.

Consider a pipe along which three pressure transducers are mounted, as in Fig. (7.1). Assuming that the transducers are equally spaced, such that $\Delta x_1 = \Delta x_2 = \Delta x$, and neglecting viscous effects, then

$$P_1 = Fe^{j\omega\Delta x/c_0} + Ge^{-j\omega\Delta x/c_0} \qquad \ldots(7.2)$$

$$P_2 = F + G \qquad \ldots(7.3)$$

$$P_3 = Fe^{-j\omega\Delta x/c_0} + Ge^{j\omega\Delta x/c_0} \qquad \ldots(7.4)$$

Therefore

$$\frac{P_1+P_3}{2P_2} = \tfrac{1}{2}(H_{12}+H_{32}) = \frac{(F+G)e^{-j\omega\Delta x/c_0}+(F+G)e^{j\omega\Delta x/c_0}}{2(F+G)}$$

$$= \cos(\omega\Delta x/c_0) \qquad \ldots(7.5)$$

This formula was applied by Bolleter [46] for the experimental measurement of the speed of sound in a pipe. He proposed that the experimental function $\tfrac{1}{2}(H_{12}+H_{32})$ should be plotted against frequency, and the speed of sound calculated by fitting a cosine curve to the experimental data using a least squares method.

In the presence of viscous effects, equation (7.5) becomes

$$\tfrac{1}{2}(H_{12}+H_{32}) = \cosh(\gamma\Delta x) \qquad \ldots(7.6)$$

$$\text{where } \gamma = \alpha+\frac{j\omega}{c} \qquad \ldots(7.7)$$

Therefore

$$\tfrac{1}{2}(H_{12}+H_{32}) = \cos(\omega\Delta x/c)\cosh(\alpha\Delta x) - j\sin(\omega\Delta x/c)\sinh(\alpha\Delta x) \qquad \ldots(7.8)$$

Consider the typical case of mineral oil at 30°C in a 20 mm bore rigid pipe, where the spacing between transducers Δx = 1m. Over the frequency range considered (> 100 Hz), $\alpha\Delta x$ <0.05, in which case cosh $(\alpha\Delta x)$ can be assumed to equal unity. Equating the real parts of equation (7.6),

$$\mathrm{Re}\left\{\tfrac{1}{2}(H_{12}+H_{32})\right\} = \cos(\omega\Delta x/c) \qquad \ldots(7.9)$$

The phase velocity c is related to the speed of sound c_0 by the wave shear number ha (section 2.2.). In order to determine the speed of sound, the function cos $(\omega\Delta x/c)$ should be fitted to the experimental values of Re$\{\tfrac{1}{2}(H_{12}+H_{32})\}$. Thus it is required to minimise E, where for n data points

$$E = \sum_{i=1}^{n} \left\{ y_t(i) - y_e(i) \right\}^2 \qquad \ldots (7.10)$$

$$y_t = \cos \omega \Delta x / c \qquad \ldots (7.11)$$

$$y_e = \mathrm{Re}\left\{ \tfrac{1}{2}(H_{12} + H_{32}) \right\} \qquad \ldots (7.12)$$

$$\text{where } \frac{c_0}{c} = \mathrm{Re}\left\{ \xi(ha) \right\} \qquad \ldots (7.13)$$

When c_0 is such that the error is at a minimum, then $\frac{\partial E}{\partial c_0} = 0$. Hence

$$\sum_{i=1}^{n} \left\{ (y_t - y_e) \frac{\partial y_t}{\partial c_0} \right\} = 0 \qquad \ldots (7.14)$$

$$\text{where } \frac{\partial y_t}{\partial c_0} = \frac{\omega \Delta x \, \mathrm{Re}(\xi)}{c_0^2} \sin \frac{\omega \Delta x \, \mathrm{Re}(\xi)}{c_0} \qquad \ldots (7.15)$$

Equation (7.11) is non-linear in c_0. For this reason it is not possible to solve equation (7.14) directly to evaluate c_0, so an iterative method must be used. The method used here is based on the Newton-Raphson formula:-

$$x_{new} = x_{old} - \frac{f(x_{old})}{f'(x_{old})} \qquad \ldots (7.16)$$

$$\text{or } \Delta c_0 = - \frac{E'(c_{0\,old})}{E''(c_{0\,old})} \qquad \ldots (7.17)$$

$$\text{where } E'(c_0) = \frac{\partial E}{\partial c_0}$$

$$E''(c_0) = \frac{\partial^2 E}{\partial c_0^2} = \sum_{i=1}^{n} \left\{ (y_t - y_e) \frac{\partial^2 y_t}{\partial c_0^2} + \left\{ \frac{\partial y_t}{\partial c_0} \right\}^2 \right\} \qquad \ldots (7.18)$$

A starting value of c_0 is required for the iteration and this can be obtained from predicted values of B_{eff} and ρ. The iteration is then carried out until either:

a) a specified maximum number of iterations has been reached, or

b) the correction Δc_0 has reduced to a specified tolerance.

Provided that the iteration is convergent, the exact value of E'' has no effect upon the final value of c_0, since E', and hence Δc, is zero at this point. It does, however, affect the speed and the stability of convergence. It is sometimes assumed [26] that the $(y_t - y_e)\frac{\partial^2 y_t}{\partial c_0^2}$ term can be neglected, since $(y_t - y_e)$ should be small, provided that the initial estimate of c_0 is reasonably accurate. It was found that this term can be ignored without having a significant effect on the speed or stability of iteration.

Provided that pressure ripple is measured at three equidistant points along the pipe, this technique can be incorporated into the standing wave analysis described in chapter 4, in order to provide an improved estimate for the value of effective bulk modulus.

Typical plots of $\mathrm{Re}\{\frac{1}{2}(H_{12}+H_{32})\}$ and $\cos(\omega \Delta x / c)$ are shown in Fig. 7.2. Experimental points in Fig. 7.2(a) show considerable scatter; in this case single channel pressure ripple measurements were recorded. Scatter is much reduced in Fig. 7.2(b) where pressure ripple was recorded in the form of transfer functions between two points. This demonstrates that, as might be expected (section 4.3.5.2.), transfer function measurements tend to be much more accurate and consistent than single channel measurements. For this reason, in all subsequent tests the speed of sound was evaluated using only transfer function measurements.

It can be seen from Fig. 7.2(b) that there is excellent correlation between the experimental points and the modelled curve. It should therefore be possible to evaluate the speed of sound with a high degree of accuracy using this method, provided that the range of $\omega \Delta x / c$ is broad enough to define the cosine curve with adequate precision.

The above technique requires that pressure ripple should be measured at three equidistant points. This conflicts with the demand that pressure ripple should be measured at unequally spaced points to avoid the half wavelength condition as described in section 4.3.3.1. In order to satisfy both requirements, it is necessary to measure pressure ripple at more than three points, thus increasing the amount of data to be acquired and the amount of instrumentation needed. For this reason, the speed of sound

measurement technique was extended to cope with unequal spacing, so that only three pressure transducers would be necessary in an experimental system.

7.1.1. Evaluation of the Experimental Speed of Sound Using Three Unequally Spaced Pressure Transducers

Consider the configuration of three pressure transducers spaced unequally along a rigid pipe, as in Fig. 7.1, where

$$P_1 = Fe^{\gamma\Delta x_1}+Ge^{-\gamma\Delta x_1} \qquad \ldots(7.19)$$

$$P_2 = F+G \qquad \ldots(7.20)$$

$$P_3 = Fe^{-\gamma\Delta x_2}+Ge^{\gamma\Delta x_2} \qquad \ldots(7.21)$$

Considering transducers 1 and 2,

$$H_{12} = \frac{Fe^{\gamma\Delta x_1}+Ge^{-\gamma\Delta x_1}}{G+H}$$

$$\text{i.e. } \frac{F}{G} = \frac{e^{-\gamma\Delta x_1}-H_{12}}{H_{12}-e^{\gamma\Delta x_1}} \qquad \ldots(7.22)$$

Similarly, considering transducers 2 and 3,

$$\frac{F}{G} = \frac{e^{\gamma\Delta x_2}-H_{32}}{H_{32}-e^{-\gamma\Delta x_2}} \qquad \ldots(7.23)$$

$$\text{therefore, } \frac{e^{-\gamma\Delta x_1}-H_{12}}{H_{12}-e^{\gamma\Delta x_1}} = \frac{e^{\gamma\Delta x_2}-H_{32}}{H_{32}-e^{-\gamma\Delta x_2}}$$

$$\text{or, } H_{12}\sinh(\gamma\Delta x_2) + H_{32}\sinh(\gamma\Delta x_1) - \sinh(\gamma(\Delta x_1+\Delta x_2)) = 0 \qquad \ldots(7.24)$$

In practice, because of experimental error, the left hand side of equation (7.24) will not equal zero. Hence, in order to evaluate the speed of sound, it is necessary to minimise the sum of squares error E, where, for n data points,

$$E = \sum_{i=1}^{n} |\epsilon|^2 = \sum_{i=1}^{n} \epsilon \bar{\epsilon} \qquad \ldots (7.25)$$

where $\epsilon = H_{12} \sinh(\gamma \Delta x_2) + H_{32} \sinh(\gamma \Delta x_1) - \sinh(\gamma(\Delta x_1 + \Delta x_2))$ $\ldots (7.26)$

Where c_0 is such that E is at a minimum, $\frac{\partial E}{\partial c_0} = 0$. A similar iterative technique to that in section 7.1., where the transducers are equally spaced, is used.

It was found that the real part of γ could be neglected without affecting the results significantly. However, resistive effects could not be ignored completely as the variation of the phase velocity with the wave shear number ha could affect the results. Equation (7.26) becomes

$$\epsilon = H_{12} \sin(\omega \Delta x_2 / c) + H_{32} \sin(\omega \Delta x_1 / c) - \sin(\omega(\Delta x_1 + \Delta x_2)/c) \qquad \ldots (7.27)$$

where, from equation (7.13), $c = c_0 / \mathrm{Re}(\xi)$.

At the point of minimum error E, $\frac{\partial E}{\partial c_0} = 0$. Since equation (7.27) is non-linear with respect to c_0, the point of minimum error must be found iteratively. In fact, the mathematical technique is simplified by letting $u = 1/c_0$ and iterating to find the value of u at which the error is minimised. Thus,

$$\epsilon = H_{12} \sin(\omega \Delta x_2 u \,\mathrm{Re}(\xi)) + H_{32} \sin(\omega \Delta x_1 u \,\mathrm{Re}(\xi)) - \sin(\omega(\Delta x_1 + \Delta x_2) u \,\mathrm{Re}(\xi)) \ldots (7.28)$$

From equation (7.25), $\frac{\partial E}{\partial u} = 2\mathrm{Re} \sum_{i=1}^{n} (\bar{\epsilon} \frac{\partial \epsilon}{\partial u})$ $\ldots (7.29)$

and $\frac{\partial \epsilon}{\partial u} = H_{12} \omega \Delta x_2 \mathrm{Re}(\xi) \cos(\omega \Delta x_2 u \,\mathrm{Re}(\xi))$

$+ H_{32} \omega \Delta x_1 \mathrm{Re}(\xi) \cos(\omega \Delta x_1 u \,\mathrm{Re}(\xi))$

$- \omega(\Delta x_1 + \Delta x_2) \mathrm{Re}(\xi) \cos(\omega(\Delta x_1 + \Delta x_2) u \,\mathrm{Re}(\xi))$ $\ldots (7.30)$

Using the Newton-Raphson iterative method, as described in equations (7.16) and (7.17),

$$u_{new} = u_{old} - \frac{\frac{\partial E}{\partial u}}{\frac{\partial^2 E}{\partial u^2}} \qquad \ldots (7.31)$$

$$\text{where } \frac{\partial^2 E}{\partial u^2} \approx 2 \sum_{i=1}^{n} \left\{ \frac{\partial \epsilon}{\partial u} \frac{\partial \bar{\epsilon}}{\partial u} \right\} \qquad \ldots (7.32)$$

Thus,

$$u_{new} = u_{old} - \frac{\text{Re} \sum_{i=1}^{n} \left\{ \bar{\epsilon} \frac{\partial \epsilon}{\partial u} \right\}}{\sum_{i=1}^{n} \left\{ \frac{\partial \epsilon}{\partial u} \frac{\partial \bar{\epsilon}}{\partial u} \right\}} \qquad \ldots (7.33)$$

The initial value of u can be obtained from estimates of B_{eff} and ρ. Iteration is carried out until the correction to u reduces to within a specified tolerance, or until a specified maximum number of iterations has been carried out.

7.1.2. Experimental Speed of Sound Results

The above techniques were applied in conjunction with a large number of component tests. Results are summarised in Fig. 7.3, in which they are plotted as a percentage difference between the predicted bulk modulus values (evaluated using equations (2.15) and (2.16)) and the experimental values, against mean pressure. It can be seen that the experimental points are scattered evenly on either side of the zero error line (the errors have a mean of -0.5% and a standard deviation of 1.7%) This indicates that the initial estimate is good, and that the effects of entrained air are minimal. At low mean pressure there appears to be a trend in which the experimental bulk modulus is reduced relative to the predicted value. This may well be due to entrained air, which would be expected to have the greatest effect at low pressure. The scatter in the experimental results is presumably due to experimental error.

In this case it would appear that the experimental evaluation of the speed of sound and bulk modulus is not particularly beneficial to the further analysis of the standing wave. The predicted value of bulk modulus appears to be a sufficiently good estimate, and any deviation from this value in its experimental evaluation seems to be due mainly to random error. However, the technique described could be particularly beneficial where the effective bulk modulus is difficult to predict, for example with a water-based fluid.

7.2. Wave Propagation Measurements using a Small Diameter Pipe

7.2.1. Measurement of the Pipe Resistance

If one considers the imaginary part of equation (7.8),

$$\mathrm{Im}\left\{\tfrac{1}{2}(H_{12}+H_{32})\right\}=\sin\omega\Delta x/c\ \sinh(\alpha\Delta x) \qquad \ldots(7.34)$$

It should be possible to evaluate α, and hence R, using this equation. However, with the 20 mm bore pipe used in the above tests, the value of ha was high and hence the resistance coefficient was low, such that any resistive effects were masked by experimental scatter. For this reason, it was attempted to increase the real part of γ by use of a smaller diameter pipe.

It was assumed previously (2.2.) that $R_{eff} = R(0.425+0.175ha)$ where $R = \frac{128\mu}{\pi d^4}$. This expression for R is obtained from the Hagen-Pouseuille formula and is not necessarily valid for turbulent flow. Tests were performed over a wide range of steady state Reynold's numbers, including turbulent flow, in order to examine the effect of Reynold's number upon the resistance and on the speed of sound.

In order to produce the high Reynold's numbers required, the mean fluid velocity $\tilde{V}$ could be high enough to cause a significant Doppler shift and affect the wave propagation velocity. For this reason it was necessary to apply a correction to the experimental data, based upon the assumption that the sole effect of this mean velocity was to increase the phase velocity of the waves travelling in the same direction as the fluid to $(1+\epsilon)c$, and to decrease the phase velocity of waves travelling in the opposite direction to $(1-\epsilon)c$, where $\epsilon = \tilde{V}/c$ [14].

Therefore $\gamma = \frac{j\omega}{c(1\pm\epsilon)} + \alpha$

If one applies the approximation

$$\frac{1}{1+\epsilon} \approx 1-\epsilon, \text{ and } \frac{1}{1-\epsilon} \approx 1+\epsilon \qquad \ldots (7.35)$$

then $P_1 \approx Fe^{j\omega\Delta x(1-\epsilon)/c} e^{\alpha\Delta x} + Ge^{-j\omega\Delta x(1+\epsilon)/c} e^{-\alpha\Delta x}$

$$= e^{-j\omega\Delta x\epsilon/c} \left\{ Fe^{\gamma\Delta x} + Ge^{-\gamma\Delta x} \right\}. \qquad \ldots (7.36)$$

Similarly,

$$P_3 \approx e^{\frac{j\omega\Delta x\epsilon}{c}} \left\{ Fe^{-\gamma\Delta x} + Ge^{\gamma\Delta x} \right\}. \qquad \ldots (7.37)$$

Therefore it is necessary to multiply the upstream pressure reading by the correction factor $e^{j\omega\Delta x\epsilon/c}$, and the downstream pressure reading by $e^{-j\omega\Delta x\epsilon/c}$.

The pipe diameter chosen was such that a sufficiently high Reynold's number could be achieved with the available flow rate without causing an excessive pressure drop or mean fluid velocity. A 7 mm bore tungum alloy pipe was chosen, with three transducers equally spaced over a 2 m length. In order to achieve a Reynold's number of 10,000 with mineral oil in the normal working temperature range there would be a pressure drop of approximately 100 bar along the pipe, which is within the system's capabilities. The mean velocity would be approximately 50 m/s which is sufficiently small compared to the speed of sound for the approximation of equation (7.35) to be applied with an error of less than 0.2%.

In theory it should be possible to evaluate c and α for each experimental point and plot them as functions of frequency, this being the approach taken by Margolis and Brown [14]. However, because of experimental scatter, this is not feasible in the present case. Instead, the following analysis was performed on the results.

a) A least squares curve fit was performed on the real part of $\frac{1}{2}(H_{12}+H_{32})$ in order to determine the speed of sound.

b) A mathematical model was then applied to the imaginary part in order to determine the resistive coefficient. This was done on the basis that the relationship between α and ha is known. From equation 7.34,

$$\mathrm{Im}\left\{\tfrac{1}{2}(H_{12}+H_{32})\right\} = \sin(\omega\Delta x/c)\sinh(\alpha\Delta x)$$

$\sin(\omega\Delta x/c)$ can be calculated using the value of c obtained from (a). Ignoring higher order terms,

$$\alpha = \frac{AR_{eff}}{2\rho c} \qquad \ldots (7.38)$$

where, for laminar flow, $R_{eff} = R(0.425+0.175ha)$

and R = steady state resistance $= \frac{128\mu}{\pi d^4}$

It was assumed that $\alpha\Delta x$ was small, allowing the approximation $\sinh(\alpha\Delta x) \approx \alpha\Delta x$ to be made. A least squares curve fit was applied to determine the experimental steady state resistance R_e. This value was compared with the theoretical value $R_t = \frac{128\mu}{\pi d^4}$.

Strictly speaking, the above analysis only applies to laminar flow. However, Margolis *et al* [14,53] showed that, in theory, the propagation constant γ for turbulent flow approaches that of laminar flow at high values of wave shear number ha. The reason for this is that at high values of ha the wavefront approaches a plane profile with shear taking place only in a thin boundary layer close to the pipe wall. If this lies within the viscous sub-layer, the behaviour of the perturbations will be virtually indistinguishable from that in laminar flow. In the range of Reynold's number under consideration, the wave shear number is high enough for this condition to apply, and therefore, in theory, there should be no variation of γ with Reynold's number. For this reason the same model for the variation of c/c_0 and R_{eff}/R was used for both laminar and turbulent flow.

7.2.2. Experimental Results

Some typical experimental results and least squares models are shown in Fig. 7.4. For the real part of $\frac{1}{2}(H_{12}+H_{32})$, there is good correlation between experimental points and the model. However, there appears to be a large degree of scatter on the imaginary part. In fact the errors are of a similar magnitude for both the real and imaginary parts of $\frac{1}{2}(H_{12}+H_{32})$, but the imaginary part is smaller than the real part so the errors are more significant. For this reason, it is possible to predict the speed of sound with much higher accuracy than the resistance.

By comparison of Figs 7.4(a) and (b), it appears that there is some correlation in the pattern of the scatter of the experimental points. This would seem to indicate that the scatter is not due to random error alone. Possible reasons for this are:

a) calibration error. The calibration of the pressure transducer/charge amplifier combinations was checked for both amplitude and phase error over the frequency range under consideration. Errors were found to be small, within about 2% and 1°.

b) inaccuracies in the mathematical model. It may be that wave propagation effects within the pipe wall are affecting the wave characteristics in the fluid. It is normally assumed that such effects are negligible for rigid pipes; however the observed effects are small, so this may well be a contributory factor.

c) lateral pipe vibration. However, it was considered that this is unlikely to affect longitudinal waves in a straight pipe.

Fig. 7.5(a) shows the variation of the percentage difference between the experimental and theoretical values of speed of sound plotted against Reynold's number. As can be seen, within the laminar region the correlation between experiment and theory is good. However, at higher Reynold's numbers there is a distinct increase in the relative experimental values, approaching approximately 5% at a Reynold's number of 10,000. A similar effect was observed by Shemer *et al* [54].

The variation with Reynold's number of the ratio of the experimentally predicted steady state resistance to the theoretically predicted value is plotted in Fig. 7.5(b). A marked increase in the experimental value with Reynold's number is observed, and the experimental value approaches the theoretical value at low Reynold's number. The reason for this discrepancy between experimental results and theoretical model is

unclear. This effect was not observed by Margolis *et al* [14,53], who achieved good correlation between experiment and theory. Further experimental tests would be necessary in order to ascertain the cause of this discrepancy.

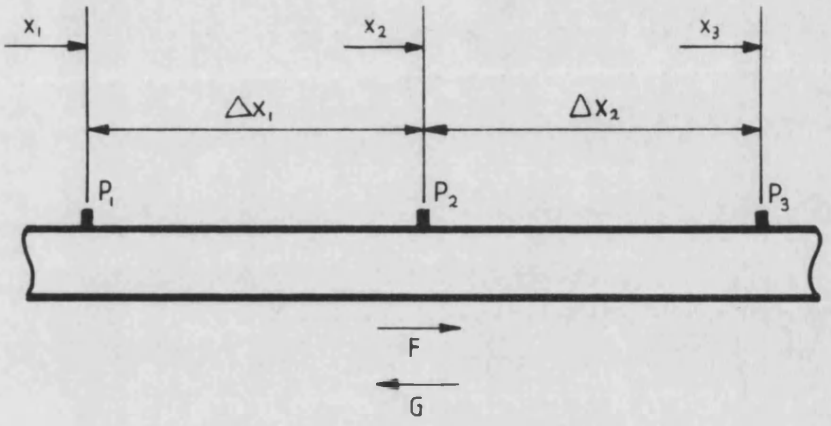

Fig. 7.1 Configuration of Transducers for Speed of Sound Measurement

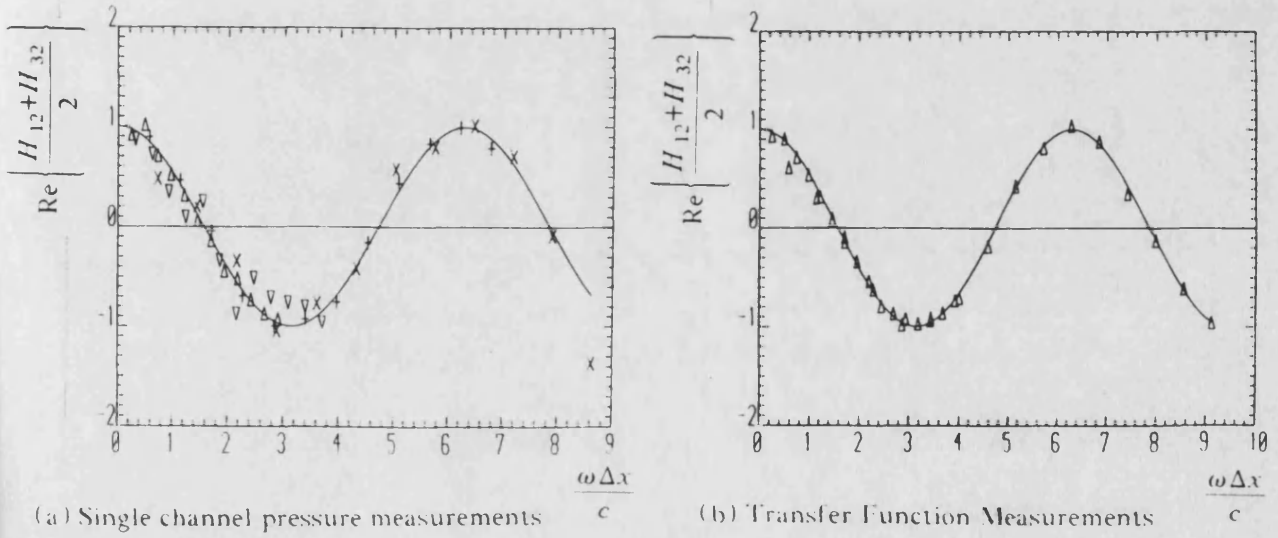

Fig. 7.2 Experimental Points and Least Squares Curve Fits used in Evaluation of Speed of Sound with 3 Equally Spaced Transducers

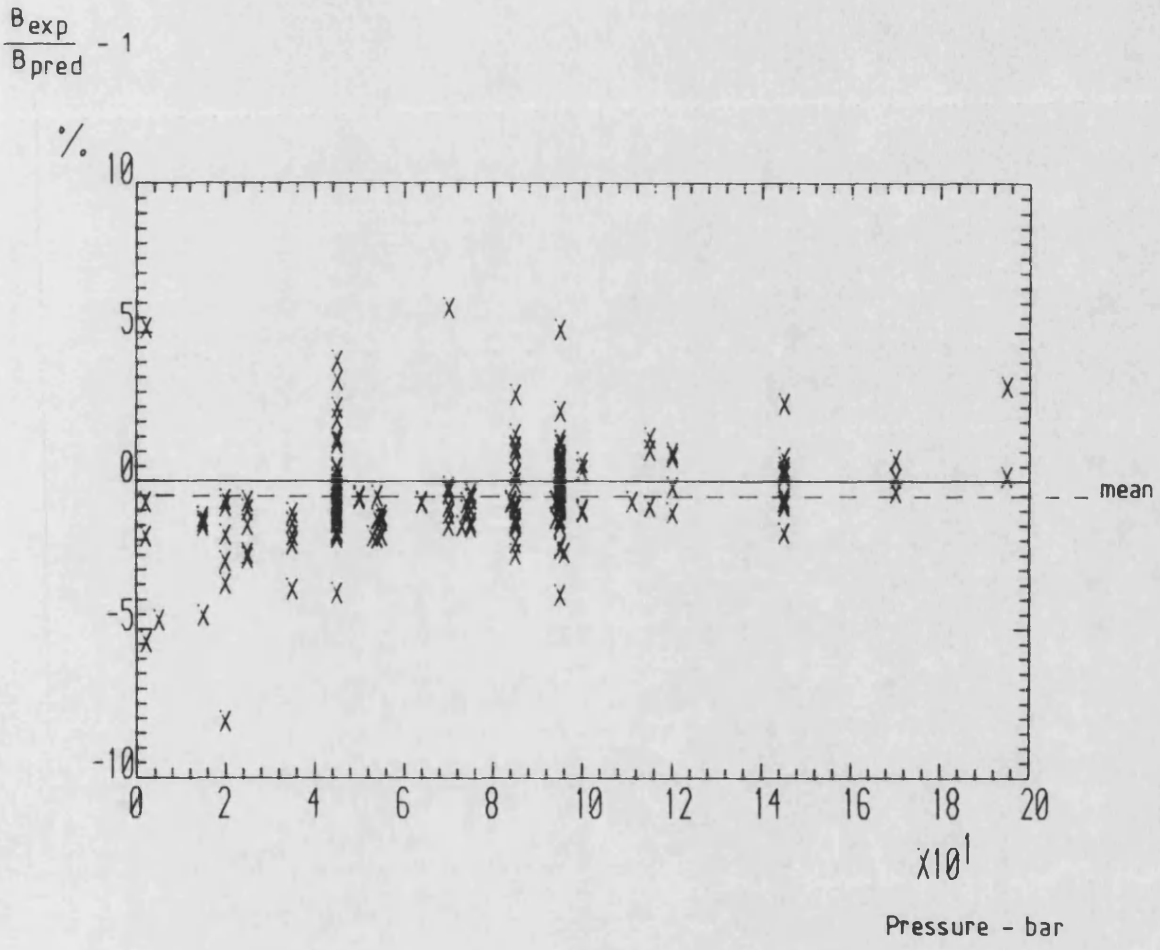

Fig. 7.3 Error between Predicted and Measured Bulk Modulus, as a Function of Mean Pressure

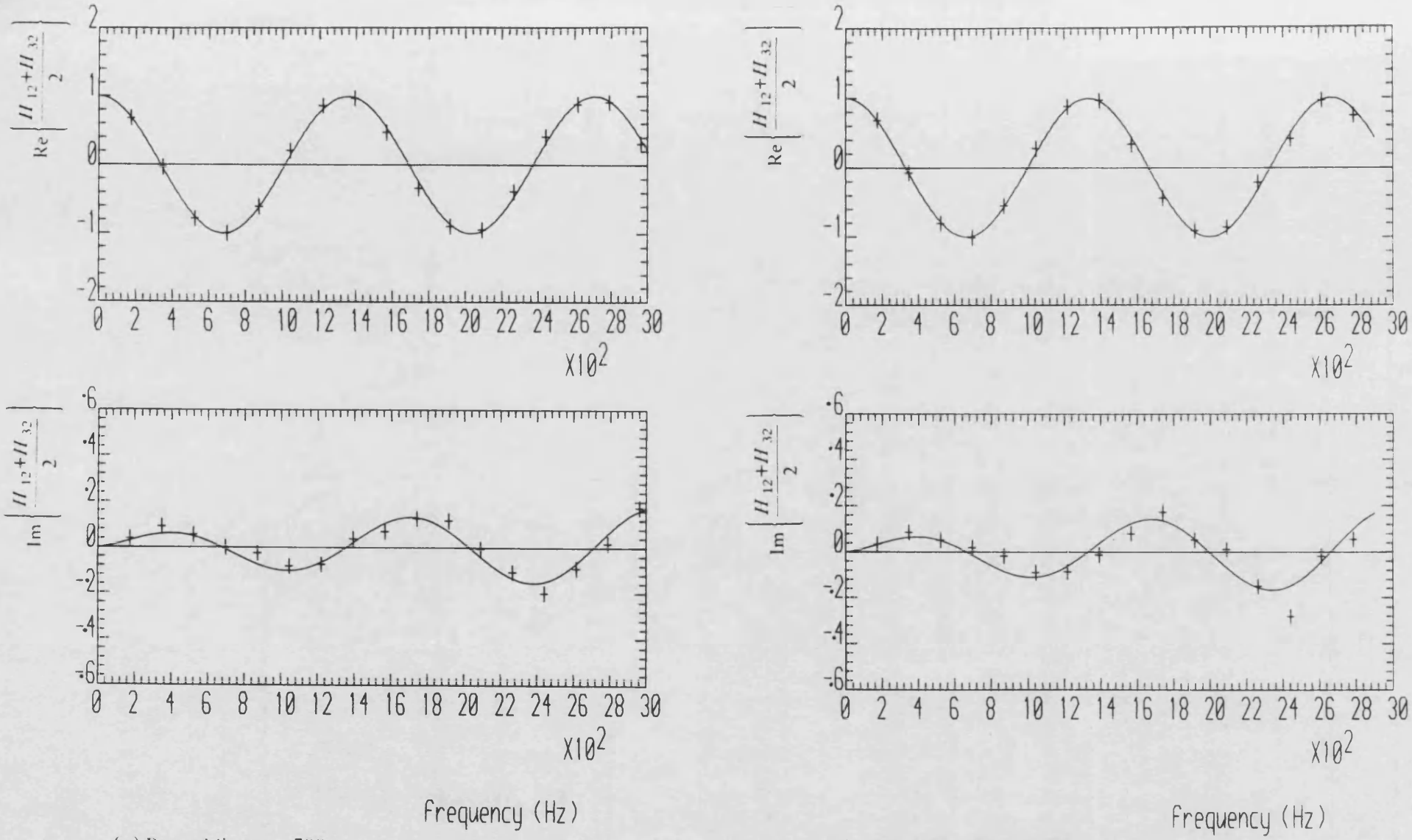

(a) Reynold's no. = 700

(b) Reynold's no. = 3000

Fig. 7.4 Experimental Points and Least Squares Curve Fits, Small Diameter Pipe

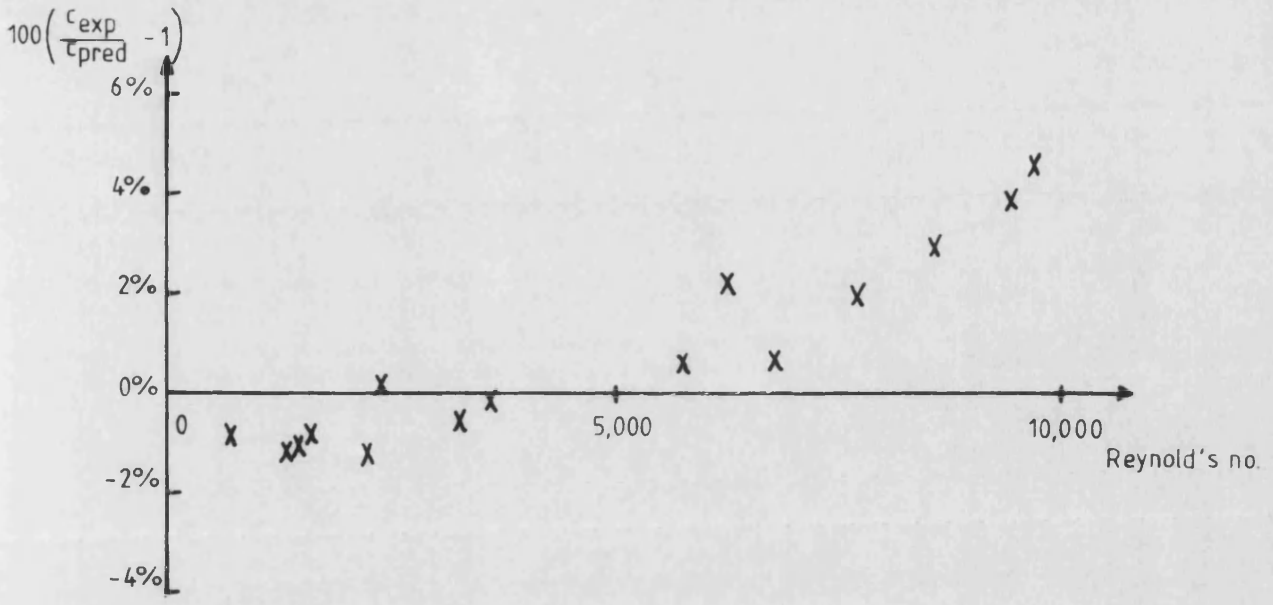

(a) Speed of Sound

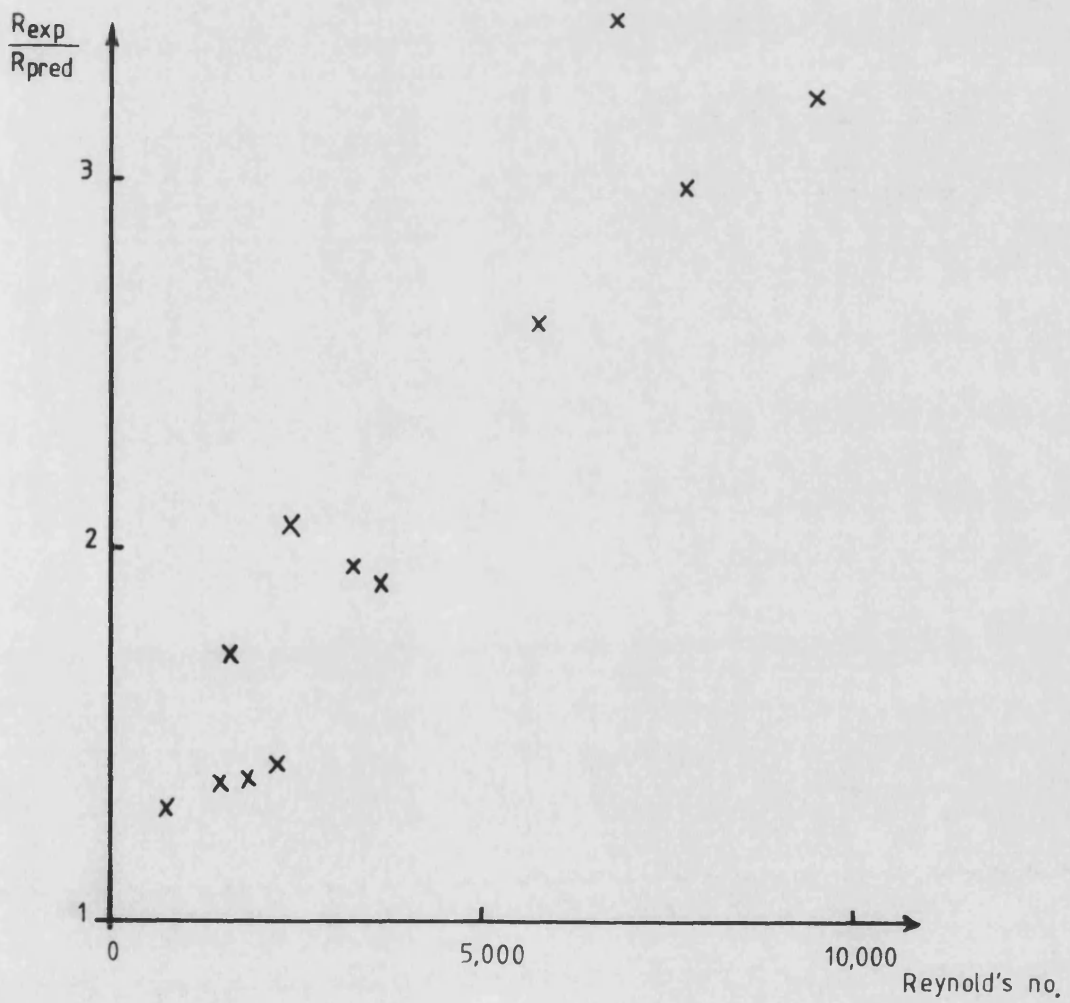

(b) Resistance Coefficient

Fig. 7.5 Relationships between Experimental and Predicted Speed of Sound and Resistance Coefficient Plotted as Functions of Reynold's number

CHAPTER 8

SIMULATION OF THE FLUID-BORNE NOISE CHARACTERISTICS OF HYDRAULIC CIRCUITS

The ability to predict the fluid-borne noise characteristics of complete hydraulic systems is clearly desirable. The pressure ripple levels in a circuit are strongly dependent upon the dimensions of the circuit and the characteristics of the individual components. A circuit may have a number of resonant frequencies, and if one or more of these coincides with an excitation frequency, such as a harmonic of the pump flow ripple, very high pressure ripple levels can be generated. Obviously such a condition needs to be avoided if possible. By careful selection of pipe lengths, for example, it may be possible to avoid such resonances.

In order to aid in the selection of suitable component dimensions at the design stage, it is necessary to be able to predict the resonant characteristics of the circuit, and this requires detailed knowledge of the characteristics of each component. For a complex circuit including branches and changes in section the equations describing the system can become extremely complicated. A computer program called 'PRASP' ('Pressure Ripple Automatic Simulation Package') has been developed to simulate the pressure ripple characteristics of hydraulic circuits of arbitrary complexity.

8.1. Mode of Operation of the Pressure Ripple Automatic Simulation Package

A detailed description of the 'PRASP' program algorithms is included in [33]. The mode of operation of the program can be broken down into several stages. These are:

a) interactive definition of circuit configuration.

b) interactive definition of component parameters, such as pipe lengths, etc.

c) interactive definition of sweep. A frequency sweep may be used, or component parameters such as pipe lengths may be varied.

d) generation and solution of simultaneous equations to calculate the pressure ripple and flow ripple at various points in the circuit.

e) output of results in the required format.

The program operation is best visualised by means of a simple example. Consider the circuit shown in Fig. 8.1(a) consisting of a pump, a length of rigid pipe, and a restrictor valve. Using standard impedance notation, the pump is represented by a flow ripple in parallel with a source impedance. The source impedance is a function of the pump discharge passageway, and can be considered to be equivalent to a length of pipe with a closed end.

8.1.1. Generation of Circuit Configuration

The program functions by breaking the circuit down into a number of separate blocks, each of which can be described by a simple set of equations. Thus the simple system shown in Fig. 8.1(a) can be represented as shown in Fig. 8.1(b). Each block has either one or two ports (inlet port and/or outlet port), and each port has two state variables, these being pressure and flow rate. Thus there are three classes of blocks:

a) those with an outlet port only, e.g. block <1> in Fig. 8.1(b). These blocks have two state variables, P_{OUT} and Q_{OUT}.

b) those with an inlet port only, e.g. blocks. <3> and <5>. The state variables are P_{IN} and Q_{IN}.

c) those with inlet and outlet ports, e.g. blocks <2> and <4>. The state variables are P_{IN}, Q_{IN}, P_{OUT} and Q_{OUT}.

The pressure and flow rate at the inlet and outlet of a block, P_{IN}, Q_{IN}, P_{OUT} and Q_{OUT}, are referred to as the 'local' state variables (LSV's), as they relate only to that block.

Block <1> represents the source flow ripple of the pump. Blocks <2> and <3> are a pipe model and a closed end model respectively, and represent the source impedance of the pump. In this case the source flow ripple is represented at the pump exit, using Norton's model. Block <4> represents the pipe, and block <5> the restrictor valve.

The blocks are connected together to form the circuit by 'links'. In this case there are three links, designated by (i), (ii) and (iii). The linking configuration is entered by the user and stored as an integer array in the computer, and for this circuit is represented as shown in table 8.1. Two types of link are defined, these being:

a) 'simple' links, where the outlet port of one block connects directly to the inlet port of another block.

b) 'junction' links, where more than one inlet port, and/or more than one outlet port, are connected.

At a simple link, such as link (ii), the outlet LSV's of one block are equal to the inlet LSV's of the other block. Thus a set of 'global' state variables (GSV's) can be defined which represent the pressure and flow rate at each link. A simple link has 2 GSV's associated with it, these being pressure and flow rate.

At a junction link, such as link (i), the flow rates from or to each block are related by the continuity equation $\sum Q_{IN} = \sum Q_{OUT}$. Each flow LSV at the junction link is assigned to one GSV. The pressure LSV's for each connected port are equivalent, so only one pressure GSV is necessary. Thus, link (i) has 6 LSV's but 4 GSV's associated with it.

Each GSV in the circuit is assigned a number, and an array is set up relating the LSV's for each block to the equivalent GSV number, as shown in table (8.1).

8.1.2. Definition of Component Parameters

Each component has a number of parameters associated with it. Thus, for example, for pipe <2> it is necessary to define the pipe length and internal diameter, and the fluid density, viscosity and effective bulk modulus.

8.1.3. Sweep Definition

Four different sweep options are available.

i) harmonic sweep. In this case, the fundamental frequency and number of harmonics are entered.

ii) linear frequency sweep. The minimum and maximum frequencies are entered, together with the number of incremental steps. The intermediate frequencies are

spaced equally between the minimum and maximum frequencies.

iii) logarithmic frequency sweep. Similar to (ii), except that the intermediate frequencies are spaced in a logarithmic manner.

iv) linear parametric sweep. In this mode it is possible to vary a number of the model parameters over a pre-defined range, at a fixed frequency. Thus, for example, the length of pipe <4> can be swept in order to determine the resonant lengths at one harmonic frequency of the pump. Up to 5 different parameters can be swept simultaneously.

8.1.4. Generation and Solution of Simultaneous Equations Defining System Response

At each step of the sweep, the following procedure is carried out. Firstly, the equations describing each model are formulated by a call to the relevant model subroutine. Single-port models generate one equation, whilst two-port models generate two equations.

Block <1>, a flow ripple source, is represented by the equation

$$Q_{OUT} = Q_S \qquad \ldots (8.1)$$

Note: Q_S is not a state variable, but is a constant input value to the system, which is entered by the user.

Blocks <2> and <4>, rigid pipe models, are represented by the following equations, which are obtained from the pipe transmission matrix (section 2.12.1.).

$$-P_{IN} + P_{OUT} \cosh \gamma l + Q_{OUT} Z_0 \sinh \gamma l = 0 \qquad \ldots (8.2)$$

$$-Q_{IN} + P_{OUT} / Z_0 \sinh \gamma l + Q_{OUT} \cosh \gamma l = 0 \qquad \ldots (8.3)$$

Block <3>, a closed end model, is represented by the equation

$$Q_{IN} = 0 \qquad \ldots (8.4)$$

Block <5>, a simple single port restrictor valve model, is represented by the equation

$$-P_{IN} + Q_{IN} Z_v = 0 \qquad \ldots (8.5)$$

The resistance of the valve is assumed to be a function of its steady state characteristic. Capacitive effects, due to the volume contained in the valve upstream of the orifice, are also considered. Thus,

$$Z_v = \frac{R_v}{j\omega V / BR_v + 1}$$

where $R_v = \frac{nP_{mean}}{Q_{mean}}$

n is the exponent of the steady state characteristic at the operating point, and normally has a value of between 1.0 (laminar flow) and 2.0 (turbulent flow).

In order to complete the circuit description, a flow continuity equation is required for junction link (i). Thus

$$Q_{OUT\ <1>} - Q_{IN\ <2>} - Q_{IN\ <4>} = 0 \qquad \ldots (8.6)$$

The model equations need to be solved simultaneously. This solution will yield the values of all the state variables. In order to solve these equations they are first collated into a single global matrix equation of the form

$$\mathbf{S\,Y = T} \qquad \ldots (8.7)$$

Y is a column matrix containing the global state variables. **T** is a column matrix containing the input values (the right-hand sides of equations (8.1) - (8.5). **S** contains the coefficients of the GSV's. Thus, each of the equations generated by the models is represented by one row in matrices **S** and **T**.

This matrix equation is solved by a process of Gaussian elimination with partial pivoting. The resultant state variables are stored in a file, and this process is repeated for each stage of the sweep.

8.1.5. Output of Results in the Required Format

The data obtained by the solution of the matrix equation need to be post-processed in order that they can be presented in a useful form. A number of different graphical formats are available, including bode plots of amplitude and phase, and inverse Fourier transformed waveform plots. Any of the state variables can be plotted individually. Alternatively, the ratio of any pair of state variables can be plotted. Thus, for example, the entry impedance of the loading circuit of the pump can be examined by plotting the ratio of GSV no. 1 (P_{IN}, block <4>) to GSV no. 4 (Q_{IN}, block <4>). The results can be multiplied by a scaling factor, if required, in order to present them in the required units.

8.2. Formulation of a Comprehensive Model for a Flexible Hose

The wave propagation characteristics of flexible hoses differ from those of rigid pipes. They generally have a lower wall stiffness which tends to reduce significantly the effective bulk modulus of the fluid, and hence the wavespeed. Together with fluid wave propagation, there is the secondary effect of wave propagation in the hose wall, which is coupled to the fluid wave. The net effect of this is that two distinct fluid wave speeds occur, and these considerably complicate the analysis of the hose behaviour.

The general wave equations for a flexible hose, representing the fluid pressure and the axial motion of the fluid and hose wall, were formulated by Longmore and Tuc [37-39], and are reproduced below:

$$U(x) = k_1 e^{-\gamma_1 x} + k_2 e^{\gamma_1 x} + k_3 e^{-\gamma_2 x} + k_4 e^{\gamma_2 x} \qquad \ldots (8.8)$$

$$W(x) = N_1(k_1 e^{-\gamma_1 x} + k_2 e^{\gamma_1 x}) + N_2(k_3 e^{-\gamma_2 x} + k_4 e^{\gamma_2 x}) \qquad \ldots (8.9)$$

$$P(x) = Z_{P1}(k_1 e^{-\gamma_1 x} - k_2 e^{\gamma_1 x}) + Z_{P2}(k_3 e^{-\gamma_2 x} - k_4 e^{\gamma_2 x}) \qquad \ldots (8.10)$$

where $U(x)$= harmonic axial displacement of fluid at position x
$W(x)$= harmonic axial displacement of hose wall
$P(x)$= harmonic pressure ripple in fluid.

Two modes of wave propagation exist in the hose, represented by the propagation constants γ_1 and γ_2. The values of k_1, k_2, k_3 and k_4 are dependent on the boundary conditions. N_1 and N_2 are known as the 'modal ratios' and specify the relative amounts of wall and fluid motion associated with each wave. Z_{P1} and Z_{P2} are referred to as the 'characteristic displacement impedances', and are related to the characteristic impedances by the equation

$$Z_P = Aj\omega Z_0. \qquad \ldots (8.11)$$

In order that the transmission matrix can be derived relating the pressure and flow (or fluid displacement), it is necessary to apply boundary conditions to the hose wall displacement. In this analysis, it is assumed that the hose is rigidly mounted at each end, so that $W(0) = 0$ and $W(l) = 0$.

The impedance matrix relates the pressure and flow by the equation:

$$\begin{bmatrix} P(0) \\ P(l) \end{bmatrix} = \mathbf{Z} \begin{bmatrix} Q(0) \\ Q(l) \end{bmatrix} \qquad \ldots (8.12)$$

$$\text{where } \mathbf{Z} = \begin{bmatrix} z_{1,1} & z_{1,2} \\ z_{2,1} & z_{2,2} \end{bmatrix} \qquad \ldots (8.13)$$

$$\text{and } Q(x) = Aj\omega U(x). \qquad \ldots (8.14)$$

Substituting the boundary conditions $W(0) = 0$ and $W(l) = 0$ into equation (8.9):

$$W(0) = 0 = N_1(k_1+k_2) + N_2(k_3+k_4) \qquad \ldots (8.15)$$

$$W(l) = 0 = N_1(k_1 e^{-\gamma_1 l} + k_2 e^{\gamma_1 l}) + N_2(k_3 e^{-\gamma_2 l} + k_4 e^{\gamma_2 l}). \qquad \ldots (8.16)$$

In order to find $z_{1,1}$ and $z_{2,1}$, we consider the hose to be connected to a load of infinite impedance. Thus, $U(l) = 0$, and from equations (8.12-8.14),

$$P(0) = z_{1,1} Aj\omega U(0) \qquad \ldots (8.17)$$

$$P(l) = z_{2,1} Aj\omega U(0). \qquad \ldots (8.18)$$

From equation (8.8),

$$U(l) = 0 = k_1 e^{-\gamma_1 l} + k_2 e^{\gamma_1 l} + k_3 e^{-\gamma_2 l} + k_4 e^{\gamma_2 l}. \quad \ldots (8.19)$$

From equations (8.16) and (8.19)

$$k_1 e^{-\gamma_1 l} + k_2 e^{\gamma_1 l} = 0 \text{ or } k_2 = -k_1 e^{2\gamma_1 l} \quad \ldots (8.20)$$

$$k_3 e^{-\gamma_2 l} + k_4 e^{\gamma_2 l} = 0 \text{ or } k_4 = -k_3 e^{2\gamma_2 l}. \quad \ldots (8.21)$$

Substituting (8.20) and (8.21) into (8.15),

$$k_3 = -\frac{k_1 N_1 (1-e^{2\gamma_1 l})}{N_2 (1-e^{2\gamma_2 l})} \quad \ldots (8.22)$$

Thus,

$$U(0) = k_1 \left[1 - \frac{N_1}{N_2}\right] e^{-2\gamma_1 l} \quad \ldots (8.23)$$

$$P(0) = k_1 \left[Z_{P1}(1+e^{-2\gamma_1 l}) - \frac{Z_{P2} N_1 (1-e^{-2\gamma_1 l})(1+e^{-2\gamma_2 l})}{N_2 (1-e^{-2\gamma_2 l})}\right] \quad \ldots (8.24)$$

$$P(l) = k_1 \left[Z_{P1} 2e^{-\gamma_1 l} - \frac{Z_{P2} N_1 (1-e^{-2\gamma_1 l}) 2e^{-\gamma_2 l}}{N_2 (1-e^{-2\gamma_2 l})}\right] \quad \ldots (8.25)$$

$$\text{but, } z_{1,1} = \frac{P(0)}{Q(0)} = \frac{1}{Aj\omega} \frac{P(0)}{U(0)} \quad \ldots (8.26)$$

$$\text{and } z_{2,1} = \frac{P(l)}{Q(0)} = \frac{1}{Aj\omega} \frac{P(l)}{U(0)}. \quad \ldots (8.27)$$

It can be shown that, substituting equations (8.23) and (8.24) into (8.27),

$$z_{1,1} = \frac{N_2 Z_{P1} \coth(\gamma_1 l) - N_1 Z_{P2} \coth(\gamma_2 l)}{Aj\omega (N_2 - N_1)}. \quad \ldots (8.28)$$

Similarly, substituting equations (8.23) and (8.25) into (8.27),

$$z_{2,1} = \frac{N_2 Z_{P1} \operatorname{cosech}(\gamma_1 l) - N_1 Z_{P2} \operatorname{cosech}(\gamma_2 l)}{A j\omega (N_2 - N_1)} \qquad \ldots (8.29)$$

or, substituting equation (8.11) into (8.28) and (8.29),

$$z_{1,1} = \frac{\frac{N_2}{N_1} Z_{01} \coth(\gamma_1 l) - Z_{02} \coth(\gamma_2 l)}{\frac{N_2}{N_1} - 1} \qquad \ldots (8.30)$$

$$z_{2,1} = \frac{\frac{N_2}{N_1} Z_{01} \operatorname{cosech}(\gamma_1 l) - Z_{02} \operatorname{cosech}(\gamma_2 l)}{\frac{N_2}{N_1} - 1}. \qquad \ldots (8.31)$$

A similar technique may be used to derive $z_{1,2}$ and $z_{2,2}$ by setting $U(0) = 0$. However, because of the inherent end-to-end symmetry of the hose, the relationship between $P(0)$ and $Q(0)$ when $Q(l) = 0$ is the same as that between $P(l)$ and $-Q(l)$ when $Q(0) = 0$. Thus $z_{2,2} = -z_{1,1}$. Similarly, the relationship between $P(l)$ and $Q(0)$ when $Q(l) = 0$ is the same as that between $P(0)$ and $-Q(l)$ when $Q(0) = 0$. Thus $z_{1,2} = -z_{2,1}$.

In order to produce a model of a hose, it is necessary to obtain values of the properties N_2/N_1, Z_{01}, Z_{02}, γ_1 and γ_2, all of which are complex and may be frequency dependent.

A number of assumptions were made by Longmore and Tuc in order to simplify the estimation of the hose properties. These assumptions were backed up by experimental work and were found to be valid.

a) The value of N_2/N_1 is independent of frequency.

b) The wave propagation coefficients γ_i can be represented in the form

$$\gamma_i = (\tilde{\alpha}_i + j\tilde{\beta}_i)\omega \qquad \ldots (8.32)$$

where $\tilde{\alpha}_i$ and $\tilde{\beta}_i$ are independent of frequency.

c) The characteristic displacement impedances Z_{Pi} are represented by the equation

$$Z_{Pi} = -\frac{\omega^2 \rho}{\gamma_i} \qquad \ldots (8.33)$$

$$\text{or } Z_{0i} = \frac{\rho}{A(\beta_i - j\alpha_i)} \qquad \ldots (8.34)$$

where ρ is the density of the oil.

Therefore, in order to model a flexible hose, the parameters N_2/N_1, α_1, β_1, α_2 and β_2 are required, as well as the internal cross-sectional area A and fluid density ρ. These parameters are dependent upon the type of hose and its internal diameter. In order to produce a model which could represent a range of different hoses, they would have to be known for each type of hose. A data base containing them could be built up from empirical values obtained from experimental tests on the hoses.

The above analysis ignores the effect of the end fittings. These can be taken into account by modelling them as short lengths of rigid pipe. The overall transmission matrix for the hose with fittings, $\mathbf{T}_{overall}$, can be calculated by multiplication of the individual transmission matrices for the hose and fittings, i.e.

$$\mathbf{T}_{overall} = \mathbf{T}_{fitting} \cdot \mathbf{T}_{hose} \cdot \mathbf{T}_{fitting} \qquad \ldots (8.35)$$

The transmission matrix of the hose, $\mathbf{T}_{hose}$, can be calculated by algebraic manipulation of the hose impedance matrix, which is derived above.

8.2.1. Evaluation of Accuracy of Hose Model

In order to check the validity of the hose model, an experimental circuit was set up with a hose for which the parameters N_2/N_1, α_1, β_1, α_2 and β_2 had already been determined empirically from experimental tests by Longmore (personal communication). Pressure ripple was measured at various points, and the entry impedance of the hose was evaluated, using the method described in chapter 6. These measurements were compared with those obtained from a simulation of the circuit. Pump 'A' was used as the source, and experimentally obtained Q_S values were used in the circuit simulation.

The experimental and simulated pressure ripple upstream of the hose, with 1 m and 3 m lengths of hose, are plotted in Fig. 8.2. Correlation between simulation and experiment can be seen to be reasonable in each case. Corresponding entry impedance bode plots are shown in Fig. 8.3. The correlation between simulation and experiment is fairly good up to about 1.5 kHz, above which large discrepancies are apparent. It is thought that these discrepancies may be attributed in part to bends in the hose during the experimental tests. The model was formulated on the assumption that the hose should be straight; however, in practical circuits, it is highly likely that hoses would be bent.

8.3. Modelling of Pump Flow Ripple Characteristics

At any particular harmonic frequency, the pressure ripple at any point in a circuit is directly proportional to the source flow ripple, Q_S. The resonant characteristics of the system are independent of the values of Q_S. Thus the accuracy of a circuit simulation is not as sensitive to Q_S as it is to, for example, the length of a pipe or the source impedance Z_S. In most situations, then, an approximation to Q_S, based upon a simple mathematical model, should be adequate.

8.3.1. External Gear Pump Flow Ripple Model

The theoretical source flow ripple from an external gear pump is well known and is described in section 2.1.2. The spectrum of this flow ripple can be determined by Fourier transformation of equation (2.2). The harmonic values can be shown to be given by

$$Q_S(i_H) = -4\frac{K}{i_H^2} \qquad \ldots (8.36)$$

where K is a constant for a particular pump and is described in section 2.1.2.

Thus the harmonic amplitude is inversely proportional to the square of the harmonic number. This means that the ideal flow ripple from a gear pump consists of a strong first harmonic and rapidly diminishing higher harmonics. In the simulation of a gear pump, then, it is unlikely to be necessary to consider more than 5 harmonics.

8.3.2. Axial Piston Pump Flow Ripple Model

A comprehensive dynamic model for simulating the flow ripple from an axial piston pump was developed by Darling [7], and its use is described in section 9.1.1. This model was found to give good results, but required detailed information about the internal geometry of the pump, information which might not be available to the user.

However, a simple empirical piston pump flow ripple model can be formulated by inspection of the general form of the harmonic spectra. Fig. 8.4 shows typical spectra obtained from tests on pumps 'A' and 'B'. It can be seen that the amplitude spectra can be approximated to a triangular envelope. It was shown in section 5.2.1. that the phase spectrum can be simplified by shifting the effective angular position of the phase reference so that the phases of the harmonics lie close to 180°. By making the simplifying assumption that the phase of each harmonic equals 180°, the following model is obtained:

$$Q_S(i_H) = -(A - Bi_H), \text{ for } 1 \leqslant i_H < A/B \qquad \ldots (8.37)$$

A and B define the harmonic amplitudes and the maximum frequency, and are dependent upon the pump type and the operating conditions. They can be determined provided that any two of the following parameters are known:

a) the total compressibility flow into a cylinder

b) the maximum significant harmonic frequency or the number of significant harmonics

c) the amplitude of the backflow.

Parameter (a) can be predicted quite easily if the cylinder volume is known at BDC, and the effective bulk modulus within the cylinder can be estimated. Parameters (b) and (c) are more difficult to determine, and can only be estimated unless detailed flow ripple characteristics are already available. Parameter (b) can be estimated empirically, either by inspection of experimental pressure ripple measurements in a circuit containing the pump in order to estimate the highest frequency component, or by using information gained from experience of the characteristics of pumps of fundamentally similar design.

It must be stressed that this model is only intended to provide a guide as to the flow ripple characteristics of the pump, and is unlikely to be as accurate as simulation results using the model developed by Darling [7], or experimental results using, for example, the 'Secondary Source' method. However, since the flow ripple has no effect on the resonant characteristics of a hydraulic circuit, it may be sufficiently accurate for use in the simulation of the fluid-borne noise characteristics in such a circuit.

The model spectrum as shown in Fig. 8.5(a) produces a waveform as shown in Fig. 8.5(b). Harmonic no. i_H is represented by the equation

$$Q_S(i_H) = -Q_0(1 - i_H f_0/f_{max}). \qquad \ldots (8.38)$$

Thus the instantaneous flow at time t is given by the equation

$$q_S(t) = -Q_0 \sum_{i_H=1}^{n_H} (1 - i_H f_0/f_{max}) \cos 2\pi f_0 i_H t. \qquad \ldots (8.39)$$

where $n_H = f_{max}/f_0$, rounded off to the nearest integer.

The value of Q_0 can be determined by consideration of the volume of the backflow pulse. Considering the graph of the flow ripple waveform shown in Fig. 8.5(b), as the mean flow is assumed to be zero the graphical area bounded by the the flow ripple above the x-axis is equal to the area bounded by the flow ripple below the x-axis. Therefore,

$$\text{pulse volume} = \frac{V_P \Delta\tilde{P}}{B_{eff}} \approx T\, q_S(T/2) \qquad \ldots (8.40)$$

where V_P is the volume contained in one cylinder at BDC, $\Delta\tilde{P}$ is the mean pressure difference across the pump, and B_{eff} is the effective bulk modulus of the fluid in the cylinder. T is the cyclic period, defined as $T = 1/f_0$.

$$\begin{aligned} \text{But } q_S(T/2) &= -Q_0 \sum_{i_H=1}^{n_H} (1 - i_H f_0/f_{max}) \cos(i_H \pi) \\ &= -Q_0 \sum_{i_H=1}^{n_H} (1 - i_H f_0/f_{max})(-1)^{i_H} \end{aligned} \qquad \ldots (8.41)$$

Therefore,

$$Q_0 = \frac{V_p \Delta \tilde{P}}{B_{eff} \sum_{i_H=1}^{n_H} (i_H / f_{max} - 1/f_0)(-1)^{i_H}} \quad \ldots (8.42)$$

The kinematic flow ripple, although normally small compared to the compressibility flow, may be significant at low mean pressures. It is simple to predict and can easily be incorporated into the model. It can be shown that the value $Q_k(i_H)$ of harmonic no. i_H can be described by the equation

$$Q_k(i_H) = \frac{2\tilde{Q}}{(i_H z)^2 - 1} \cos(\pi i_H z/2)\, e^{j i_H z \pi/2} \quad \ldots (8.43)$$

where $\tilde{Q}$ is the mean flow from the pump, and z is the number of cylinders in the pump (note: if z is odd the amplitudes of the even harmonics will equal zero). Thus the overall modelled flow ripple is given by the equation

$$Q_S(i_H) = -Q_0(1 - i_H f_0/f_{max}) + 2\frac{\tilde{Q}}{(i_H z)^2 - 1} \cos(\pi i_H z/2)\, e^{j i_H z \pi/2} \quad \ldots (8.44)$$

where $Q_0 = \dfrac{V_p \Delta \tilde{P}}{B_{eff} \sum_{i_H=1}^{n_H} (i_H / f_{max} - 1/f_0)(-1)^{i_H}}$ $\quad \ldots (8.45)$

Typical results obtained by applying this model to pump 'A' are shown in Figs. 8.6(b) and 8.7(b), at mean pressures of 25 bar and 100 bar respectively. A cut-off frequency f_{max} of 3.5 kHz was assumed. It can be seen by comparison with Figs. 8.6(a) and 8.7(a) that there is reasonably good agreement between the model and experimental results, although the model is unable to simulate the overshoot and oscillation characteristics displayed by the experimental results.

8.4. Validation of Simulation Results

In order to assess the validity of simulations performed using the 'PRASP' package, comparisons were made between experimental pressure ripple measurements and corresponding simulation results on a number of different hydraulic circuits. One such circuit is shown in Fig. 8.8(a). The corresponding 'PRASP' block diagram for this is shown in Fig. 8.8(b). The pump source impedance was predicted from the measured internal volume and length of the pump discharge passageway.

Fig. 8.9(a) shows a typical experimental pressure ripple waveform, and Fig. 8.9(b) shows the equivalent simulated pressure ripple, evaluated using source flow ripple data obtained from experimental tests using the 'Secondary Source' method. The corresponding amplitude spectra are shown in Fig. 8.10(a) and (b). Good correlation is apparent, particularly between the amplitude spectra. The correlation between the peak-to-peak values is good. Fig. 8.9(c) and 8.10(c) show the simulated waveform and amplitude spectrum in which the source flow ripple model is obtained using the empirical model described in section 8.3.2. It can be seen that, although the waveform and amplitude spectrum have similar shapes to the experimental ones, the amplitudes are smaller. This is due to the fact that the simple model predicts a smaller flow ripple than the experimentally measured flow ripple. However, the overall shapes of the amplitude spectra in Fig. 8.10(a) and (c) are very similar, indicating that the simple flow ripple model is sufficiently representative to give a good indication of the circuit characteristics. In both experimental and simulated amplitude spectra, it is apparent that there is a minimum at the second harmonic and maxima at the fourth and seventh harmonics. This indicates that the simulations provide good predictions of the resonant characteristics of the circuit.

8.5. Simulation of Pump Source Impedance Characteristics

By applying distributed parameter models to the source impedance results, it is possible to evaluate the 'apparent length' and 'apparent volume' of the pump discharge passageway. The apparent length is dependent upon the measured first anti-resonant frequency, and the apparent volume on the measured capacitive impedance at low frequency. Apparent lengths and volumes were compared with physically measured lengths and volumes for several pumps by Edge [32]. Very large discrepancies were reported in some cases. It was found that the apparent volumes were between 5% and 300% greater than the measured volumes. Similarly, the apparent lengths were between 20% and 200% greater than the measured lengths. Possible reasons for these discrepancies are considered to be:

a) difficulty in measuring the discharge volume and length. The volume was measured by pouring oil into the discharge port. This was difficult to perform accurately, because of the difficulty in expelling trapped air from the chamber. However, it was considered unlikely that this could cause some of the large variations reported.

b) local reduction in the effective bulk modulus due to compliance of the casing and moving parts, and/or due to cavitation. This would tend to increase the apparent length and volume.

c) the complex geometry of the discharge passageway. Any changes in the characteristic impedance along its length, due either to changes in the cross-sectional area or changes in the effective bulk modulus, could have a significant effect on the anti-resonant frequency, and hence the apparent length.

Simulations were performed on the source impedance characteristics of pumps 'A', 'C' and 'D'. The internal dimensions of the discharge passageways were measured after the pumps had been dismantled. It was necessary to make some simplifications to the geometry for the simulation to be viable without being over-complex. Thus only significant changes in cross-sectional area were modelled. Frictional effects were ignored in the simulations. Because the effective bulk modulus inside the pump was not known, the value used in the simulations was adjusted by trial and error, where necessary, in order to produce good agreement between experiment and theory.

8.5.1. Source Impedance Simulation - Pump 'A'

In order to measure the discharge volume of this pump, it was necessary to make certain assumptions. Being a 7 cylinder axial piston pump, either three or four cylinders are open to the discharge port at any one time, so that the effective volume fluctuates. It was postulated by Wing [26], however, that since the change in this volume is periodic, then it may be accounted for as a flow ripple effect. The variation in volume is small, however, so its effect may be negligible. It was assumed that the simulated volume was equal to the mean volume, by including the volume contained by 3½ cylinders with their pistons at mid-stroke. For simplicity, the cylinders were lumped together and modelled as one equivalent passageway.

The simplified model is shown in Fig. 8.11(a). The simulated frequency characteristics are compared with measured results in Fig. 8.11(b). The bulk modulus used in the simulation was that of the fluid alone. A reasonable correlation between experiment and theory is obtained, the magnitude of the simulated impedance being about 2 dB (25%) less than the experimental results. Thus in this case the effective volume is less than the measured volume.

8.5.2. Source Impedance Simulation - Pump 'C'

The model used in the simulation of this pump is shown in Fig. 8.12(a). Considering Fig. 8.12(b), correlation between simulation and experimental results is shown to be good. However, in order to obtain this correlation, it was necessary to reduce the effective bulk modulus to 4×10^8 N/m^2, about 25% of that of the fluid itself.

8.5.3. Source Impedance Simulation - Pump 'D'

Fig. 8.13(a) shows the model used, and Fig. 8.13(b) shows the comparison between experiment and simulation. To achieve good agreement, it was necessary to use different values of bulk moduli along the length of the discharge passageway, such that the bulk modulus in the gear cavity was less than that in the discharge port. This could be the case in practice: compliance of the gear bearings or thrust plates could cause a local reduction in the gear cavity.

Considering the simulations of the gear pumps, 'C' and 'D', the modelled discharge passageway has a small diameter discharge port and large diameter internal chamber. This geometry is similar to that of a Helmholz resonator. Such a geometry will cause an anti-resonance at a lower frequency than that of a similar length of uniform cross-section. This may explain why Edge [32] found the effective length for gear pumps to be much greater than the measured length.

The above simulations highlight the difficulty in the prediction of the source impedance characteristics from measurement of the pump dimensions. The prediction of the effective bulk modulus within the pump appears to be the main problem: a 4:1 ratio between the effective bulk moduli was observed in the above simulations on different pumps.

Block no.	Type	Link no.		GSV no.			
		Inlet	Outlet	P_{IN}	Q_{IN}	P_{OUT}	Q_{OUT}
<1>	QS	...	(i)	...	...	1	2
<2>	PIPE	(i)	(ii)	1	3	5	6
<3>	CLOSE	(ii)	...	5	6	...	...
<4>	PIPE	(i)	(iii)	1	4	7	8
<5>	RV1P	(iii)	...	7	8	...	...

Table 8.1 'PRASP' Linking Configuration for Simple Hydraulic Circuit

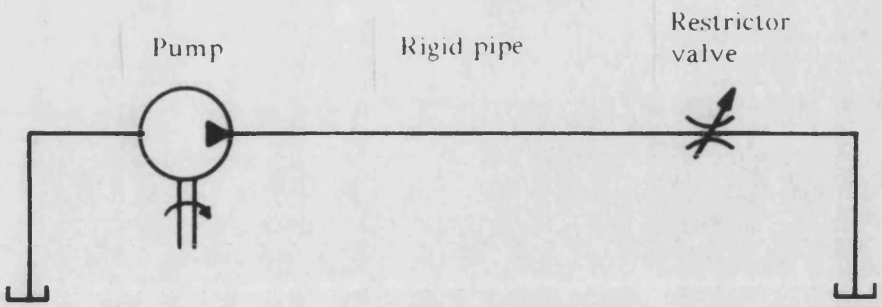

(a) Simple circuit

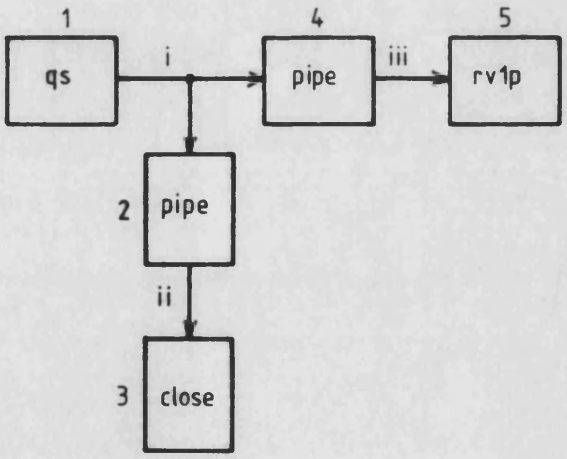

(b) Block diagram

Fig. 8.1 Simple Hydraulic Circuit and Representation in Block Diagram Form

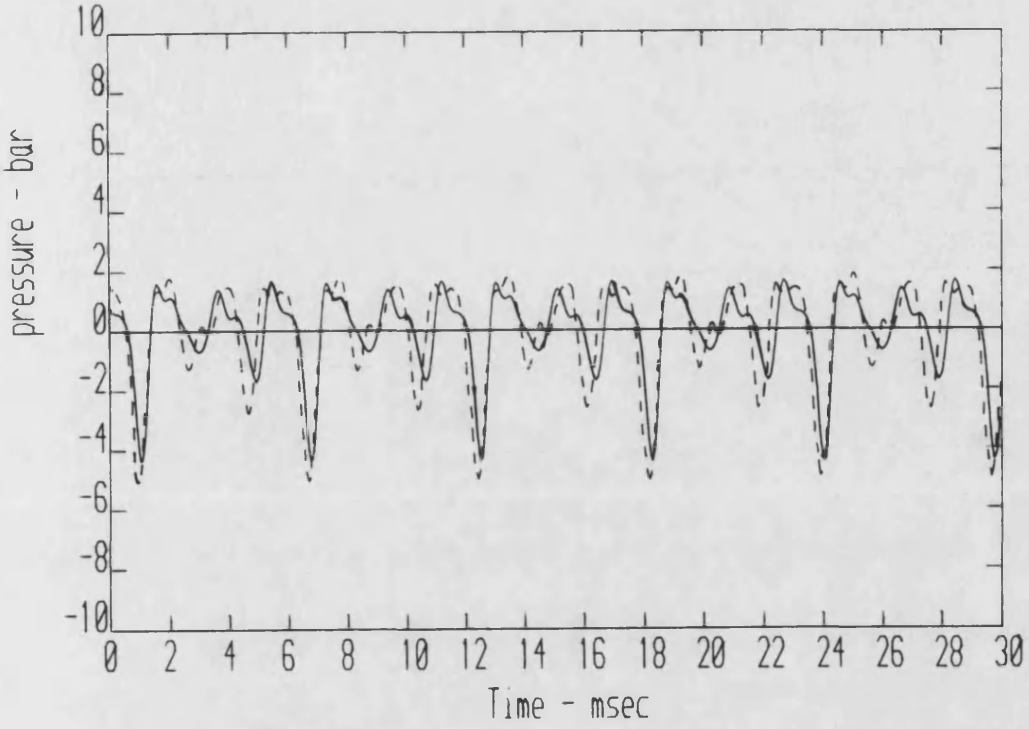

(a) Hose length = 0.8 m

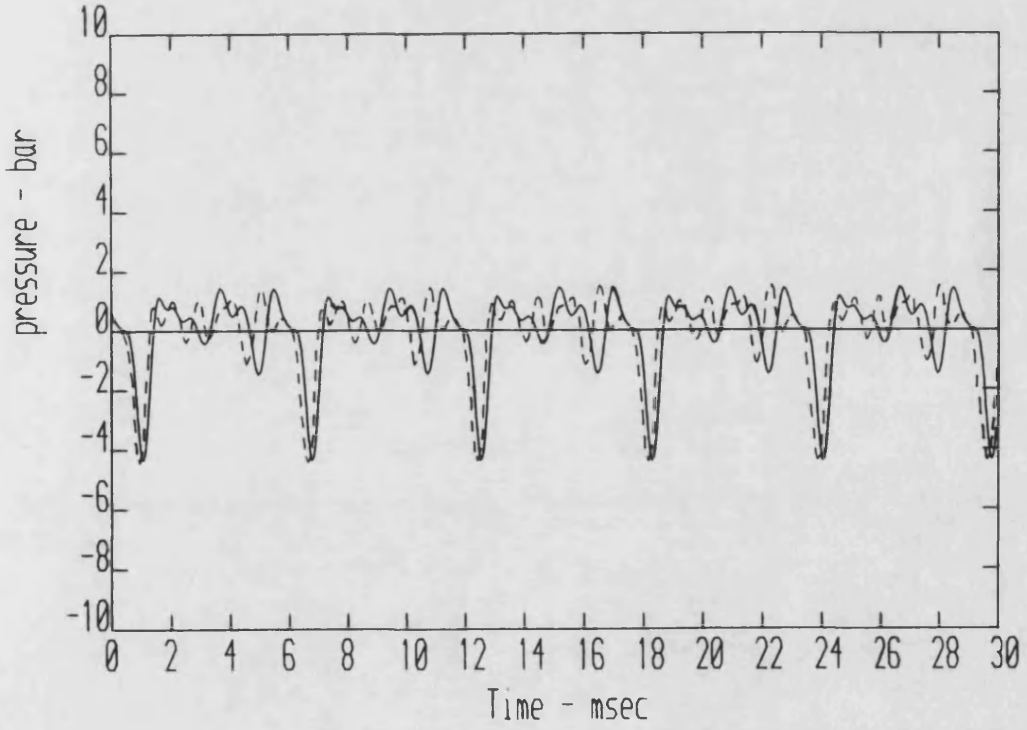

(b) Hose length = 2.8 m

measured
simulated

Fig. 8.2 **Experimental and Simulated Pressure Ripple Waveforms in Circuit with Hose**

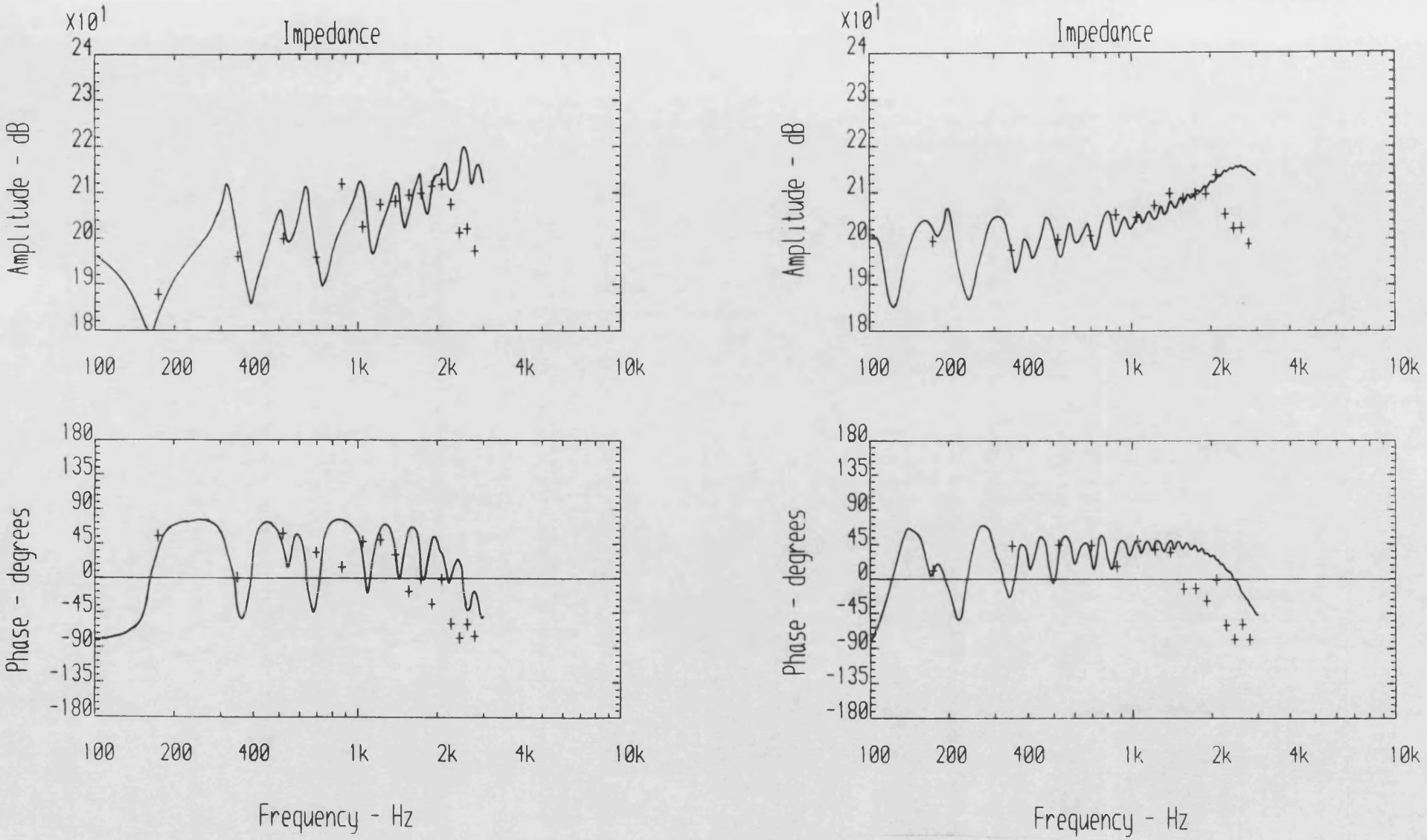

(a) Hose length = 0.8 m

(b) Hose length = 2.8 m

Fig. 8.3 Experimental and Simulated Hose Entry Impedances

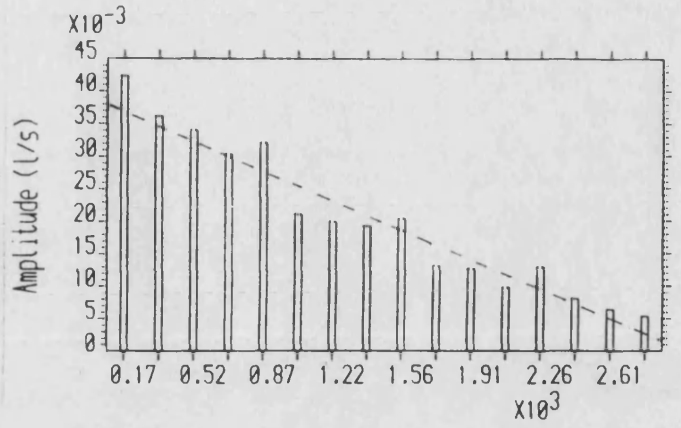

(a) Pump 'A', 175 bar, 1500 rev/min

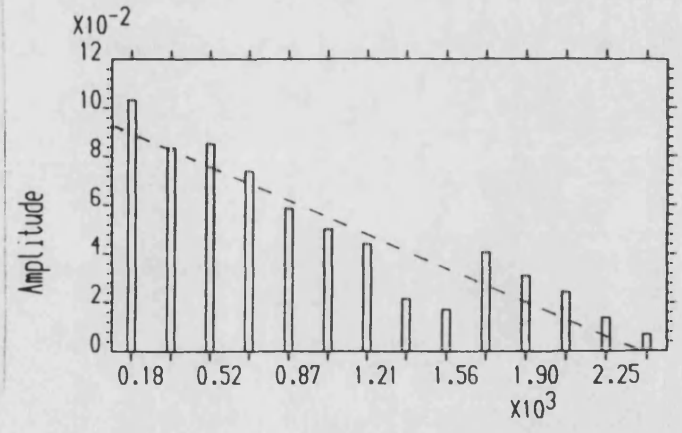

(b) Pump 'B', 150 bar, 1500 rev/min

Fig. 8.4 **Axial Piston Pump Harmonic Amplitude Spectra, and Representation using Triangular Envelope**

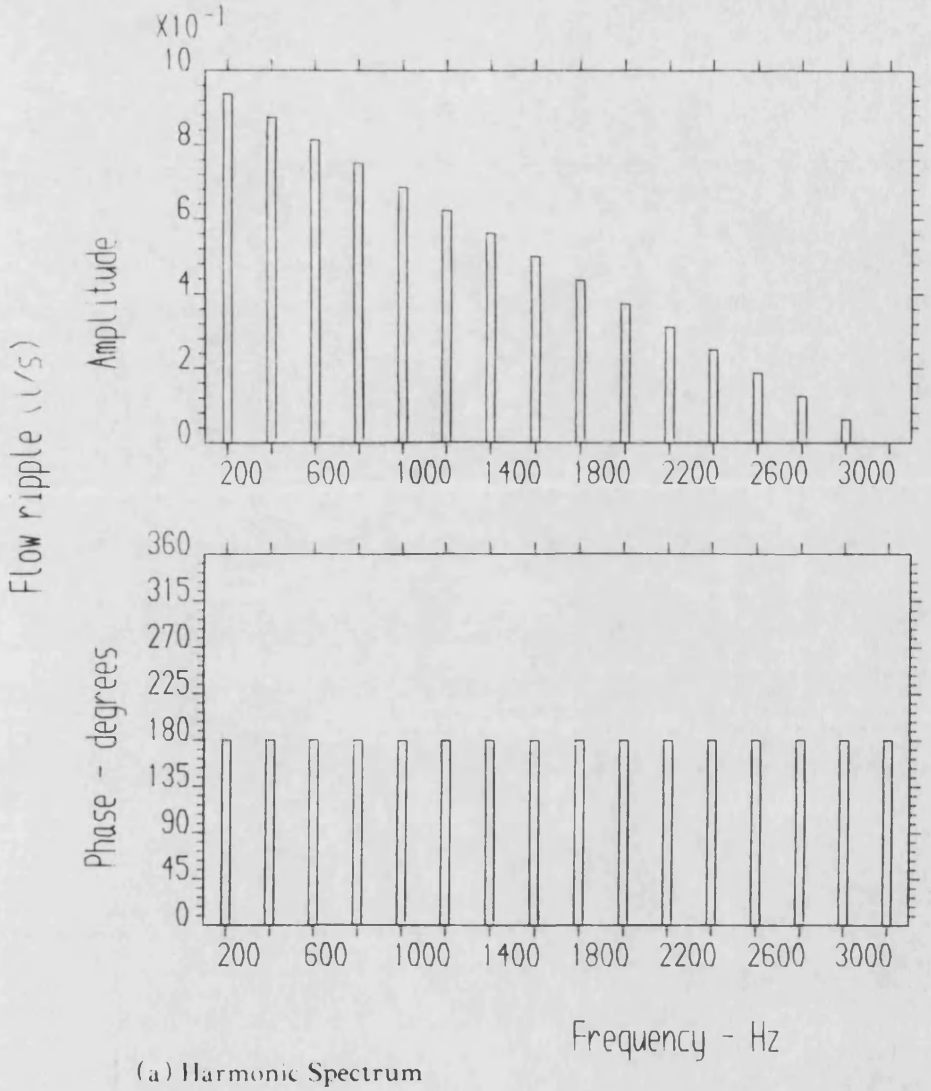

(a) Harmonic Spectrum

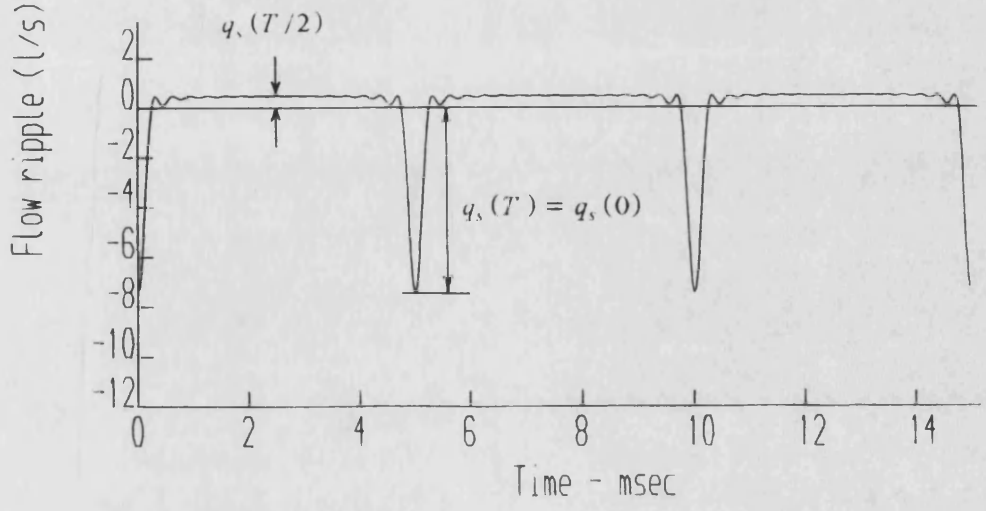

(b) Waveform

Fig. 8.5 **Simple Piston Pump Flow Ripple Model**

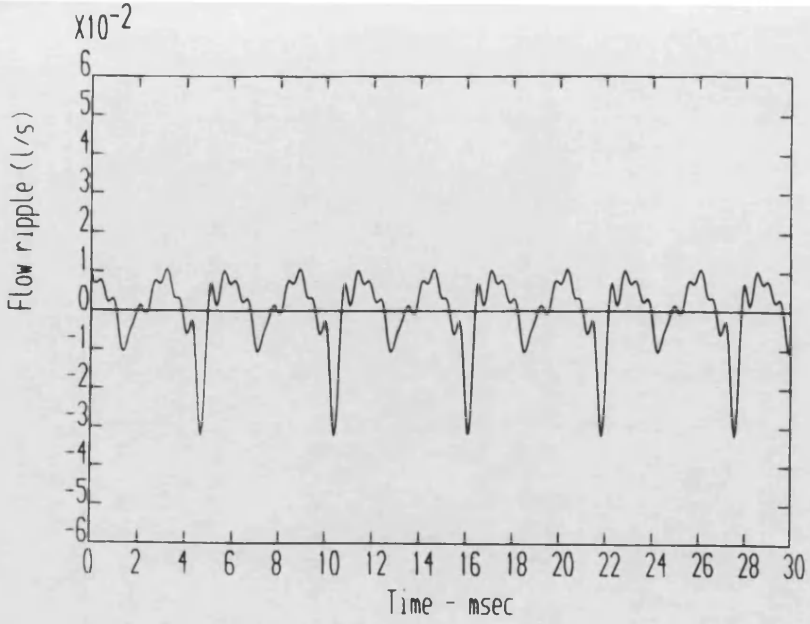

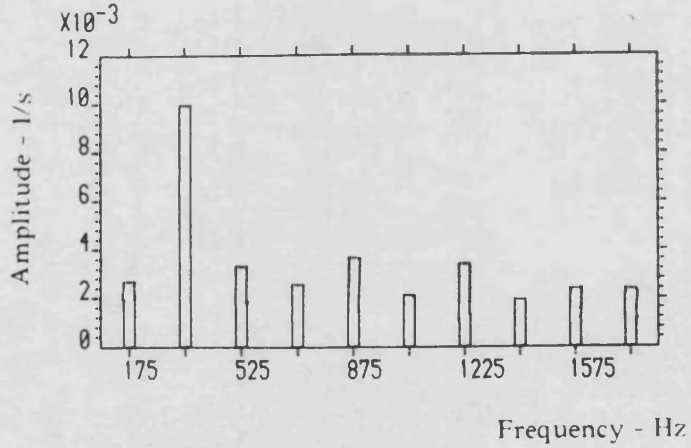

(a) experimental

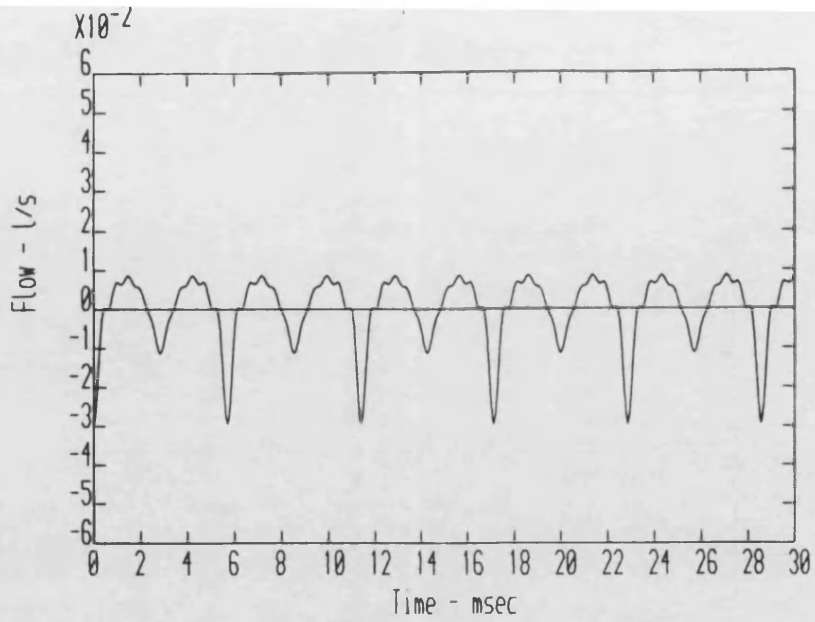

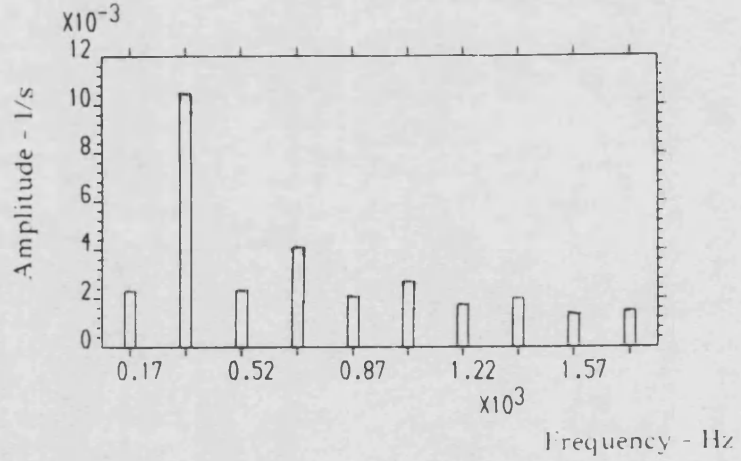

(b) simulated

Fig. 8.6 Experimental and Simulated Source Flow Ripple - Pump 'A', 25 bar

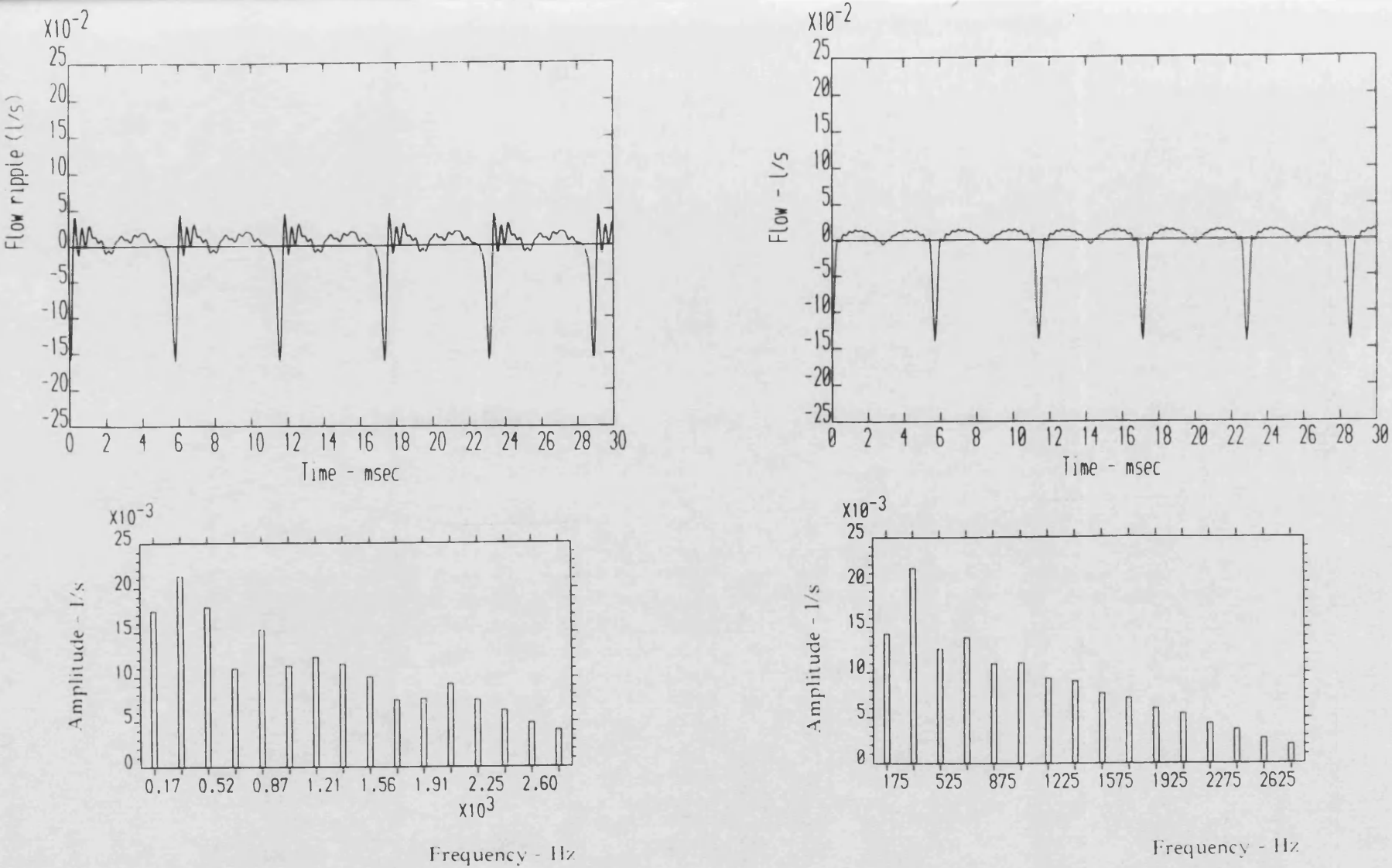

(a) experimental

(b) simulated

Fig. 8.7 Experimental and Simulated Source Flow Ripple - Pump 'A', 100 bar

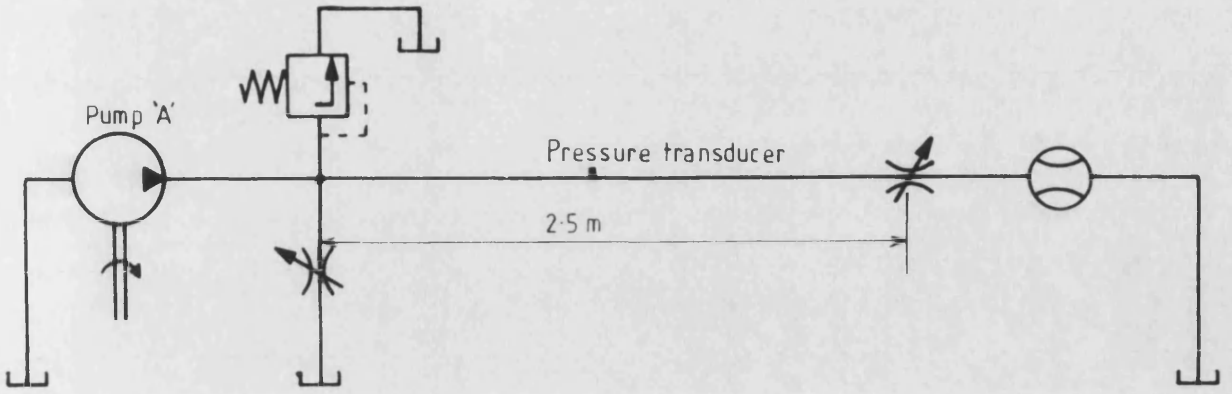

(a) Hydraulic circuit

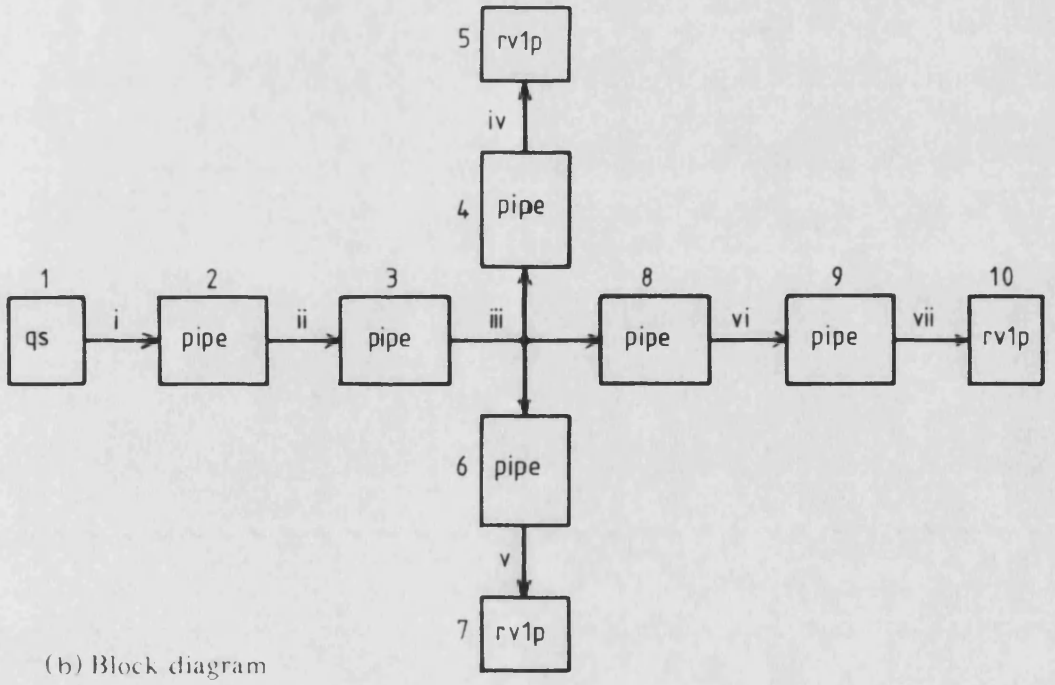

(b) Block diagram

Fig. 8.8 Hydraulic Circuit and Block Diagram Representation

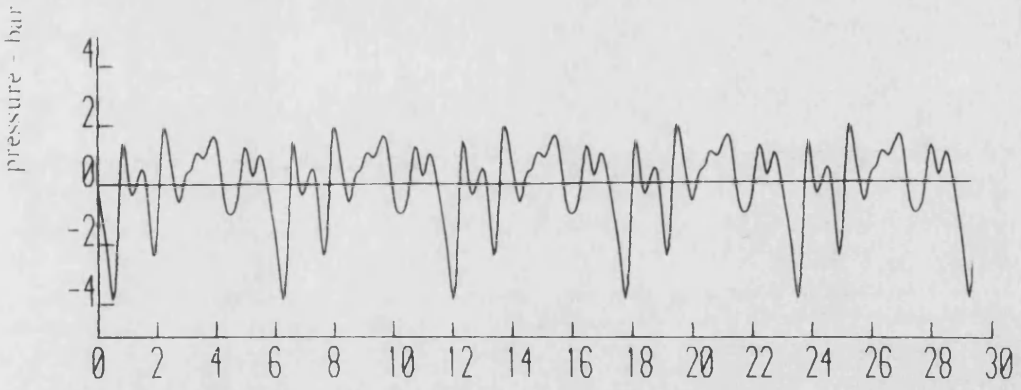

(a) Experimental

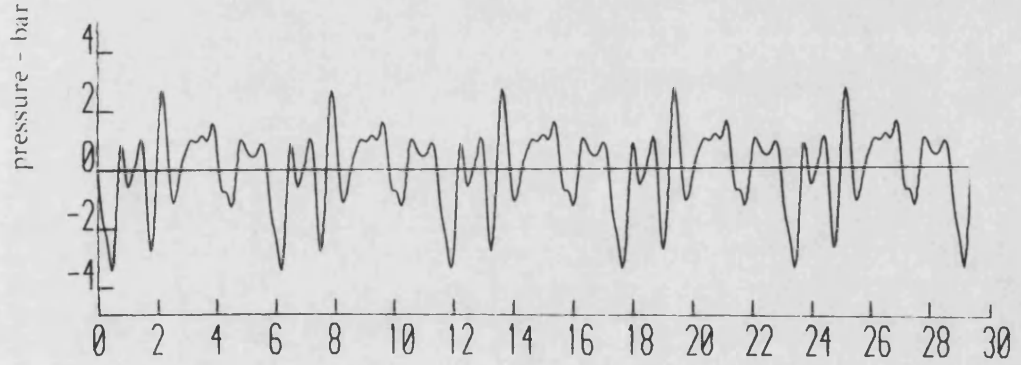

(b) Simulated, using experimentally measured Q_s

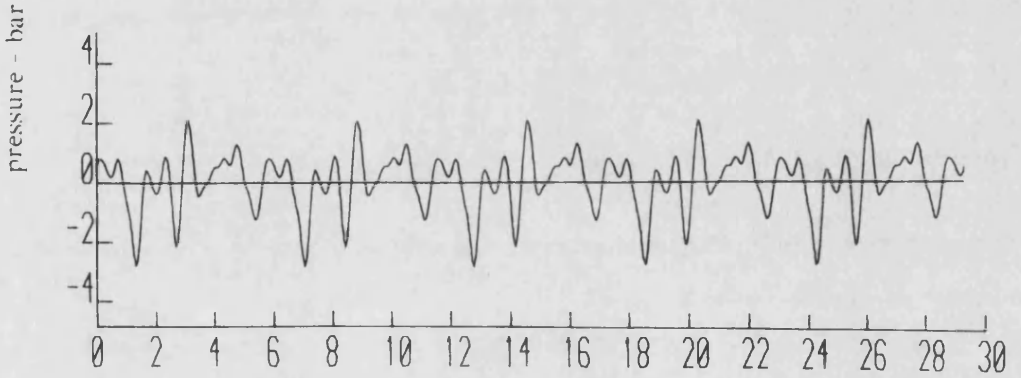

(c) Simulated, using empirical source flow ripple model

Fig. 8.9 **Measured and Simulated Pressure Ripple Waveforms**

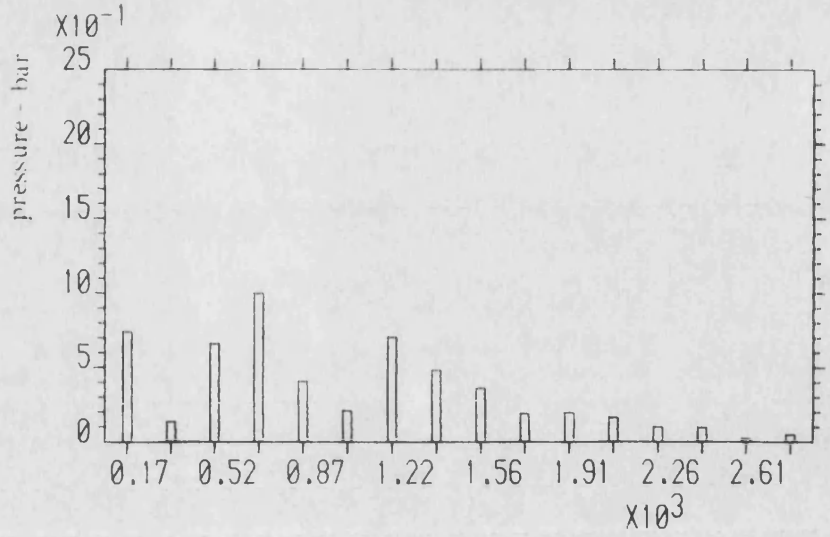

(a) Experimental

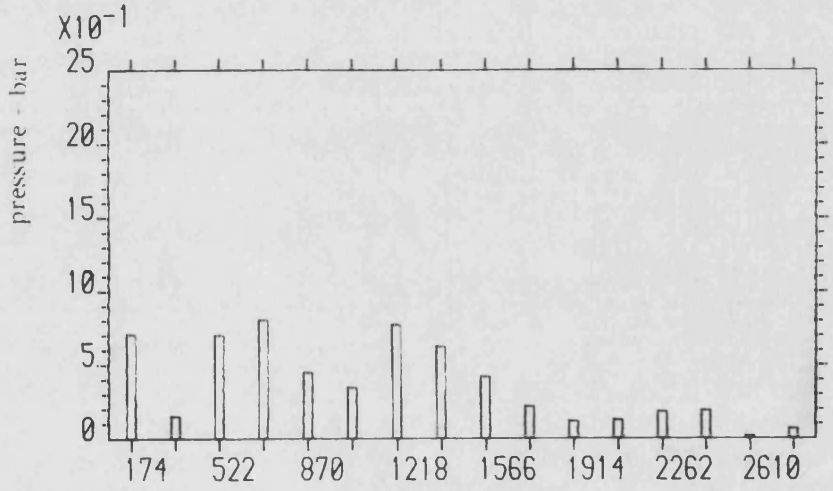

(b) Simulated, using experimentally measured Q_s

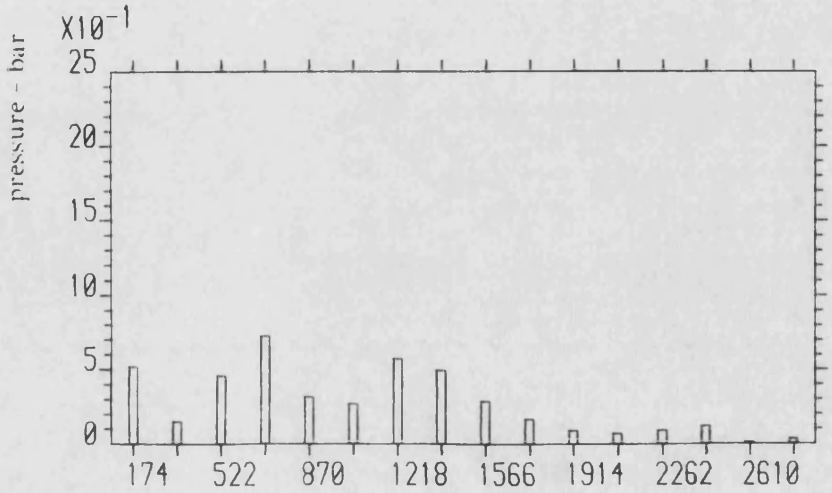

(c) Simulated, using empirical source flow ripple model

Fig. 8.10 **Measured and Simulated Pressure Ripple Amplitude Spectra**

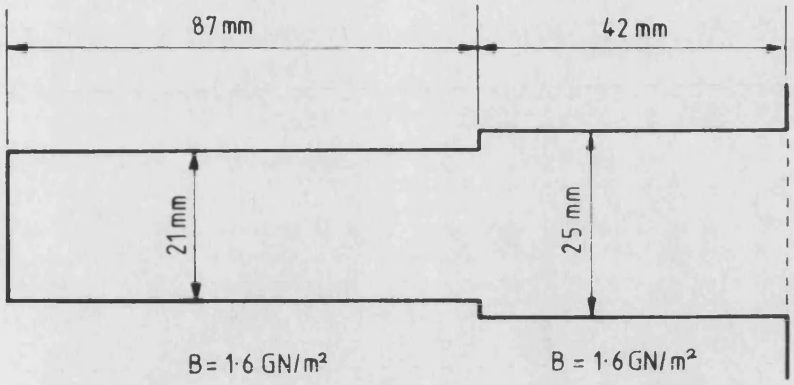

(a) Dimensions of simulated discharge passageway

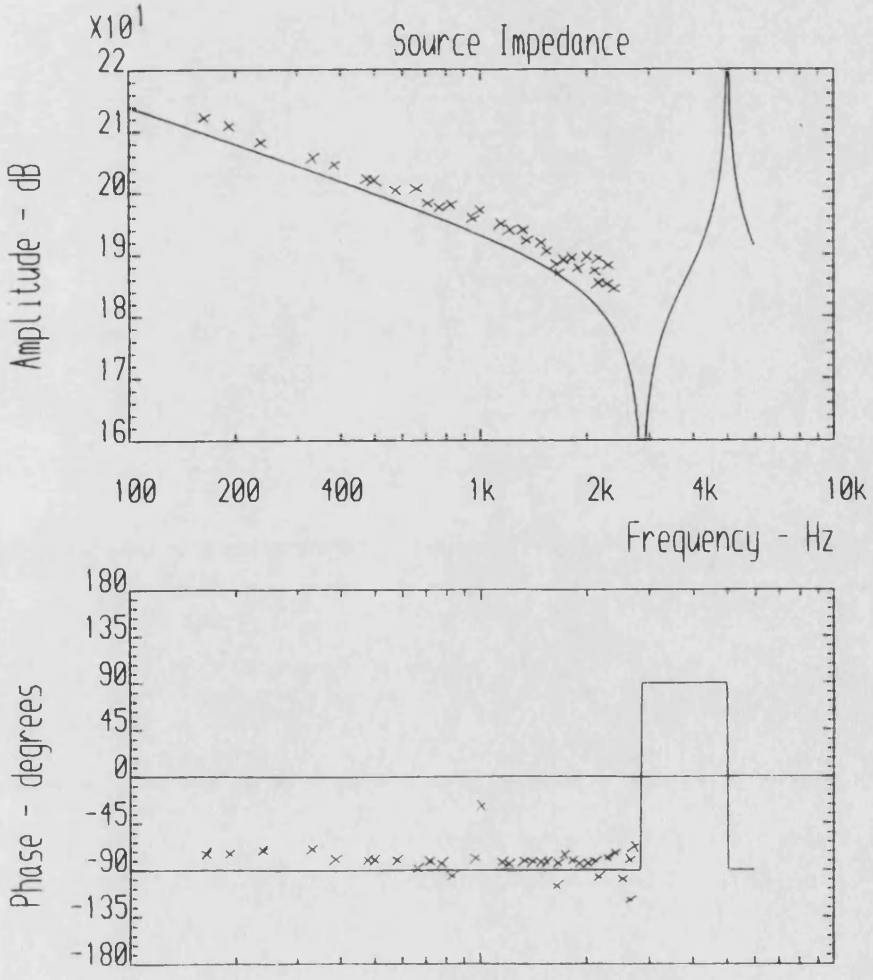

(b) Experimental and simulated source impedance

Fig. 8.11 Pump 'A' Source Impedance Simulation

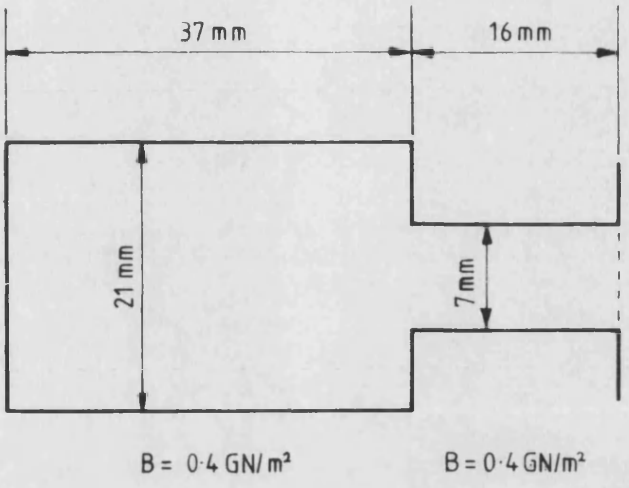

(a) Dimensions of simulated discharge passageway

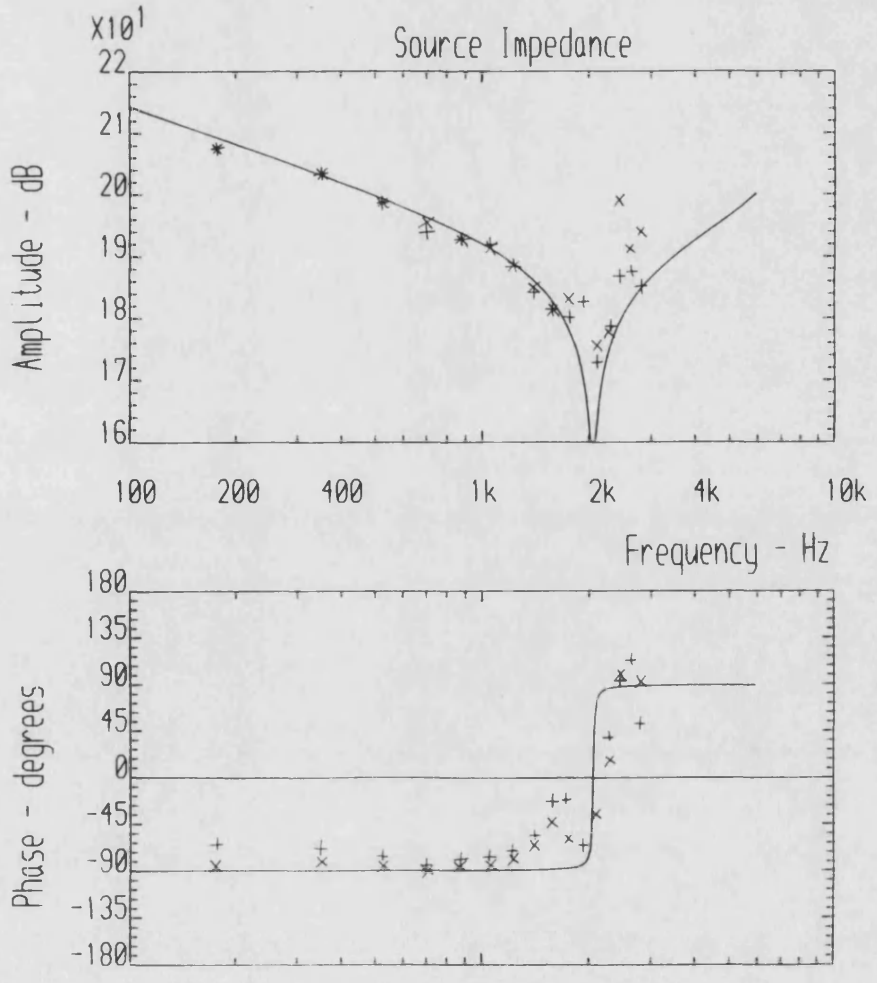

(b) Experimental and simulated source impedance

Fig. 8.12 Pump "C" Source Impedance Simulation

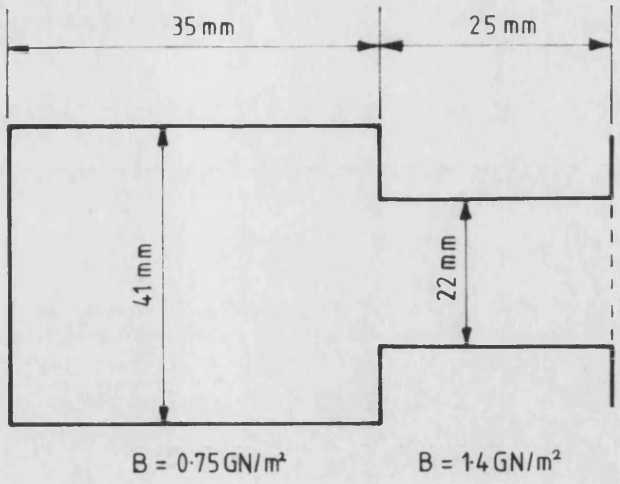

(a) Dimensions of simulated discharge passageway

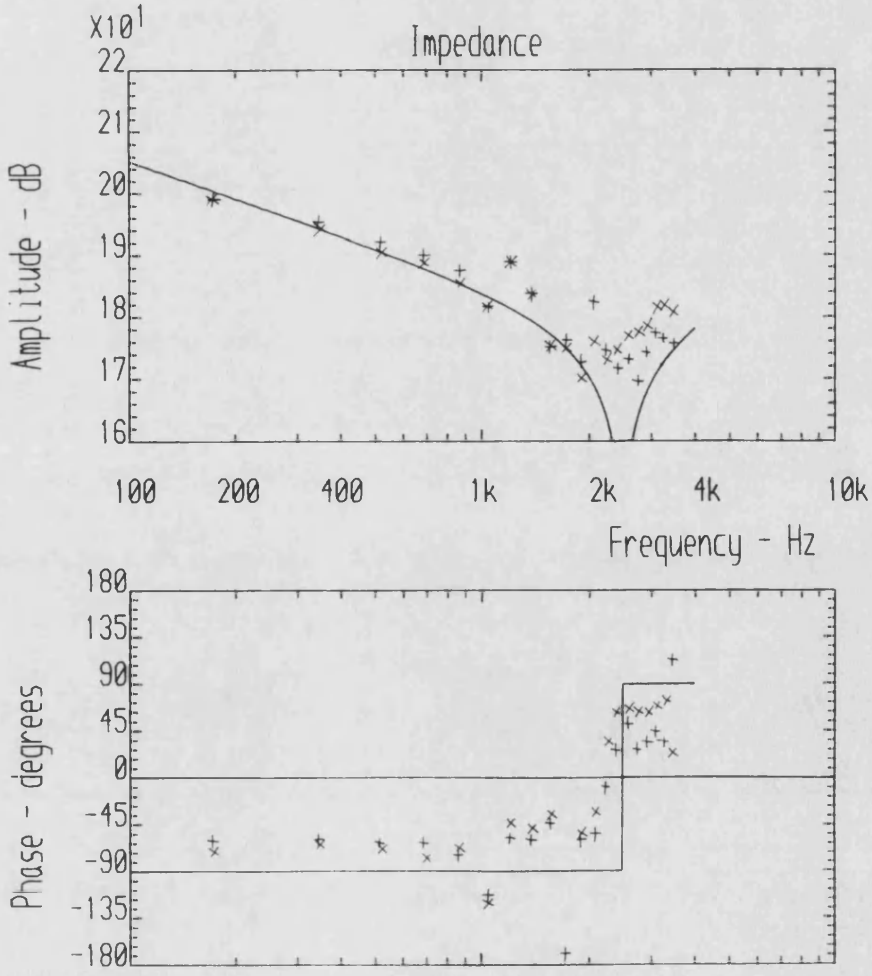

(b) Experimental and simulated source impedance

Fig. 8.13 Pump 'D' Source Impedance Simulation

CHAPTER 9

PRACTICAL METHODS OF REDUCTION OF FLUID-BORNE NOISE

A number of different approaches can be followed in attempting to reduce the fluid-borne noise levels in hydraulic systems. These can be broken down into three main categories, as follows:

a) Reduction of pump/motor source flow ripple.

b) Tuning of the circuit in order to avoid resonant conditions.

c) Use of a silencer or pulsation damper.

9.1. Reduction of the Source Flow Ripple of Positive Displacement Pumps

The flow ripple of a pump is one of the fundamental sources of fluid-borne noise in a system (other sources may be valve oscillation or cavitation; these are not considered in this thesis). A reduction in the source flow ripple should produce a similar reduction in the pressure ripple levels generated in a system. Reduction in the flow ripple levels of a pump can normally only be achieved at the pump design stage.

The source flow ripple generated by a pump is dependent upon a large number of factors, and is linked with other pump characteristics such as volumetric and mechanical efficiency, pump wear and pump vibration. In any attempt to reduce the flow ripple, the effect of the modifications on these other factors must be considered, and cost must also, of course, be taken into account. It is difficult to draw any generalisations as to what steps should be taken to produce a low flow ripple pump; however, there are numerous established techniques which may be beneficial in particular cases. Some of these techniques are discussed below.

9.1.1. Case study: Axial Piston Pump Flow Ripple Simulation

A number of simulations were performed on a 7 cylinder, 300 cm^3/rev fixed swash plate axial piston pump in order to assess the effect of various modifications on the flow ripple. The simulations were performed using an existing suite of computer programs developed by Darling [7] and based on the 'Hydraulic Automatic Simulation Package' ('HASP') which was developed at the University of Bath Fluid Power Centre [55]. The computer model takes into account the effects of fluid compressibility in the cylinders and fluid inertia in the port-plate slots as the fluid passes through at high velocity. The following assumptions were made in the model.

a) No leakage is present in the pump. This has been found to be a reasonable assumption; the effect of leakage on the source flow ripple tends to be insignificant for pumps with typical volumetric efficiencies.

b) The discharge pressure remains constant. As long as the peak-to-peak pressure ripple is small compared with the mean pressure this assumption should be valid.

c) No interaction occurs between individual cylinders. In fact the simulations were performed on one cylinder only, in order to determine the flow from that cylinder alone. The flow from this cylinder was then delayed by suitable fractions of a revolution of the pump in order to represent the flow from the other cylinders, and the individual flows were added together.

d) There is perfect coupling between the swash plate and the piston. In practice, there will be some compliance between the slipper pads and the swash plate, and the slipper pads may lift off under certain conditions.

The flow ripple was simulated at pump rotational speeds of 1500 rev/min and 2000 rev/min, and at mean pressures of 2000 lbf/in^2, 3000 lbf/in^2 and 4000 lbf/in^2 (140, 210, and 280 bar). Two different port plate designs were simulated, these being:

a) Symmetrical port-plate with pressure relief grooves, as shown in Fig. 9.1(a).

b) Uni-directional port-plate with retarded inlet and delivery ports, without pressure relief grooves (Fig. 9.1(b)).

Simulations were performed with both hollow and solid pistons, with corresponding unswept volumes per cylinder of 74.9 cm^3 and 32.5 cm^3 respectively.

Some representative results, at a mean pressure of 4000 lbf/in^2 (280 bar) and a speed of 1500 rev/min, are presented in Figs. 9.2-9.4.

The flow ripple waveform tends to be strongly dependent upon the effective bulk modulus of the fluid in the pump. From previous work by Darling [7], it has been found that, in order to obtain reasonable correlation between experiment and simulation for flow ripple and source impedance, a reduced value of bulk modulus should be used in the model. This takes into account possible air release in the oil and the effects of pump casing compliance (section 4.3.9.). A value for the effective bulk modulus of $1.0\times10^9\ N/m^2$ was found by Darling to give good correlation between previous simulations and experimental results.

9.1.1.1. Effect of Port Plate Modification

A simulated flow ripple waveform for the pump with the symmetrical port plate with silencing grooves, and hollow pistons, is shown in Fig. 9.2(a). The form of this flow ripple is characteristic of axial piston pumps and clearly shows the backflow and kinematic ripple associated with such pumps. The equivalent flow ripple with the unidirectional port plate without silencing grooves is shown in Fig. 9.3(a). It can clearly be seen that there is an increase in the amplitude of the backflow, and a severe oscillation is apparent directly after the backflow. This oscillation is due to the fact that the cylinder opens to the discharge port very rapidly, causing a very high fluid velocity in the vicinity of the port plate slot. The inertia of the fluid in this region, together with the compressibility of the fluid within the cylinder, causes an effect similar to that of a mass-spring-damper system, the 'mass' being that of the volume of fluid in the port plate slot, the 'spring' being the compliance of the fluid within the cylinder, with a small amount of damping provided by viscous or turbulent losses. From a comparison of the harmonic spectra with both port plates as shown in Fig. 9.4, it can be seen that the pump without the silencing grooves produces a broader flow ripple spectrum with a larger proportion of high frequency harmonics. These high frequency components are the ones most likely to cause noise problems in practice. The simulations show, therefore, that correctly designed silencing grooves can produce a significant reduction in flow ripple, and hence fluid-borne noise.

9.1.1.2. Effect of Port Plate Timing

If the opening of the delivery port is delayed beyond bottom dead centre, it is possible to build up the pressure of the fluid contained within the cylinder as it is compressed by the movement of the cylinder. If the port can be arranged to open when the pressure in the cylinder equals the delivery pressure, then no backflow will be produced. This is the reasoning behind the retarded openings of the slots of the port plate shown in Fig. 9.1(b). However, the degree of precompression provided by this port plate is insufficient and a greater retardation would be necessary for it to cause a significant reduction of the backflow. The optimum retardation would be strongly dependent upon the discharge pressure and swash setting; at other pressure or swash conditions the flow ripple amplitude might be increased by the retardation.

9.1.1.3. Effect of Solid Pistons

It is common for the pistons to be hollow at the cylinder end. Their substitution by solid pistons will have the effect of reducing the unswept fluid volume within the cylinder. Thus a smaller additional volume of fluid is required to compress the fluid in the cylinder, and so the backflow should be smaller. This effect is apparent by comparison of the simulated flow ripples in Figs. 9.2(a) and 9.3(a), for the port plate with silencing grooves, and Figs. 9.2(b) and 9.3(b) for the port plate without silencing grooves. Unlike the port plate modification, however, the overall shape of the flow ripple is relatively unchanged by this modification.

The disadvantage of this simple modification is that the mass of the piston is increased. This increased inertia may cause problems with the tracking of the slipper on the port plate, possibly with increased mechanical vibration or wear, particularly at high shaft speeds and swash settings.

The above simulations show that the inclusion of silencing grooves can lead to a significant improvement in the fluid-borne noise characteristics of an axial piston pump. Such a technique may also be applicable to certain other forms of pump and motor, such as vane pumps. Use of solid pistons or retarded port plate slots may be beneficial, but care would need to be taken in the design or they could have a detrimental effect under certain conditions.

9.1.2. Reduction of External Gear Pump Flow Ripple

Several techniques for the reduction of the flow ripple from external gear pumps were described by Molton [4]. These include:

a) increasing the number of teeth. In theory, the peak-to-peak flow ripple is inversely proportional to the square of the number of teeth, assuming ideal relief grooves. Thus by increasing the number of teeth, a substantial reduction in the flow ripple could be obtained.

A similar approach would be to use two sets of out-of-phase gears. This would have the effect of doubling the number of gear teeth, and in theory would reduce the flow ripple by 75%.

b) the use of well designed relief grooves. Poor relief groove design can seriously worsen the fluid-borne noise characteristics. Similarly, badly designed peripheral chamfers on the end faces can adversely affect the flow ripple, in particular at higher frequencies.

c) a cam and plunger mechanism could be used to cancel out the pump flow ripple [56]. By fitting this in parallel with the main pump, and by designing the cam profile to produce an inverted image of the pump flow ripple, both the inlet and outlet flow ripples could be eliminated. Some success has been obtained by this method. However, this would incur extra manufacturing cost, particularly since the cam profile needs to be quite precise in order to cancel out the higher harmonics.

d) reduction of the gear backlash. The aim of this would be for the gears to seal on both the leading and trailing edges. With suitably modified relief grooves, the effect would be equivalent to a doubling of the number of gear teeth, with a theoretical 75% reduction in flow ripple. In practice, however, very tight manufacturing tolerances would be required, with a consequent increase in cost.

9.2. Source Impedance Modification

The source impedance of a pump can have a significant effect on the pressure ripple generated in a system. By increasing the discharge volume, the amplitude of the source impedance will be reduced, thus decreasing the blocked acoustic pressure. This may have a beneficial effect in reducing the pressure ripple. However, any benefits would be extremely system specific: altering the source impedance characteristics would affect the source reflection coefficient and hence the resonant characteristics of the system. Therefore, whereas in one particular system the pressure ripple may be reduced, the opposite effect may be produced in a different system.

In order to demonstrate the effect of source impedance modification, simulations were performed on a simple system consisting of a pump, a 1 m length of pipe of 20 mm internal diameter, and a closed end. The effective length of the pump discharge passageway was assumed to be 0.2 m, and the effect of increasing the diameter of the discharge passageway from 14 mm to 28 mm was examined. Bode plots, showing the amplitude of the pressure ripple at the pump exit for unit source flow ripple, are shown in Fig. 9.5 for both cases. It can be seen that the effect of increasing the discharge diameter is to cause a reduction in the pressure ripple over most of the frequency range. However, the reduction is small, being within 2 dB below 300 Hz, and within 10 dB over most of the frequency band. The resonant characteristics of the circuit are altered slightly so that there is a large increase in the pressure ripple at about 500 Hz. Thus if a harmonic of the source flow ripple occurred near this frequency, it is likely that the source impedance modification would cause a worsening of the overall pressure ripple levels.

The above modification is probably unrealistically large, representing a 4:1 increase in the volume of the pump discharge passageway. However, the improvements in the circuit pressure ripple characteristics are small and strongly dependent on frequency. Thus it is concluded that source impedance modification is not an effective method for reducing the fluid borne noise characteristics of hydraulic systems.

This demonstrates how the blocked acoustic pressure may be misleading as a pump FBN rating. An increase in the discharge volume of the pump decreases the blocked acoustic pressure at a specific harmonic but does not necessarily result in a decrease in the amplitude of that harmonic of pressure ripple generated in a circuit, and may in certain circumstances cause an increase in the pressure ripple.

9.3. Tuning of the Overall Hydraulic System

It was shown in section 2.5. that, for the simple pump-pipe-restrictor system, the length of pipe could have a great effect upon the pressure ripple levels. This also applies to more complicated systems. Thus by judicious selection of pipe lengths, it may be possible to cause a significant reduction in the pressure ripple levels.

Fig. 9.6 shows a graph of the simulated peak-to-peak and r.m.s. pressure ripple at the pump exit in a typical hydrostatic transmission consisting of a piston pump, a length of flexible hose, a length of rigid pipe and a motor, for a range of different rigid pipe lengths. Only the pressure ripple from the pump is considered in this simulation; the motor is modelled as a passive termination. It can be seen that there is a very large variation in the simulated pressure ripple levels, from about 20 bar peak-to-peak to about 180 bar peak-to-peak. Very severe resonant peaks are apparent with extremely high pressure ripple levels. It would be very important to avoid these resonances. It should be noted that, with these extremely high pressure ripple levels, some of the assumptions made in the simulation may break down and non-linear effects could become significant in practice, so that the simulations could become less accurate under these conditions. In particular, the source flow ripple from the pump could be affected by the pressure ripple.

In order to select a suitable pipe length, the characteristics of the circuit components need to be known. This may be difficult in practice, particularly if hoses or complex valves are included. Furthermore, a complex circuit, including branches and changes in section, would be difficult to analyse. The simulation package 'PRASP' could be of great use in this analysis.

Problems would be encountered with a variable speed pump, in that the resonant lengths of the system are dependent upon the frequencies of the harmonics. Thus if the pump has a wide operating speed range, it may be difficult or impossible to avoid the resonant condition over the whole range.

The tuning of the pipe lengths in a system, then, can in many cases be of great benefit in reducing fluid-borne noise. The selection of suitable lengths can be very difficult; the 'PRASP' program could be a useful tool in this respect.

9.4. Fluid-Borne Noise Attenuators

A wide range of proprietary fluid-borne noise attenuators (silencers, pulsation dampers) is available. These, when used correctly, can be extremely effective in reducing the fluid-borne noise in a circuit, reductions of 20-40 dB being typical [57,58]. However, they tend to be bulky, heavy and expensive, so normally they are only suitable for situations in which the fluid-borne noise level is very critical.

It is possible to construct fluid-borne noise attenuators from standard hydraulic components. While these may be less effective than purpose-built attenuators, they can form an inexpensive and practical solution. The effectiveness of a standard gas filled accumulator and a simple pipe loop known as a 'Herschel-Quincke tube' are analysed below.

9.4.1. Accumulators as Fluid-Borne Noise Attenuators

It is commonly assumed that hydraulic accumulators can be used to reduce the level of the pressure pulsations in a system. Considering the simple system consisting of a pump discharging into an entry impedance Z_E, the pressure ripple at the pump exit is given by the equation:

$$P_0 = \frac{Q_S Z_S Z_E}{Z_S + Z_E} = Q_S Z_{sys} \qquad \ldots (9.1)$$

$$\text{where } Z_{sys} = \frac{Z_S Z_E}{Z_S + Z_E} \qquad \ldots (9.2)$$

If an accumulator is added at the pump exit, this presents an additional impedance Z_a, in parallel with the original impedance, so that the pressure ripple at the pump exit becomes:

$$P_0' = \frac{Q_S Z_{sys}}{1 + Z_{sys}/Z_a} \qquad \ldots (9.3)$$

The 'Insertion Loss' is a measure of the pressure ripple reduction obtained by inclusion of the accumulator, and is given by the equation:

$$IL = 20 \log_{10} \left| \frac{P_0}{P_0'} \right| = 20 \log_{10} \left| 1 + \frac{Z_{sys}}{Z_a} \right| \quad \ldots (9.4)$$

Thus a large insertion loss can be achieved by a low accumulator impedance Z_a.

In dynamic systems analysis an accumulator is commonly assumed to be equivalent to a capacitance. This is valid for low frequencies, below about 10 Hz. It can be seen from the results in section 6.1.3., however, that at higher frequencies the accumulator has an inductive characteristic. An anti-resonance occurs between 10 Hz and 100 Hz, around which the impedance is very low. Thus within this range the accumulator should be effective as a pulsation damper.

To assess the performance of this accumulator as a fluid-borne noise attenuator, the characteristics of a simple system with an accumulator were simulated. The system simulated was that of a pump, a rigid pipe and a termination consisting of a closed end or a simple restrictor. Simulations were performed with and without an accumulator situated at the pump exit.

The modelled impedance of the accumulator is shown in Fig. 9.7(a). The value of its inductance was estimated from the experimental results. Simulation results, with the pipe terminated by a closed end, are shown in Fig. 9.7(b). It can be seen that, below about 700 Hz, the overall effect of the accumulator is to reduce the pressure ripple at the termination. However, the resonant characteristics of the system are altered, so that at certain frequencies the accumulator causes an increase in the pressure ripple. These resonances correspond to the condition where

$$\left| 1 + \frac{Z_{sys}}{Z_a} \right| \rightarrow 0 \quad \ldots (9.5)$$

$$\text{i.e. } Z_{sys} \approx -Z_a . \quad \ldots (9.6)$$

Between 1 kHz and 2 kHz, the accumulator appears to cause a general worsening of the pressure ripple.

Corresponding simulation results, with the pipe terminated by a simple resistor valve, are shown in Fig. 9.7(c). This termination is rather less reflective that the closed end, so that the system resonances are less severe. The accumulator is fairly effective below 700 Hz, causing no significant worsening at any frequency in this range. However, Between 1 kHz and 2 kHz it again causes a slight worsening of the pressure ripple.

It can be concluded that this particular accumulator would be ineffective as a high frequency pressure ripple attenuator, although it might be effective at low frequencies, provided that care was taken to avoid excitation at the resonant frequencies. An accumulator with a lower inductive characteristic might be more effective as a pulsation damper.

9.4.2. The Herschel-Quincke Tube

The Herschel-Quincke tube [59] is a simple form of silencer which was developed in the early part of the 19th century. It consists of two pipes of different length connected together in parallel to form a loop, as shown in Fig. 9.8. In its standard form the two pipes have equal diameters, and the cross-sectional area of each is equal to half that of the connected pipes, so that the mean flow velocity is unchanged.

This forms a simple, lightweight and inexpensive pulsation damper which can be constructed from standard components. The behaviour of it is quite complex, and it provides narrow-band attenuation in two distinct ways:

a) high attenuation when $\omega(l_1-l_2)/c = (2n-1)\pi$, where n is an integer. This is equivalent to the behaviour of a closed-ended branch line of length $(l_1-l_2)/2$. The effect can be explained simply by interference between the waves in each pipe as they recombine at the outlet of the loop. This could be utilised to cancel odd components of a harmonic series, but the even components would not be cancelled out.

b) high attenuation when $\omega(l_1+l_2)/c = 2n\pi$, provided that $\omega(l_1-l_2)/c \neq 2m\pi$ at that frequency, where m and n are independent integers. The reason for this effect is not obvious, and is due to the fact that the waves travel about the circuit in a very complex manner. This feature, which does not occur with a simple closed-ended branch line, could have most potential in practice.

9.4.2.1. Analysis of the Herschel-Quincke Tube

Because of its closed loop configuration, the Herschel-Quincke tube is very difficult to analyse using standard impedance techniques. However, it is ideally suited to analysis using the transfer matrix approach. In the following analysis, frictional effects are ignored.

Consider the 'admittance matrix' for each branch (section 2.12.1.):

$$\begin{bmatrix} Q_{IN\,1} \\ Q_{OUT\,1} \end{bmatrix} = \mathbf{Y}_1 \begin{bmatrix} P_{IN} \\ P_{OUT} \end{bmatrix} \qquad \ldots (9.7)$$

and $$\begin{bmatrix} Q_{IN\,2} \\ Q_{OUT\,2} \end{bmatrix} = \mathbf{Y}_2 \begin{bmatrix} P_{IN} \\ P_{OUT} \end{bmatrix} \qquad \ldots (9.8)$$

where $$\mathbf{Y}_i = \begin{bmatrix} \cot\beta_i & -\mathrm{cosec}\beta_i \\ \mathrm{cosec}\beta_i & -\cot\beta_i \end{bmatrix} \qquad \ldots (9.9)$$

and $$\beta_i = \frac{\omega l_i}{c} \qquad \ldots (9.10)$$

By applying flow continuity to the inlet and outlet,

$$Q_{IN} = Q_{IN\,1} + Q_{IN\,2} \qquad \ldots (9.11)$$

$$Q_{OUT} = Q_{OUT\,1} + Q_{OUT\,2} \qquad \ldots (9.12)$$

Therefore,

$$\begin{bmatrix} Q_{IN} \\ Q_{OUT} \end{bmatrix} = (\mathbf{Y}_1 + \mathbf{Y}_2) \begin{bmatrix} P_{IN} \\ P_{OUT} \end{bmatrix} = \mathbf{Y}_Q \begin{bmatrix} P_{IN} \\ P_{OUT} \end{bmatrix} \qquad \ldots (9.13)$$

where $$\mathbf{Y}_Q = \begin{bmatrix} (\cot\beta_1 + \cot\beta_2) & -(\mathrm{cosec}\beta_1 + \mathrm{cosec}\beta_2) \\ (\mathrm{cosec}\beta_1 + \mathrm{cosec}\beta_2) & -(\cot\beta_1 + \cot\beta_2) \end{bmatrix} \qquad \ldots (9.14)$$

The 'Transmission Loss' is a commonly used measure of the performance of a pulsation damper. It is independent of the system to which the unit is connected, and is defined by the equation

$$TL = 20 \log_{10} \left| \frac{F}{P_{OUT}} \right| \qquad \ldots (9.15)$$

when discharging into a reflectionless line of impedance Z_0, equal to the characteristic impedance of the upstream pipe. F is the pressure wave travelling in the forward direction at the inlet to the silencer, in a pipe of the same characteristic impedance as the termination.

Thus $Q_{OUT} = \dfrac{P_{OUT}}{Z_0}$ ... (9.16)

$P_{IN} = F + G$ ... (9.17)

$Q_{IN} = \dfrac{(F - G)}{Z_0}$ ... (9.18)

hence $F = (P_{IN} + Z_0 Q_{IN})/2.$ ... (9.19)

Consider the general case, where the admittance matrix of the silencer is represented by

$$\mathbf{Y} = \begin{bmatrix} y_{1,1} & y_{1,2} \\ y_{2,1} & y_{2,2} \end{bmatrix} \quad \text{... (9.20)}$$

Thus $Q_{IN} = y_{1,1} P_{IN} + y_{1,2} P_{OUT}$ ... (9.21)

$Q_{OUT} = y_{2,1} P_{IN} + y_{2,2} P_{OUT}$ ... (9.22)

By algebraic manipulation of the above equations,

$$P_{IN} = \frac{Q_{OUT}}{y_{2,1}} - \frac{y_{2,2}}{y_{2,1}} P_{OUT} \quad \text{... (9.23)}$$

$$= P_{OUT} \left[\frac{1}{y_{2,1} Z_0} - \frac{y_{2,2}}{y_{2,1}} \right] \quad \text{... (9.24)}$$

$$Q_{IN} = P_{OUT} \left[\frac{y_{1,1}}{y_{2,1} Z_0} - \frac{y_{1,1} y_{2,2}}{y_{2,1}} + y_{1,2} \right] \quad \text{... (9.25)}$$

Therefore, the transmission loss is given by

$$TL = -20 \log_{10} \left| \frac{2 y_{2,1} Z_0}{1 + (y_{1,1} - y_{2,2}) Z_0 - (y_{1,1} y_{2,2} + y_{1,2} y_{2,1}) Z_0^2} \right| \quad \text{... (9.26)}$$

For the Herschel-Quincke tube, the transmission loss can be shown to be

$$TL = -20 \log_{10} \left| \frac{4 \sin (\beta_1 + \beta_2)/2 \cos (\beta_1 - \beta_2)/2}{2 \sin (\beta_1 + \beta_2) + j [1 - 2 \cos (\beta_1 + \beta_2) + \cos (\beta_1 - \beta_2)]} \right| \quad \text{... (9.27)}$$

When $\cos(\beta_1-\beta_2)/2 \rightarrow 0$, the transmission loss is large. This corresponds to condition (a) described above. When $\sin(\beta_1+\beta_2)/2 \rightarrow 0$, the transmission loss may also be large, corresponding to condition (b).

9.4.2.2. Simulation Results

A number of simulations were performed on a typical Herschel-Quincke tube using the 'PRASP' simulation program. The transmission loss characteristics are shown in Fig. 9.9, where the lengths of the two pipes are 0.90 m and 0.38 m respectively. Attenuation bands corresponding to condition (a) above are apparent at about 1.2 kHz and 3.7 kHz, and bands corresponding to condition (b) are apparent at 1 kHz, 2 kHz, 3 kHz and 4 kHz.

Although the transmission loss is a unique characteristic of the pulsation damper alone, its performance in practice will be dependent upon the characteristics of the system in which it is inserted. In order to assess its performance, simulations were performed under different load conditions, and the pressure ratio between the outlet and inlet of the Herschel-Quincke tube calculated. Fig. 9.10(a) shows the pressure ratio $|P_{OUT}/P_{IN}|$ for the case of a non-reflective termination. It can be seen that the form of this curve is similar to that of the transmission loss, in that attenuation occurs at the same frequencies, although at some frequencies (about 1.5 kHz and 3.5 kHz) the pressure ratio exceeds unity. It can be seen, however, that the attenuation bands are very narrow, particularly those at 2 kHz and 3 kHz. Therefore, the device would need to be tuned very accurately for it to work efficiently in practice, and its performance would be affected strongly by pump speed variation or changes in the fluid properties.

Fig. 9.10(b) shows the pressure ratio with a partially reflective load consisting of a simple restrictor valve, for which $Z_T/Z_0 \approx 5$ and $\rho_T \approx 0.67$. It can be seen that the troughs at 2 kHz and 3 kHz have become extremely narrow. Fig. 9.10(c) shows the pressure ratio with a closed end, such that $|Z_T/Z_0| = \infty$. In this case it can be seen that the troughs around 1 kHz, 2 kHz and 3 kHz have disappeared altogether. However, the troughs at 1.2 kHz and 3.7 kHz are still well defined.

The above simulations show that the attenuation properties of the Herschel-Quincke tube where $\omega(l_1+l_2)/c \rightarrow 2n\pi$ are strongly dependent upon the system characteristics. The rejection bandwidth tends to be extremely narrow and varies with the load impedance, so that in practice it would be very difficult to make use of this attenuation property.

Where $\omega(l_1-l_2)/c \rightarrow (2n-1)\pi$, the Herschel-Quincke tube appears to provide good attenuation with a reasonably broad bandwidth, irrespective of the load condition. However, a simple closed ended branch line would also provide this characteristic, and would probably be a simpler and more compact solution.

The above simulations show that the transmission loss may be misleading in certain conditions, as it only pertains to the special case of a non-reflective termination. In a different circuit the actual attenuation characteristics may be significantly worse. However, with this reservation, the transmission loss forms a useful rating of the overall performance characteristics of a silencer.

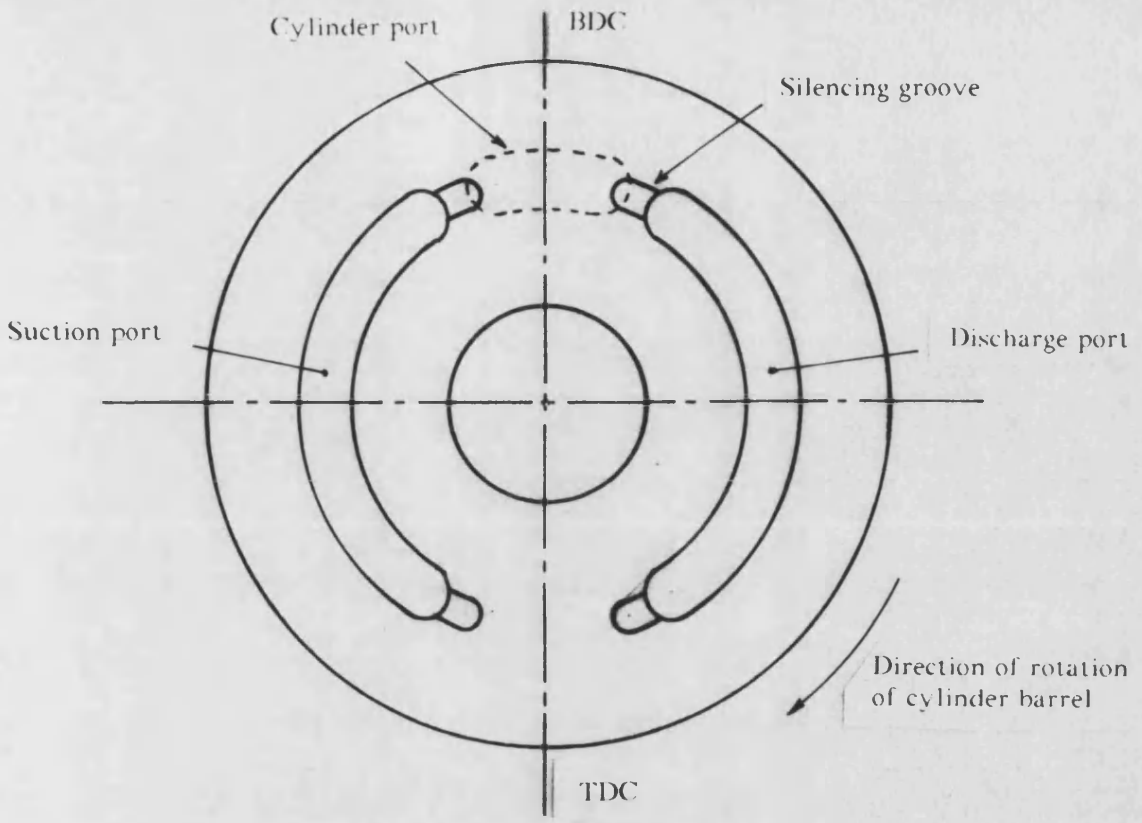

(a) Symmetrical, with silencing grooves

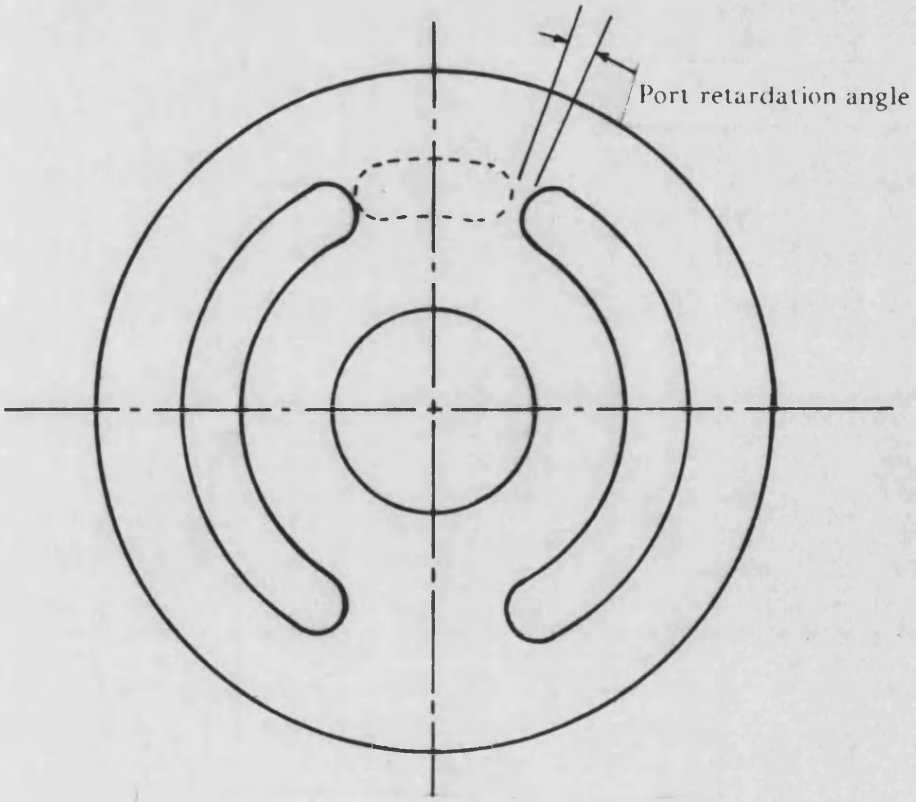

(b) Unidirectional, without silencing grooves

Fig. 9.1 Simulated Port Plate Designs

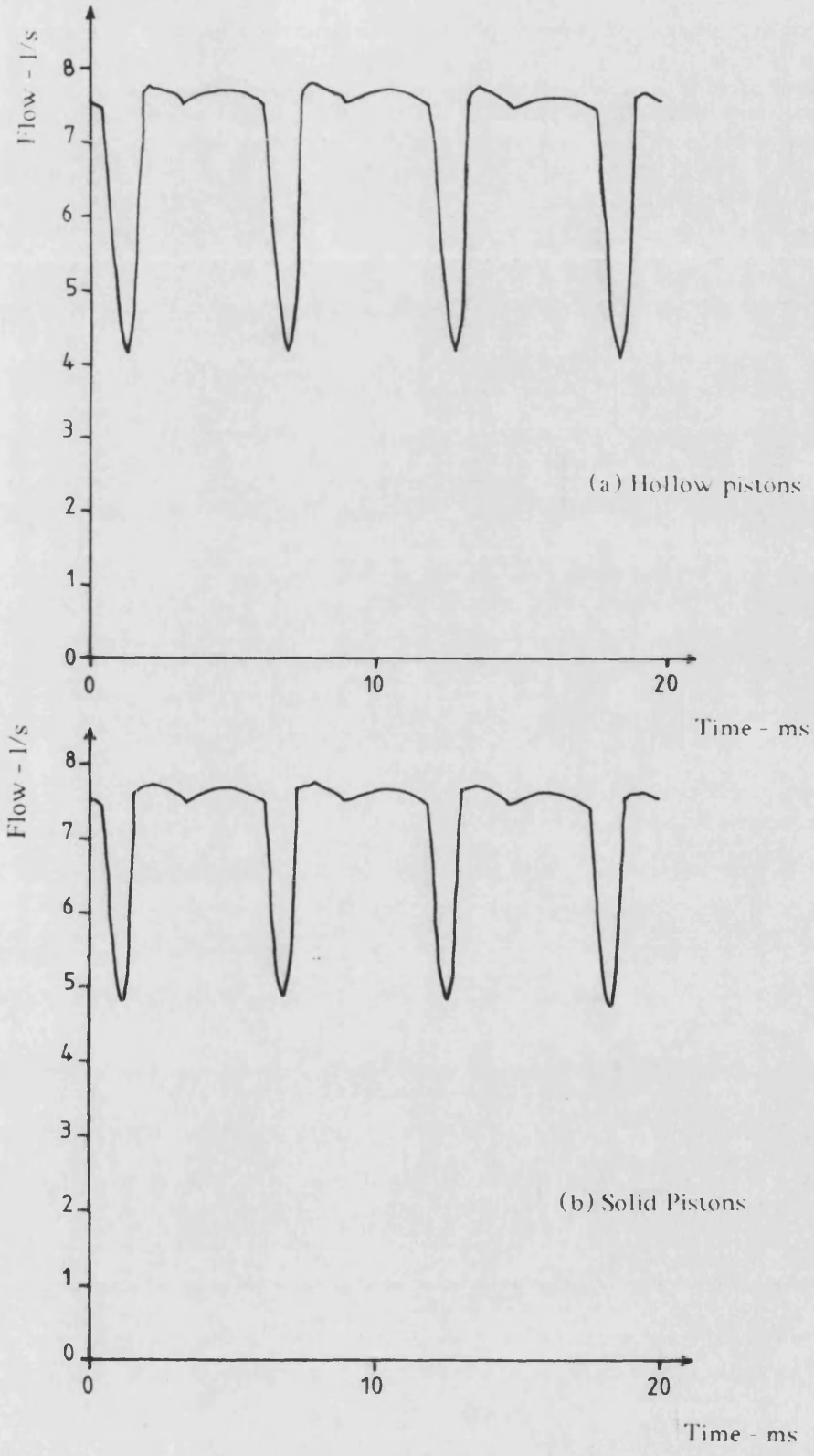

Fig. 9.2 **Simulated Flow Ripple Waveforms, 1500 rev/min, 275 bar Symmetrical, Silenced Port Plate**

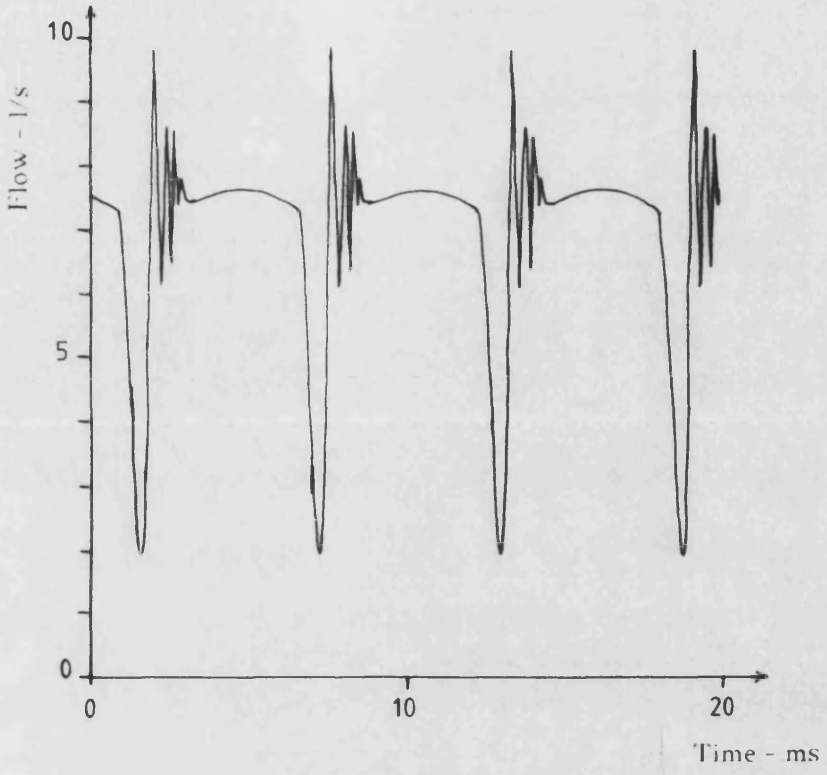

(a) Hollow pistons

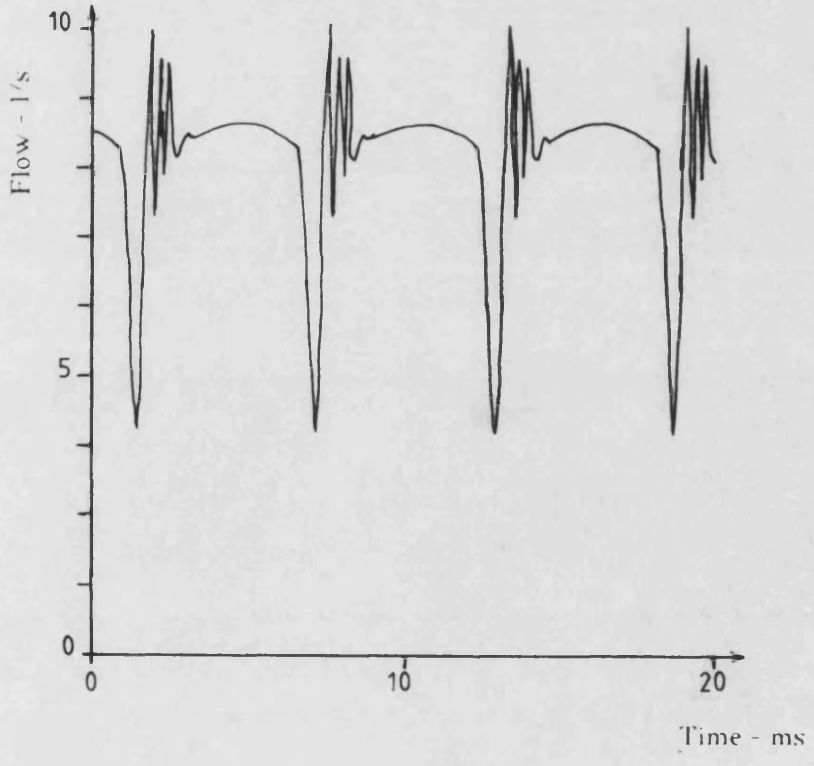

(b) Solid Pistons

Fig. 9.3 **Simulated Flow Ripple Waveforms, 1500 rev/min, 275 bar Unidirectional, Unsilenced Port Plate**

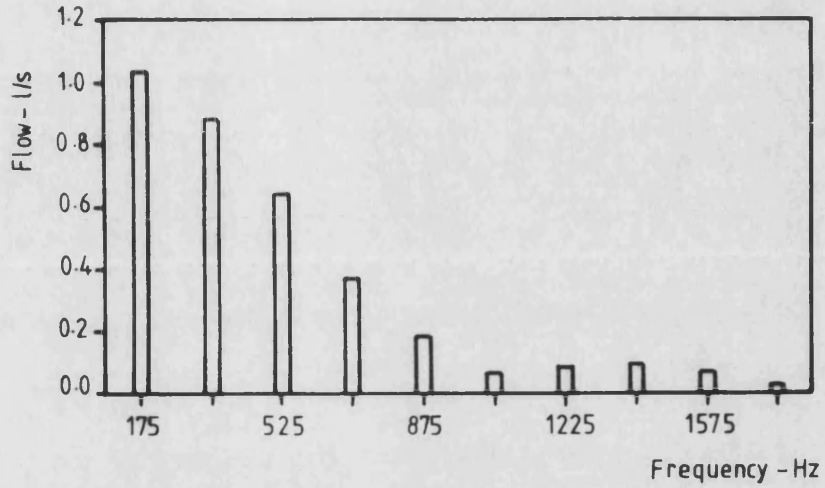

(a) Symmetrical port plate, hollow pistons

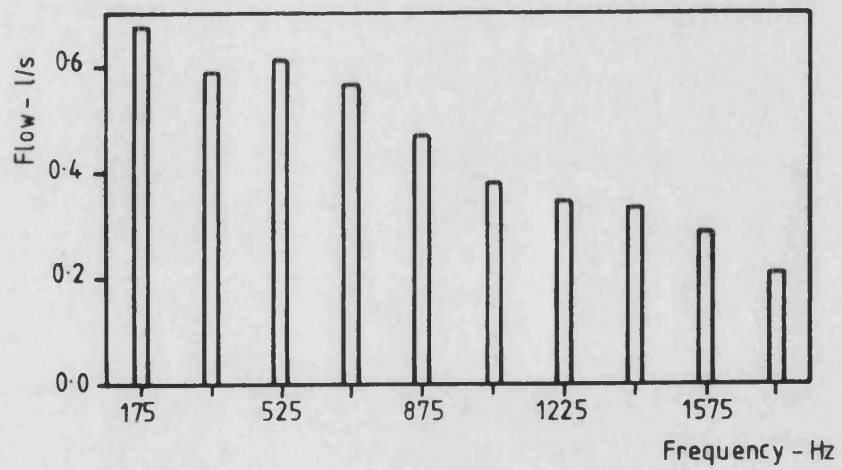

(b) Unidirectional port plate, hollow pistons

Fig. 9.4 **Harmonic Spectra of Simulated Pump Flow Ripple, 1500 rev/min, 275 bar**

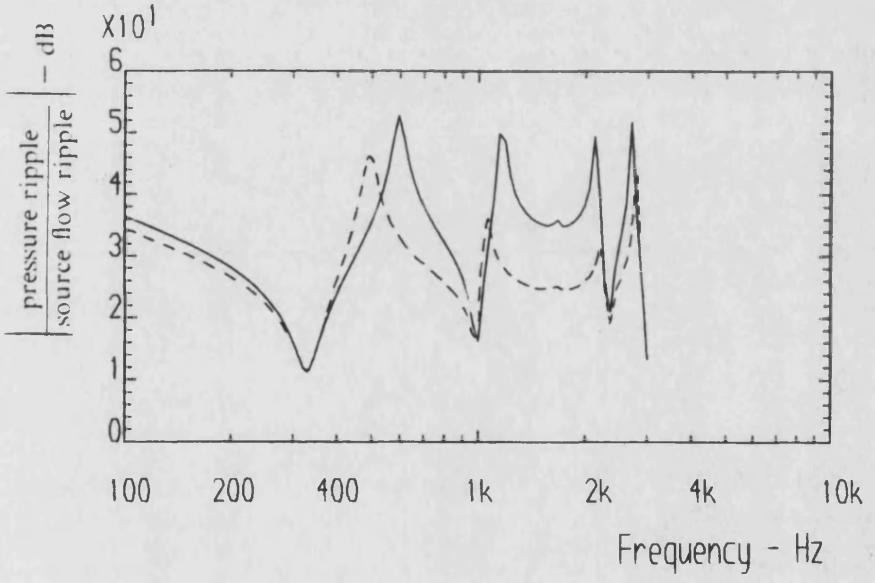

- - - - - - Discharge passageway diameter = 28 mm

——— Discharge passageway diameter = 14 mm

Fig. 9.5 **Effect of Source Impedance Modification on Pressure Ripple in a Simple Circuit**

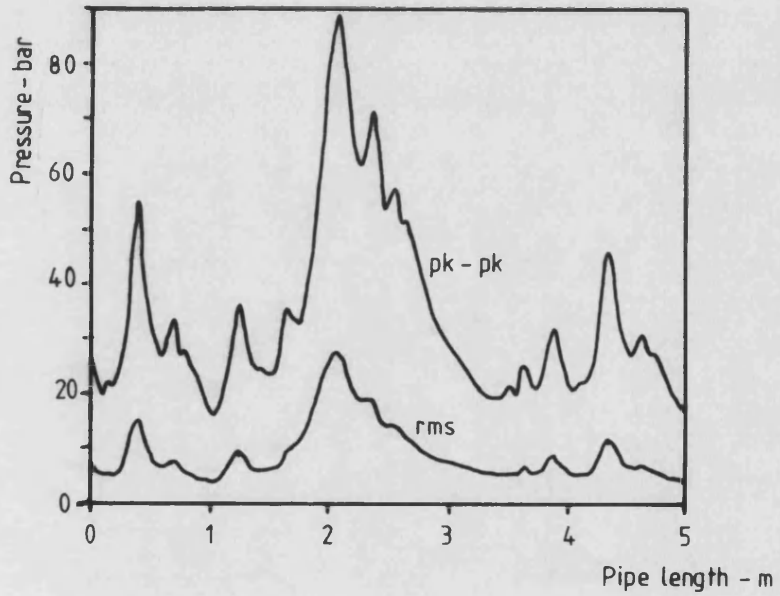

Fig. 9.6 Variation of Simulated Peak-to-Peak and RMS Pressure Ripple with Pipe Length, at one point in a Hydraulic Circuit

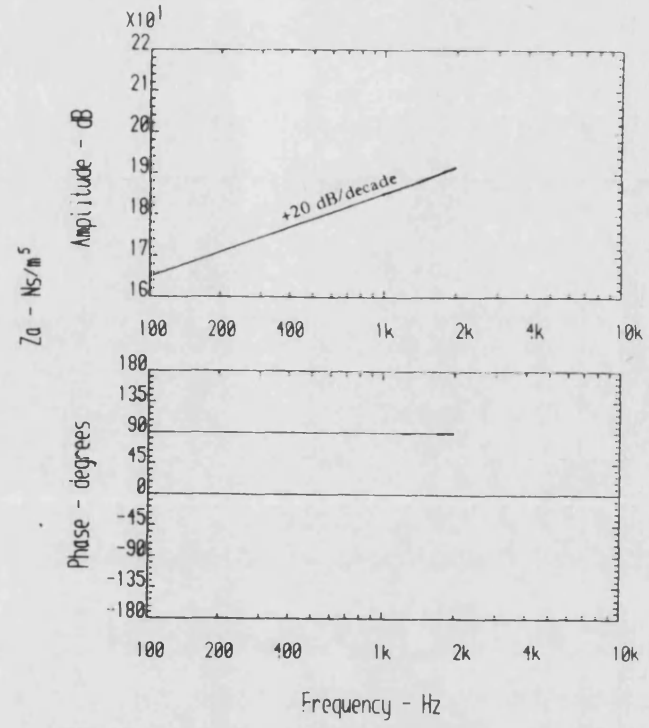

(a) Accumulator Impedance

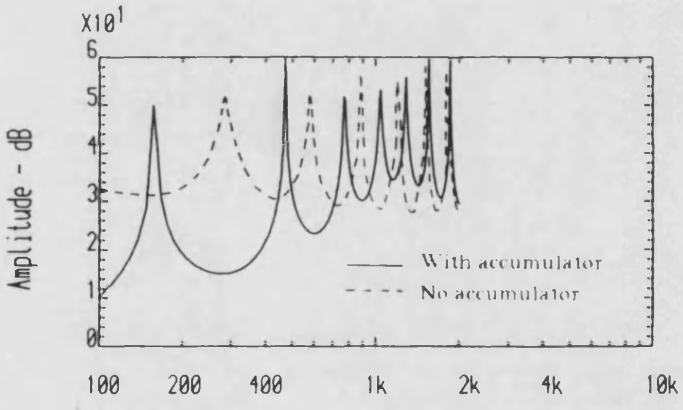

(b) Pressure at Termination per Unit Flow Ripple, Closed End

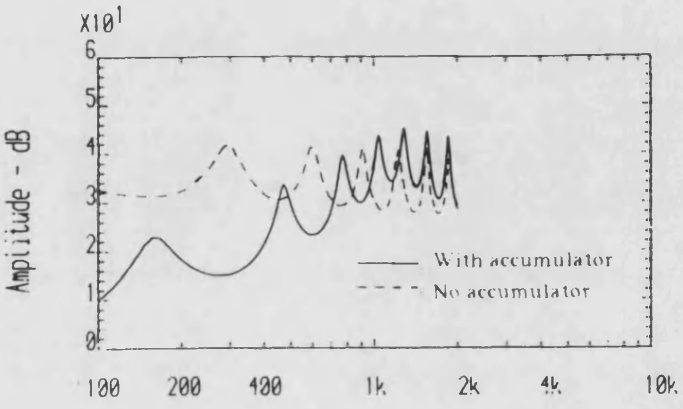

(c) Pressure at Termination per Unit Flow Ripple, Valve Termination

Fig. 9.7 Effect of an Accumulator on FBN Characteristics in a Typical Circuit

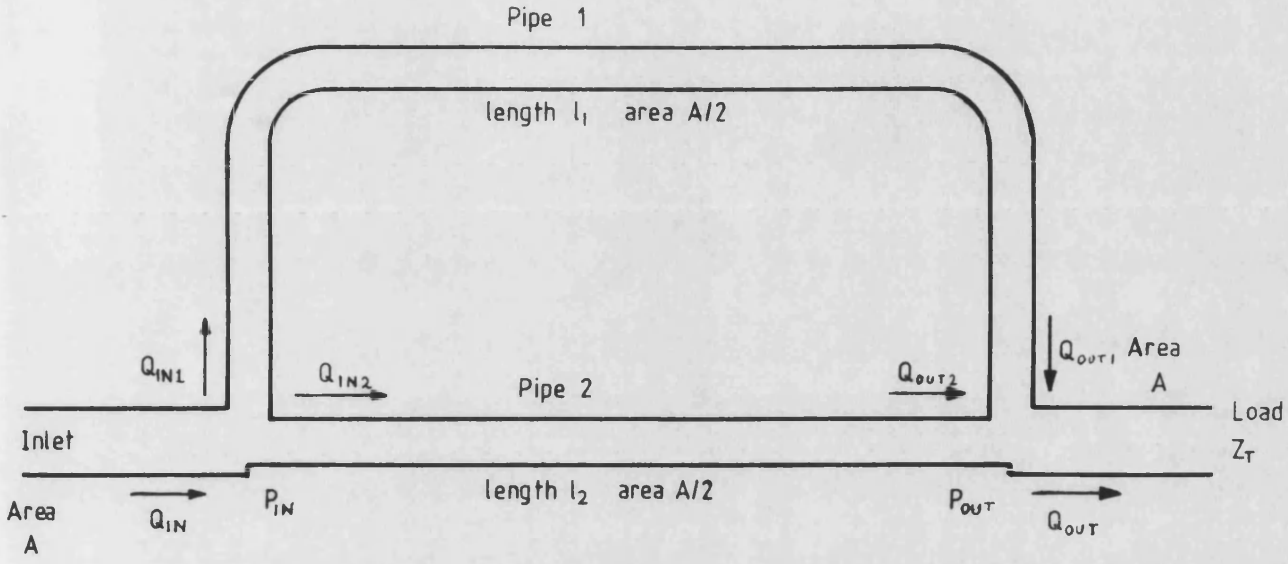

Fig. 9.8 Schematic Diagram of Quincke Tube

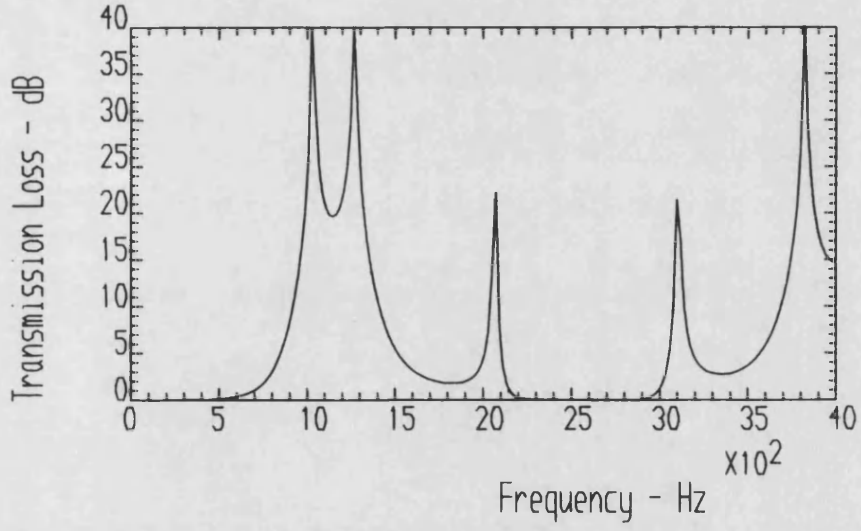

Fig. 9.9 Typical Simulated Transmission Loss Characteristics of Quincke Tube

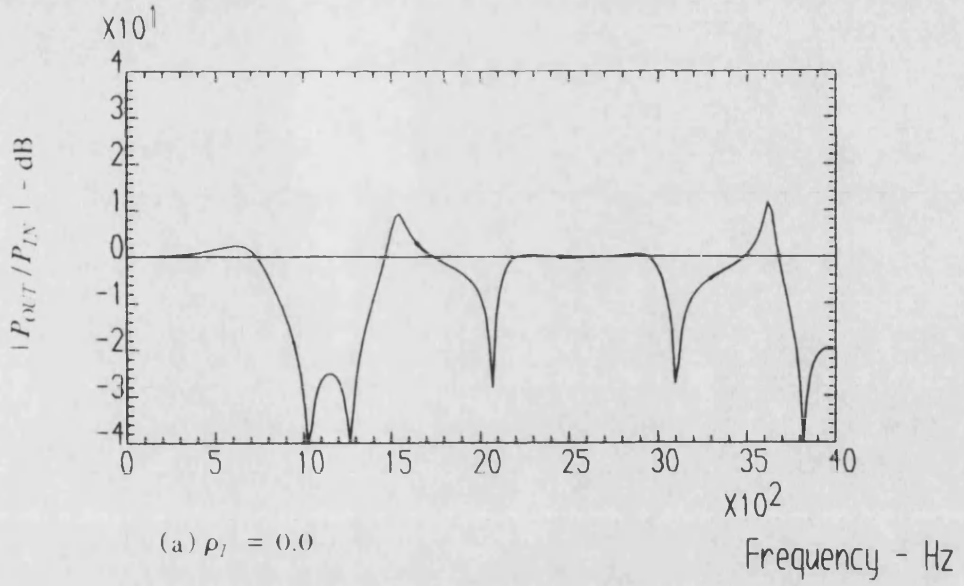

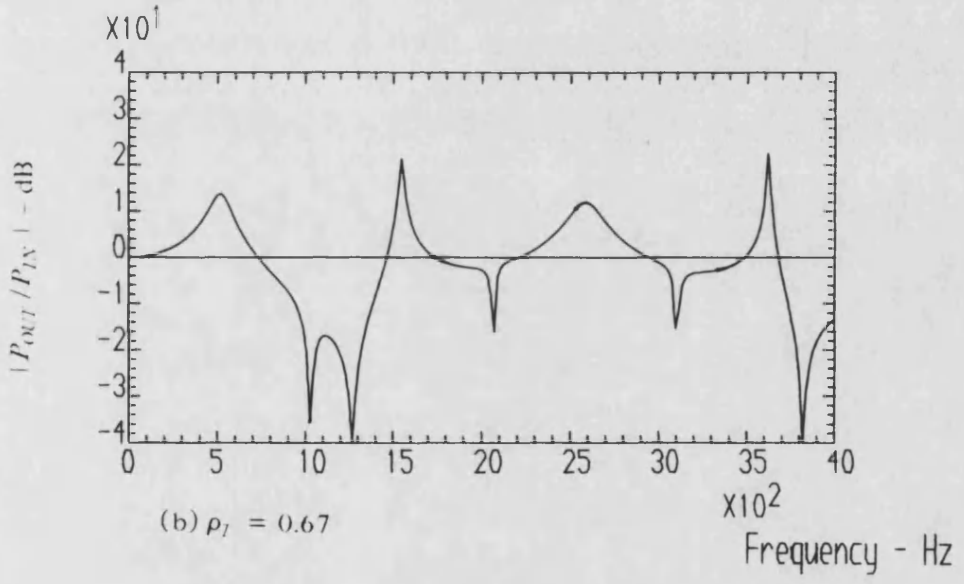

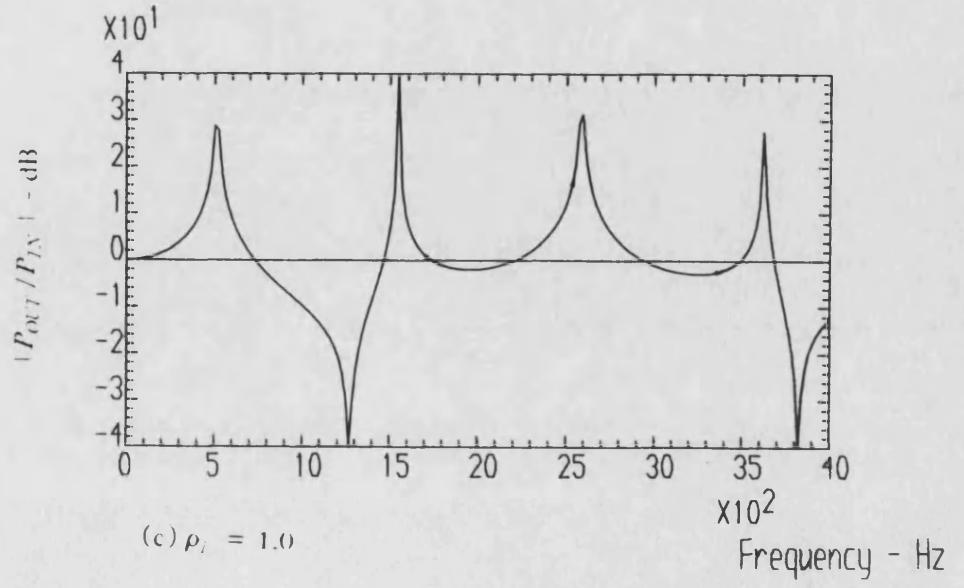

Fig. 9.10 **Ratio of Outlet Pressure Ripple Amplitude to Inlet Pressure Ripple Amplitude for Quincke Tube, for different Termination Impedances**

CHAPTER 10

CONCLUSIONS

The work reported in this thesis is mainly concerned with the development of a new technique for the measurement of the source flow ripple and source impedance of hydraulic pumps and motors. The method is based upon the analysis of the standing wave characteristics of the pressure ripple in a rigid pipe. By measuring the pressure ripple at several points in the pipe it is possible to calculate the reflection coefficient at the termination, and hence calculate the termination impedance. However, it is not possible to isolate the pump flow ripple and source impedance by this means, and further steps need to be taken. An earlier method developed at the University of Bath, commonly known as the 'Hydraulic Trombone' technique, employed a circuit in which the pump discharged into a variable length of pipe. By measuring pressure ripple at several points in the pipe for several different pipe lengths, the source flow ripple and source impedance could be evaluated by means of a complex mathematical curve fitting procedure. This technique produced some good results, but was time-consuming in data acquisition and data reduction, and under certain conditions it proved difficult to obtain reliable results.

The new method is known as the 'Secondary Source' technique, and employs a second source of fluid-borne noise which is mounted in the same circuit as the pump under test, at the opposite end of the pipe into which the pump discharges. By analysis of the pressure standing wave produced by this secondary source in the pipe, the pump source impedance can be determined. Once this is known, the source flow ripple can then be evaluated by analysis of the pressure standing wave produced by the pump under test.

A wide range of tests were performed on several different pumps, and the test technique was found to be successful. Tests could be performed quickly; a typical experimental test took between 5 and 15 minutes, excluding time taken in setting up and 'warming up' the apparatus, and the computer-based data reduction took 5 minutes or less. Accurate and repeatable results were obtained, and the test was versatile and successful under most conditions. Two different types of secondary FBN source were employed, these being an axial piston pump and a simple rotary valve arranged to provide an intermittent bleed flow. The axial piston pump was found to be successful, as it produced a broad band of stable pressure ripple. The rotary valve was also effective, but the frequency range of the pressure ripple produced by it was limited to below 1 kHz with accurate

measurement being very difficult above this frequency.

Source flow ripple results for axial piston pumps, obtained using the Secondary Source technique, conform well to the form expected from such pumps, displaying the characteristic reverse flow spike followed by a damped oscillation. From tests on external gear pumps, the source flow ripple is shown to be strongly dependent upon the geometry of the relief grooves.

The test method can also be adapted to the measurement of the impedance characteristics of components such as valves and accumulators. Tests on an accumulator yielded accurate results which show good correlation with the theoretical model. Results for a simple restrictor valve, a pressure compensated flow control valve and a single stage relief valve show that the modelling of such valves as simple resistances, based on their steady state characteristics, is over-simplistic. Fluid compressibility and inertia, valve vibration and the characteristics of the circuit downstream of the valve are all found to have an influence, but if the effect of these is measured and allowed for, the net valve impedance does indeed show good correlation with the simple resistive model. Tests were performed on some two-stage relief valves, and their impedance characteristics are shown to be very complex. Mathematical models are developed for these valves, and some qualitatively similar features are apparent in the experimental and modelled results.

A method was also developed for the accurate assessment of the speed of sound in the fluid, from which the effective bulk modulus could be evaluated. The method is based upon the analysis of the transfer function relationships between three pressure ripple measurements in a rigid pipe, and was applied as an integral part of the 'secondary source' technique. Good results are obtained using this technique, and it is found that there is good agreement between the experimentally predicted bulk modulus and the values derived from the fluid manufacturer's empirical fluid properties data.

A computer-based simulation package for predicting the fluid-borne noise characteristics of hydraulic circuits was developed. This package is able to simulate circuits of a high degree of complexity; the accuracy of such simulations is strongly dependent on the validity of the modelled characteristics of the individual circuit components. The validity of the simulation package is investigated by comparison with experimental pressure ripple measurements in a range of simple circuits, and good correlation is achieved. An empirical model for the flow ripple from an axial piston pump was developed for use with this package.

Finally, the effectiveness of several different techniques for the reduction of fluid-borne noise is discussed, with reference to simulations and to experimental results obtained using the 'secondary source' method. It is shown that a standard accumulator would be unsuitable as a high frequency pulsation damper, and that a simple asymmetric pipe loop, known as a 'Herschel-Quincke tube', might be effective but could be difficult to apply in practice.

10.1. Recommendations for Further Work

The work reported in this thesis highlights a number of different areas in which further research could be fruitful.

The 'Secondary Source' method could be further refined, with the aim of its proposal as a standard technique, perhaps as an addition to the 'High Impedance Pipe' method, which has already been adopted as a British Standard [25]. In order to assess the flexibility of the technique it could be applied to a range of problems, such as pump suction line flow ripple or motor flow ripple. Different classes of pump or motor, perhaps using different types of fluid, could also be tested.

Further work could be aimed at extending the bandwidth of the pulse generator. It is thought that the main factor limiting its bandwidth is the inductive effect due to the inertia of the fluid within the slots. If this inductance could be reduced then the frequency range could be increased. A bandwidth of 2-3 kHz would be desirable for use with the Secondary Source method.

The mathematical modelling of two stage relief valves, and other complex valves, could be extended further. To do this, it would probably be desirable to have the facilities to measure the pressure ripple in the internal chambers of the valve and the movement of the poppets. This analysis could be linked with simulation performed on the HASP simulation package [52].

The 'PRASP' simulation program could be extended and improved by development of a wider range of more accurate models, and the evaluation of the characteristics of a wide range of flexible hoses.

Further work could be undertaken on the measurement of the speed of sound. It has been shown that, for mineral oil at high pressure, the speed of sound can be predicted accurately from fluid properties data. However, this may not be the case at lower pressures, where air release may cause a significant reduction in the effective bulk modulus. Also, detailed information may not be available for the properties of synthetic fluids or hybrid fluids such as oil/water emulsions.

There is scope for the reduction of the flow ripple characteristics of positive displacement pumps. One possibility might be the development of variable port-plate timing for axial piston pumps. If the opening of the discharge port can be delayed, the fluid in the cylinder can be pre-compressed before it is exposed to the high pressure port. The correct degree of precompression could virtually eliminate the flow ripple backflow, but the delay angle required would be strongly dependent on the load pressure and the swash angle. The possibility exists of providing a variable delay, perhaps using hydraulic or electro-hydraulic control based on measurement of the transient pressure in the cylinders. This might present some complex mechanical and control difficulties which would have to be overcome.

REFERENCES

[1] Bonacini, C.
'On Flow in Gear Pumps'
(Translation from Italian)
The Engineer - Official Journal of the Italian National Association of Engineers and Architects (ANIAI)
1961 - no. 9

[2] Yudin, E. M.
'Gear Pumps: Principal Parameters and their Calculation'
(Translation from Russian)
Pub. Nat. Lending Library for Science and Technology 1967

[3] Bihendi, I.M., Foster, K., Taylor, R.
'Computer Predictions of Cyclic Excitation Sources for an External Gear Pump'
I. Mech. E. Seminar - Computer Aided Design in High Pressure Hydraulic Systems
London, Nov. 1983

[4] Molton, G.R.
'Techniques for Reducing Fluid Borne Noise from Gear Pumps and their Circuits'
7th Int. Fluid Power Symposium, Bath, England, Sept. 1986

[5] Foster, K., Hannan, D.
'Fundamental Fluidborne and Airborne Noise Generation of Axial Piston Pumps'
I. Mech E. conference- Quiet Oil Hydraulic Systems
London Nov. 1977

[6] Kojima, E., Shinada, M.
'Characteristics of Fluid Borne Noise Generated by Fluid Power Pump (3rd report, Discharge Pressure Pulsation of external gear Pump)'
Bulletin of J.S.M.E., vol. 27, no. 232, Oct. 1984

[7] Darling, J.
'Piston Cylinder Dynamics in Oil Hydraulic Axial Piston Pumps'
PhD Thesis, University of Bath, 1986

[8] Butler, M.D.
'Pressure Ripple Propagation in Hydraulic Systems'
PhD thesis, University of Bath, 1983

[9] Tilley, D.G., Butler, M.D.
'The Generation and Transmission of Fluid Borne Pressure Ripple
in Hydraulic Systems'
I. Mech. E. seminar- Quieter Oil Hydraulics
London, October 1980

[10] Bowns, D.E., McCandlish, D.
'Pressure Ripple Propagation'
I. Mech. E. Conf.- Quiet Oil Hydraulic Systems
London, Nov. 1977

[11] Edge, K.A., Tilley, D.G.
'The Use of Plane Wave Theory in the Modelling of Pressure Ripple
in Hydraulic Systems'
Trans. Inst. M.C., vol. 5, no. 4, 1983

[12] Foster, K., Parker, G.A.
'Transmission of Power by Sinusoidal Wave Motion Through Hydraulic Oil
in a Uniform Pipe'
Proc. Inst. Mech. Engrs., 1964-65, vol. 179 pt. 1 no. 19

[13] Brown F.T.
'The Transient response of Fluid Lines'
Journal of Basic Engineering, Trans. A.S.M.E., Dec. 1962

[14] Margolis, D.L., Brown, F.T.
'Measurement of the Propagation of Long-Wavelength Disturbances through
Turbulent Flow in Tubes'
Journal of Fluids Engineering, Trans. A.S.M.E., March 1976

[15] Uchida, S.
'The Pulsating Viscous Flow Superimposed on the Steady Laminar Motion of Incompressible Fluid in a Circular Pipe'
Z.A.M.P., 1956, 7(5), 403-421

[16] Wylie, B.E., Streeter, V.L.
'Fluid Transients'
FEB Press, Ann Arbor, 1982

[17] Stecki, J.S., Davis, D.C.
'Fluid Transmission Lines - Distributed Parameter models'
Part 1 - 'A Review of the State of the Art'
Proc. Instn. Mech. Engrs., vol. 200, no. A4, 1986

[18] Willekens, F.A.M.
'Fluid Borne Noise in Hydraulic Systems'
1st European Fluid Power Conference
East Kilbride, Scotland, 1973

[19] Chipman, R.A.
'Theory and Problems of Transmission Lines'
Schaum Outline Series, 1968

[20] Unruh, D.R.
'Outlet Pressure Ripple Measurement of Positive Displacement Hydraulic Pumps'
Nat. Conf. on Fluid Power, Chicago, Oct. 1975

[21] Szerlag, S.F.
'Rating Pump Fluidborne Noise'
S.A.E. Paper 750830, Sept. 1975

[22] Larsson, P., Palmberg, J., Weddfelt, K.
'Analysis and Measurement of Pressure Ripple of Fluid Power Pumps'
8th IASTED Int. Symposium, Taormina, Italy, Sept. 1986

[23] Bowns, D.E., Edge, K.A., McCandlish D.
'Factors Affecting the Choice of a Standard Method for the Determination of Pump Pressure Ripple'
I. Mech. E. seminar- Quieter Oil Hydraulics
London, October 1980

[24] Bowns, D.E., Edge, K.A., Tilley, D.G.
'The Assessment of Pump Fluid Borne Noise'
I. Mech. E. Conf.- Quiet Oil Hydraulic Systems
London, Nov. 1977

[25] 'Methods for Determining Pressure Ripple Levels Generated in Hydraulic Fluid Power Systems and Components'
Part 1 - 'High Impedance Method for Pumps'
British Standard no. 6335, 1983

[26] Wing, T.J.
'The Fluid-Borne Noise Characteristics of Hydraulic Components and their Measurement'
PhD Thesis, University of Bath, 1982

[27] Edge, K.A., Wing, T.J.
'The Measurement of the Fluid Borne Pressure Ripple Characteristics of Hydraulic Components'
Proc. Inst. Mech. Engrs., 1983, vol. 197

[28] Davidson, L., Taylor, D.W.
'The Internal Impedance of Positive Displacement Pumps: Experimental Determination and Effects on System Noise'
Nat. Conf. on Fluid Power, Cleveland, October 1976

[29] Fielding, D., Taylor, R., Foster, K.
'Notes on the Selection of a Standard Delivery Condition for the Theoretical Prediction and Experimental Measurement of Pressure Ripple'
5th Int. Fluid Power Symposium, Durham, England, Sept. 1978

[30] Freitas, F.J.T.
'The Generation and Transmission of Pressure Fluctuations in Pump Suction Lines'
PhD Thesis, University of Bath, 1982

[31] Tilley, D.G.
'The Measurement of Transient Flow in High Pressure Hydraulic Systems'
PhD Thesis, University of Bath, 1976

[32] Edge, K.A.
'The Theoretical Prediction of the Impedance of Positive Displacement Pumps'
I. Mech. E. seminar- Quieter Oil Hydraulics
London, October 1980

[33] Johnston, D.N.
'Program Documentation for the 'Secondary Source' Method and the 'Pressure Ripple Automatic Simulation Package''
Report no. 883, School of Mech. Eng., University of Bath, 1987

[34] Trikha, A.K.
'An Efficient Method for Simulating Frequency-Dependent Friction in Transient Fluid Flow'
Journal of Fluids Eng., Trans. A.S.M.E., March 1975

[35] Waller, E.J.
'Fundamental Analysis of Unsteady Pressure Variations in Pipeline Systems'
Oklahoma Eng. Exp. Station Pub. no. 92, 1954

[36] Pearsall, I.S.
'The Velocity of Water Hammer Waves'
Proc. Inst. Mech. Engrs., 1965-66, vol. 180 pt. 3E

[37] Longmore, D.K.
'The Transmission and Attenuation of Fluid Borne Noise in Hydraulic Hose'
I. Mech. E. Conf.- Quiet Oil Hydraulic Systems
London, Nov. 1977

[38] Longmore, D.K., Tuc, B.
'Reduction of Fluid Borne Noise in Hydraulic Circuits by means of Flexible Hoses'
I. Mech. E. seminar- Quieter Oil Hydraulics
London, October 1980

[39] Tuc, B.
'The Use of Flexible Hoses for Reducing Pressure Ripple in Hydraulic Systems'
PhD Thesis, University of Bath, 1981

[40] Johnson, B.L., Wandling, D.E.
'Transfer Functions and Input Impedances of Pressurised Piping Systems'
Journal of Basic Eng., Trans. A.S.M.E., June 1967

[41] Wylie, E.B.
'Resonance in Pressurised Piping Systems'
Journal of Basic Eng., Trans. A.S.M.E., December 1965

[42] Henderson, A.R., Whitson, R.J.
'New Developments in the Measurement and Analysis of Fluid-borne Noise in Hydraulic Systems'
Dep't of Trade and Industry Publication,
N.E.L., East Kilbride, 1986

[43] B.H.R.A. Publication.
'Quieter Fluid Power Handbook'
B.H.R.A. Fluid Engineering, Cranfield, Bedford

[44] Theissen, H.
'Volumenstrompulsation von Kolbenpumpen'
Oilhydraulik und Pneumatik 24 (1980) No. 8

[45] Whitson, R.J.
'The Measurement of Acoustic Properties and Transmission Loss of components in Oil Hydraulic Pipe Systems using a Two-Point Technique'
2nd Int Conf on Acoustic Intensity,
CETIM, Senlis (France), Sept 1985

[46] Bolleter, U.
'Using Transfer Function Measurements to Determine Energy Propagation in Fluid Lines, with Application to Centrifugal Pump Systems'
International Congress on Recent Developments in Acoustic Intensity Measurement
CETIM, Senlis (France), 1981

[47] Mitchell, G.J.
'Design of a Variable Speed Test Rig and an Investigation of Fluid Borne Noise'
MSc Thesis, University of Bath, 1979

[48] Davidson, L.C.
'The Internal Impedance of Centrifugal and Positive Displacement Pumps'
A.S.M.E. conf.- Noise and Fluids Eng., Atlanta, Georgia, Nov-Dec 1977

[49] Centre Technique des Industries Mechaniques
'Les Memoires Techniques de CETIM: Etude du Comportement Dynamique des Lignes Hydrauliques'
September 1976

[50] McCloy, D., Martin, H.R.
'Control of Fluid Power: Analysis and Design'
2nd edition, Ellis Horwood, 1980

[51] Lichtarowicz, A., Duggins, R.K., Markland, E.
'Discharge Coefficients for Incompressible Non-Cavitating Flow through Long Orifices'
Journal Mech. Eng. Sci., Vol. 7 No. 2, 1965

[52] Wang, L.
Phd Thesis (to be submitted), University of Bath

[53] Brown, F.T., Margolis, D.L., Shah, R.P.
'Small Amplitude Frequency Behaviour of Fluid Lines with Turbulent Flow'
Journal of Basic Eng., Trans. A.S.M.E., December 1969

[54] Shemer, L., Kit, E., Wygnanski, I.
'On the Impedance of the pipe in Laminar and Turbulent Pulsating Flows'
Exps in Fluids 3, 185-189 1985

[55] Bowns, D.E., Tomlinson, S.P., Dugdale, S.K.
'Progress Towards a General Purpose Hydraulic Simulation Language'
6th Int. Fluid Power Symposium, Cambridge, U.K., April 1981

[56] Lipscombe, B.
'The Reduction of Gear Pump Pressure Ripple by Source Flow Modification'
PhD Thesis, University of Bath, 1986

[57] Whitson, R.J.
'The Measured Transmission Loss Characteristics of some Hydraulic Attenuators'
I. Mech. E. seminar- Quieter Oil Hydraulics
London, October 1980

[58] Andersson, B.
'A New Effective Way to Reduce Fluid Borne Sound to Avoid Problems with Structure Borne Noise'
Int. Conf. on Fluid Power
Tampere University of Technology, Finland, March 1987

[59] Stewart, G.W.
'The Theory of the Herschel-Quincke Tube'
Physical Review, Vol. 31, April 1928

APPENDIX 1

DETAILS OF COMPONENTS

Pump 'A'	REYROLLE HYDRAULICS model A200 Variable capacity axial piston swash plate pump Displacement 0 - 32.8 cm^3/rev 7 cylinders
Pump 'B'	LUCAS model HD 900 Axial piston swash plate pump Displacement 68 cm^3/rev 7 cylinders
Pumps 'C'	SUNDSTRAND HYDRATEC External gear pumps (7 units) Displacement 14.8 cm^3/rev (16.1 cm^3/rev) 9 teeth (12 teeth)
Pumps 'D1', 'D2'	COMMERCIAL HYDRAULICS model P50 External gear pumps Displacement 82 cm^3/rev 10 teeth Unit 'D1' - bidirectional thrust plates Unit 'D2' - unidirectional thrust plates
Pump 'E'	SPERRY VICKERS model 25V Balanced vane pump Displacement 81 cm^3/rev 10 vanes

Pump 'A' was driven by a constant speed electric motor at 1500 rev/min. Pumps 'B', 'C', 'D' and 'E' were driven by a variable speed hydrostatic transmission (0-3000 rev/min).

Accumulator 'A1'	GREER MERCIER type BA1633 bladder type nitrogen filled accumulator capacity 1.14 l max. pressure 350 bar
Valve 'V1'	ASHFORD type 115A C/S needle valve size 3/4" bsp
Valve 'V2'	ABEX DENISON type 2F1C03-01-A-5-C pressure compensated flow control valve flow range 0-111 l/min max. pressure 350 bar
Valve 'V3'	STERLING HYDRAULICS type A1B 125 single stage cartridge relief valve flow range 0-200 l/min cracking pressure 0.5-50 bar max. pressure 350 bar
Valve 'V4'	STERLING HYDRAULICS type A3A 125 pilot operated poppet type cartridge relief valve flow range 0-200 l/min cracking pressure 2-350 bar
Valve 'V5'	REXROTH type DB 20-3-30 pilot operated poppet type relief valve flow range 0-600 l/min

A1.1. Details of Instrumentation

Pressure Transducers

VIBROMETER type 6QP500 piezoelectric pressure transducers

max. working pressure	470 bar
max. working temperature	240° C
linearity	< ±1%

natural frequency	67 kHz
sensitivity	approx. 7 pC/bar

Charge Amplifiers

type: custom built	
gain	approx. 10 mV/pC
frequency response (3 dB)	1.6 Hz - 340 kHz

Note: each pressure transducer/charge amplifier combination was calibrated individually.

Frequency Response Analyser

SOLARTRON model 1250	
including Synchroniser unit 12501	
frequency range	1 mHz - 65 kHz
2 input channels	
output resolution	0.01 dB, 0.01°
output accuracy	±0.03 dB, ±0.3°

(note: the accuracy is strongly affected by the stability of the signal and the shaft speed. It was found that accurate results could be obtained below 600 Hz, but considerable scatter was obtained above this frequency.)

Digital Spectrum Analyser (DSA)

HEWLETT PACKARD model 3582A	
frequency range	0.02 Hz - 25 kHz
2 input channels	
amplitude (linear or log.) and phase output	
output resolution	0.1 dB, 1°
output accuracy:	
single channel measurements	±0.5 dB, ±10°
transfer function measurements	±0.8 dB, ±5°

(note: the accuracy can be increased by signal averaging)

APPENDIX 2

DESCRIPTION OF PULSE GENERATOR

Fig. a2.1 shows a sectional view of the assembled Pulse Generator (PG). Basically, it consists of a stepped shaft which is free to rotate in a housing. The shaft is driven by an electric motor. The housing block has two main ports, the high pressure (inlet) port on the side, and the low pressure (return) port on the end, concentric with the shaft. The two smaller ports are normally linked together, and serve to provide a drain path from one end of the shaft to the other. The shaft is hollow over part of its length, and has a small narrow slot, as shown, cut between the inside and outside. The high pressure port is connected to the shaft housing by a similar slot, so that once every revolution of the shaft the two slots meet up. In this way, a drain path is created, so that with the shaft rotating at a constant speed, a periodical flow pulse of short duration occurs once for each revolution.

Four grooves are cut around the circumference of the shaft. The two inner grooves are connected to the high pressure port via two small holes in the housing block. The purpose of these grooves is to equalise the pressure around the shaft circumference, in order to reduce any lateral force on the shaft, and help to prevent hydraulic lock. A pressure gradient will occur around the slot in the shaft; except when the slots in the shaft and housing meet, the pressure at the shaft slot will be high so there will be a leakage flow and a pressure variation around this area. This pressure variation is limited to a small area, however, by the circumferential grooves, so the resultant lateral force will be small (approximately 2 kN at an inlet pressure of 200 bar). A leakage flow occurs from the two inner circumferential grooves to the ends of the large diameter section of shaft, and this flow ensures that there is a continuous film of oil around the shaft in order to provide hydrodynamic lubrication. A shaft/housing clearance of 25 μm (10^{-3} in) was used.

The longitudinal position of the shaft in the housing is maintained by the step change in diameter. This behaves as a hydrostatic thrust bearing. The outlet pressure acts on a differential area between the end face and the annular area of the shaft step, resulting in a net force. This force is small but sufficient to maintain the shaft *in situ*.

The smaller diameter shaft section fits in a clearance hole in the housing. This region is maintained at outlet line pressure, and a lip seal is fitted to prevent escape of fluid. The seal is held in place by a retaining disc.

The shaft protrudes from the housing block and is coupled to a small electric motor, with a constant speed of 1500 rev/min. The motor used was rated at 2 hp (1.5 kW), though a significantly lower rating could be used, the power requirement of the PG being estimated at a maximum of roughly 300 W. A magnetic pick-off was fitted to the shaft assembly, providing one pulse per revolution to correspond to the single flow pulse produced by the PG.

The housing was manufactured from steel, and the shaft from brass, in order to help prevent seizure of the components should a metal-to-metal bearing contact arise.

With the PG driven at 1500 rev/min, the flow ripple has a fundamental frequency of 25 Hz. Because of the very small mark-space ratio of the flow ripple pulse train, a large number of strong harmonics should be produced. The main factor limiting the number of significant harmonics in practice is likely to be the fluid inertia in the slots.

It was found in practice that the PG produced significant harmonics up to a frequency of approximately 1500 Hz (60 harmonics). The shaft speed was found to be extremely stable, so accurate harmonic analysis was possible over the whole of this range. The oversized electric motor with its high inertia was probably beneficial in this respect.

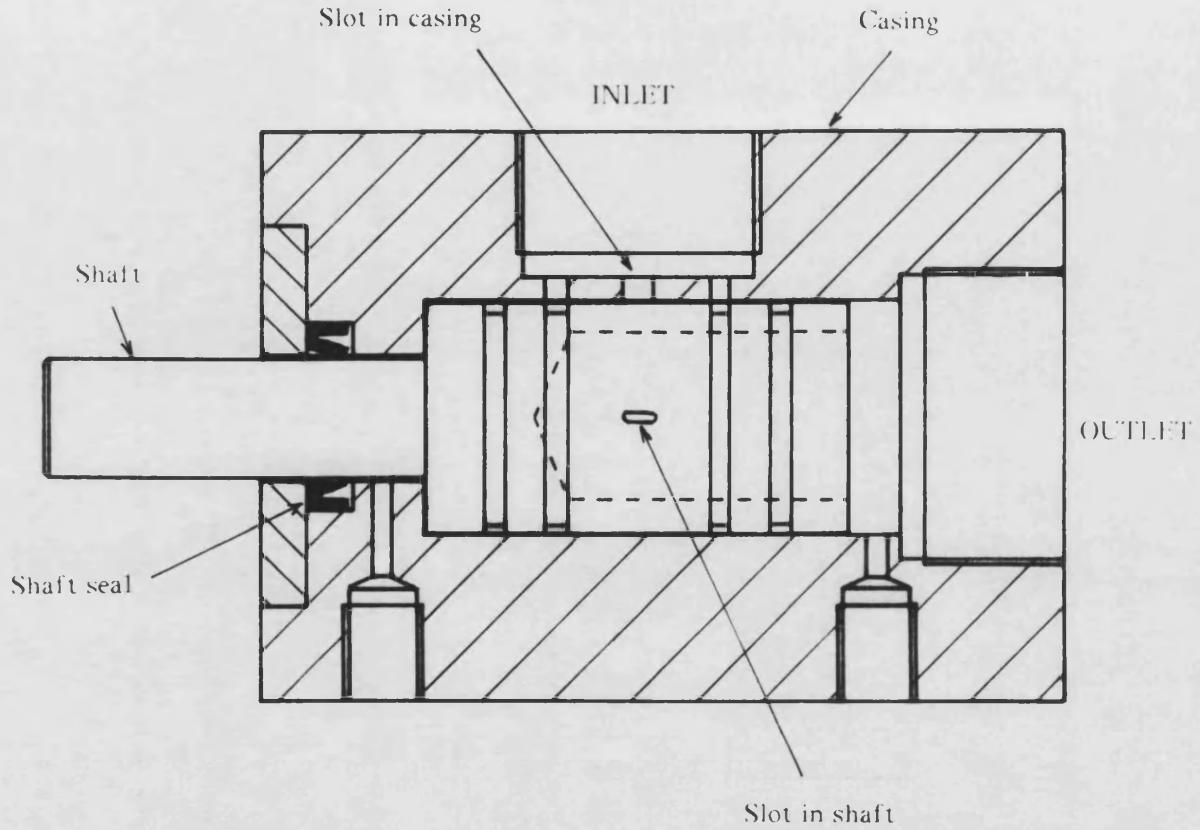

Fig. a2.1 Sectional View of Rotary Pulse Generator (approx. full scale)

APPENDIX 3

ALGORITHM USED FOR THE ANALYSIS OF THE PRESSURE STANDING WAVE

As described in section 4.3.1., it is necessary to fit a mathematical function to experimental pressure ripple data in order to estimate the form of the pressure standing wave, for any particular harmonic frequency. It is known (section 2.2.) that the standing wave can be described by the general equation

$$P_t(x) = Fe^{-\gamma x} + Ge^{\gamma x}. \qquad \ldots (a3.1)$$

The complex variables F and G need to be determined such that the sum of the squares of the absolute error between the experimental values $P_e(x)$ and the modelled values $P_t(x)$ for all the data points is at a minimum.

i.e. for m data points, it is required to minimise E, where

$$E = \sum_{k=1}^{m} \left| P_t(x_k) - P_e(x_k) \right|^2 \qquad \ldots (a3.2)$$

i.e.

$$E = \sum_{k=1}^{m} \left\{ P_t(x_k) - P_e(x_k) \right\} \left\{ \overline{P_t}(x_k) - \overline{P_e}(x_k) \right\} \qquad \ldots (a3.3)$$

where $\overline{P_t}$ and $\overline{P_e}$ denote the complex conjugates of P_t and P_e respectively.

It is necessary to find the values of F and G at which E is at a minimum. At this point the differentials of E with respect to the real and imaginary parts of F and G will be zero.

putting $F = c_1 + jc_2$ ... (a3.4)

$$G = c_3 + jc_4 \quad \text{... (a3.5)}$$

then $P_t(x) = c_1 e^{-\gamma x} + jc_2 e^{-\gamma x} + c_3 e^{\gamma x} + jc_4 e^{\gamma x}$ ... (a3.6)

and $\frac{\partial E}{\partial c_i} = 0$ for i = 1 to 4 ... (a3.7)

where

$$\frac{\partial E}{\partial c_i} = \sum_{k=1}^{m} \left\{ \left[\overline{P_t}(x_k) - \overline{P_e}(x_k) \right] \frac{\partial P_t(x_k)}{\partial c_i} + \left[P_t(x_k) - P_e(x_k) \right] \frac{\partial \overline{P_t}(x_k)}{\partial c_i} \right\}$$

$$= 2 \sum_{k=1}^{m} \mathrm{Re} \left\{ \left[P_t(x_k) - P_e(x_k) \right] \frac{\partial \overline{P_t}(x_k)}{\partial c_i} \right\} = 0 \quad \text{for i = 1 to 4} \quad \text{... (a3.8)}$$

$$\text{or } \sum_{k=1}^{m} \mathrm{Re} \left\{ P_t(x_k) \frac{\partial \overline{P_t}(x_k)}{\partial c_i} \right\} = \sum_{k=1}^{m} \mathrm{Re} \left\{ P_e(x_k) \frac{\partial \overline{P_t}(x_k)}{\partial c_i} \right\} \quad \text{... (a3.9)}$$

$$\text{now } \frac{\partial P_t(x)}{\partial c_1} = e^{-\gamma x} \quad \text{... (a3.10)}$$

$$\frac{\partial P_t(x)}{\partial c_2} = je^{-\gamma x} \quad \text{... (a3.11)}$$

$$\frac{\partial P_t(x)}{\partial c_3} = e^{\gamma x} \quad \text{... (a3.12)}$$

$$\frac{\partial P_t(x)}{\partial c_4} = je^{\gamma x} \quad \text{... (a3.13)}$$

$$\text{hence } P_t(x) = \sum_{j=1}^{4} \left[c_j \frac{\partial P_t(x)}{\partial c_j} \right]. \quad \text{... (a3.14)}$$

Therefore,

$$\sum_{k=1}^{m} \mathrm{Re} \left\{ \frac{\partial \overline{P_t}(x_k)}{\partial c_i} \sum_{j=1}^{4} \left[c_j \frac{\partial P_t(x_k)}{\partial c_j} \right] \right\} = \sum_{k=1}^{m} \mathrm{Re} \left\{ P_e(x_k) \frac{\partial \overline{P_t}(x_k)}{\partial c_i} \right\}. \quad \text{... (a3.15)}$$

The above equation can be expressed in matrix form as

$$\begin{bmatrix} s_{1,1} & s_{1,2} & s_{1,3} & s_{1,4} \\ s_{2,1} & s_{2,2} & s_{2,3} & s_{2,4} \\ s_{3,1} & s_{3,2} & s_{3,3} & s_{3,4} \\ s_{4,1} & s_{4,2} & s_{4,3} & s_{4,4} \end{bmatrix} \begin{bmatrix} c_1 \\ c_2 \\ c_3 \\ c_4 \end{bmatrix} = \begin{bmatrix} t_1 \\ t_2 \\ t_3 \\ t_4 \end{bmatrix} \quad \ldots (a3.16)$$

$$\text{where } s_{i,j} = \sum_{k=1}^{m} \mathrm{Re}\left\{ \frac{\partial \overline{P_t}(x_k)}{\partial c_i} \frac{\partial P_t(x_k)}{\partial c_j} \right\} \quad \ldots (a3.17)$$

$$t_i = \sum_{k=1}^{m} \mathrm{Re}\left\{ P_e(x_k) \frac{\partial \overline{P_t}(x_k)}{\partial c_i} \right\} \quad \ldots (a3.18)$$

$$\text{or } \mathbf{S}\,\mathbf{C} = \mathbf{T} \quad \ldots (a3.19)$$

This matrix equation can be solved in order to evaluate **C** using a standard Gaussian elimination routine. F and G can then be found using equations (a3.4) and (a3.5). This technique is similar to that used by Wing [26]. In this case, however, the model equation (a3.6) is linear with respect to coefficients c_{1-4}, so that equation (a3.14) can be applied. Where the equation is non-linear, it may be difficult or impossible to solve equation (a3.7) analytically, in which case an iterative solution must be sought.

A3.1. Calculation of the Source Flow Ripple

As stated in section 4.3., the flow ripple is calculated independently of the source impedance and the termination impedance. Z_S and Z_T are determined using pressure transfer function measurements, whereas Q_S requires single channel pressure measurements. From section 4.3.,

$$Q_S = \frac{F(Z_S + Z_0)(1 - \rho_S \rho_T e^{-2\gamma l})}{Z_S Z_0}. \quad \ldots (a3.20)$$

Provided that Z_S and Z_T are known from a previous analysis on transfer function data, then it is only necessary that F be determined from the experimental pressure readings for Q_S to be found.

now $\rho_T = \frac{G}{F} e^{2\gamma l}$ ... (a3.21)

thus $P_t(x) = F(e^{-\gamma x} + \rho_T e^{-\gamma(2l-x)})$. ... (a3.22)

In this case, there is only one complex variable to be determined.

Putting $F = c_1 + jc_2$ ... (a3.23)

then $P_t(x) = c_1(e^{-\gamma x} + \rho_T e^{-\gamma(2l-x)}) + jc_2(e^{-\gamma x} + \rho_T e^{-\gamma(2l-x)})$. ... (a3.24)

Using a similar technique to that above, we obtain the matrix expression

$$\begin{bmatrix} s_{1,1} & s_{1,2} \\ s_{2,1} & s_{2,2} \end{bmatrix} \begin{bmatrix} c_1 \\ c_2 \end{bmatrix} = \begin{bmatrix} t_1 \\ t_2 \end{bmatrix}. \quad \text{... (a3.25)}$$

It can be shown that, for m data points,

$$s_{1,1} \text{ and } s_{2,2} = \sum_{k=1}^{m} \left| (e^{-\gamma x} + \rho_T e^{-\gamma(2l-x)}) \right|^2$$

$$s_{1,2} \text{ and } s_{2,1} = 0$$

$$t_1 = \sum_{k=1}^{m} \mathrm{Re}\left\{ P_e(x_k) \overline{(e^{-\gamma x} + \rho_T e^{-\gamma(2l-x)})} \right\}$$

$$t_2 = \sum_{k=1}^{m} \mathrm{Re}\left\{ P_e(x_k) \overline{j(e^{-\gamma x} + \rho_T e^{-\gamma(2l-x)})} \right\} = \sum_{k=1}^{m} \mathrm{Im}\left\{ P_e(x_k) \overline{(e^{-\gamma x} + \rho_T e^{-\gamma(2l-x)})} \right\}$$

$$\text{therefore, } c_1 \sum_{k=1}^{m} \left| (e^{-\gamma x} + \rho_T e^{-\gamma(2l-x)}) \right|^2 = \sum_{k=1}^{m} \mathrm{Re}\left\{ P_e(x_k) \overline{(e^{-\gamma x} + \rho_T e^{-\gamma(2l-x)})} \right\}$$

$$c_2 \sum_{k=1}^{m} \left| (e^{-\gamma x} + \rho_T e^{-\gamma(2l-x)}) \right|^2 = \sum_{k=1}^{m} \mathrm{Im}\left\{ P_e(x_k) \overline{(e^{-\gamma x} + \rho_T e^{-\gamma(2l-x)})} \right\}$$

thus $F = c_1 + jc_2 = \frac{t}{s}$ ... (a3.26)

where $t = \sum_{k=1}^{m} \left\{ P_e(x_k) \overline{(e^{-\gamma x} + \rho_T e^{-\gamma(2l-x)})} \right\}$ ... (a3.27)

and $s = \sum_{k=1}^{m} \left| (e^{-\gamma x} + \rho_T e^{-\gamma(2l-x)}) \right|^2$. ... (a3.28)

Therefore it is not necessary to use matrix methods in this case.

APPENDIX 4

ALGORITHM USED FOR THE MATHEMATICAL MODELLING OF THE SOURCE IMPEDANCE OF A PUMP

It was stated in section 4.3. that the 'Secondary Source' method requires the mathematical modelling of the source impedance. The 'goodness of fit' between this model and the experimental values of source impedance is crucial to the accuracy of the source flow ripple results subsequently obtained.

The form of the model used is described in section 4.3.9.1. The modelled source impedance can be represented by the equation

$$Z_{St} = \frac{c_1(1+c_3/(j\omega c_2))}{j\tan(c_2\omega - jc_3)} \qquad \ldots (a4.1)$$

where $c_1 = \frac{\rho c_0}{A_p}$ $\qquad \ldots (a4.2)$

$$c_2 = \frac{l_p}{c_0} \qquad \ldots (a4.3)$$

$$c_3 = \alpha \qquad \ldots (a4.4)$$

The model coefficients c_1, c_2 and c_3 are determined such that the sum of the squares of the magnitude of the error between the experimental values and the modelled values is minimised.

The form of the source impedance is such that its amplitude can vary over a very wide range with frequency. This means that the error in the data points at those frequencies at which the source impedance is small will be almost completely masked by the error where Z_S is large. In order to avoid this problem, it is proposed that the least squares model should be applied to the source reflection coefficient as opposed to the source impedance. This is because the range of ρ_S is much smaller, and $|\rho_S|$ will be approximately equal to 1 at all frequencies.

Thus it is required to minimise E, where, for m data points,

$$E = \sum_{i=1}^{m} |\rho_{St} - \rho_{Se}|^2 \qquad \ldots (a4.5)$$

where $\rho_{St} = \dfrac{Z_{St} - Z_0}{Z_{St} + Z_0}$

$$= \frac{c_1(1+c_3/(j\omega c_2)) - j\ Z_0 \tan(c_2\omega - jc_3)}{c_1(1+c_3/(j\omega c_2)) + j\ Z_0 \tan(c_2\omega - jc_3)} \qquad \ldots (a4.6)$$

Where the error E is at a minimum, then $\dfrac{\partial E}{\partial c_i} = 0$ for $i = 1$ to 3. The expressions where $\dfrac{\partial E}{\partial c_1}$, $\dfrac{\partial E}{\partial c_2}$ and $\dfrac{\partial E}{\partial c_3}$ are equated to zero are termed the normal equations, and must be solved simultaneously in order to evaluate the optimum values of c_1, c_2 and c_3.

let $\rho_{St} = \dfrac{u}{v}$ $\qquad \ldots (a4.7)$

where $u = c_1(1+c_3/(j\omega c_2)) - j\ Z_0 \tan(c_2\omega - jc_3)$ $\qquad \ldots (a4.8)$

$$v = c_1(1+c_3/(j\omega c_2)) + j\ Z_0 \tan(c_2\omega - jc_3) \qquad \ldots (a4.9)$$

Thus the normal equations are represented by

$$\frac{\partial E}{\partial c_i} = 2\mathrm{Re} \sum_{k=1}^{m} (\overline{\rho_{St} - \rho_{Se}}) \frac{\partial \rho_{St}}{\partial c_i} = 0 \qquad \ldots (a4.10)$$

where $\dfrac{\partial \rho_{St}}{\partial c_i} = \dfrac{v\dfrac{\partial u}{\partial c_i} - u\dfrac{\partial v}{\partial c_i}}{v^2}$ $\qquad \ldots (a4.11)$

and $\dfrac{\partial u}{\partial c_1} = 1 + \dfrac{c_3}{j\omega c_2}$ $\qquad \ldots (a4.12)$

$$\frac{\partial v}{\partial c_1} = \frac{\partial u}{\partial c_1} \qquad \ldots (a4.13)$$

$$\frac{\partial u}{\partial c_2} = -\frac{c_1 c_3}{j\omega c_2^2} - j\omega Z_0 \sec^2(c_2\omega - jc_3) \qquad \ldots (a4.14)$$

$$\frac{\partial v}{\partial c_2} = -\frac{c_1 c_3}{j\omega c_2^2} + j\omega Z_0 \sec^2(c_2\omega - jc_3) \qquad \ldots (a4.15)$$

$$\frac{\partial u}{\partial c_3} = -\frac{c_1}{j\omega c_2} - Z_0 \sec^2(c_2\omega - jc_3) \qquad \ldots (a4.16)$$

$$\frac{\partial v}{\partial c_3} = -\frac{c_1}{j\omega c_2} + Z_0 \sec^2(c_2\omega - jc_3) \qquad \ldots (a4.17)$$

Equation (a4.6) is non-linear with respect to the coefficients c_1, c_2 and c_3 and so the normal equations cannot be solved directly. An iterative method must therefore be employed. The method used is based on the Newton-Raphson method and is described in detail by Wing [26].

Initial estimates of c_1, c_2 and c_3 are required in order to start the iteration. Corrections are then applied to these coefficients until the iteration converges to the solution. The values of these corrections are obtained by solution of the matrix equation

$$\mathbf{T} + \mathbf{S}\,\partial\mathbf{C} = \mathbf{0} \qquad \ldots (a4.18)$$

where $\mathbf{T}$ and $\partial\mathbf{C}$ are column matrices with 3 elements, and $\mathbf{S}$ is a square matrix with (3×3) elements.

The i_{th} term of $\mathbf{T}$ is given by

$$t_i = \frac{\partial E}{\partial c_i} = 2\mathrm{Re}\sum_{k=1}^{m}(\overline{\rho_{St} - \rho_{Se}})\frac{\partial \rho_{St}}{\partial c_i} \qquad \ldots (a4.19)$$

and the ij_{th} term of $\mathbf{S}$ is given by

$$s_{ij} = \frac{\partial^2 E}{\partial c_i \partial c_j} \approx 2\mathrm{Re}\sum_{k=1}^{m}\frac{\partial \rho_{St}}{\partial c_i}\overline{\frac{\partial \rho_{St}}{\partial c_j}} \qquad \ldots (a4.20)$$

The partial derivatives are evaluated at the estimation point. Iteration proceeds in this way until all the corrections have decreased to within a specified tolerance.

A4.1. Stability of Iteration

The curve fitting algorithm was applied to several sets of experimental source impedance results and was found to be convergent in most cases. Problems could be encountered under certain conditions, however, in which the iteration diverged or converged to a false result. Best results were obtained when the following criteria were satisfied:

a) The initial estimates of the coefficients were reasonably close to the solution.

b) The anti-resonant frequency was reasonably well-defined by the experimental points. Problems were encountered when the anti-resonant frequency was higher than the highest frequency of the experimental points, in which case the effective length was ill-defined. Under such conditions it was necessary to use an alternative, simpler model based solely on a lumped volume.

In order to improve the stability of the iteration, a relaxation technique described by Wing [26] was employed. This entailed evaluating the sum of squares error at each successive stage of the iteration, and comparing it with the error at the previous stage. If the error had decreased no action was taken and the iteration was continued. If the error had increased, however, this indicated that the iteration was diverging. The new values of the coefficients were then re-calculated from the previous values, but with the corrections halved, and the sum of squares error evaluated again. This was again compared with the error at the previous iteration. If the new error was less than the previous error, then the iteration process was continued, otherwise the corrections were repeatedly halved until either the error had decreased or a specified maximum number of halving operations had been performed, after which the iteration process was continued. This method was found to significantly increase the range of starting values for which the iteration was convergent, thus increasing the stability of iteration.

The relationship between the model coefficients and the sum of squares error can be visualised by considering Fig. a4.1. This shows a contour plot of the sum of squares error as a function of the pump discharge passageway diameter d_p (x-axis) and length l_p (y-axis). The model used in this case is simplified in that friction is ignored, such that c_3 is assumed to be zero. The model is applied to experimental results for 16 harmonics for pump 'E'. The point of minimum error can clearly be seen, where d_p = 36 mm and l_p = 0.2 m. The error increases steadily in all directions, and there are no localised minima to which the iteration could converge to provide false results. Therefore, provided that the initial estimate of c_1 and c_2 lay within the bounds of this graph, then the iteration should converge to the correct solution. As the graph covers quite a large range of

discharge lengths and diameters, it should generally be possible to obtain estimates within this region.

In the above example, the anti-resonant frequency is sufficiently well defined by the experimental points. Consider the case where the model is applied to just the first 6 harmonics of the same results on pump 'E'. These harmonics all lie below the anti-resonant frequency. The contour plot of the error is shown in Fig. a4.2. As can be seen, the point of minimum error is very poorly defined; instead there is a line of minimum error which follows a line of constant volume. Therefore, the model is able to estimate the discharge volume precisely, but the discharge length and diameter are poorly defined. In this case, a lumped parameter model representing the source impedance as a simple capacitance might be more acceptable.

Inclusion of the resistive coefficient c_3 was found not to have a significant effect on the stability of iteration. It is, in general, a minor term and is the least significant of the three coefficients. Therefore, the above analysis, where only two coefficients are considered, is applicable to the model with three coefficients.

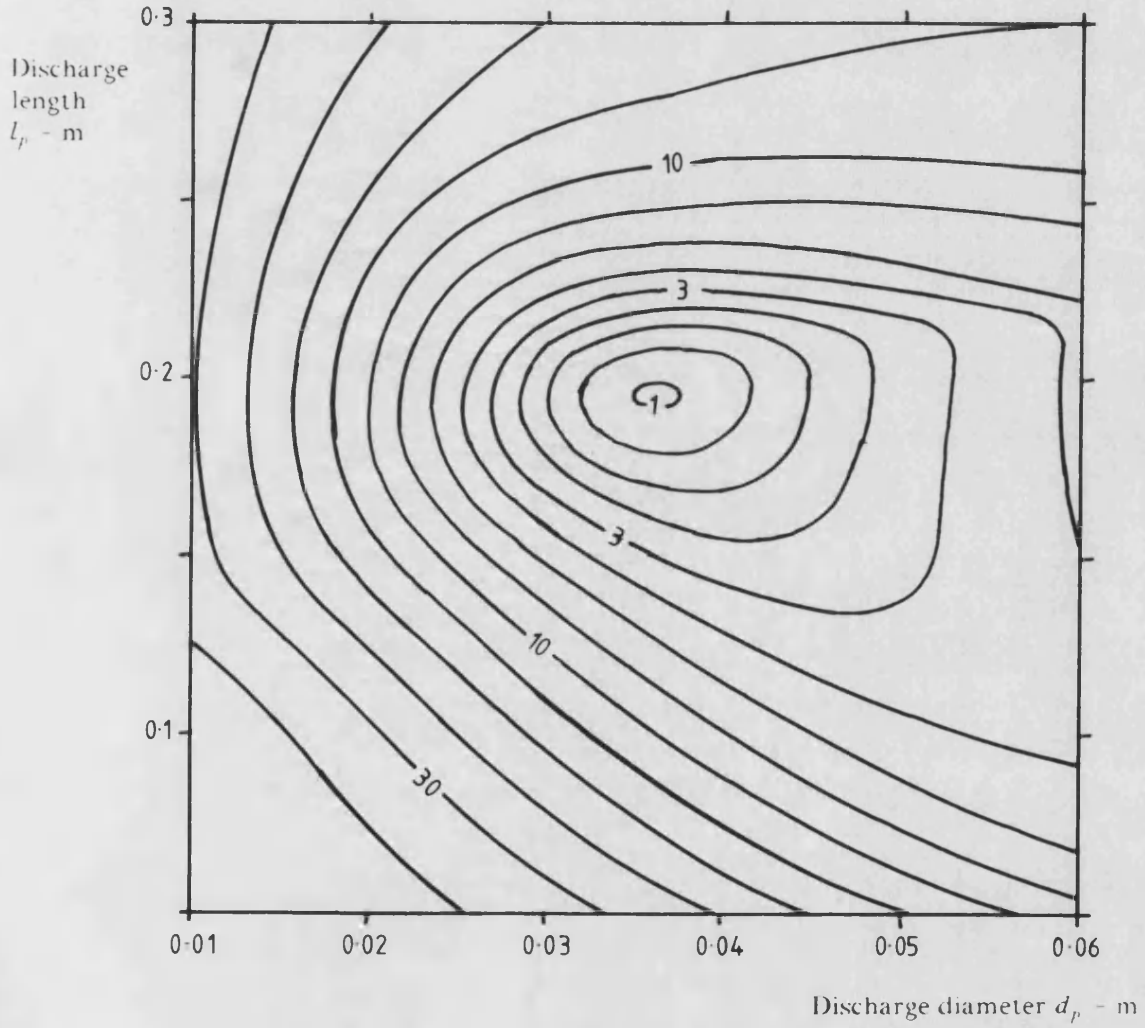

Fig. a4.1 Contour Plot showing Error in Source Impedance Model (14 harmonics)

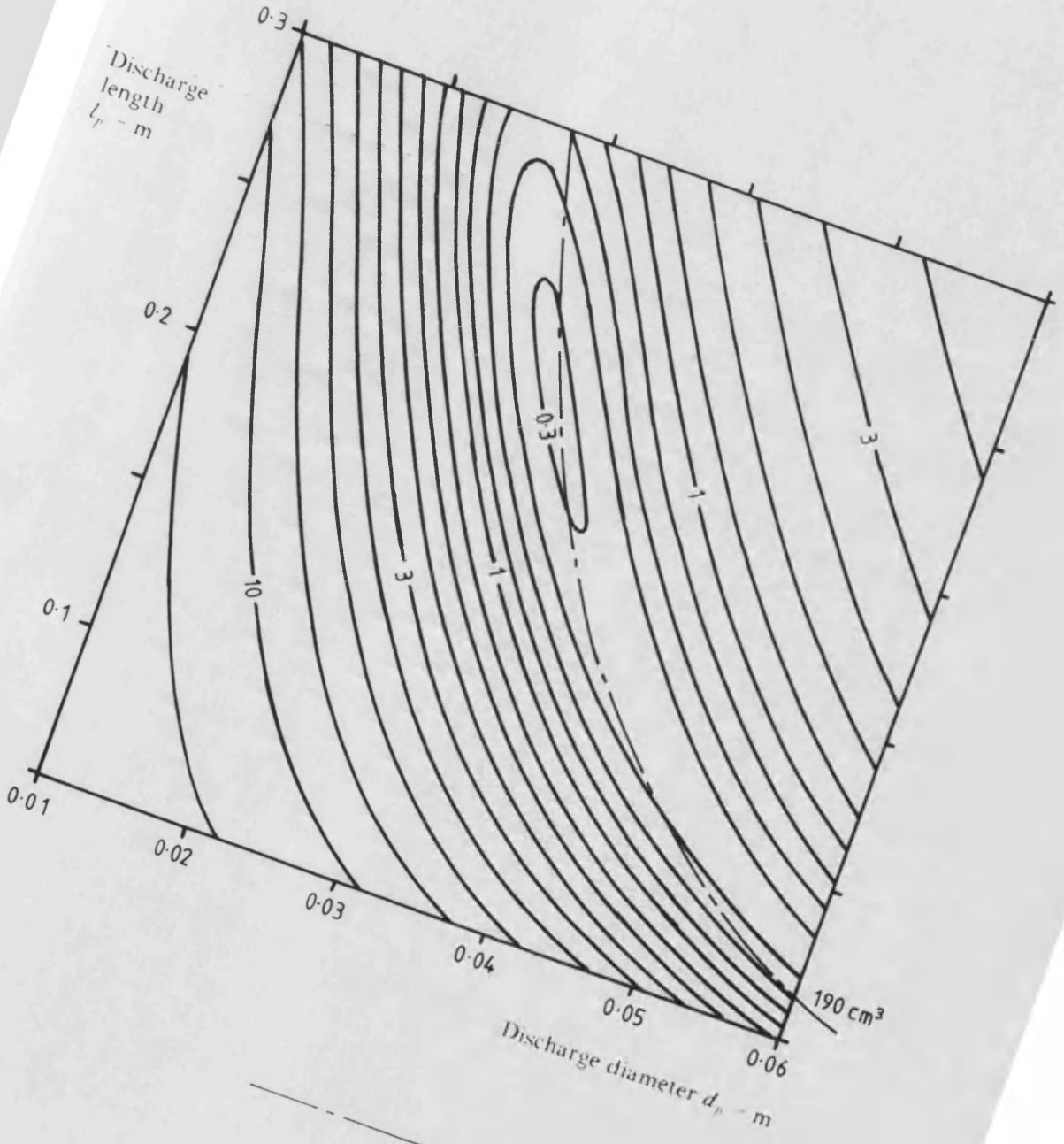

Fig. a4.2 Contour Plot showing Error in Source Impedance Model (6 harmonics only)